NIELS BOHR INSTITUTE
FACULTY OF SCIENCE
UNIVERSITY OF COPENHAGEN

PhD thesis

Susanne Lilja Buchardt

Basal melting and Eemian ice along the main ice ridge in northern Greenland

Academic advisor: Dorthe Dahl-Jensen

Submitted: 31/05/09

CENTRE FOR
ICE AND CLIMATE

Second edition

This is the second edition of my PhD thesis which was submitted for evaluation on 31 May 2009. The changes made in this second edition are correction of grammatical and typing errors and minor changes to a few figures.

Abstract

The variation of the basal melt rate and the location of the Eemian layer in the ice column are investigated along the ice divide between the NorthGRIP and the NEEM ice core drill sites in northern Greenland. At NorthGRIP an ice core was drilled in the period 1996–2004, and the stable isotope record (δ^{18}O) from this core is used to infer past accumulation rates at the site. Under the assumption that the present accumulation rate pattern in the area has remained unchanged through the last glacial cycle, this accumulation history is used to calculate the accumulation rates at other sites along the line. A Dansgaard-Johnsen model is then used to simulate the ice flow along the flow line from NorthGRIP to NEEM. One- and two-dimensional approaches are taken. The basal melt rates and other unknown flow parameters are determined using a Monte Carlo method. The Monte Carlo solution is constrained by isochrones revealed in radio-echo sounding images of the ice. The obtained results indicate a high spatial variability in the basal melt rate in the area, and values between zero and 25 mm/yr are found. The results indicate that there is little or no basal melting at NEEM. The location of the Eemian layer is determined using the Monte Carlo-determined flow parameters. The results obtained agree with observations at NorthGRIP and predict that a full Eemian record will be found at NEEM. The layer is estimated to be 70 m thick and located in the depth range 2230–2300 m, which is 200 m above bedrock.

Dansk resumé

Den rumlige variation af bundsmelteraten og placeringen af is deponeret under Eemtiden er undersøgt langs isdeleren i området mellem iskerneborestederne NordGRIP og NEEM i Nordgrønland. Ved NordGRIP blev der boret en iskerne til bunden i årene 1996–2004, og det stabile isotopforhold (δ^{18}O) herfra er brugt til at estimere akkumulationshistorien ved NordGRIP. Ved at antage, at akkumulationsmønsteret i området har været konstant over den sidste istidscyklus, kan man bruge denne akkumulationshistorie til at beregne nedbørshistorier for andre steder langs isdeleren. Denne akkumulationsmodel og en Dansgaard-Johnsen model er brugt til at simulere isflydningen langs med isdeleren i både en og to dimensioner. Smelteraterne ved bunden og en række andre flydeparametre er ubekendte og bestemmes ved hjælp af en Monte Carlo metode. Løsningen er bundet af observerede isochroner i isen, som kan ses på radarbilleder af iskappen. Resultaterne viser en stærkt varierende bundsmelterate langs profilet med værdier mellem 0 og 25 mm/yr. Ved NEEM er der fundet lav eller slet ingen smeltning. Placeringen af Eemlaget hen langs linien kan bestemmes ud fra de fundne flydeparametre. De beregnede dybder stemmer overens med observationerne ved NordGRIP, og ved NEEM forudsiges det, at isen fra hele Eemperioden er bevaret. Laget forudsiges at være 70 m tykt og befinde sig i dybdeintervallet 2230–2300 m, hvilket er 200 m over bunden.

Contents

Preface

This thesis is submitted in partial fulfillment of the requirements for the PhD degree at the University of Copenhagen, Denmark. The project was carried out at Centre for Ice and Climate at the Niels Bohr Institute, University of Copenhagen, and it was financed by The Danish Council for Strategic Research and granted through The Danish Council for Independent Research, Natural Sciences. It was supervised by Prof. Dorthe Dahl-Jensen, whose outstanding supervision and support throughout the project is greatly appreciated.

During the course of the study, I spent six months at The Center for Remote Sensing of Ice Sheets (CReSIS) at the University of Kansas in Lawrence, Kansas. I would like to express my thanks to Prof. Prasad Gogineni for making this visit possible and for providing excellent radar data. I would also like to thank Dr. Árný Sveinbjörnsdóttir for hosting me at the Institute of Earth Sciences during several short visits at The University of Iceland in Reykjavík.

In the summer of 2007 I participated for 5 weeks in the NorthGRIP to NEEM traverse in Greenland. Furthermore, a three-month leave was taken during the 2008/2009 Antarctic field season in order to participate in the West Antarctic Ice Sheet Divide ice core drilling project in Antarctica.

I would like to thank all my colleagues at the Centre for Ice and Climate for support and interesting collaborations on many projects, and especially Bo Vinther and Sune Olander Rasmussen for valuable input on several aspects of the thesis and the PhD study in general.

Finally, my very special thanks go to Héðinn Björnsson and Maria Mygind for continued encouragement and support throughout my PhD study and for many helpful discussions, suggestions, and corrections, especially during the final phase of the project, which have greatly improved the quality of the final manuscript.

Copenhagen, May 2009 Susanne Lilja Buchardt

Chapter 1

Motivation and outline

The cryosphere plays an important role in the dynamics of the global climate. The consequences of receding ice cover due to increasing global temperature are therefore far reaching and complex. One of these consequences is sea-level rise. At present global sea level is rising at a rate of 3.0 mm/yr and the contribution from the Greenland and Antarctic ice sheets has been estimated to 0.35 mm/yr (Shepherd and Wingham, 2007), based on estimated mass losses from Greenland and Antarctica of 100 and 25 Gt/yr, respectively. The relatively low contribution from Antarctica arises because thinning in West Antarctica is to some degree balanced by mass gain in East Antarctica due to increased snow accumulation. Furthermore, recent studies indicate that the present mass loss from the Greenland ice sheet could be even higher than the 100 Gt/yr suggested above (Chen et al., 2006; Rignot and Kanagaratnam, 2006).

Understanding the present and future changes of the Greenland ice sheet is thus crucial in order to assess future changes in global sea level. During the past decade, satellite radar and laser altimetry have been used to monitor changes in ice volume (see Shepherd and Wingham (2007) for an overview). However, the processes determining the mass balance of the Greenland ice sheet are complex, and a change in ice thickness can not readily be converted to a mass balance estimate, since other processes such as density changes and changes in flow also can contribute to the measured thickness changes. Therefore, the satellite data need to be combined with ice sheet models in order to determine the state of the Greenland ice sheet. Furthermore, models combined with proxy data or predicted changes in climate can be used to gain information on the mass balance in the past and future, respectively. They are also a great tool for investigating which processes are most important for the mass balance.

Ice is melting at the base in a large area in northern Greenland (Fahnestock et al., 2001a; Dahl-Jensen et al., 2003). Basal melting in northern Greenland was first suggested by C. Bull in 1956 (Hamilton et al., 1956). Bull used seismic data obtained during the British North Greenland Expedition 1952–1954 to conclude that the ice could be at the melting point at the base in the central part of north Greenland. This hypothesis was definitively confirmed in 2003 when the ice core drill penetrated the ice sheet at the NorthGRIP site and basal melt water was found. The geometry of observed internal layers in the ice indicates that the area of basal melting may be as large as $4{\cdot}10^5$ km^2 (Dorthe Dahl-Jensen, personal communication 2005). The basal melt rate is, however, highly variable over short distances, and in some areas it is as high as 5 cm/yr (Dahl-Jensen et al., 2003; Fahnestock et al., 2001a). Basal melting thus constitutes a significant part of the mass balance in this area where the surface accumulation rates can be as low as 10–15 cm/yr (Ohmura and Reeh, 1991).

As basal melting significantly influences both the mass balance and the flow properties of the ice, knowledge concerning the amount and spatial variability of the basal melting is important for the performance of thermo-mechanical ice sheet models used to model the changes of the Greenland ice sheet. The aim of this thesis is to map the basal conditions along the ice divide in northern Greenland between the NorthGRIP and NEEM ice core drill sites. More specifically, simple ice flow models and internal layers seen on radio-echo sounding images obtained over the ice sheet will be used to infer basal melt rates. A second aim of the thesis is to use the derived basal melt rates and the ice flow model to calculate the depth-age relationship along the ice ridge. This can be used to estimate where ice deposited during the Eemian interglacial 130–115 kyr b2k (before 2000 A.D.) is likely to be found. Obtaining a full unbroken Eemian record is the main objective of the NEEM ice core drilling project that commenced in 2007. The ice flow model and the derived basal melt rates will be used to investigate the depth-age relationship at NEEM and to predict the location and the thickness of the Eemian layer here. The area of study is the ice ridge between NorthGRIP and NEEM (see Fig. 1.1). The ice flows NNW along the ice ridge, and investigations will be done with one-dimensional (1D) models at six locations in the area and with a two-dimensional (2D) model along the ice ridge in the area between the two drill sites.

The structure of the thesis is outlined below.

Chapter 2 presents the radio-echo sounding data. In the first part of the chapter, a general introduction to the cause and nature of internal reflectors in the Greenland ice sheet is given, while the second part introduces the two data sets used in the present study.

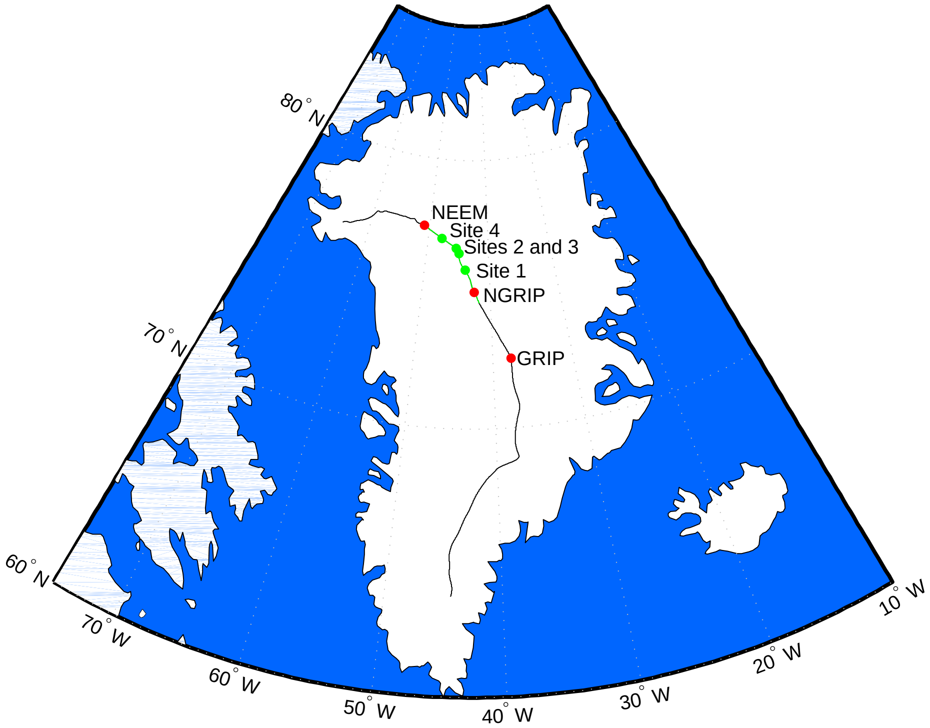

Figure 1.1: The ice divide in Greenland. Main ice core drill sites are marked in red, while green dots show other locations for which investigations have been carried out using the 1D ice flow model. The part of the ice ridge that has been investigated with the 2D model is shown in green.

Chapter 3 gives a description of the Dansgaard-Johnsen ice flow model used to simulate the ice flow along the ice divide in northern Greenland. Both one- and two-dimensional versions of the model are used in the present study. The accumulation model used to infer past accumulation rates in the area is also introduced, and the input data are described.

Chapter 4 introduces relevant concepts of inverse Monte Carlo theory and the random walk used to solve the problem at hand is derived.

Chapter 5 presents the results found from the model studies, while

Chapter 6 is a general discussion of the main results.

Chapter 7 summarizes the main conclusions, and gives suggestions for future studies in continuation of the present work.

Finally, the thesis also includes two appendices:

Appendix A contains supplementary figures illustrating the statistical properties of the sets of accepted model parameter values for the different inverse problems solved in the thesis.

Appendix B contains reprints of three manuscripts. Two of them are published and present results from studies similar to those presented in this thesis. The main results from these papers are briefly summarized in Section 5.5. The third manuscript is currently submitted for publication and deals with surface elevation changes inferred from stable isotopes. The gist of the paper is described in Section 3.1.4.

Chapter 2

Radio-echo sounding data

Today, radio-echo sounding data play an important role in glaciology. This chapter gives a short introduction to the causes of radar reflections within the ice sheets and presents the data sets used in the present study.

2.1 Internal layers in the ice

The glaciological investigation of the great ice sheets in Greenland and Antarctica using radar started in the early 1960s, but the first discoveries indicating that glacier ice could be transparent to electromagnetic radiation at radio frequencies were made in the 1930s (Gogineni et al., 1998). In 1946, aircraft pilots reported that radio altimeters were unreliable over the Antarctic ice. This led to an investigation by U.S. Army researchers, and in the late 1950s it was shown that a radar altimeter could be used to determine the thickness of a glacier (Waite, 1959; Waite and Schmidt, 1962). During the 1960s several radar systems were developed specifically for carrying out radio-echo soundings of polar ice sheets (Gogineni et al., 1998). Since then, many measurements have been carried out with different radar systems, and the radio-echo sounding (RES) data thus obtained have greatly increased our knowledge on smaller glaciers as well as the ice sheets. The ice thicknesses obtained with radar have been verified against ice core data and seismic and gravity-based methods (Drewry, 1975).

In addition to the echoes from the ice surface and the boundary between ice and the underlying material, the RES images reveal internal layers in the ice. Individual layers can be followed for hundreds of km in the images, and they have proven useful for determining flow fields (Weertman, 1976; Parrenin et al., 2006; Leysinger Vieli et al., 2007). In the present study, they will be used to infer basal melt rates and accumulation rate patterns.

2.1.1 The basic equations

The internal layers appear on the RES images because their electric properties differ from those of the surrounding ice. For an ice layer of thickness l and admittance[1] $Y + \Delta Y$ embedded in ice of admittance Y, the power reflection coefficient R is given by Paren and Robin (1975):

$$R = 4\sin^2\left(\frac{2\pi l}{\lambda_m}\right) \cdot \left|\frac{1}{2}\frac{\Delta Y}{Y}\right|^2, \tag{2.1}$$

where λ_m is the wavelength of the radio-waves in ice. Since

$$Y = i\omega C_0 \epsilon, \tag{2.2}$$

where i denotes the imaginary unit, ω is the angular frequency, C_0 is the geometrical capacitance, and ϵ is the complex permittivity of the ice, Eq. (2.1) may be rewritten as

$$R = 4\sin^2\left(\frac{2\pi l}{\lambda_m}\right) \cdot \left|\frac{1}{2}\frac{\Delta \epsilon}{\epsilon}\right|^2 \tag{2.3}$$

It is seen from Eq. (2.3) that layers of different power reflection coefficients must have different complex permittivities. Thus the studies of the complex permittivity of the ice may provide valuable information on the nature of the observed layers. Ice is a dielectric, and its complex permittivity is given by

$$\epsilon = \epsilon' + i\epsilon'', \tag{2.4}$$

where ϵ' is the dielectric constant and ϵ'' is the relative loss factor. The average permittivity of the ice increases with depth, but small scale stratified irregularities occur (Dowdeswell and Evans, 2004). Eq. (2.4) may also be written as

$$\epsilon = \epsilon'(1 - i\tan\delta), \tag{2.5}$$

where

$$\tan\delta = \frac{\epsilon''}{\epsilon'} = \frac{\sigma}{\omega\epsilon_0\epsilon'}. \tag{2.6}$$

Here δ is the phase angle between the displacement current and the total current in an alternating electric field, σ is the dielectrical conductivity (not to be confused with the direct current conductivity $\sigma_{d.c.}$, though this contributes to σ), and ϵ_0 is the permittivity of free space. $\tan\delta$ is known as the "loss tangent" because it describes the absorption of electromagnetic energy in the ice. From Eq. (2.5) it is seen that ϵ will be affected by changes in either the dielectric constant ϵ' or in the loss tangent (Evans, 1965; Bogorodsky et al., 1985).

---

[1] Admittance is the inverse of impedance.

2.1.2 The cause of internal reflections

There has been some dispute as to the cause of the changes in ϵ that give rise to radar reflections. Several authors conclude that the most likely cause of the shallow reflectors is changes in ϵ' due to density changes (Harrison, 1973; Paren and Robin, 1975; Clough, 1977), but Hammer (1980) and Hempel et al. (2000) find that changes in loss tangent caused by raised impurity levels from volcanic fallout is the best explanation. In the case of the deep reflectors there seems to be a general agreement that density changes alone cannot explain the strength of the observed reflections (Harrison, 1973; Paren and Robin, 1975). Paren and Robin (1975) find that changes in loss tangent is the most likely explanation for deep reflectors. This is supported by the works of Hammer (1980), Millar (1981), and Hempel et al. (2000), who find that reflectors and layers of increased acidity from major volcanic events are found at the same depths, and that the resulting changes in loss tangent are sufficient to explain the observed power reflection coefficients. However, Harrison (1973) and Fujita and Mae (1994) argue that the primary cause of the deep reflectors is changes in ϵ' due to changes in crystal orientation. Fujita et al. (1999) used the fact that the loss tangent, but not the dielectric constant, is frequency dependent to estimate the relative importance of changes in these two parameters. Through a two-frequency radar experiment carried out in East Antarctica they found that changes in the loss tangent dominate at intermediate depths while changes in fabric dominate at greater depths.

2.1.3 Interpretation of the internal layers

Layers where the permittivity changes are caused by variations in density or in impurity content are generally accepted to represent former deposition surfaces (Gudmandsen, 1975; Bogorodsky et al., 1985; Miners et al., 2002). This means that they are layers of equal age - *isochrones*. Thus the radar sections may provide valuable information on the ice flow field throughout the ice sheet. Generally, the shape of shallow isochrones is affected mostly by the spatial variability of the accumulation rate, while the deep layers often are shaped by bedrock topography and/or spatial variability of the basal melt rates (Dahl-Jensen et al., 2003). Furthermore, if layers have been dated from their observed depths at an ice core drill site, knowledge of the depth-age relationship can be derived for locations far away by following the internal layers (Fahnestock et al., 2001b). This information can be used when choosing new locations for deep ice core drilling as was the case with the NorthGRIP drill site (Dahl-Jensen et al., 1997) and the NEEM drill site.

Figure 2.1: Radar power amplifiers (left) and electronics chassis (right) installed inside the P-3 aircraft. Photos from Jezek et al. (2007).

2.2 RES data used in the present study

2.2.1 Deep radar data

In 1991, NASA commenced a polar research initiative aimed at determining the mass balance of the Greenland ice sheet. As a part of this, the Center for Remote Sensing of Ice Sheets (CReSIS) at the University of Kansas, US, collected an extensive data set from the Greenland ice sheet using primarily airborne coherent radar systems (Gogineni et al., 2001). In September 2007, they collected a data set along the ice divide in northern Greenland (CReSIS, 2007). The radar system was installed inside a NASA P-3 aircraft (see Fig. 2.1), with four 150 MHz dipole antennae mounted under each wing (see Fig. 2.2). The two inboard antenna elements were used for transmitting and the six outboard elements were used to receive. The radar operated at a centre frequency of 150 MHz, and a 3 μs or 10 μs chirp with a bandwidth of 20 MHz was used (Jezek et al., 2007). Details on the operating parameters of the radar system are given in Table 2.1. The depth resolution in ice is 5 m and the horizontal resolution is 160 m. The position of the aircraft was determined from GPS data.

In the present study, we use data collected along the ice divide between NorthGRIP and NEEM. The section is 435 km long and starts 50 km up-

Figure 2.2: Four 150 MHz dipole antennae mounted under the right wing of a P-3 aircraft. Photo from Jezek et al. (2007).

Carrier frequency	150 MHz
Sampling frequency	120 MHz
Chirp bandwidth	20 MHz
Pulse duration	3 or 10 μs
Transmit power	200 W
Flight elevation	500 m above ice surface
Depth resolution	5 m in ice

Table 2.1: Operating parameters for the radar used to collect the deep RES data used in the present study. The data were collected by CReSIS in September 2007.

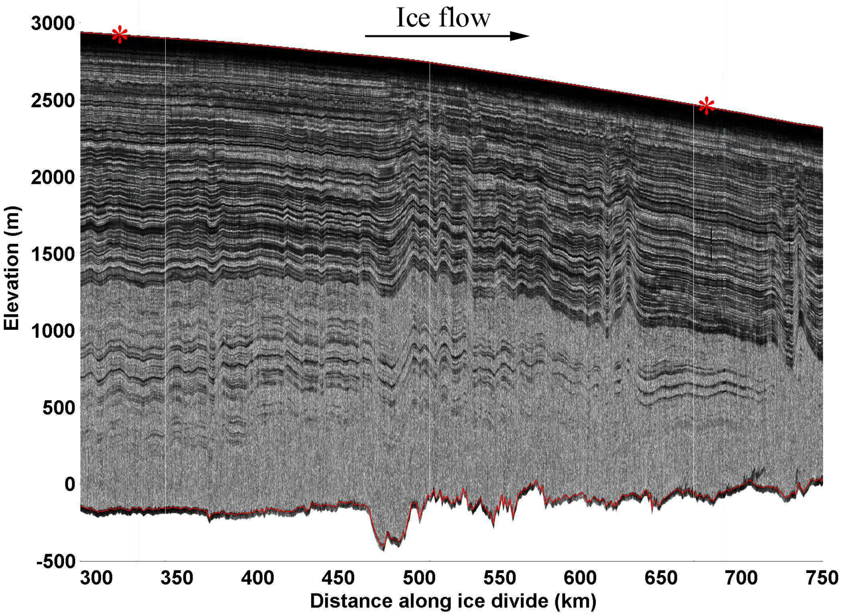

Figure 2.3: RES image collected along the ice divide between NorthGRIP (left asterisk) and NEEM (right asterisk) by CReSIS in September 2007. The ice is flowing along the ice divide from NorthGRIP towards NEEM.

stream from NorthGRIP and stops 20 km downstream from NEEM. Fig. 2.3 shows the data set that is used in this study, and the flight line is shown in green on a map of Greenland in Fig. 1.1. It is readily seen from Fig. 2.3 that numerous layers can be traced all the way from NorthGRIP to NEEM. At NorthGRIP, deep RES layers coincide with major changes in the ECM[2] level, which is a measure of the DC conductivity of the ice (see Fig. 2.4). Thus the NorthGRIP data indicate that the deep reflectors are caused by varying impurity content in connection with abrupt climate changes or volcanic eruptions. Furthermore, Miners et al. (2002) compared synthetic radargrams created from GRIP DEP[3] data to measured RES data and concluded that changes in conductivity are the main cause of internal reflections in Greenland. Therefore, we will treat the internal layers in the image in Fig. 2.3 as isochrones.

The internal structure of the ice along the ice divide exhibits several distinct features in the area of interest. Some of the features are matched by bedrock topography, while others are not. The most distinct feature of the bedrock

---

[2] Electrical conductivity measurement.

[3] Dielectric properties.

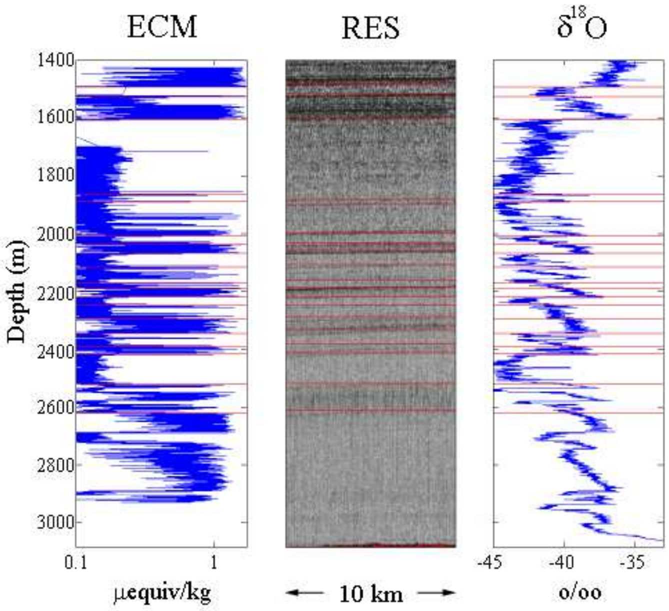

Figure 2.4: Left: ECM data for the lower part of the NorthGRIP ice core. Middle: RES data. The NorthGRIP drill site is located at the right hand egde of the image. Right: The lower part of the δ^{18}O curve from NorthGRIP. The red lines indicate isochrones observed in the radio-echo image. These are seen to coincide with major changes in the ECM level connected to abrupt climate changes. Figure from D. Dahl-Jensen (personal communication 2005).

is the deep trough around 475 km from GRIP. The depression is ~30 km wide and ~300 m deep with very steep sides. This feature has clearly shaped the internal layers above it. Another area where the isochrones show undulations with almost as big an amplitude as seen over the trough is found upstream from NEEM around 625 km along the x-axis, where there is only little bedrock topography. Also, upstream from the trough the bedrock is quite smooth but we still see significant undulations of the isochrones. Such undulations must have a different cause.

Possible causes for the existence of isochrone undulations that are not obviously generated by bedrock topography include changes in accumulation rates, variations in the ice flow perpendicular to the ice ridge, and changes in the basal melt rates caused by variations in the geothermal heat flux. Dahl-Jensen et al. (1997) used a 1D model to investigate the effect of accumulation rate variations on the depths of internal layers in the area between GRIP and NorthGRIP and found that the accumulation rate variations needed to explain the large undulations seen in the internal layers were unrealistically high. Furthermore, the effect of accumulation rates on isochrone shapes decreases with depths whereas the undulations of the isochrones are seen to increase towards the base of the ice sheet. Therefore, we rule out accumulation rate variations as a cause for the undulations of the deep layers. As for variations in the flow conditions perpendicular to the ice ridge, Dahl-Jensen et al. (2003) concluded from radio-echo data collected in a close net around NorthGRIP (Göktas, 1999) that there was no indications of rapid changes in the flow properties perpendicular to the ice ridge at NorthGRIP. Though we cannot rule out that processes transverse to the ridge have an effect on the shape of the isochrones further north, we will in the following assume that their shapes are created by spatial changes in the basal melt rates.

By digitising the layers seen in the RES image we can now create a data set of observed isochrones that are dated from their depths at NorthGRIP using the GICC05 timescale (Vinther et al., 2006; Rasmussen et al., 2006; Andersen et al., 2006; Svensson et al., 2006, 2008). The optimal set of isochrones would consist of layers spanning all the major climatic periods represented in the ice column. However, the reflections grow weak with depth, and the deepest layer that can be traced all the way from NorthGRIP to NEEM is 51 kyr old. Numerous Holocene isochrones can be traced, while only 3 continuous layers are visible below the layer that marks the onset of the Bølling interstadial 14.7 kyr b2k. From the Holocene period we choose isochrones that are easily traced and evenly distributed. Together with the Bølling isochrone and the three glacial isochrones these constitute a set of 12 isochrones traced continuously from NorthGRIP to NEEM. However, including isochrones as old as possible is crucial in order to find a solution to the inverse problem that gives reliable results for model runs that run for a full glacial cycle or more. Therefore, we chose to include a deeper isochrone, dated to 74.6 kyr, that is clearly visible in some areas but disappears at other locations. The layer can be followed from NorthGRIP and 270 km downstream where it becomes impossible to trace for the next ~70 km. About 20 km upstream from NEEM a we see the start of a ~40 km section of what we believe to be the same layer (cf. Fig 2.5). Thus there is a ~70 km long gap upstream from NEEM, where the layer can not be seen. The problem with using this layer is, that when it is not possible to trace it continuously to NorthGRIP, we can not be absolutely certain that it is the same layer we see downstream from the gap (i.e. at NEEM). However, both upstream and downstream from the gap, the shape of the layer is consistent with that of the isochrones immediately above it, and there is a characteristic shadow below it. Thus we feel confident that it is the same layer we see on both sides of the gap.

The final set of 13 isochrones is shown in Fig. 2.5, and the ages and depths of these at NorthGRIP are given in Table 2.2.

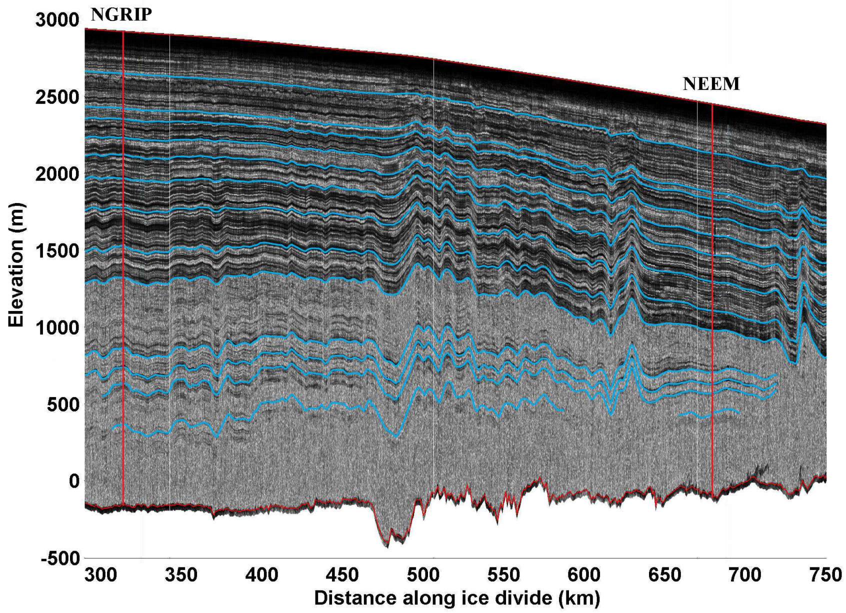

Figure 2.5: RES image collected along the ice divide between NorthGRIP and NEEM. The 13 isochrones used in this study are marked in blue.

Age (kyr)	Depth (m)	z (m)
1.4	273	2644
2.7	501	2416
3.2	571	2346
4.0	689	2229
4.8	802	2116
5.9	955	1963
7.5	1146	1771
10.2	1396	1521
14.6	1600	1318
37.7	2055	863
45.0	2182	735
51.0	2284	633
74.6	2553	365

Table 2.2: Age, depth at NorthGRIP, and elevation above sea level (z) at NorthGRIP for the 13 isochrones.

Bandwidth	0.5–2.0 GHz
Pulse duration	4 ms
Transmit power	100 mW
Depth resolution	10 cm in firn

Table 2.3: Operating parameters for the radar used to collect the shallow RES data used in the present study.

2.2.2 Shallow radar data

During the surface traverse from NorthGRIP to NEEM in 2007, CReSIS carried out radar measurements using a UHF system (0.5–2 GHz). Operating parameters for the radar system are given in Table 2.3. Radar systems operating at these frequencies are used to map internal layers in the upper parts of the ice. Fig. 2.6 shows the data set collected between NorthGRIP and NEEM. It reveals shallow continuous layers in the firn. These layers are caused by seasonal density changes in the firn and are thus isochrones (Vaughan et al., 2004). The shape of the layers is dominated by the changes in accumulation rate along the ice divide, and in the present study they will be used to infer the present accumulation rates along the ice divide.

2.3 Summary

Radio-echo sounding data reveal internal layers in the ice. The reflections are caused by changes in the complex permittivity of the ice due to variations in density, impurity content and/or fabric. In the present study, we use the data set shown in Fig. 2.5 and assume the internal layers to be isochronous. Furthermore, undulations of the internal layers that can not be explained from bedrock topography or spatial changes in accumulation rate are assumed to be caused by spatial changes in the basal melt rate. A set of 13 isochrones was obtained from the radar data. These isochrones are dated from their depths at NorthGRIP. The ages and NorthGRIP depths of these 13 layers are given in Table 2.2.

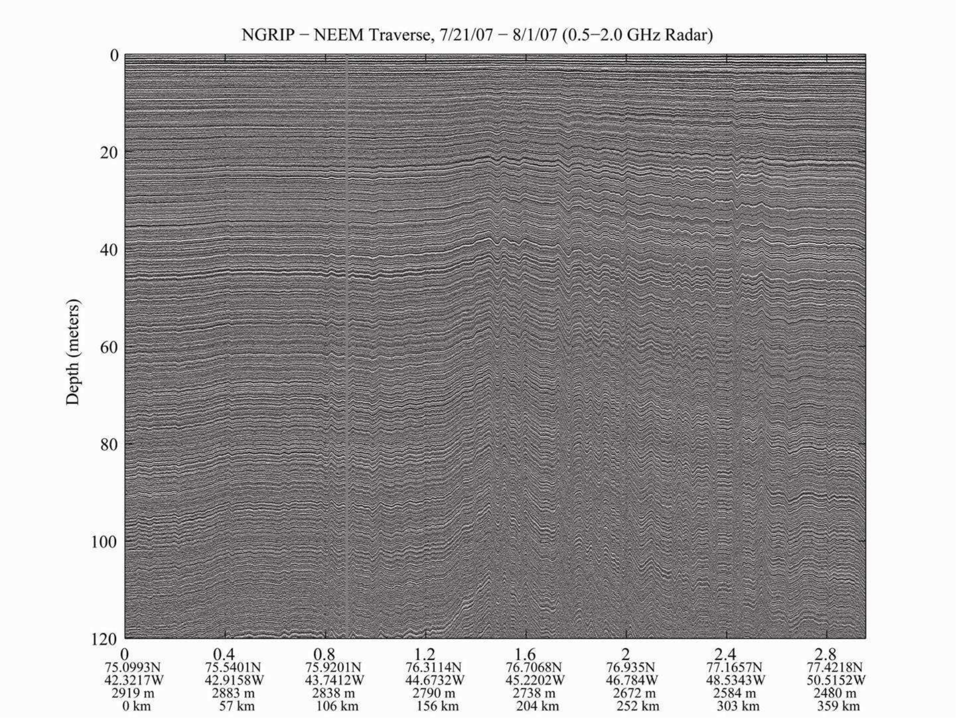

Figure 2.6: Surface near RES data collected along the ice divide between NorthGRIP (left) and NEEM (right) using a surface based UHF radar system. The grey vertical line is a 1.2 km long stretch where no data were collected due to receiver problems. The data were collected by CReSIS in July–August 2007. Figure from Claude Laird (personal communication 2008).

Chapter 3

Modelling the ice flow

The NorthGRIP and NEEM sites are both located on the ice ridge that runs from the summit of the ice sheet and some 550 km NNW before it splits into two. The NEEM site is located on the western branch some 100 km from the bifurcation point. The ice flows NNW along the ice ridge, and we want to study the ice flow along this flow line in the area between NorthGRIP and NEEM. We will use both a 1D and a 2D version of the Dansgaard-Johnsen model (Dansgaard and Johnsen, 1969). This model was chosen because it is a simple model, and yet it has given good results when creating timescales at the ice core drill sites (Dansgaard and Johnsen, 1969; Johnsen and Dansgaard, 1992; Johnsen et al., 1995).

3.1 1D-modelling

3.1.1 The Dansgaard-Johnsen model

For the following calculations we use a coordinate system with horizontal x-axis pointing in the direction of the flow, y-axis perpendicular to the flow line, and a vertical z-axis pointing upwards.

A Dansgaard-Johnsen model is used to simulate the ice flow along the ice divide in the area between NorthGRIP and NEEM. The Dansgaard-Johnsen model (the DJ-model) was developed to create a time scale for the Camp Century ice core. It is an approximation to Glen's law (Glen, 1955) as illustrated in Fig. 3.1. In the present work, the model from Dansgaard and Johnsen (1969) has been modified to account for basal melting and sliding.

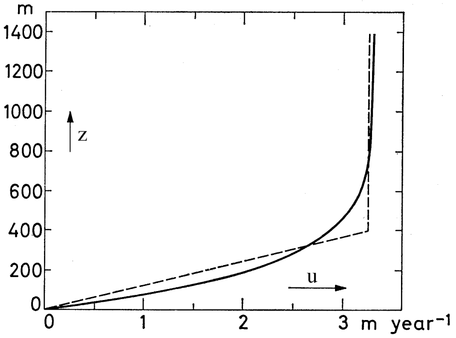

Figure 3.1: Full curve: horizontal velocity profile at Camp Century calculated from Glen's law. Dashed curve: Velocity profile from the Dansgaard-Johnsen model. Figure from Dansgaard and Johnsen (1969) modified to match the nomenclature of this work.

Thus, it assumes a horizontal velocity profile given by:

$$u(z) = \begin{cases} u_{\text{sur}} & z \in [h, H] \\ u_{\text{sur}} \left(F_B + (1 - F_B) \dfrac{z}{h} \right) & z \in [0, h[, \end{cases} \tag{3.1}$$

where u is the horizontal velocity, u_{sur} is the horizontal surface velocity, z is ice equivalent height above the ice-bedrock interface, $F_B = \frac{u_{\text{bed}}}{u_{\text{sur}}}$ is the fraction of the surface velocity attributable to basal sliding, and h is called the kink height.

Assuming ice is incompressible the continuity equation can be used. It states:

$$\frac{\partial u}{\partial x} + \frac{\partial v}{\partial y} + \frac{\partial w}{\partial z} = 0 \quad \Leftrightarrow \quad \frac{\partial w}{\partial z} = -\frac{\partial u}{\partial x} - \frac{\partial v}{\partial y}, \tag{3.2}$$

where w is the vertical velocity, and u and v are the horizontal velocities along and perpendicular to the ice ridge, respectively. Assuming that the horizontal velocity profile perpendicular to the ice ridge has the same shape as the horizontal velocity profile along the ice divide, and that F_B and h do not vary horizontally, we get from differentiation of Eq. (3.1) that

$$\frac{\partial w}{\partial z} = \begin{cases} -\dfrac{\partial u_{\text{sur}}}{\partial x} - \dfrac{\partial v_{\text{sur}}}{\partial y} & z \in [h, H] \\ \left(-\dfrac{\partial u_{\text{sur}}}{\partial x} - \dfrac{\partial v_{\text{sur}}}{\partial y} \right) \left(F_B + (1 - F_B) \dfrac{z}{h} \right) & z \in [0, h[. \end{cases} \tag{3.3}$$

Integrating this and substituting $\frac{\partial w}{\partial z}\big|_{\text{sur}} = -\frac{\partial u_{\text{sur}}}{\partial x} - \frac{\partial v_{\text{sur}}}{\partial y}$ (cf. Eqs. (3.1) and (3.2)) we arrive at the following expression for the vertical velocity

$$w(z) = \begin{cases} w_b + \dfrac{\partial w}{\partial z}\Big|_{\text{sur}} \left(z - \dfrac{1}{2} h (1 - F_B) \right) & z \in [h, H] \\ w_b + \dfrac{\partial w}{\partial z}\Big|_{\text{sur}} \left(F_B z + \dfrac{1}{2} (1 - F_B) \dfrac{z^2}{h} \right) & z \in [0, h[, \end{cases} \tag{3.4}$$

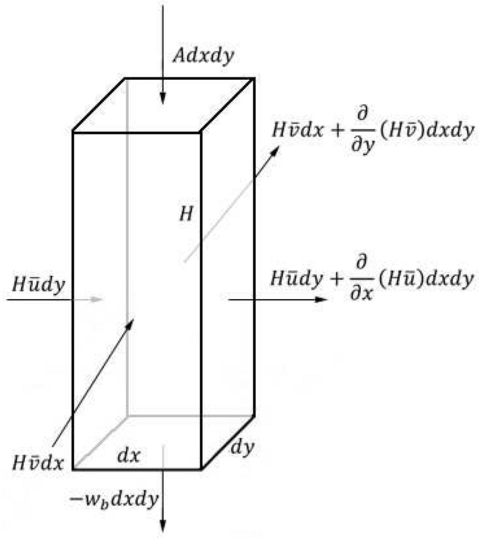

Figure 3.2: Conservation of mass on an ice column.

where w_b is the vertical velocity at the base. The basal melt rate is given by $-w_b$. Conservation of mass on an ice column (see Fig. 3.2) gives

$$\frac{\partial H}{\partial t} = A + w_b - \frac{\partial (H\overline{u})}{\partial x} - \frac{\partial (H\overline{v})}{\partial y}, \tag{3.5}$$

where t is time, A is the annual ice equivalent accumulation, and $\overline{u}$ and $\overline{v}$ are the mean horizontal velocities over the entire height of the ice column along and perpendicular to the ice ridge, respectively. $\overline{u}$ is found by integration of Eq. (3.1), such that

$$\overline{u} = \frac{1}{H}\int_0^H u(z)\,dz \quad \Rightarrow \quad H \cdot \overline{u} = u_{\text{sur}}\left(H - \frac{1}{2}h(1 - F_B)\right). \tag{3.6}$$

The expression for $H \cdot \overline{v}$ is derived similarly. Inserting this into Eq. (3.5) gives

$$\frac{\partial H}{\partial t} = A + w_b + \left.\frac{\partial w}{\partial z}\right|_{\text{sur}}\left(H - \frac{1}{2}h(1 - F_B)\right). \tag{3.7}$$

Rearranging this gives the following expression for $\left.\frac{\partial w}{\partial z}\right|_{\text{sur}}$

$$\left.\frac{\partial w}{\partial z}\right|_{\text{sur}} = \frac{\frac{\partial H}{\partial t} - A - w_b}{H - \frac{1}{2}h(1 - F_B)}. \tag{3.8}$$

In the present study, we are interested in following modelled isochrones as they sink down through the ice sheet. In order to do so, we need an expression that allows calculation of the new location z_{new} of an isochrone at time $t_{\text{new}} = t + \Delta t$ from its position z at time t. From the relation $w = \frac{dz}{dt}$ we get

$$\int_z^{z_{\text{new}}} \frac{1}{w} dz' = \int_t^{t_{\text{new}}} dt'. \tag{3.9}$$

The expression for w is different for $z < h$ and $z \geq h$ (cf. Eq. (3.4)). The two cases are treated separately below.

$z \in [h, H]$: Inserting the expression for w from Eq. (3.4) gives

$$\int_z^{z_{\text{new}}} \left(w_b + \left.\frac{\partial w}{\partial z}\right|_{\text{sur}} \left(z' - \frac{1}{2} h \left(1 - F_B\right) \right) \right)^{-1} dz' = \int_t^{t_{\text{new}}} dt', \tag{3.10}$$

and defining

$$\alpha = w_b - \frac{1}{2} \left.\frac{\partial w}{\partial z}\right|_{\text{sur}} h \left(1 - F_B\right) \qquad \text{and} \qquad \beta = \left.\frac{\partial w}{\partial z}\right|_{\text{sur}} \tag{3.11}$$

this can be written as

$$\int_z^{z_{\text{new}}} \frac{dz'}{\beta z' + \alpha} = \int_t^{t_{\text{new}}} dt'. \tag{3.12}$$

Performing the integration we get

$$\frac{1}{\beta} \ln \frac{\beta z_{\text{new}} + \alpha}{\beta z + \alpha} = t_{\text{new}} - t = \Delta t, \tag{3.13}$$

which leads to the following expression for the new location of the layer

$$z_{\text{new}} = \frac{\beta z + \alpha}{\beta} \exp\left(\beta \Delta t\right) - \frac{\alpha}{\beta}. \tag{3.14}$$

$z \in [0, h[$: By substituting the appropriate expression for w in Eq. (3.4) into Eq. (3.9) we get

$$\int_z^{z_{\text{new}}} \left(w_b + \left.\frac{\partial w}{\partial z}\right|_{\text{sur}} \left(F_B z' + \frac{1}{2} \left(1 - F_B\right) \frac{z'^2}{h} \right) \right)^{-1} dz' = \int_t^{t_{\text{new}}} dt'. \tag{3.15}$$

Defining

$$a = \frac{1}{2h} \left.\frac{\partial w}{\partial z}\right|_{\text{sur}} \left(1 - F_B\right), \quad b = \left.\frac{\partial w}{\partial z}\right|_{\text{sur}} F_B \quad \text{and} \quad c = w_b \tag{3.16}$$

Eq. (3.15) can be written as

$$\int_z^{z_{\text{new}}} \frac{dz'}{a z'^2 + b z' + c} = \int_t^{t_{\text{new}}} dt'. \tag{3.17}$$

This leads to different expressions for z_{new} depending on the values of a, b, and c:

$b^2 - 4ac > 0$: In this case, we have

$$\int \frac{dz}{az^2+bz+c} = \frac{1}{\sqrt{b^2-4ac}} \ln\left(\ln \frac{2az+b-\sqrt{b^2-4ac}}{2az+b+\sqrt{b^2-4ac}} \right) \tag{3.18}$$

and Eq. (3.17) can be written as

$$\left[\frac{1}{\sqrt{b^2-4ac}} \ln\left(\frac{2az'+b-\sqrt{b^2-4ac}}{2az'+b+\sqrt{b^2-4ac}} \right) \right]_{z}^{z_{\text{new}}} = \left[t' \right]_{t}^{t_{\text{new}}}. \tag{3.19}$$

Defining

$$d = \sqrt{b^2-4ac}, \quad \text{and} \quad E = \frac{2az+b-d}{2az+b+d} \tag{3.20}$$

Eq. (3.19) can be written as

$$\frac{1}{d}\left(\ln\left(\frac{2az_{\text{new}}+b+d}{2az_{\text{new}}+b+d} \right) - \ln E \right) = t_{\text{new}} - t = \Delta t. \tag{3.21}$$

Solving for z_{new} leads to the following expression

$$z_{\text{new}} = \frac{(b+d)\,E\exp\left(d\Delta t\right) - (b-d)}{2a\left(1 - E\exp\left(d\Delta t\right)\right)}. \tag{3.22}$$

$b^2 - 4ac < 0$: We have

$$\int \frac{dz}{az^2+bz+c} = \frac{2}{\sqrt{4ac-b^2}} \arctan\left(\frac{2az+b}{\sqrt{4ac-b^2}} \right). \tag{3.23}$$

Defining

$$f = \sqrt{4ac-b^2} \tag{3.24}$$

and inserting the appropriate limits we get

$$\frac{2}{f}\left(\arctan\left(\frac{2az_{\text{new}}+b}{f} \right) - \arctan\left(\frac{2az+b}{f} \right) \right) = t_{\text{new}} - t = \Delta t. \tag{3.25}$$

Solving for z_{new} we arrive at

$$z_{\text{new}} = \frac{f}{2a} \tan\left(\frac{1}{2} f\Delta t + \arctan\left(\frac{2az+b}{f} \right) \right) - \frac{b}{2a}. \tag{3.26}$$

$b^2 - 4ac = 0$: In this case $c = \frac{b^2}{4a}$ and the left hand side of Eq. (3.17) reduces to

$$\frac{1}{a}\int_{z}^{z_{\text{new}}} \frac{dz'}{(z'+\frac{b}{2a})^2} = \frac{1}{a}\left[\frac{-1}{z'+\frac{b}{2a}} \right]_{z}^{z_{\text{new}}}. \tag{3.27}$$

From this and Eq. (3.17) we get the following expression

$$z_{\text{new}} = \left(\frac{1}{z + \frac{b}{2a}} - a\Delta t \right)^{-1} - \frac{b}{2a}. \tag{3.28}$$

We must also consider the possibility that one or more of the parameters a, b, and c is zero:

$\boldsymbol{a = 0}$**:** In this case Eq. (3.17) reduces to

$$\int_{z}^{z_{\text{new}}} \frac{dz'}{bz' + c} = \int_{t}^{t_{\text{new}}} t', \tag{3.29}$$

which is solved equivalently to Eq. (3.12). The following expression for z_{new} is obtained

$$z_{\text{new}} = \frac{bz + c}{b} \exp(b\Delta t) - \frac{c}{b}. \tag{3.30}$$

$\boldsymbol{b = 0}$**:** For the indefinite integral we have

$$\int \frac{dz}{az^2 + c} = \frac{1}{a} \int \frac{dz}{z + \frac{c}{a}} = \frac{1}{a} \sqrt{\frac{a}{c}} \arctan\left(\sqrt{\frac{a}{c}} z \right). \tag{3.31}$$

From this and Eq. (3.17) we get

$$z_{\text{new}} = \sqrt{\frac{c}{a}} \tan\left(\Delta t \sqrt{ac} + \arctan\left(\sqrt{\frac{a}{c}} z \right) \right). \tag{3.32}$$

$\boldsymbol{c = 0}$**:** We have

$$\int \frac{dz}{az^2 + bz} = \frac{1}{b} \ln\left(\frac{z}{az + b} \right). \tag{3.33}$$

Thus Eq. (3.17) becomes

$$\left[\frac{1}{b} \ln\left(\frac{z'}{az' + b} \right) \right]_{z}^{z_{\text{new}}} = \left[t' \right]_{t}^{t_{\text{new}}}, \tag{3.34}$$

which leads to the following expression for z_{new}

$$z_{\text{new}} = \frac{bz \exp(b\Delta t)}{az\,(1 - \exp(b\Delta t)) + b}. \tag{3.35}$$

If more than one of the constants a, b, and c are zero the integral in Eq. (3.17) is reduced to very simple integrals that are not treated here.

The time step where an isochrone moves below the kink height h needs to be treated in a special way. We calculate the time interval Δt_2 that the layer is located below h in the given time step:

$$\Delta t_2 = t_{\mathrm{new}} - t_{\mathrm{h}}. \tag{3.36}$$

An expression for t_{h} can be found from Eq. (3.12) by changing the upper bounds for the integration to $z = h$ and $t = t_{\mathrm{h}}$

$$\int_z^h \frac{dz'}{\beta z + \alpha} = \int_t^{t_{\mathrm{h}}} dt'. \tag{3.37}$$

Carrying out the integration and solving for t_{h} leads to

$$t_{\mathrm{h}} = \frac{1}{\beta} \ln\left(\frac{\beta h + \alpha}{\beta z + \alpha}\right) + t. \tag{3.38}$$

Inserting this result into Eq. (3.36) gives

$$\Delta t_2 = \Delta t - \frac{1}{\beta} \ln\left(\frac{\beta h + \alpha}{\beta z + \alpha}\right). \tag{3.39}$$

To find the position after the time step, during which the layer passes the kink height, we integrate Eq. (3.17) from h to z_{new} and from t_{h} to t_{new}.

We have now derived all the relevant expressions needed to do 1D simulations of isochrones moving down through the ice sheet. For simulations done in the present study, the origin of the coordinate system is placed at GRIP at sea level, and the x-axis runs along the ice divide between NorthGRIP and NEEM.

The following sections deals with the different input parameters to the model.

3.1.2 The accumulation model

The surface mass balance is a crucial parameter in ice flow modelling, and in order to obtain good results with the ice flow model it is important to establish a good estimate for the accumulation history.

Clausen et al. (1988) and Dahl-Jensen et al. (1993) found a correlation between accumulation rates and δ^{18}O values, such that low δ^{18}O values correspond to low accumulation rates and high δ^{18}O values to high accumulation rates. This correlation exists because a high water vapour mixing ratio in a cloud leads to a high accumulation rate, and precipitation with high δ^{18}O values originates from clouds with high mixing ratios (Clausen et al., 1988).

For the dating of the GRIP ice core Johnsen et al. (1995) used the following model to calculate ice equivalent accumulation rates from $\delta^{18}\mathrm{O}$ values

$$A(t) = A_0 \cdot \exp\left(k_2\left(\delta^{18}\mathrm{O}(t) - \delta^{18}\mathrm{O}_w\right) + \frac{1}{2}k_1\left(\delta^{18}\mathrm{O}(t)^2 - \delta^{18}\mathrm{O}_w^2\right)\right) \tag{3.40}$$

$$k_1 = \frac{c_1 - c_2}{\delta^{18}\mathrm{O}_w - \delta^{18}\mathrm{O}_c}, \quad k_2 = c_1 - \delta^{18}\mathrm{O}_w \cdot k_1. \tag{3.41}$$

Here A_0 is the present ice equivalent accumulation rate at the site and $\delta^{18}\mathrm{O}_w = -35.2‰$ and $\delta^{18}\mathrm{O}_c = -40.0‰$ are typical $\delta^{18}\mathrm{O}$ values for warm and cold climate conditions at the site, respectively. The constants c_1 and c_2 denote the sensitivity of A to changes in $\delta^{18}\mathrm{O}$ during warm and cold conditions, respectively:

$$c_1 = \frac{1}{A}\frac{\partial A}{\partial \delta^{18}\mathrm{O}}\bigg|_{\delta^{18}\mathrm{O}_w}, \quad c_2 = \frac{1}{A}\frac{\partial A}{\partial \delta^{18}\mathrm{O}}\bigg|_{\delta^{18}\mathrm{O}_c}. \tag{3.42}$$

The value of c_1 has been estimated for the Summit region from field studies (Clausen et al., 1988) and from a precipitation model Johnsen et al. (1989), and both approaches indicate a 7–9% change in the accumulation rate for a 1‰ change in the $\delta^{18}\mathrm{O}$ value during the Holocene, i.e. $c_1 \in [0.07 - 0.09]$. The value of c_2 is expected to be at least twice as big as c_1 (Johnsen et al., 1995). Johnsen et al. (1995) used c_1=0.08 and c_2=0.18 to obtain a good modelled timescale for the GRIP ice core.

By comparing this model with accumulation rates derived from observed annual layer thicknesses in the GRIP ice core it is possible to get an indication of how well the model fits the observations. The GICC05 timescale (Vinther et al., 2006; Rasmussen et al., 2006; Andersen et al., 2006; Svensson et al., 2006, 2008) provides observed annual layer thicknesses for GRIP with a resolution of 20 yrs back to 60 kyr b2k. Older layers are too thin for annual layer counting to be possible. Using a DJ-model to correct the observed annual layer thicknesses (λ) for the strain that the ice has been subjected to since deposition, we get the layer thicknesses at the time of deposition (λ_0), i.e. the ice equivalent accumulation rates. A scatter plot of these strain-corrected observed layer thicknesses against the measured $\delta^{18}\mathrm{O}$ values of the layers is shown in Fig 3.3. Only data from below the firn-ice transition, i.e. below 120 m, are shown in this figure. Fig. 3.3 also shows the accumulation rate calculated from Eq. (3.40) using sea-water-corrected $\delta^{18}\mathrm{O}$ values on the GICC05 timescale, c_1=0.08, c_2=0.18 and the observed present accumulation rate A_0=0.23 m/yr. In the DJ-model used to calculate the strain corrections h=1500 m, F_B=0.17, and w_b=0. It is seen that the model represents the data points well.

A similar plot for NorthGRIP (using h=1800 m, F_B=0.1, w_b=-7 mm/yr, A_0=0.193 m/yr, and c_1 and c_2 as above) is shown in Fig. 3.4. To account

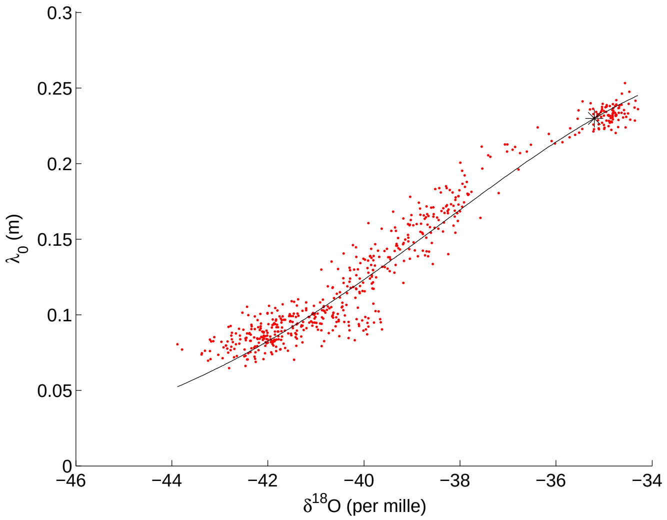

Figure 3.3: Strain-corrected observed annual layer thicknesses versus δ^{18}O for the last 60 kyr in the GRIP ice core. The solid line is the accumulation relation from Eq. (3.40). The black asterisk denotes the present values at GRIP. Parameter values used to create the plot are c_1=0.08, c_2=0.18, A_0=0.230 m/yr, h=1500 m, F_B=0.17, and w_b=0.

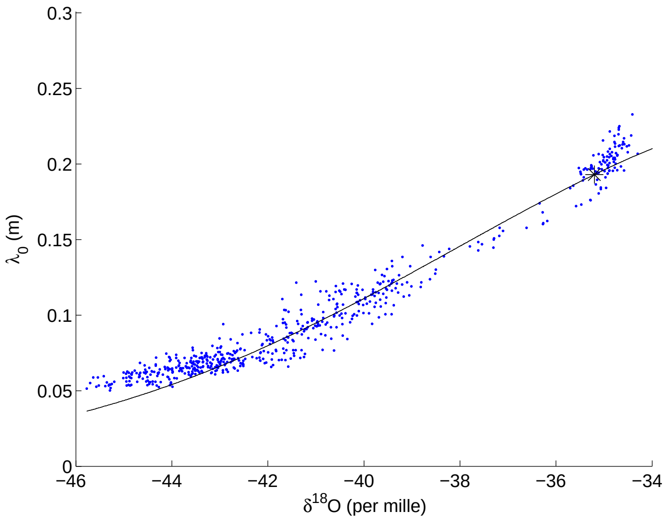

Figure 3.4: Strain-corrected observed annual layer thicknesses versus δ^{18}O for the last 60 kyr in the NorthGRIP ice core. The solid line is the accumulation relation from Eq. (3.40) with c_1=0.08, c_2=0.18, A_0=0.193 m/yr, h=1800 m, F_B=0.1, and w_b=-7 mm/yr. The black asterisk denotes the present values at NorthGRIP.

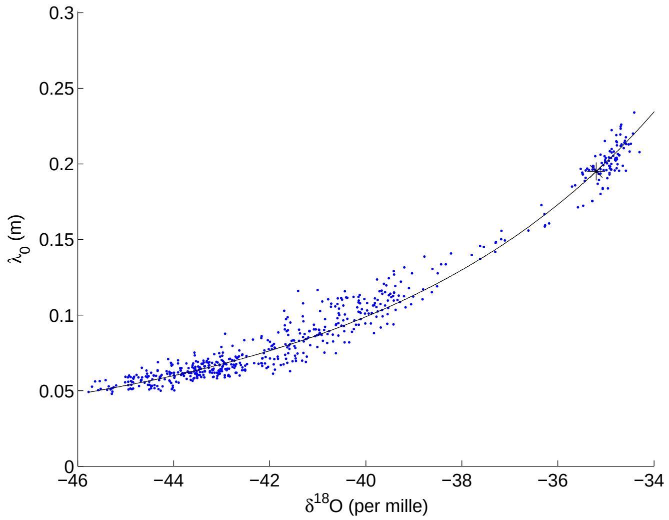

Figure 3.5: Strain-corrected observed annual layer thicknesses versus δ^{18}O for the last 60 kyr in the NorthGRIP ice core. The solid line is the accumulation relation from Eq. (3.40) with Monte Carlo-determined parameters used in the DJ-model: c_1=0.15, c_2=0.13, A_0=0.195 m/yr, h=1970 m, F_B=0.15, and w_b=-7 mm/yr. The black asterisk denotes the present values at NorthGRIP.

for NorthGRIP having generally lower δ^{18}O values than GRIP during cold periods, we use $\delta^{18}\mathrm{O}_c = -42.0‰$. It is seen that the accumulation model is not a good match for the NorthGRIP data for these values of the parameters. Therefore, new values are found from a Monte Carlo solution (cf. Chapter 4) to the 1D inverse problem at NorthGRIP constrained by the 13 isochrones from Fig. 2.5. All the parameters are well determined by the Monte Carlo solution, and the obtained best estimates for the parameter values are c_1=0.15, c_2=0.13, A_0=0.195 m/yr, h=1970 m, F_B=0.23, and w_b=-7 mm/yr. The resulting δ^{18}O-accumulation relationship is depicted in Fig. 3.5.

The Monte Carlo-determined values for c_1 and c_2 deviate significantly from the expected values for Central Greenland. However, from Figs. 3.3 and 3.4 it is seen that the NorthGRIP data do not show the significant s-shape that the GRIP data do. Where the GRIP data flatten out towards the higher δ^{18}O values this does not seem to be the case at NorthGRIP. Thus, it may be better to use a different relation between δ^{18}O values and accumulation rates. When looking at the shape of the data in the scatter plot in Fig. 3.4, two simple models readily come to mind: One, called A1, that consists of two straight lines – one to be fitted to data with δ^{18}O values below -42‰ and one for data with δ^{18}O values from -42‰ and above

$$A(t) = \begin{cases} C_1 \cdot \delta^{18}\mathrm{O}(t) + C_2 & \delta^{18}\mathrm{O}(t) < -42‰ \\ C_1' \cdot \delta^{18}\mathrm{O}(t) + C_2' & \delta^{18}\mathrm{O}(t) \geq -42‰. \end{cases} \tag{3.43}$$

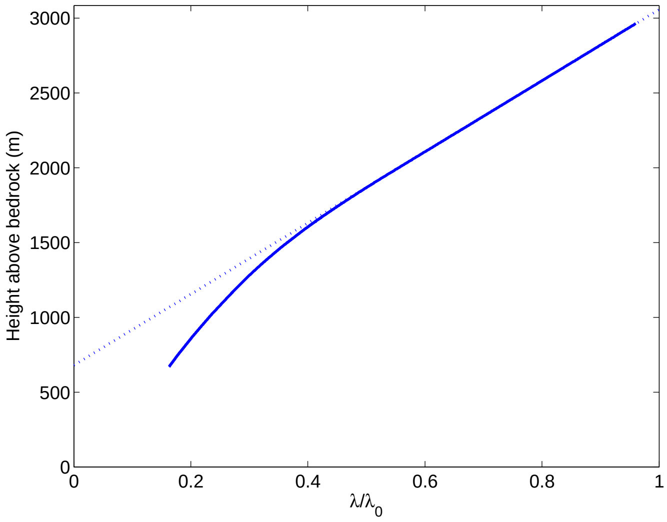

Figure 3.6: Solid line: Observed annual layer thicknesses divided by the strain corrected layer thicknesses for the last 60 kyr in the NorthGRIP ice core. Dotted line: Extension of the linear part of the solid curve. The dotted curve intersects the vertical axis at $\frac{1}{2}h\,(1-F_B) - w_b\left(\frac{\partial w}{\partial z}\Big|_{\mathrm{sur}}\right)^{-1}$, which can be used to calculate the value of h.

The other model, A2, is a second degree polynomial with coefficients p_1, p_2, and p_3

$$A(t) = p_1 \cdot \delta^{18}\mathrm{O}(t)^2 + p_2 \cdot \delta^{18}\mathrm{O}(t) + p_3. \tag{3.44}$$

In the following the usefulness of these two very simple accumulation models for the NorthGRIP site will be investigated.

First, we look at A1. When using the DJ-model to calculate the strain correction it requires an accumulation history as input. This complicates matters when trying to use the scatter plot (e.g. Fig. 3.4) to find a suitable accumulation model. The approach chosen here is to use the model from Eq. (3.40) to calculate the strain correction used to create the first scatter plot. A new δ^{18}O-accumulation relation is then derived from the scatter plot and used to calculate new strain corrections. For this second calculation of the strain corrections we also use a new value for h derived from the previous strain history: In a plot of z versus λ/λ_0 (see Fig. 3.6) the straight part of the graph would, if extended, cross the vertical axis at $\frac{1}{2}h\,(1-F_B) - w_b\left(\frac{\partial w}{\partial z}\Big|_{\mathrm{sur}}\right)^{-1}$ (cf. Eq. (3.4)), which can be used to derive the new value of h. This procedure is continued several times to see, if the obtained δ^{18}O-accumulation relation yields consistent modelling results. Fig. 3.7 shows four steps of this process for model A1. It is seen that the model fits data well, and that the value of h does not change much from one calculation to the next. Thus this model is a good candidate to replace Eq. (3.40).

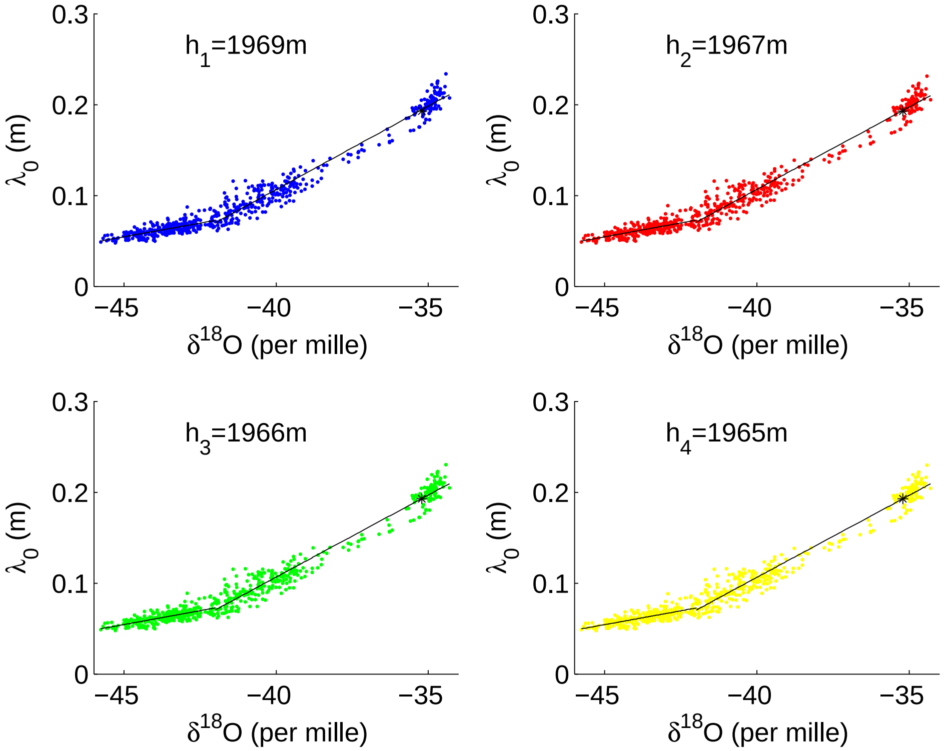

Figure 3.7: Coloured points: Strain-corrected observed annual layer thicknesses versus δ^{18}O for the last 60 kyr in the NorthGRIP ice core. Solid black lines: Best fit of the accumulation model A1 from Eq. (3.43) to the points. The strain corrections used to calculate the points in the first plot (blue) were obtained using Eq. (3.40), whereas the strain corrections used to create the following scatter plots (red, green, and yellow) are calculated from the δ^{18}O-accumulation relation inferred from the previous plot using A1. The value of h used in the strain correction calculations for each step is indicated in the corresponding plot.

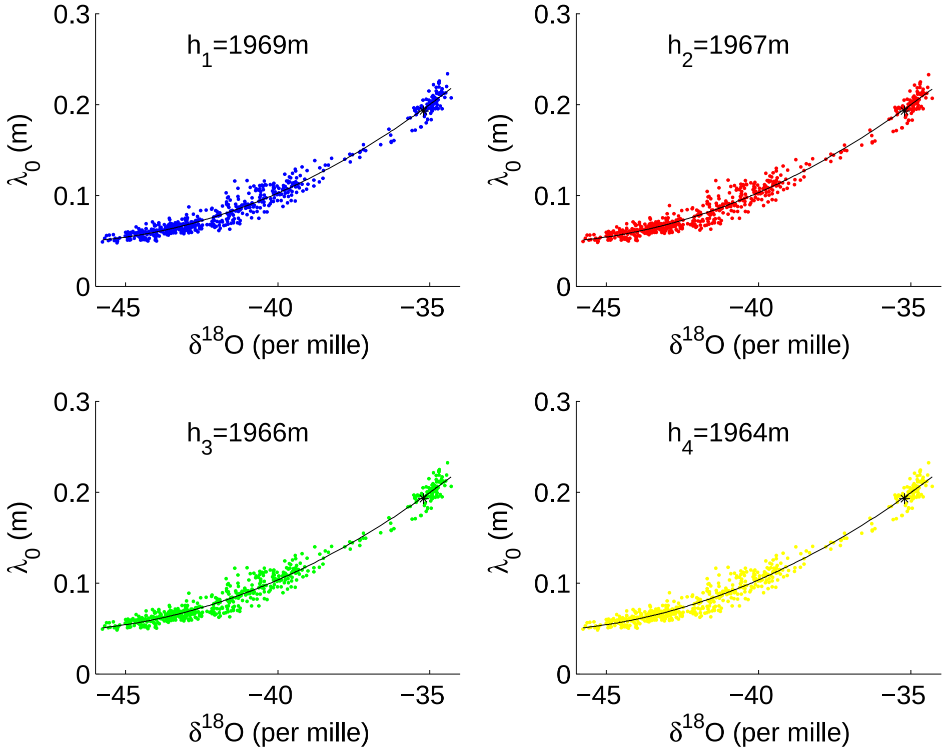

Figure 3.8: Coloured points: Strain-corrected observed annual layer thicknesses versus δ^{18}O for the last 60 kyr in the NorthGRIP ice core. Solid black lines: Best fit of the accumulation model A2 from Eq. (3.44) to the points. The strain corrections used to calculate the points in the first plot (blue) were obtained using Eq. (3.40), whereas the strain corrections used to create the following scatter plots (red, green, and yellow) are calculated from the δ^{18}O-accumulation relation inferred from the previous plot using A2. The value of h used in the strain correction calculations for each step is indicated in the corresponding plot.

Model A2 is investigated in the same way as A1, and the results can be seen in Fig. 3.8. It is seen that this model also fits data well, and that the value of h is stable.

Thus both models are found to be good candidates to replace Eq. (3.40) in the following ice flow simulations. The problem is, however, that the data set investigated here contains data only back to 60 kyr b2k. Thus we have data from the Holocene, the LGM and the last part of the glacial period, but the very warm isotopic values like those found in Eemian ice are not represented in the data set. The big question is how the models will behave for Eemian δ^{18}O values. The model from Eq. (3.40) tends to get very high (0.3 m/yr or higher) Eemian accumulation rates, when the coefficients are determined from the Monte Carlo solution to the inverse problem. Using either of the models A1 or A2 results in more moderate Eemian accumulation rates, and it was chosen to use model A2 to calculate the accumulation input to the DJ-model in this study. The reason for choosing A2 over A1 was that it has only three unknown parameters to be determined (p_1, p_2, and p_3), whereas A1 has four (C_1, C_2, C_1', and C_2').

At locations where there is no ice core and thus no δ^{18}O record, the values of p_1, p_2, and p_3 determined at NorthGRIP will be used. If we assume that the accumulation pattern along the ice ridge is constant in time, the accumulation at a location x is given by

$$A(x,t) = k_A(x) \cdot A(x_{\mathrm{NGRIP}}, t), \quad k_A(x) = \frac{A_0(x)}{A_0(x_{\mathrm{NGRIP}})}, \tag{3.45}$$

where x_{NGRIP} is the location of the NorthGRIP drill site and k_A is a site specific constant.

3.1.3 The δ^{18}O record from NorthGRIP

The δ^{18}O record from NorthGRIP has been dated using the counted GICC05 timescale back to 60 kyr b2k and before that the modelled ss09sea timescale (Johnsen et al., 2001). The δ^{18}O values have been corrected for temporal changes in the isotopic composition of ocean water due to the build-up of ice on the continents (Waelbroeck et al., 2002). The oldest ice from NorthGRIP has been dated to 123 kyr (North Greenland Ice Core Project members, 2004). This means that accumulation rate estimates for periods prior to 123 kyr b2k cannot be made from the δ^{18}O record from NorthGRIP. In order to make it possible to use the model to simulate ice deposited prior to 123 kyr b2k, a rough estimate of δ^{18}O values for the period 123–150 kyr has been made in the following way:

123–130 kyr: A linear interpolation is made between the observed δ^{18}O value at 123 kyr and the value of -32‰ at 130 kyr.

130–140 kyr: A linear interpolation is made between the above mentioned point at 130 kyr and -43‰ at 140 kyr.

140–150 kyr: A constant value of -43‰ is used.

The resulting δ^{18}O series is shown in Fig. 3.9.

The accumulation rates will be calculated from Eq. (3.44) using 100 yr means of the δ^{18}O values. When using oxygen isotopes of the ice to calculate past accumulation rate, it is best to use mean values over at least a couple of bags[1]

---

[1] 1 bag equals 55 cm

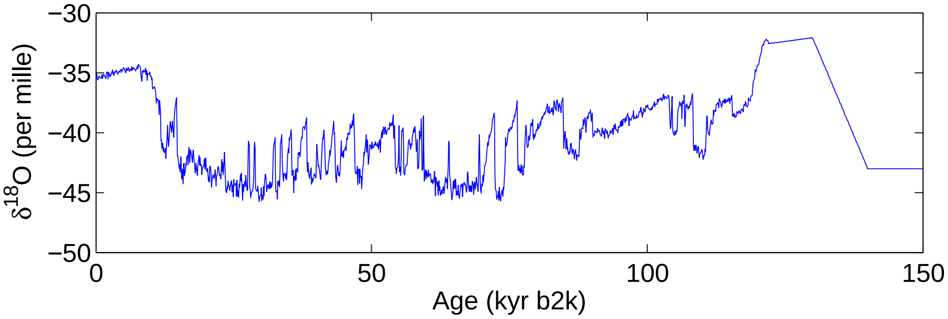

Figure 3.9: The δ^{18}O history used to calculate past accumulation rates at NorthGRIP. The values for the most recent 123 kyr are measured NorthGRIP δ^{18}O values (North Greenland Ice Core Project members, 2004) corrected for temporal changes in the ocean (Waelbroeck et al., 2002). The values prior to 123 kyr b2k are estimated (cf. page 32).

(Sigfús Johnsen, personal communication 2008) to avoid effects of noise in the isotopic signal. Fig. 3.10 shows λ as a function of depth for the NorthGRIP ice core. It is seen that close to the bed the annual layer thickness is ∼1 cm. Using means of 100 yrs is thus equivalent to using an average over ∼1 m, which is roughly 2 bags.

3.1.4 Other input parameters

As seen from Eqs. (3.4) and (3.8) the 1D DJ-model requires the following input parameters: The ice thickness H, its temporal change rate $\frac{\partial H}{\partial t}$, the kink height h, the fraction of basal sliding F_B, the basal melt rate $-w_b$, and the accumulation history $A(t)$. The present ice thickness is known from the length of the ice core at NorthGRIP. A firn correction of 25 m has been used to correct for the air in the upper layers of the ice sheet. Model runs were done both with and without including temporal changes in the ice thickness. Two different histories of ice thickness are investigated.

The first history is calculated by Guðfinna Aðalgeirsdóttir, Danish Meteorological Institute, using the SICOPOLIS model from Greve (2005). This is a 3D dynamic/thermodynamic ice sheet model. The geothermal heat flux map used in the calculations is shown in Fig. 3.11. The surface elevation histories at the six 1D sites calculated from the SICOPOLIS model are shown in Fig. 3.12.

The second ice thickness history is from Vinther et al. (subm), who used the δ^{18}O records from Renland and Agassiz to infer surface elevation changes during the Holocene at four sites on the Greenland ice sheet (Dye-3, GRIP, NorthGRIP, and Camp Century). It is believed that the stable isotope

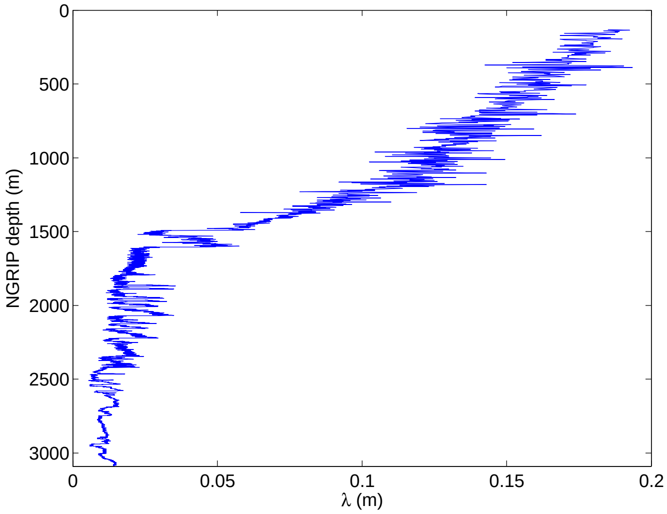

Figure 3.10: Annual layer thicknesses (λ) at NorthGRIP. It is seen, that the annual thickness is roughly 1 cm in the lower part of the ice core.

records from these two small marginal ice caps on either side of the Greenland ice sheet are not significantly affected by elevation changes during the Holocene. The δ^{18}O records from the two sites are remarkably similar leading the authors to the assumption that the same millennial scale δ^{18}O trend would be present in the isotope records from the Greenland ice sheet, had it not been for the changes in surface elevation. The elevation changes were then derived from the differences between the δ^{18}O records from Greenland and those from Renland and Agassiz. Estimates of surface elevation changes prior to 12 kyr b2k are based on Renland data only (Bo Vinther, personal communication 2008). As these surface elevation estimates exist only for places, where we have a dated isotope record, we will use interpolated values in the area of study. Fig. 3.13 shows the resulting surface elevation history for the NorthGRIP drill site and those found at the other five 1D sites by interpolation between the elevation histories calculated at NorthGRIP and at Camp Century. As the NorthGRIP record reaches back only to 123 kyr b2k, the surface elevation history also reaches only this far back in time.

We are left with six unknown input parameters for the 1D model at NorthGRIP: h, F_B, w_b, p_1, p_2, and p_3. At NorthGRIP these six parameters will be estimated using a Monte Carlo technique (cf. Chapter 4). For other sites, the fraction of accumulation rate at the site to that at NorthGRIP, k_A, will be determined, while p_1, p_2, and p_3 will be fixed at their NorthGRIP values. Thus there are only four unknowns for these sites.

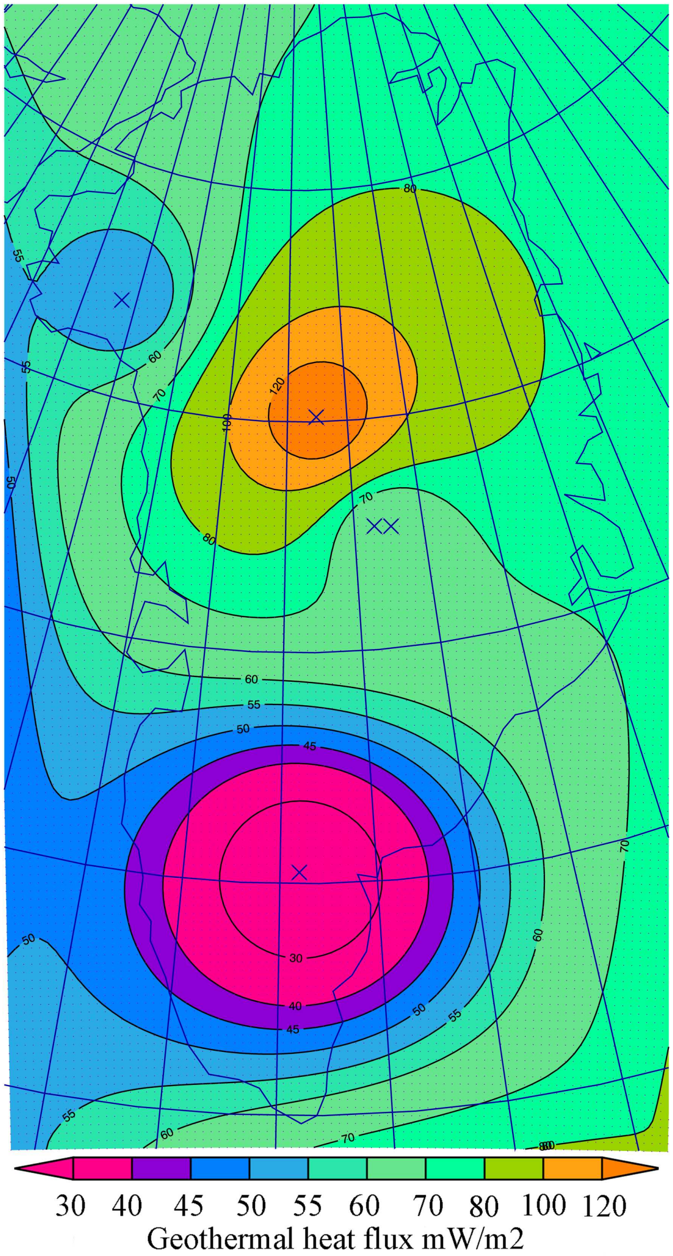

Figure 3.11: Map of geothermal flux values in Greenland. The map was created by Greve (2005) by modifying the data from Pollack et al. (1993) to match observed values at the four drill sites Dye-3, GRIP, NorthGRIP and Camp Century. Figure from Guðfinna Aðalgeirsdóttir (personal communication 2009).

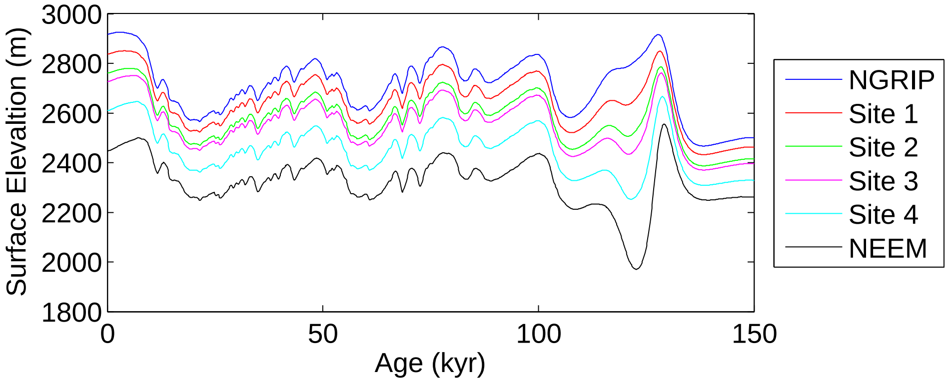

Figure 3.12: Changes in surface elevation for the last 150 kyr for the six 1D sites. These changes were calculated by Guðfinna Aðalgeirsdóttir, Danish Meteorological Institute, using the SICOPOLIS ice sheet model from Greve (2005).

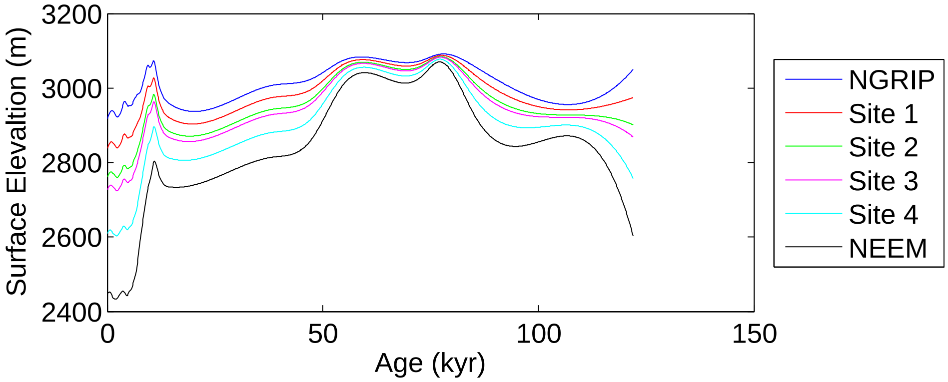

Figure 3.13: Changes in surface elevation for the last 123 kyr for the six 1D sites. Holocene elevation changes at NorthGRIP are from Vinther et al. (subm), while elevation changes prior to 12 kyr b2k were provided by Bo Vinther (personal communication 2008). Surface elevation changes at the other locations are interpolated values between the calculated elevation histories at NorthGRIP and Camp Century.

dt (yrs)	20	50	100	200
Max. depth difference (m)	1.6	3.7	5.8	11.5

Table 3.1: The maximum difference in the depths of the 13 fixpoints calculated with different values of dt and those calculated with dt=1 yr. For the present study dt=50 yrs was chosen.

3.1.5 Computational approach

Before solving the inverse problem we need to decide on a size of the time step, dt, in the forward model. Therefore, we look into the effect of changing the value of dt. For different values of dt (1, 20, 50, 100, and 200 yrs) the depths of the 13 layers at NorthGRIP are calculated using the 1D DJ-model. Then the difference between the depths calculated with dt=1 year and those calculated with the higher values is calculated. The maximum difference for each value of dt is listed in Table 3.1. As the uncertainty on the observed depths of the isochrones is 5 m, we choose the largest time step, where the maximum difference to the depths calculated with dt=1 yr is still smaller than 5 m. Thus we choose dt=50 yrs.

3.2 2D-modelling

In 2D model simulations, isochrones consisting of 1 point for each kilometre along the ice ridge are started at the surface and followed as they sink down through the ice sheet. As in the 1D case we use a coordinate system with origin at GRIP at sealevel and x- and z-axes pointing along the flow and upwards, respectively.

3.2.1 Input parameters

In addition to the input parameters mentioned above the 2D model also requires the horizontal surface velocity as input (cf. Eq. (3.1)). Furthermore, the variation of some of the parameters along the ice divide requires attention.

The accumulation rate pattern

The accumulation rates along the ice ridge are not well known except for the present values at NorthGRIP and NEEM that have been determined from studies of shallow ice cores. Ohmura and Reeh (1991) published an accu-

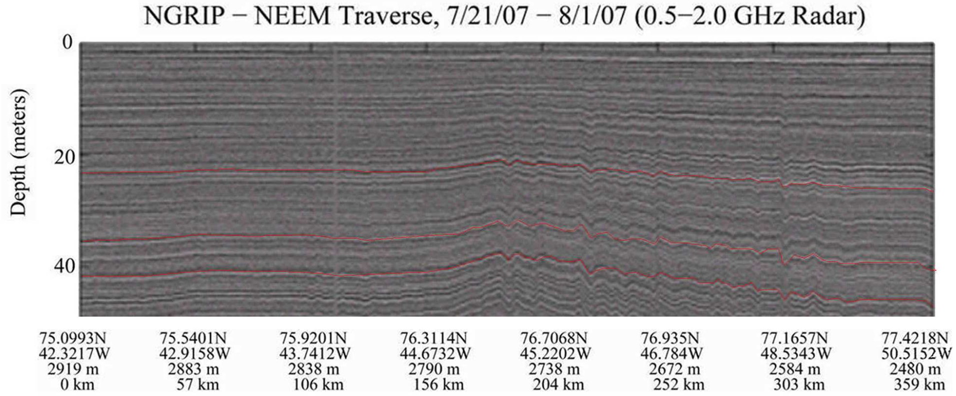

Figure 3.14: RES image collected along the ice ridge between NorthGRIP (left) and NEEM (right). Traced layers are marked in red. The three layers are used to infer accumulation rates along the ice ridge. The ages of the layers are 70, 110, and 140 yrs. Figure from Dorthe Dahl-Jensen (personal communication 2009.)

mulation map of Greenland based on more than 250 point measurements, but the resolution of this data set may be too coarse to capture the features of the accumulation pattern to a degree optimal for this study. To further investigate the accumulation pattern along the ice ridge we use shallow radar reflectors to estimate accumulation rates.

Three layers have been traced between NorthGRIP and NEEM, and their ages have been estimated from their depths at NorthGRIP to be 70, 110, and 140 yrs (see Fig. 3.14). Assuming that the shallow layers are not influenced significantly by the basal conditions, we use a 1D DJ model with $w_b = F_B = 0$ to obtain average accumulation rates. Thus the mean accumulation rate in the period since deposition is given by

$$\overline{A} = \frac{2H - h}{2t} \ln\left(\frac{2H - h}{2z - h}\right), \tag{3.46}$$

where t is the age of the layer. The obtained average accumulation rates are normalized to match the observed present accumulation rate at NorthGRIP. The resulting accumulation patterns are shown in Fig. 3.15 together with the accumulation pattern from Ohmura and Reeh (1991) modified to match the observed values at NorthGRIP and NEEM. Whereas the overall shape of the curves are the same, there are significant differences between the modified pattern from Ohmura and Reeh (1991) and those inferred from the radar layers, especially around 500 km from GRIP, where the radar layers indicate a lower accumulation rate. There seems to be no trend with age in the accumulation rate derived from the three layers, which is an indication that the assumption of no influence from basal conditions is valid. It is also worth noting that by normalizing the accumulation rate from the RES layers

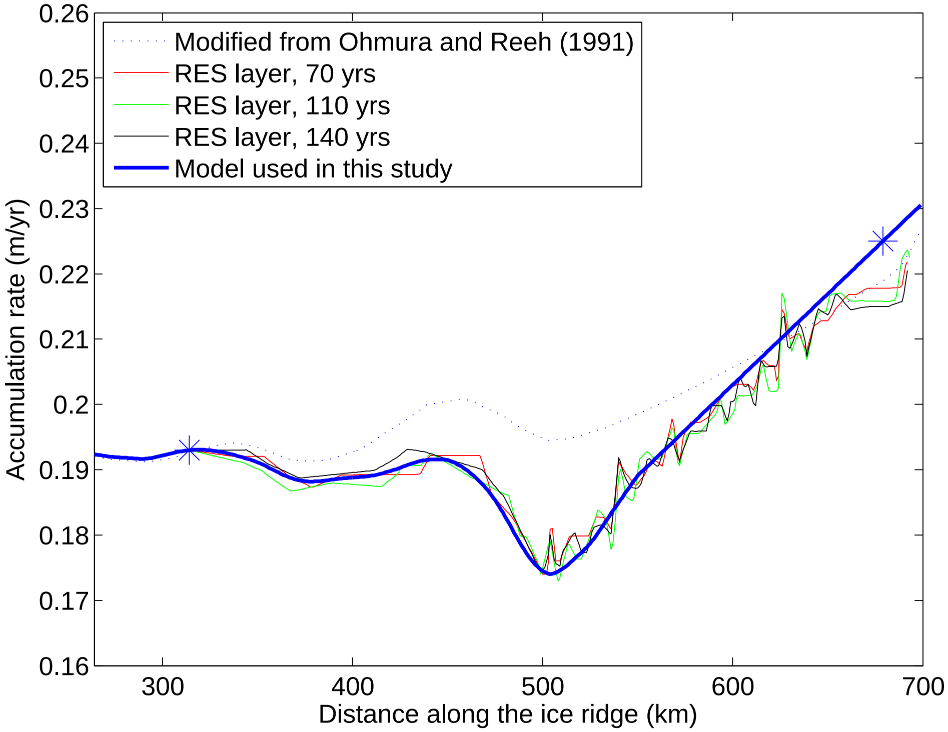

Figure 3.15: Comparison between the accumulation pattern from Ohmura and Reeh (1991) modified to match observed values and the accumulation pattern found from shallow RES layers and normalized to match the observed value at NorthGRIP. The values at the NorthGRIP and NEEM drill sites are marked with asterisks. The model adapted in this study is shown in blue (heavy line).

to the accumulation rate at NorthGRIP the values found at NEEM (0.215–0.218 m/yr) are close to the observed value of 0.225 m/yr at the site (Anders Svensson, personal communication 2008). For these reasons we choose to use a smoothed version of the mean of the accumulation rate patterns obtained from the three RES layers tuned to match the observed values at the drill sites. This accumulation rate pattern is also shown in Fig. 3.15 (heavy blue line). In the model calculations this accumulation pattern will be assumed constant in time.

The surface velocity u_{sur}

The current horizontal surface velocity along the ice ridge in northern Greenland is only well known at a few locations. In the NorthGRIP area it was calculated from strain net measurements from 1996 to 2001 (Hvidberg et al., 2002), and at the NEEM drill site it has been estimated from 1 year's strain net measurements from 2007 to 2008 (Lars Berg Larsen, personal commu-

Site	u_{sur} (m/yr)
The summit	0
NGRIP	1.329 ± 0.015
NEEM	5.5 ± 1.0[a]
CC	3.5 ± 0.2

---

[a] The high uncertainty stated is due to the fact that the 5.5 m/yr are based on measurements over only 1 year.

Table 3.2: Measured horizontal surface velocities in northern Greenland, see text for references.

nication 2009). Furthermore, at Camp Century it was measured from the movement of the meteorological tower from 1977 to 1986 (Gundestrup et al., 1987). Table 3.2 shows the surface velocities of the mentioned locations and of the summit of the ice sheet.

A model is needed to infer surface velocities at other locations along the ice ridge between NorthGRIP and NEEM. In simple ice flow models the surface velocity is often tied to the surface slope, $\frac{\partial S}{\partial x}$. Dahl-Jensen et al. (2003) used the following model to calculate surface velocities for a 2D model study of the flow along the ice ridge in the area around NorthGRIP:

$$u_{\mathrm{sur}}(x) = u_{\mathrm{sur}}(x_{\mathrm{NGRIP}}) \left(\frac{H(x)}{H(x_{\mathrm{NGRIP}})} \right)^4 \left(\frac{\frac{\partial S(x)}{\partial x}}{\frac{\partial S}{\partial x}(x_{\mathrm{NGRIP}})} \right)^3 . \tag{3.47}$$

The surface velocities calculated with this model in the area around the NorthGRIP drill site are in agreement with those found by Hvidberg et al. (2002) using the strain net measurements (Dahl-Jensen et al., 2003). However, further north where the surface slope is higher, Eq. (3.47) yields surface values that are much too high (see Fig. 3.16, blue curve). Therefore, we choose another relation between surface velocity and surface slope to see if we can get more realistic values in the area under consideration. A third degree polynomial (Fig. 3.16, green curve) is fitted to all 4 points in Table 3.2. The surface velocities calculated with this model do not vary significantly from those calculated using Eq. (3.47) in the NorthGRIP area, but further north along the ice ridge lower surface velocities are obtained in better agreement with the observations at NEEM. Because Camp Century is located much closer to the edge of the ice sheet than the other three sites it may be interesting to see what happens if this point is disregarded. A second degree polynomial is fitted to the other three points (Fig. 3.16, red curve). It is seen that for the area between NorthGRIP and NEEM the two polynomials give similar results, while they have very different values around Camp Century. Thus both models can be used in the area of study. It was chosen to use the model based on all four points. This means that the present surface velocity

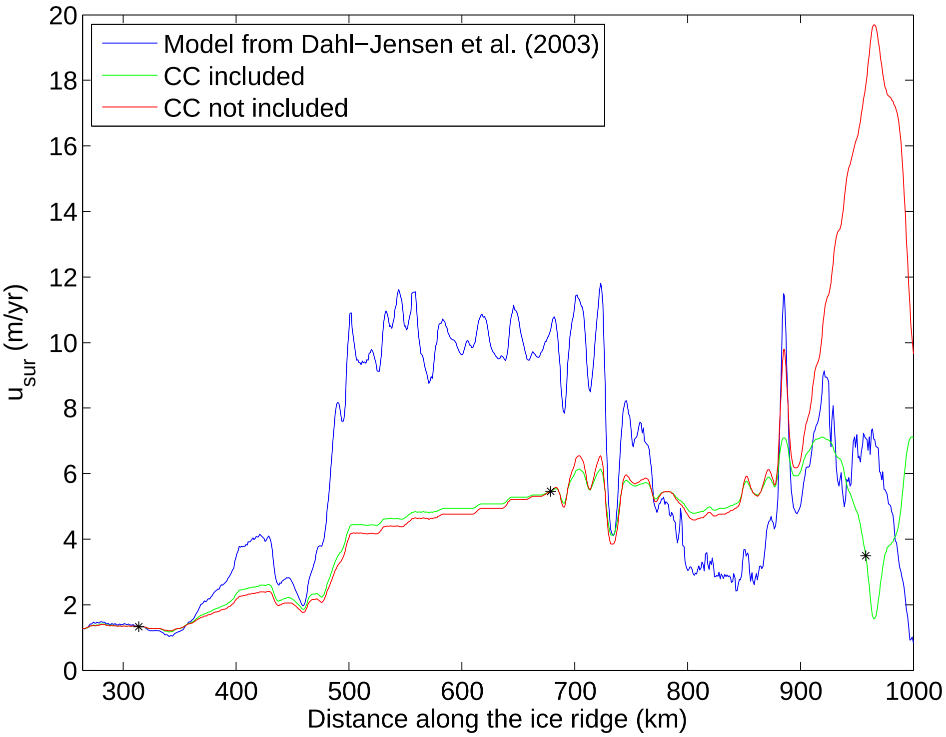

Figure 3.16: Surface velocity calculated from three different models relating u_{sur} to the surface slope. Blue: The model from Dahl-Jensen et al. (2003). Green: A third degree polynomial fitted to the 4 points from Table 3.2. Red: A second degree polynomial fitted to the same data but leaving out Camp Century. The observed values of u_{sur} at NorthGRIP, NEEM, and Camp Century are indicated with black asterisks.

will be calculated from the following expression:

$$u_{\mathrm{sur}}(x) = q_1 \left(\frac{\partial S(x)}{\partial x}\right)^3 + q_2 \left(\frac{\partial S(x)}{\partial x}\right)^2 + q_3 \frac{\partial S(x)}{\partial x}, \tag{3.48}$$

where $S(x)$ is the surface elevation, and the coefficients are q_1=0.6783, q_2=2.7184, and q_3=-0.2402 for $\frac{\partial S(x)}{\partial x}$ given in m/km.

As the shape of the ice sheet changes with time, the surface velocity changes as well. To account for temporal changes in the surface velocity, we scale the current values with the relative changes in accumulation:

$$u_{\mathrm{sur}}(x,t) = \frac{A(x_{\mathrm{NGRIP}},t)}{A(x_{\mathrm{NGRIP}},0)} u_{\mathrm{sur}}(x,0). \tag{3.49}$$

The ice thickness H, and its temporal changes $\frac{\partial H}{\partial t}$

The ice thickness, H, along the line is known from radio-echo soundings (Gogineni et al., 2001), and a firn correction of 25 m is used.

The two ice thickness histories for the area over the last glacial cycle were described in Section 3.1.4.

The kink height h

Because flow conditions change along the ice ridge, we expect the value of h to change with position along the x-axis. To reduce the number of unknowns to be determined, we tie h linearly to the ice thickness:

$$h = k_h H, \tag{3.50}$$

where k_h is a constant to be determined from the Monte Carlo solution to the 2D inverse problem.

The basal melt rates w_b and the fraction of basal sliding F_B

A different approach is taken for the vertical velocity at the bed, w_b. The profile along the ice ridge is divided into sections of 8 km within which w_b is assumed constant. The value of w_b for each section is found by solving the inverse problem. Since the section considered in this work is 435 km long we have 55 unknown values of w_b along the line.

F_B is tied linearly to w_b:

$$F_B = k_F w_b, \tag{3.51}$$

and is thus also considered constant within the 8 km long intervals. k_F is a constant and both w_b and F_B are assumed to be constant in time.

To sum up, the 2D problem has 57 unknowns, that need to be determined by solving the inverse problem. These are k_h, k_F, and 55 values of w_b.

3.2.2 Computational approach

When using the DJ-model to do simulations along a flow line (2D), we also need to calculate the new position, x_{new} of the point in the x-direction from its current position, x. The velocity along the x-axis (as given by Eq. (3.1)) is a function of z, u_{sur}, F_B, and h. These all vary slowly with x, so if

dt (yrs)	10	20	50	100	200
Max. depth difference (m)	<1	<1	2	4	8
Max. difference in x (m)	<1	6	16	31	63

Table 3.3: Maximum differences between locations of isochrones as calculated from the analytical expressions derived in Section 3.1.1 and the approximation in Eq. (3.53) using different time steps *dt*.

small time steps are used, the movement in the x-direction is small, and u may be considered constant within each time step Δt without loosing much precision. With this assumption we arrive at the following simple expression for the new position

$$x_{\text{new}} = x + u\Delta t, \tag{3.52}$$

where u is calculated from Eq. (3.1) evaluated at x.

In the 1D model we follow only 13 points in the forward model, but in the 2D model we follow hundreds of points along the ice ridge. Thus the calculation time for the 2D forward model can be several orders of magnitude longer than for the 1D model. As the forward model is to be run hundreds of thousands of times, this is a potential problem. Therefore, we investigate the effect of using an approximation for the movement in the z-direction instead of the analytic equations derived in Section. 3.1.1. We adopt a relation equivalent to the one used in the x-direction:

$$z_{\text{new}} = z + w\Delta t, \tag{3.53}$$

where w is given by Eq. (3.4) evaluated at z. By running the forward model with the same input parameter values using first the analytical expressions and then the approximation we can compare the resulting locations of the 13 points. Table 3.3 shows the maximum difference in position of the 13 points for different values of dt. If dt is chosen sufficiently small, using the approximation instead of the analytical expressions will cause only small changes in the position and shape of the modelled isochrones. However, the gain in saved computational time is high (there is a factor of 10 between the run times). Therefore, it was chosen to use the approximation in the 2D case. The same value was chosen for the time step length as for the 1D case: dt=50 yrs.

When horizontal movement is included in the calculations we have to consider what happens close to the bedrock, where melting and sliding often occur, i.e. the ice moves parallel to the bed. Therefore, the velocity vector calculated from Eqs. (3.1) and (3.4) is rotated to be parallel to the bed at the ice-bedrock interface. The rotation is assumed to happen linearly from the kink height h and down, because the basal conditions are assumed to have little effect above h.

3.3 Summary

The ice flow in the area of study is simulated using a modified Dansgaard-Johnsen model, where the horizontal and vertical velocity components are assumed to be given by Eqs. (3.1) and (3.4), respectively. The dynamic accumulation model in Eq. (3.44) is used to estimate past accumulation rates from NorthGRIP δ^{18}O values. Past accumulation rates at other locations along the line are calculated by assuming that the present accumulation rate pattern in the area (see Fig. 3.15) has been constant with time. Surface velocities along the ice ridge are calculated from the slope of the ice surface using Eqs. (3.48) and (3.49). Two different ice thickness histories (Figs. 3.12 and 3.13) are used in the 1D model. It was decided to use time steps of 50 yrs. For 1D model simulations, analytical expressions derived in Section 3.1.1 for the new locations of an isochrone are used, whereas the approximation in Eq. (3.53) is used for 2D simulations in order to save computation time.

Chapter 4

A Monte Carlo method - theory and application

Several model parameters for the model presented in the previous chapter are unknown, and we wish to derive estimates for them by solving the inverse problem using a Monte Carlo method. This chapter gives an introduction to inverse Monte Carlo theory. Relevant concepts of inverse theory and probability densities are described and the Monte Carlo algorithm is deduced. Finally, the method is applied to the inverse problem treated in the present study, and the random walk used to solve it is derived.

4.1 Theory

4.1.1 Inverse problems

Consider a system described by a model with a finite number of model parameters and by data obtained from observations on the system. Ignoring the measuring noise, the relationship between data and model parameters can be expressed as

$$\boldsymbol{d} = \boldsymbol{g}(\boldsymbol{m}), \tag{4.1}$$

where $\boldsymbol{d} \in \mathbb{R}^m$ and $\boldsymbol{m} \in \mathbb{R}^n$ are vectors containing the exact data and the model parameters[1], respectively. The vector operator $\boldsymbol{g}$ represents the theoretical model. The problem of solving Eq. (4.1) for the data vector $\boldsymbol{d}$ is called the forward problem: Given a theoretical model with known model

---

[1] In inverse problem theory, a given realization of the model vector $\boldsymbol{m}$ is often referred to as *a model*. This should not be confused with the theoretical model linking data and model parameters.

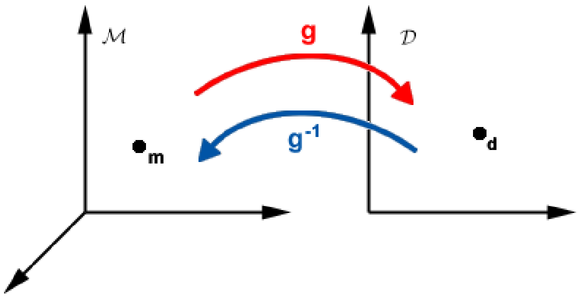

Figure 4.1: The mapping of the model vector $\boldsymbol{m}$ from the model space $\mathcal{M}$ into the data vector $\boldsymbol{d}$ in the data space $\mathcal{D}$ by the operator $\boldsymbol{g}$. The inverse operator $\boldsymbol{g}^{-1}$ performs the opposite mapping.

parameters, the data can be predicted. However, in geophysics it is more often the case that the data are known from measurements and the model parameters are unknown. In that case Eq. (4.1) needs to be solved for $\boldsymbol{m}$. This is called the inverse problem, and it can be expressed as

$$\boldsymbol{m} = \boldsymbol{g}^{-1}(\boldsymbol{d}), \tag{4.2}$$

where $\boldsymbol{g}^{-1}$ is the inverse of the operator $\boldsymbol{g}$ in Eq. (4.1). If the vectors $\boldsymbol{d}$ and $\boldsymbol{m}$ are considered as points in the data space $\mathcal{D}$ and the model space $\mathcal{M}$, respectively, the operator $\boldsymbol{g}$ performs a mapping from $\mathcal{M}$ into $\mathcal{D}$. The dimensions of $\mathcal{D}$ and $\mathcal{M}$ need not be the same, and generally they are not. In order to solve the inverse problem in Eq. (4.2) we need to construct the inverse operator $\boldsymbol{g}^{-1}$ that performs the mapping from $\mathcal{D}$ into $\mathcal{M}$ (see Fig. 4.1).

Simple linear inverse problems may be solved using damped least squares or singular value decomposition (Menke, 1989). However, most geophysical problems are not simple, and it is often impossible to construct the inverse operator $\boldsymbol{g}^{-1}$. Indeed, sometimes even the relation $\boldsymbol{g}$ exists only in the form of a numerical algorithm. In such cases the inverse problem may be solved using a Monte Carlo method. In order to explain the Monte Carlo method, some concepts from probability theory are introduced below.

4.1.2 Introducing probability densities

In the following, all expressions for probability density functions will be given without a possible multiplicative normalization constant.

In Section 4.1.1 the measurement noise was ignored. Accounting for the noise Eq. (4.1) becomes

$$\boldsymbol{d}_{\text{obs}} = \boldsymbol{g}(\boldsymbol{m}) + \boldsymbol{n}, \tag{4.3}$$

where $\boldsymbol{d}_{\mathrm{obs}} \in \mathbb{R}^m$ and $\boldsymbol{n} \in \mathbb{R}^m$ are vectors containing the observed data and the noise, respectively. As measurements can never provide us with the exact data vector, it is not practical to view $\boldsymbol{d}$ and $\boldsymbol{m}$ as points in $\mathcal{D}$ and $\mathcal{M}$. A better approach is to work with a probability density function $\rho(\boldsymbol{d}, \boldsymbol{m})$ in the system space $\mathcal{S}$ given by the Cartesian product of the data and model spaces. All *a priori* information - all the information we have before any mathematical analysis is done - is contained in ρ, which is called the *a priori* probability density function. *A priori* information consists of the observed data, their uncertainties and constraints on the model parameters (Tarantola and Valette, 1982). The case of no *a priori* information is represented by the null information function μ. By definition, the *a priori* information on $\boldsymbol{m}$ is independent of the observations and we have

$$\rho(\boldsymbol{d}, \boldsymbol{m}) = \rho_d(\boldsymbol{d})\rho_m(\boldsymbol{m}) \tag{4.4}$$

and

$$\mu(\boldsymbol{d}, \boldsymbol{m}) = \mu_d(\boldsymbol{d})\mu_m(\boldsymbol{m}), \tag{4.5}$$

where ρ_d and ρ_m are the *a priori* marginal probability density functions and μ_d and μ_m represent the null information in $\mathcal{D}$ and $\mathcal{M}$, respectively.

The theoretical relationship $\boldsymbol{g}$ between the data and the model parameters is not exact but merely a simplified description of the real world. Even given the model parameters $\boldsymbol{m}$, we are not able to calculate the *true* values for $\boldsymbol{d}$. We therefore replace the exact theory with a theoretical probability density function $\theta(\boldsymbol{d}, \boldsymbol{m})$. This may be interpreted as "putting error bars on the exact theory" (Tarantola and Mosegaard, 2000).

All our information is now contained in the probability density functions ρ and θ. A new state of information the is given by the conjunction of these

$$\sigma(\boldsymbol{d}, \boldsymbol{m}) = \frac{\rho(\boldsymbol{d}, \boldsymbol{m})\theta(\boldsymbol{d}, \boldsymbol{m})}{\mu(\boldsymbol{d}, \boldsymbol{m})}. \tag{4.6}$$

This new state of information, σ, is called the *a posteriori* probability density function. The *a posteriori* marginal probability density functions are given by

$$\sigma_d(\boldsymbol{d}) = \int \frac{\rho(\boldsymbol{d}, \boldsymbol{m})\theta(\boldsymbol{d}, \boldsymbol{m})}{\mu(\boldsymbol{d}, \boldsymbol{m})} d\boldsymbol{m} \tag{4.7}$$

and

$$\sigma_m(\boldsymbol{m}) = \int \frac{\rho(\boldsymbol{d}, \boldsymbol{m})\theta(\boldsymbol{d}, \boldsymbol{m})}{\mu(\boldsymbol{d}, \boldsymbol{m})} d\boldsymbol{d}, \tag{4.8}$$

where σ_d and σ_m are the *a posteriori* probability density functions in $\mathcal{D}$ and $\mathcal{M}$, respectively. Eq. (4.7) solves the general forward problem and Eq. (4.8) solves the general inverse problem (Tarantola and Valette, 1982). Fig. 4.2 gives a geometrical illustration of the different probability density functions introduced in this section.

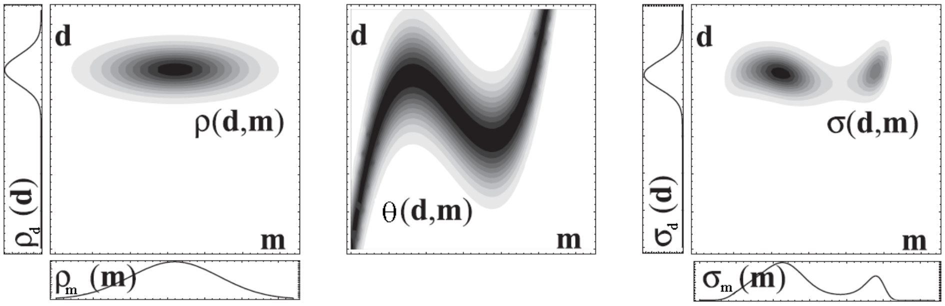

Figure 4.2: Left: The knowledge of observed data $\rho_{\boldsymbol{d}}$ in $\mathcal{D}$, the *a priori* information on the model parameters $\rho_{\boldsymbol{m}}$ in $\mathcal{M}$, and the joint probability density $\rho\left(\boldsymbol{d}, \boldsymbol{m}\right)$ in $\mathcal{D} \times \mathcal{M}$. Middle: The theoretical (non-exact) relation $\theta(\boldsymbol{d}, \boldsymbol{m})$ between $\boldsymbol{d}$ and $\boldsymbol{m}$. Right: The *a posteriori* probability density functions $\sigma(\boldsymbol{d}, \boldsymbol{m})$ and the marginal probability density functions $\sigma_{\boldsymbol{d}}$ and $\sigma_{\boldsymbol{m}}$. The difference between $\rho_{\boldsymbol{m}}$ and $\sigma_{\boldsymbol{m}}$ is caused by the information gained from the data $\rho_{\boldsymbol{d}}$ and the theoretical relation $\theta(\boldsymbol{d}, \boldsymbol{m})$. Figure from Tarantola (2005), modified to match the nomenclature used in this study.

4.1.3 The likelihood function

Assume we have a data set $\boldsymbol{d}$ and a non-linear model with model parameters $\boldsymbol{m}$, and that the *a priori* information and theoretical knowledge are contained in $\rho(\boldsymbol{d}, \boldsymbol{m})$ and $\theta(\boldsymbol{d}, \boldsymbol{m})$, respectively. We seek *a posteriori* information on the model parameters. Thus we need to solve Eq. (4.8).

The theoretical model puts no constraints on $\boldsymbol{m}$. Therefore we have

$$\theta(\boldsymbol{d}, \boldsymbol{m}) = \theta(\boldsymbol{d}|\boldsymbol{m})\mu_m(\boldsymbol{m}), \tag{4.9}$$

where $\theta(\boldsymbol{d}|\boldsymbol{m})$ is the conditional theoretical probability density function, that is, the theoretical probability density function for $\boldsymbol{d}$ given $\boldsymbol{m}$. From Eqs. (4.4), (4.5), (4.8), and (4.9) we get

$$\sigma_m(\boldsymbol{m}) = \rho_m(\boldsymbol{m}) \int \frac{\rho_d(\boldsymbol{d})\theta(\boldsymbol{d}|\boldsymbol{m})}{\mu_d(\boldsymbol{d})} d\boldsymbol{d}. \tag{4.10}$$

Defining the likelihood function

$$L(\boldsymbol{m}) \equiv \int \frac{\rho_d(\boldsymbol{d})\theta(\boldsymbol{d}|\boldsymbol{m})}{\mu_d(\boldsymbol{d})} d\boldsymbol{d} \tag{4.11}$$

we have

$$\sigma_m(\boldsymbol{m}) = \rho_m(\boldsymbol{m})L(\boldsymbol{m}). \tag{4.12}$$

The likelihood function can be interpreted as a measure of the agreement between the observed data and the data calculated from the model parameters (Mosegaard, 1998). Assuming that the noise on the data is Gaussian, the likelihood function takes the form

$$L(\boldsymbol{m}) = \exp\left(-S\left(\boldsymbol{m}\right)\right), \tag{4.13}$$

where $S(\boldsymbol{m})$ is the misfit function given by

$$S(\boldsymbol{m}) = \frac{1}{2} \sum_i \left(\frac{d_i - g_i(\boldsymbol{m})}{s_i} \right)^2. \tag{4.14}$$

Here s_i denotes the uncertainty on a data point d_i. Solving the inverse problem in Eq. (4.2) can now be seen as an optimization problem, where the misfit function in Eq. (4.14) needs to be minimized (Mosegaard, 2006).

4.1.4 The Metropolis algorithm

The general inverse problem is now reduced to determining $\rho_m(\boldsymbol{m})$ and $L(\boldsymbol{m})$ over the entire model space $\mathcal{M}$, but as $\mathcal{M}$ is usually of high dimension this may be a considerable task. Moreover, evaluation of $\boldsymbol{g}(\boldsymbol{m})$, which is required to calculate $S(\boldsymbol{m})$, may be possible only through a time consuming numerical algorithm. However, the necessary amount of work can be reduced considerably if a random walk is used to investigate $\mathcal{M}$.

A random walk is characterized by the conditional transition probability $P(\boldsymbol{m_i}|\boldsymbol{m_j})$ that the next step will take us to $\boldsymbol{m_i}$ if we are currently at $\boldsymbol{m_j}$. The unconditional probability $P(\boldsymbol{m_i}, \boldsymbol{m_j})$ that the next step will be from $\boldsymbol{m_j}$ to $\boldsymbol{m_i}$ is given by

$$P(\boldsymbol{m_i}, \boldsymbol{m_j}) = P(\boldsymbol{m_i}|\boldsymbol{m_j}) p(\boldsymbol{m_j}), \tag{4.15}$$

where p is the equilibrium probability of the random walk (Mosegaard and Tarantola, 1995). The equilibrium probability is unique if it is possible for the random walk to go from any one point in the model space to any other in a sufficient number of steps (Feller, 1970).

Assume that after a number of steps the equilibrium has been reached. We want to maintain this equilibrium if we keep walking, that is we require microscopic reversibility

$$P(\boldsymbol{m_i}|\boldsymbol{m_j}) \sigma_m(\boldsymbol{m_j}) = P(\boldsymbol{m_j}|\boldsymbol{m_i}) \sigma_m(\boldsymbol{m_i}). \tag{4.16}$$

From this and Eq. (4.12) we get

$$P(\boldsymbol{m_i}|\boldsymbol{m_j}) \rho_m(\boldsymbol{m_j}) L(\boldsymbol{m_j}) = P(\boldsymbol{m_j}|\boldsymbol{m_i}) \rho_m(\boldsymbol{m_i}) L(\boldsymbol{m_i}). \tag{4.17}$$

This requirement is met if $P(\boldsymbol{m_j}|\boldsymbol{m_i})$ is chosen so that it is proportional to $\rho_m(\boldsymbol{m_j}) L(\boldsymbol{m_j})$ (Mosegaard, 1998).

Our goal is to construct a random walk with equilibrium probability density σ_m. Assume that we have a random walk that equilibrates at the *a priori* probability density ρ_m. We will now modify this random walk to sample the *a posteriori* probability density σ_m instead. As opposed to accepting every step suggested by the random walk and thereby sample the *a priori* probability density, we will sometimes discard the step and stay where we are. We will use the Metropolis criterion

$$P_{\text{accept}} = \min\left(1, \frac{L\left(\boldsymbol{m_i}\right)}{L\left(\boldsymbol{m_j}\right)}\right) \tag{4.18}$$

to decide whether or not to take the step from $\boldsymbol{m_j}$ to $\boldsymbol{m_i}$: If the likelihood of the suggested model $\boldsymbol{m_i}$ is higher than or equal to that of the current model $\boldsymbol{m_j}$ the step is accepted. Otherwise the step is accepted with the probability $\frac{L(\boldsymbol{m_i})}{L(\boldsymbol{m_j})}$. It can be shown that this new random walk samples the *a posteriori* probability density (Mosegaard and Tarantola, 1995).

The algorithm described above is called the Metropolis algorithm and was developed by Metropolis and Ulam (1949), Metropolis et al. (1953), and Hastings (1970). It is a Markov chain Monte Carlo optimization method. Generally, a Monte Carlo method is an algorithm that uses random numbers to solve a computational problem, and a Markov chain Monte Carlo method is one, that has no memory, i.e. each step depends only on the previous step (Tarantola, 2005).

4.2 Obtaining basal melt rates from RES data

In the following sections the theory described above is applied to the problem at hand. The radar data presented in Chapter 2 constitute the observed data and the ice flow model introduced in Chapter 3 is the forward theoretical model. The model parameters to be determined are the basal melt rates and other flow parameters.

4.2.1 *A priori* information

The *a priori* knowledge in the data space $\mathcal{D}$ consists of the depths and ages of the 13 isochrones shown in Fig. 2.5, and the corresponding uncertainties.

The *a priori* information in the model space $\mathcal{M}$ consists of constraints on the model parameters. The model parameter vector $\boldsymbol{m}$ is different for the different situations described in Chapter 3. For the 1D problem we have (cf. Section 3.1.4) for NorthGRIP

$$\boldsymbol{m}_{\text{NGRIP}} = [p_1, p_2, p_3, h, F_B, w_b] \tag{4.19}$$

Segment	Start (km)	End (km)	Length (km)
NGRIP	264	464	200
Middle	392	638	246
NEEM	512	699	187

Table 4.1: Start and end points for the three segments that the line has been divided into in order to solve the 2D inverse problem.

and for the other 1D sites

$$\boldsymbol{m}_{\text{1D}} = [k_A, h, F_B, w_b] . \tag{4.20}$$

For the 2D problem we have

$$\boldsymbol{m}_{\text{2D}} = [p_1, p_2, p_3, k_h, k_F, w_{b1}, w_{b2}, ..., w_{b55}] , \tag{4.21}$$

where $w_{b1}, w_{b2}, ..., w_{b55}$ are the vertical velocities at the base in the 55 melt rate intervals. These 55 melt rate intervals cover the full section of 435 km, and changing the value of w_b in one 8 km interval along the line only affects the isochrone geometry in the vicinity of that interval. Thus a lot of computing time is wasted when the misfit is calculated for the whole 435 km long section when the conditions are only changed in a small part of the line. Therefore, it was decided to divide the line into three smaller sections and solve the 2D inverse problem for each of these segments separately. The start and end points of the three segments are given in Table 4.1. The segments are chosen so that each of the six sites NorthGRIP, Sites 1–4, and NEEM are located at least 50 km downstream from the start of a segment. Furthermore, there is an overlap between segments. The parameters p_1, p_2, and p_3 from the accumulation model will be determined from the segment containing the NorthGRIP drill site, and a scaled version of the accumulation history found here will be used for the other segments. Thus the three 2D inverse problems with the following model vectors will need to be solved

$$\boldsymbol{m}_{\text{sec1}} = [p_1, p_2, p_3, k_h, k_F, w_{b1}, w_{b2}, ..., w_{b22}] \tag{4.22}$$

$$\boldsymbol{m}_{\text{sec2}} = [k_h, k_F, w_{b17}, w_{b18}, ..., w_{b47}] \tag{4.23}$$

$$\boldsymbol{m}_{\text{sec3}} = [k_h, k_F, w_{b32}, w_{b33}, ..., w_{b55}] . \tag{4.24}$$

The number of unknowns for each of the three inverse problems to be solved in the 2D case are thus 27, 33, and 26, respectively.

The constraints on the model parameters consists of intervals to which the different model parameters are confined. This knowledge arises from the

Parameter	Constraint
p_1	$0\leq A$
p_2	$0\leq A$
p_3	$0\leq A$
$k_A = A_{\text{site}}/A_{\text{NGRIP}}$	$0\leq k_A\leq 2$
h	$0\leq h \leq H$
F_B	$0\leq F_B\leq 1$
w_b	$w_b\leq 0$
$k_h = h/H$	$0\leq k_h \leq 1$
$k_F = F_B/w_b$	$k_F\leq 0$

Table 4.2: The *a priori* knowledge in $\mathcal{M}$ consists of constraints on the model parameters. This knowledge is based on the physical nature of the parameters. The constraints on p_1, p_2, and p_3 are given through the accumulation rate A.

physical nature of the parameters, e.g. the accumulation rate cannot be negative, the kink height must be smaller than the ice thickness etc. The constraints on the model parameters are given in Table 4.2. The *a priori* knowledge described above corresponds to an *a priori* probability density function ρ_m in $\mathcal{M}$ that is constant for all values within the interval of possible values for each parameter and 0 elsewhere.

4.2.2 The likelihood function

We assume that the uncertainties on the observed data are Gaussian, so we will use the likelihood function from Eqs. (4.13) and (4.14).

4.2.3 The random walk

It is straightforward to construct a random walk that samples the *a priori* probability density ρ_m in the model space. It merely has to pick all values in the interval with equal probability and not pick values outside of the interval. Using the Metropolis criterion from Eq. (4.18) to accept or reject the suggested values, this random walk is modified to sample the *a posteriori* probability density σ_m instead.

In every step of the random walk, one entry m_i of the model vector $\boldsymbol{m}$ is altered:

$$m_{i,\text{new}} = m_{i,\text{old}} + (2n-1)\cdot \Delta m_i. \tag{4.25}$$

Here n is a uniformly distributed random number between 0 and 1 and Δm_i is the maximum step size for the i^{th} entry of the model vector. The step size for each parameter is chosen so that the accept rates for all parameters are within 30–60%. If the step size is chosen too small, the search of the model space will proceed very slowly, and if it is chosen too big, a large number of steps will be rejected.

Now we have all the tools we need to solve the problem. The algorithm used is outlined below:

1. Make a starting guess $\boldsymbol{m_j}$ for the model vector
2. Run the forward model using $\boldsymbol{m_j}$
3. Calculate the likelihood function $L(\boldsymbol{m_j})$
4. Perturb the model vector $\boldsymbol{m_j} \longrightarrow \boldsymbol{m_i}$ in agreement with ρ_m
5. Run the forward model with the perturbed model vector $\boldsymbol{m_i}$
6. Calculate the likelihood function $L(\boldsymbol{m_i})$
7. Accept or reject the perturbed model according to the Metropolis criterion from Eq. (4.18).
8. Repeat from step 4

Every time the forward model is run, we follow the 13 isochrones as they one by one get deposited on the ice surface and sink down through the ice sheet. The better these modelled isochrones match the observed ones, the smaller is the misfit. The accepted values for the model parameters are stored and after sufficiently many steps by the random walker, the set of accepted models represents the *a posteriori* probability density function σ_m.

Ideally we want independent samples of the *a posteriori* probability density function, but since only one entry of the model vector is changed at a time, the accepted models will inevitably be highly correlated. This problem can be solved by keeping only accepted models that are separated by a large enough number of steps that they are uncorrelated (Tarantola, 2005). The number of steps needed between models to obtain a set of uncorrelated models can be estimated from the autocorrelation of the likelihood function.

Because the random walk is started at guessed values for the model parameters there will most likely be a burn-in time, where the likelihood function grows. The burn-in time is the time it takes to move from the initial (guessed) state to a state of high probability. After the burn-in period, the value of the likelihood function will settle around a constant level. The model vectors accepted during the burn-in period should be discarded before analysis is done on the set of accepted models.

4.3 Summary

The inverse problem consisting of internal isochrones in the ice seen in RES images (observed data), the ice flow model presented in Chapter 3 (the forward model), and unknown flow parameters (the unknown model parameters) can be solved using the Metropolis algorithm. The *a priori* knowledge of the model parameters is summed up in Table 4.2, and the random walk used to solve the problem is described in Section 4.2.3.

Chapter 5

Results

Investigations using the 1D flow model have been carried out for the two drill sites as well as for four other locations on the ice ridge (see Fig. 1.1). In this chapter the results of the investigations done with both the 1D and the 2D model are presented and analysed.

5.1 1D modelling - constant ice thickness

The results presented in this section were obtained using the 1D model with the constraint $\frac{\partial H}{\partial t} = 0$. Results obtained when accounting for past changes in ice thickness are found in Section 5.2.

The locations of the sites where the 1D inverse problem has been solved are indicated on the RES image in Fig. 5.1. Their positions are 314 km, 414 km, 490 km, 514 km, 586 km, and 679 km from GRIP, respectively. The locations were chosen so that the 1D problem will be solved for at least every 100 km between the two drill sites at locations where the oldest of the 13 isochrones is visible (cf. Section 2.2.1). Furthermore, an extra site, Site 2, was placed at the slope leading up from the deep trench in the bedrock upstream from Site 3, to be able to compare how the 1D and 2D model behave under such conditions.

5.1.1 NorthGRIP

NorthGRIP is the only place in the area studied in this thesis where an ice core has been drilled to bedrock providing us with a dated δ^{18}O record reaching far back in time. Therefore, this site was investigated first in order

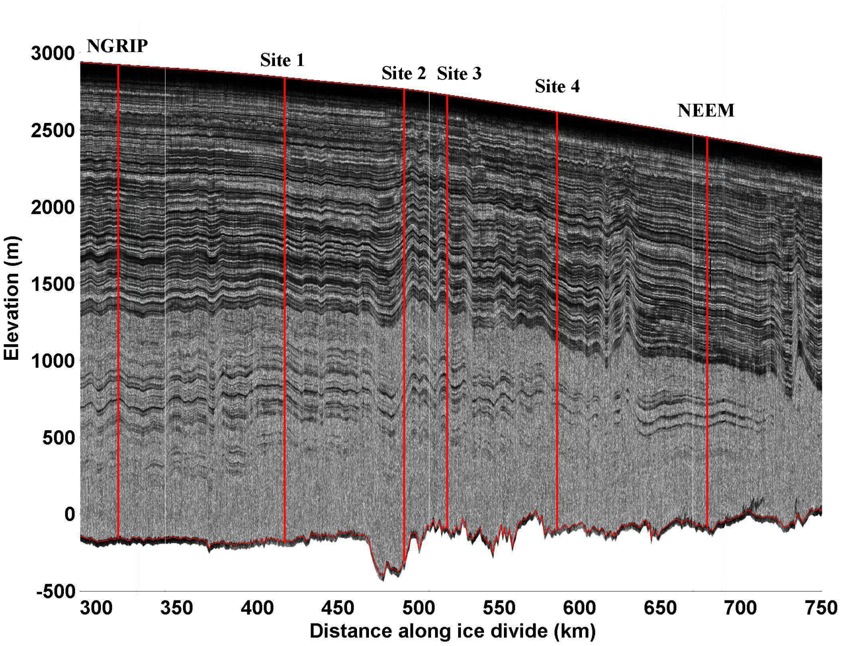

Figure 5.1: Radar image collected along the ice divide in northern Greenland. The sites where 1D model investigations have been done are indicated in red.

to obtain an accumulation history, which is required in order to carry out simulations at other locations along the ice divide.

A total of $2.1 \cdot 10^6$ accepted models were collected during the random walk. The individual accept rates for the Monte Carlo parameters were around 50%. By looking at the accepted values for the individual model parameters, it can be seen that the burn-in period is quite long (see Fig. 5.2). It was chosen to discard the first 700,000 accepted models in the further analysis.

Fig. 5.3 shows histograms of the values of the six model parameters for all the accepted models after the burn-in period. Gaussian distributions fitted to the sets of accepted model parameters are shown for comparison. It is seen, that all parameter distributions except that for F_B resemble a Gaussian distribution. The inverse problem was solved with the the restriction that $F_B > 0$, i.e. the ice flows in the same direction at the surface and at the base. This could be a contributing factor to the distribution for F_B having a different shape than the others. However, the distribution shows only one maximum indicating that the value of F_B is unambiguously determined from the Monte Carlo solution.

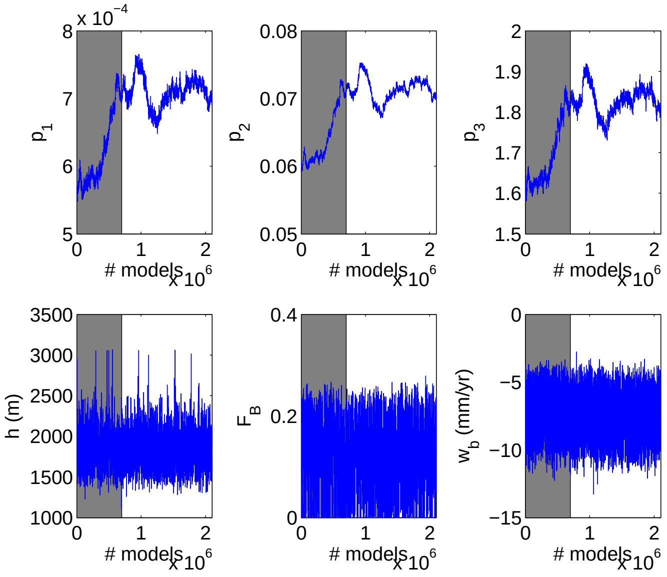

Figure 5.2: Accepted values for the six Monte Carlo-determined parameters at North-GRIP. It is seen that there is a significantly longer burn-in period for p_1, p_2, and p_3 than for the other three parameters. The burn-in period of 700,000 accepted steps is indicated in grey.

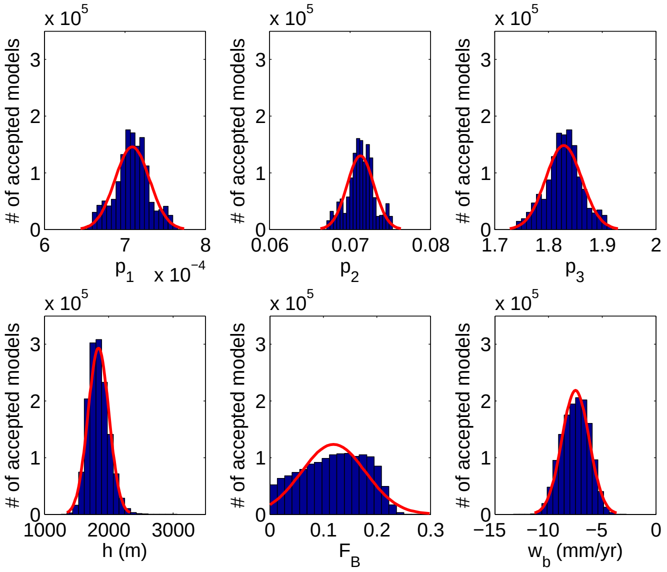

Figure 5.3: Blue: Histogram of the parameter values for the accepted models at North-GRIP after the burn-in period. Red: Gaussian distribution fitted to the accepted model parameters. These results were obtained using the 1D model with $\frac{\partial H}{\partial t} = 0$.

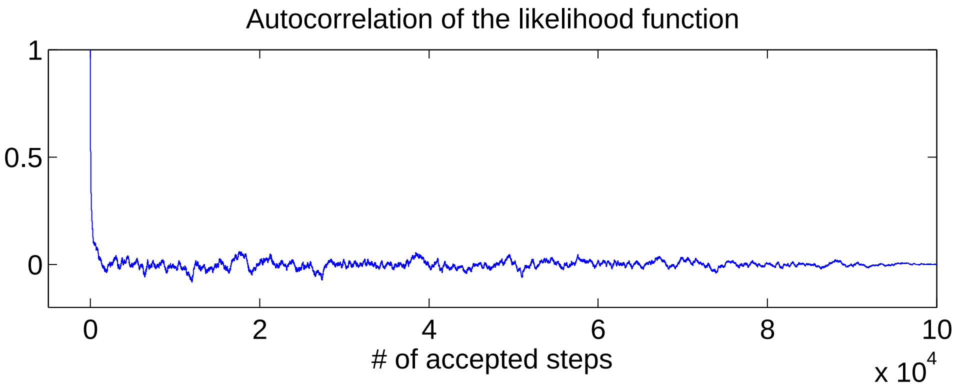

Figure 5.4: Autocorrelation for the first 100,000 accepted models after the burn-in period. The correlation length is read off where the curve crosses 0 for the first time, which happens around step # 1350.

Having obtained a set of accepted values and established a burn-in period, there is one more aspect that needs to be addressed before we can proceed to infer best values for the Monte Carlo parameters from the sets of accepted values for the model parameters. In the Monte Carlo algorithm used in this study, only the value of one model parameter is changed at a time, and thus models accepted right after each other tend to be highly correlated. In such cases it can be useful to only use accepted models separated by the correlation length. Fig. 5.4 shows the autocorrelation for the first 100,000 accepted models after the burn-in period. The correlation length can be found from this graph by reading off where the curve reaches 0 for the first time. The correlation length is found to be 1350 accepted steps. To get uncorrelated models we then pick out only every 1350^{th} model after the burn-in period, which brings the number of accepted independent models down to just over 1,000. However, as seen from Fig. 5.5, using only uncorrelated models changes neither the shape of the distributions nor the locations of the maxima for any of the parameters. The reason for this could be that in the problem at hand we only have six model parameters, so changing one parameter could actually change the model vector significantly. It was decided to use the whole suite of models accepted after the burn-in period.

The resulting values for the six model parameters and the uncertainties on their determination from the Monte Carlo solution are found in Table 5.1. For all parameters but F_B the best values for a parameter is found by taking the mean of the distribution of accepted values in Fig. 5.3. Because of the different shape of the histogram of accepted values for F_B the mean of the fitted Gaussian distribution does not coincide with the maximum of the histogram of accepted values. It was chosen to use the highest point of the distribution as best value.

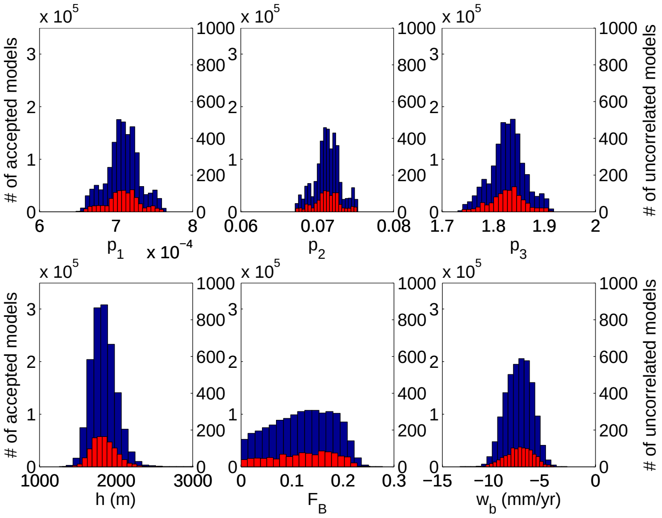

Figure 5.5: Comparison of histograms for the parameter values for NorthGRIP for all the accepted models after the burn-in period (blue, left hand vertical axis) and those for only uncorrelated models (red, right hand vertical axis). The results were obtained from the 1D model with $\frac{\partial H}{\partial t} = 0$.

Parameter	Value	σ_{std}
p_1 (m/yr ‰$^{-2}$)	$7.1 \cdot 10^{-4}$	$0.2 \cdot 10^{-4}$
p_2 (m/yr ‰$^{-1}$)	$7.1 \cdot 10^{-2}$	$0.2 \cdot 10^{-2}$
p_3 (m/yr)	1.83	0.03
A_0 (m/yr)	0.197	0.002
h (m)	1840	160
F_B	0.14	0.06
w_b (mm/yr)	-7.5	1.3

Table 5.1: The values of the Monte Carlo parameters for the 1D model for NorthGRIP determined from a Monte Carlo solution to the inverse problem constrained by 13 fixpoints. The value and uncertainty of A_0 as calculated from the sets of accepted values of p_1, p_2, and p_3 are also included.

	p_1	p_2	p_3	h	F_B	w_b
p_1	1					
p_2	0.97	1				
p_3	0.91	0.98	1			
h	-0.04	0.05	0.17	1		
F_B	-0.05	0.09	0.19	0.62	1	
w_b	0.03	0.04	0.06	0.52	0.75	1

Table 5.2: Correlation coefficients between the Monte Carlo-determined model parameters for the 1D model for NorthGRIP using $\frac{\partial H}{\partial t} = 0$.

The uncertainty, σ_{std}, stated for each parameter in Table 5.1 is merely the standard deviation of the distribution of accepted model values. This value is a measure only of how well-determined the value is from the Monte Carlo solution and does not include other uncertainties due to e.g. model insufficiencies or assumptions. Thus the true uncertainty is higher, and the uncertainties listed in Table 5.1 can be viewed as a lower limit for the true uncertainties.

The parameters p_1, p_2, and p_3 are highly correlated (see Table. 5.2). From the set of accepted values for p_1, p_2, and p_3 (not including values accepted during the burn-in period) we get the NorthGRIP accumulation history shown in Fig. 5.6. The obtained uncertainties on the accumulation rate vary with time between $\sim 2 \cdot 10^{-3}$ m/yr and $\sim 5 \cdot 10^{-3}$ m/yr (cf. Fig 5.18, blue curve). The histogram of values for the present ice equivalent accumulation rate at NorthGRIP as calculated from the accepted values of p_1, p_2, and p_3 after the burn-in period is shown in Fig. 5.7. The best value is found to be 0.197±0.002 m/yr, which is in agreement with the observed value of 0.193±0.005 m/yr.

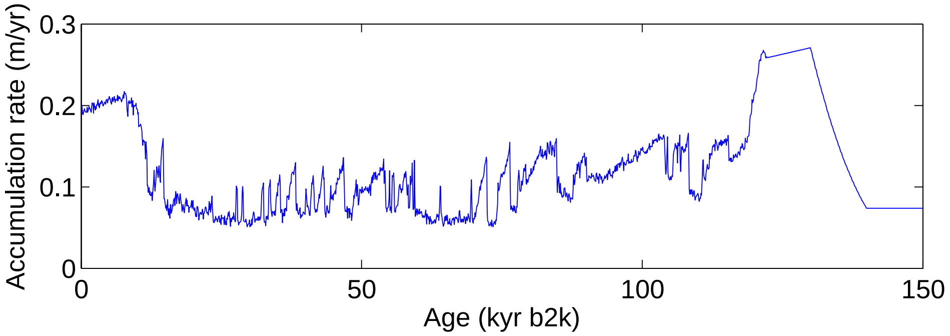

Figure 5.6: Best estimate of the accumulation history at NorthGRIP as calculated from Eq. 3.44 using the sets of accepted values for p_1, p_2, and p_3 found using the 1D model with $\frac{\partial H}{\partial t} = 0$.

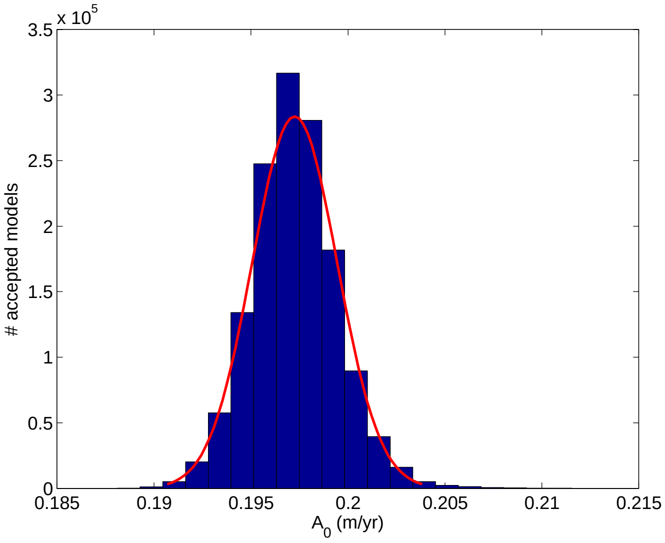

Figure 5.7: Values of A_0 calculated from the accepted values of p_1, p_2, and p_3 for the 1D model at NorthGRIP with $\frac{\partial H}{\partial t} = 0$.

A comparison of the obtained δ^{18}O-accumulation relation with strain corrected observed annual layer thicknesses (cf. Section 3.1.2) is shown in Fig. 5.8. The accumulation relation from Eq. (3.44) is extended to also show what the model looks like for Eemian δ^{18}O values which are typically around -33‰.

Fig. 5.9 shows histograms of the differences between the observed depths of the 13 isochrones and the modelled depths calculated from the accepted values of the model parameters. It is seen that there is a good agreement between observed and modelled isochrones. The differences between the observed depths and the best values from the histograms of modelled depths are shown in Table 5.3.

5.1.2 NEEM

NEEM is located 365 km from NorthGRIP when traveling along the ice divide. Drilling at the NEEM site commenced in 2007, and a δ^{18}O record is not yet available from there. It is assumed that the accumulation rate at this site is proportional to that at NorthGRIP with $k_A = \frac{A_{\text{NEEM}}}{A_{\text{NGRIP}}}$ being the proportionality constant at all times (cf. Eq. (3.45)).

Thus, four model parameters, k_A, h, F_B, and w_b were estimated from the Monte Carlo solution to the inverse problem. A total of 800,000 accepted models were collected (Fig. 5.10), and the burn-in period was determined to

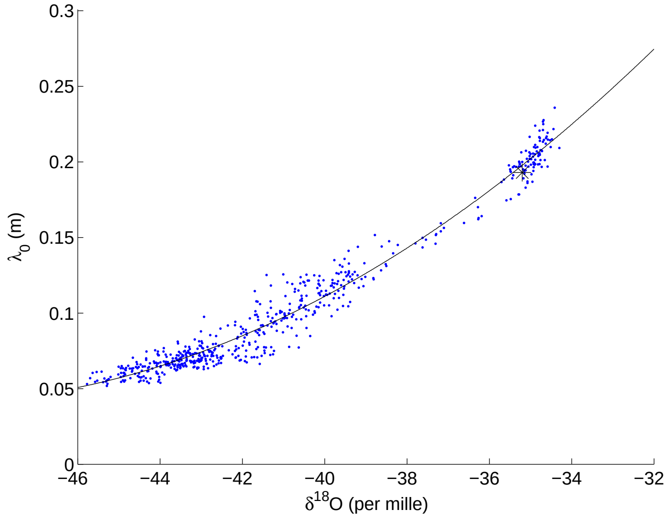

Figure 5.8: Strain-corrected observed annual layer thicknesses versus δ^{18}O for the last 60 kyr in the NorthGRIP ice core. The solid line is the accumulation relation from Eq. (3.44) with parameter values determined from the Monte Carlo solution to the 1D inverse problem (see Table 5.1). The black asterisk denotes the observed present values at NorthGRIP.

Age (kyr)	NGRIP	Site 1	Site 2	Site 3	Site 4	NEEM
1.4	1	2	3	7	-10	0
2.7	-4	-6	1	-6	7	5
3.2	-6	-1	-1	1	-13	-21
4.0	0	1	6	9	1	-2
4.8	0	2	10	10	5	7
5.9	2	1	-16	-27	-8	6
7.5	6	0	-2	3	13	27
10.2	5	4	5	1	10	25
14.6	-8	-7	-8	-1	0	-1
37.7	-2	1	2	4	-10	-23
45.0	1	0	2	8	-6	-15
51.0	4	9	10	4	-6	-9
74.6	-2	-6	-8	-10	8	-11

Table 5.3: The difference in m between observed and modelled depths of the isochrones. The modelled depths are calculated from the accepted values of the model parameters of the 1D model with $\frac{\partial H}{\partial t} = 0$.

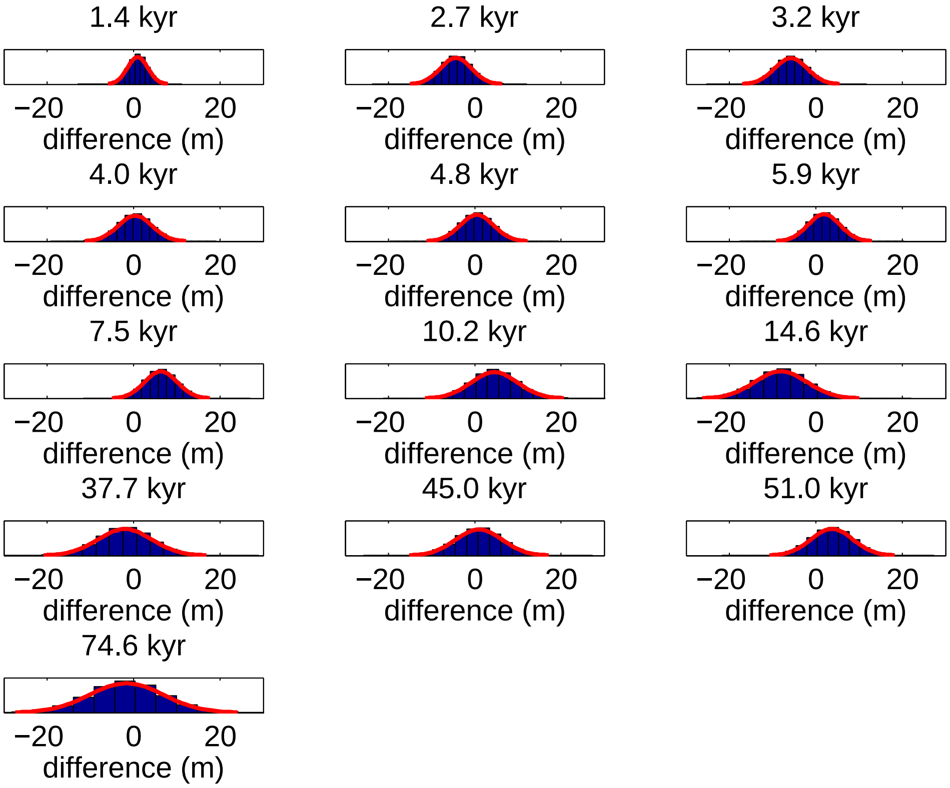

Figure 5.9: Difference between observed depths of the 13 isochrones and the depths calculated from the accepted values of the model parameters for the 1D model for NorthGRIP using $\frac{\partial H}{\partial t} = 0$. The vertical scale is 0 to $3.5 \cdot 10^5$ for every plot, at the age of the corresponding isochrone is given above each distribution.

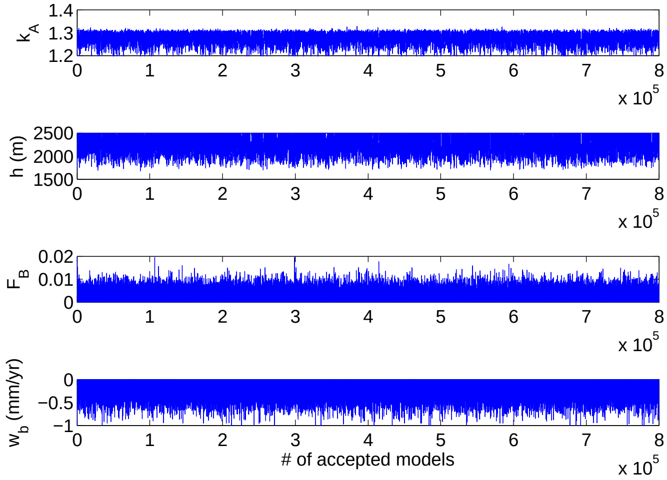

Figure 5.10: Accepted values for the four Monte Carlo parameters for NEEM.

be 1,000 models. The correlation length was found to be ∼1,000 models but, as was the case for NorthGRIP, using only the uncorrelated models leads to no significant changes in the parameter values (cf. Fig. 5.11), and it was chosen to use all accepted models.

Fig. 5.12 shows histograms of the accepted values after the burn-in period for the four Monte Carlo parameters as well as a Gaussian distribution fitted to the data. None of the distributions are well represented by the fitted Gaussian distributions. In the cases of h, F_B, and w_b this is explained by the most likely value being located very close to an upper or lower limit for the parameter value. The distribution of accepted values of k_A does not have this problem, but the highest point of the histogram is shifted off to the side. However, the distribution shows only one maximum, lending us confidence that the value is well determined by the Monte Carlo solution. For all four parameters we choose the location of the top of the histogram as the best estimate of the value of the parameter. The obtained best values are found in Table 5.4. The best value of k_A indicates that the accumulation rate at NEEM is almost 30% higher than at NorthGRIP, i.e. the present accumulation rate should be 0.254±0.005 m/yr (cf. Table 5.5). This is significantly higher than the observed value of 0.225±0.005 m/yr. It is also interesting to note that the results indicate that there is no significant basal melting at NEEM.

The differences between the observed and modelled depths of the isochrones are given in Table 5.3.

A comparison between the annual layer thicknesses at NorthGRIP and NEEM is shown in Fig. 5.13. Due to the lack of basal melting, the layers close to

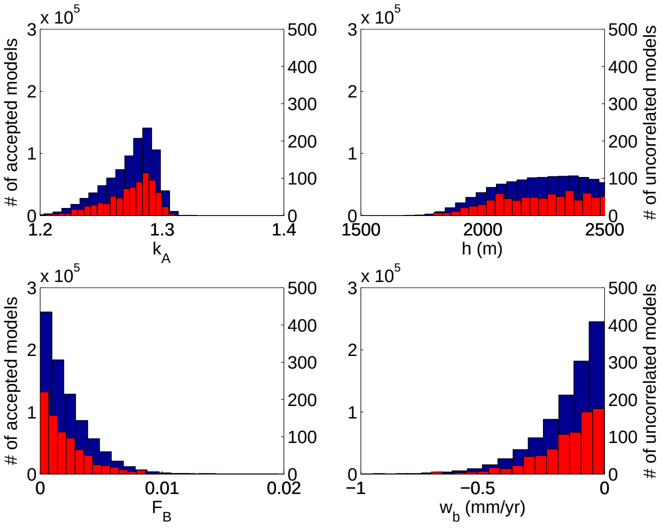

Figure 5.11: Comparison of histograms for the parameter values for NEEM for all the accepted models after the burn-in period (blue, left hand vertical axis) and those for only uncorrelated models (red, right hand vertical axis).

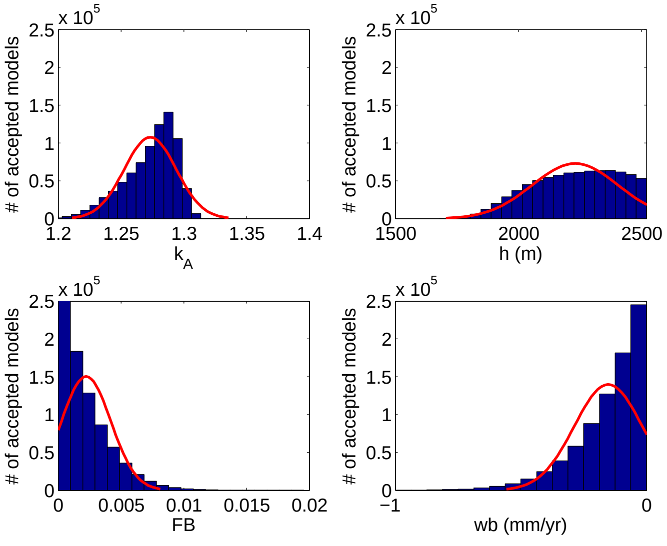

Figure 5.12: Histograms of the accepted values after the burn-in period for the four Monte Carlo parameters in the 1D model at NEEM. A Gaussian distribution fitted to the accepted model parameters is shown in red.

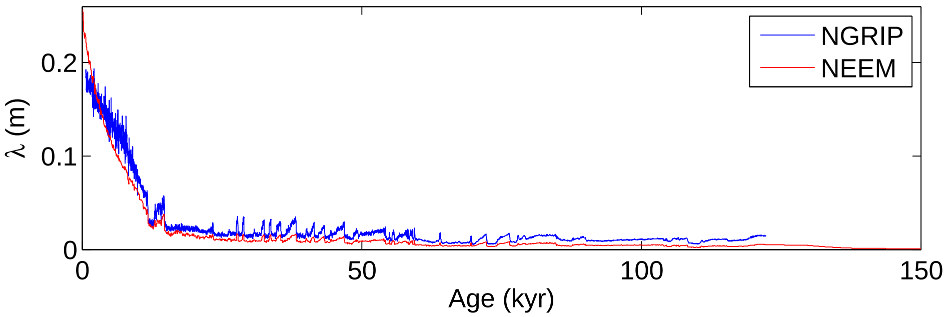

Figure 5.13: Annual layer thicknesses at NorthGRIP (blue) and NEEM (red). The annual layer thickness at NorthGRIP are based on the GICC05 timescale for the most recent 60 kyr and on the ss09sea timescale before that. The annual layer thicknesses at NEEM are calculated from the results of the present study.

bedrock at NEEM are thinner than at NorthGRIP.

The δ^{18}O history used in this study reaches back only to 150 kyr b2k (cf. page 32). Using the results from the present study, ice of this age is found at z=130±10 m at NEEM. Thus it is likely that the ice at the base is more than 200 kyr old.

5.1.3 Sites 1–4

In this section the results from the remaining four 1D sites are presented.

As for NEEM, only four model parameters need to be determined for the four sites, and the considerations regarding burn-in period and correlation of accepted models are similar to those at NEEM. The plots of accepted model values and histograms of accepted values are found in App. A (Figs. A.1–A.12). As was the case for NorthGRIP and NEEM there is no difference between the statistics for the complete set of accepted values after the burn-in period and those of only uncorrelated models, and all models accepted after the burn-in period were used.

The best values of the model parameters for the four sites as well as other site-specific information are summarized in Tables 5.4 and 5.5.

The differences between observed and modelled depths at all six 1D locations are given in Table 5.3. Generally, the misfit increases with distance from NorthGRIP, which is to be expected because the assumptions of constant accumulation pattern and ice thickness with time is probably getting less accurate the further we move away from the centre of the ice sheet.

Site	k_A	h (m)	F_B	w_b (mm/yr)
NGRIP	1	1840±160	0.14±0.06	-7.5±1.3
Site 1	0.99±0.02	2030±200	0.09±0.03	-2.0±0.9
Site 2	0.88±0.01	1850±190	0.11±0.03	-2.2±1.0
Site 3	0.86±0.02	1950±290	0.06±0.02	-1.2±0.7
Site 4	1.09±0.02	1770±170	0±0.01[a]	-1.5±0.7
NEEM	1.29±0.02	2370±170	0±0.002[a]	0±0.1[b]

---

[a] The parameter is strictly non-negative, so only the plus option applies.

[b] The parameter is strictly non-positive, so only the minus option applies.

Table 5.4: Monte Carlo-determined values of different input parameters to the 1D ice flow model.

Site	x (km)	H (m)	z_{sur} (m)	A_0 (m/yr)	k_h	k_F
NGRIP	314	3065	2918	0.197±0.002	0.60	-15
Site 1	414	2995	2837	0.196±0.004	0.68	-13
Site 2	490	3072	2761	0.173±0.003	0.60	-13
Site 3	514	2790	2726	0.170±0.004	0.70	0
Site 4	586	2694	2609	0.215±0.005	0.66	0
NEEM	679	2520	2447	0.254±0.005	0.95	0

Table 5.5: Location (distance from GRIP along the ice divide), ice equivalent ice thickness, surface elevation, and Monte Carlo-determined present ice equivalent accumulation rate, and values of k_h and k_F at the six sites. The parameters k_h and k_F are used in the 2D model (cf. Eqs. (3.50) and (3.51)). Here, they are calculated from the accepted values of h, F_B, and w_b from the 1D model in order to assess the assumption of keeping these parameters constant in the 2D model (cf. Section 5.1.6).

The following sections summarize what can be inferred from the 1D studies with $\frac{\partial H}{\partial t} = 0$ about the spatial variability of the accumulation rate, the location of the Eemian layer along the ice divide between NorthGRIP and NEEM, the validity of assumptions used in the 2D model, and the stability of the solution to the choice of dt.

5.1.4 The accumulation rate pattern

From the 1D model results at the six locations, we can calculate the corresponding present accumulation rate at each site. These are shown in Fig. 5.14 together with the accumulation rates obtained from shallow radar layers (cf. Section 2.2.2). The present accumulation rates obtained from the 1D model studies support the shape of the accumulation rate pattern obtained from the shallow radar layers, and for NorthGRIP and Sites 1–3 the values obtained by the two methods also agree fairly well. For Site 4 and NEEM, however, the 1D model investigations indicate significantly higher accumulation rates than the shallow radar layers do. Two main things could contribute to this. First, the ice thickness was assumed constant in time when the 1D problem was solved for these locations. This assumption is acceptable for the central parts of the ice sheet, but it becomes increasingly problematic as we move coastward along the ice divide, because the changes in ice thickness over the past glacial cycle are larger here (Marshall and Cuffey, 2000). Secondly, the accumulation rate pattern was also assumed constant in time, which is probably not a good assumption because changes in the surface elevation are very likely to cause a change in accumulation rate.

5.1.5 Eemian Ice

The distributions for the location of the top and bottom of the Eemian layer and the corresponding thickness of the layer at NEEM calculated from the sets of accepted values of the model parameters are shown in Fig. 5.15. The positions in the ice column and the thickness of the Eemian layer at the various 1D sites are given in Table 5.6, and shown in Fig. 5.16, that depicts the profile from NorthGRIP to NEEM.

The results indicate that the full Eemian layer is preserved at all locations except NorthGRIP, where Eemian ice is predicted to occupy the bottom 50±40 m of the ice column. This is in agreement with the results from ice core studies that show that the isotope record from the NorthGRIP ice core indicates that Eemian ice was found in the bottom 85 m of the core (North Greenland Ice Core Project members, 2004). At Sites 2–4 the model results reveal Eemian layer thicknesses between 96±9 m and 151±14 m and predict

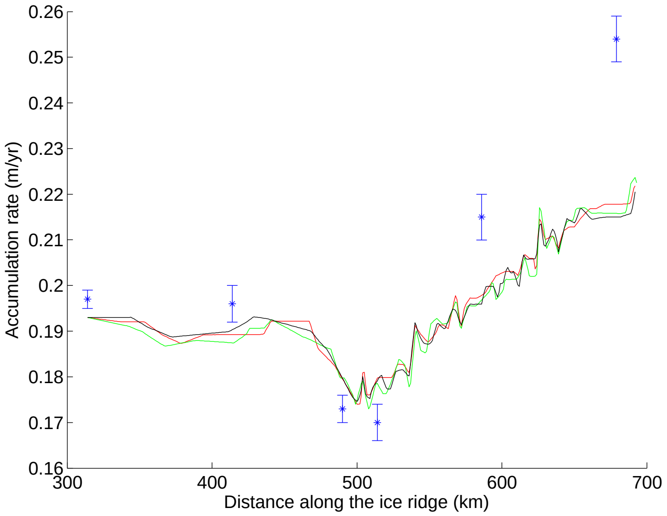

Figure 5.14: Comparison between the accumulation rate pattern obtained from shallow radar layers tuned to match the observed value at NorthGRIP (red, green, and black) and the results from solving the 1D inverse problem at the six sites (blue asterisks). The error bars on the 1D results indicate the precision to which each value is determined from the Monte Carlo solution.

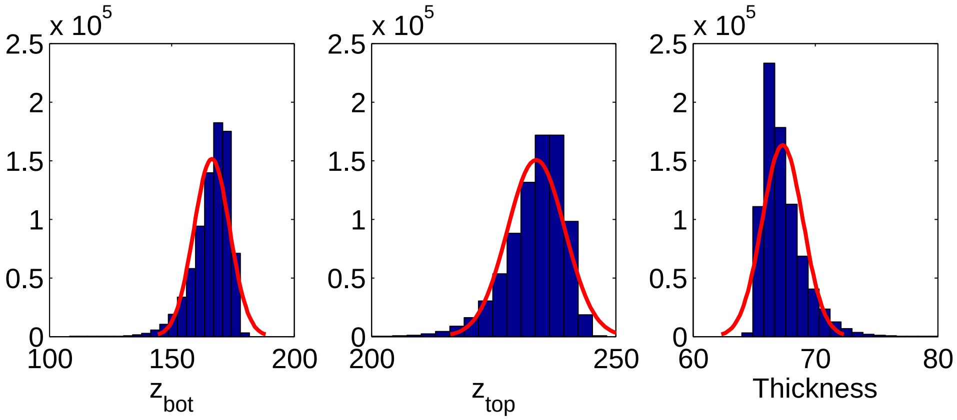

Figure 5.15: Histograms of the positions of the top ($z_{\rm top}$) and bottom ($z_{\rm bot}$) of the Eemian layer at NEEM and of the corresponding thicknesses of the layer. The positions are calculated from the accepted model parameters.

	Bedrock (m)	$z_{\rm bot}$ (m)	$z_{\rm top}$ (m)	Thickness (m)
NGRIP	-171	-171[a]	-121±40	50±40[b]
Site 1	-179	30±35	175±20	131±13
Site 2	-328	-97±40	65±30	151±14
Site 3	-124	178±30	305±20	123±9
Site 4	-100	124±30	223±20	96±9
NEEM	-98	169±7	238±6	66±2

---

[a] All accepted models indicate that the early Eemian ice is lost.

[b] With the early Eemian ice being lost, the uncertainty on the thickness of the Eemian layer is given by the uncertainty on the position of the top of the layer.

Table 5.6: The location of the Eemian layer in the ice column at the 1D locations. Note that the full Eemian is not present at NorthGRIP. Thus, the given layer thickness is for the part of the period that is still present.

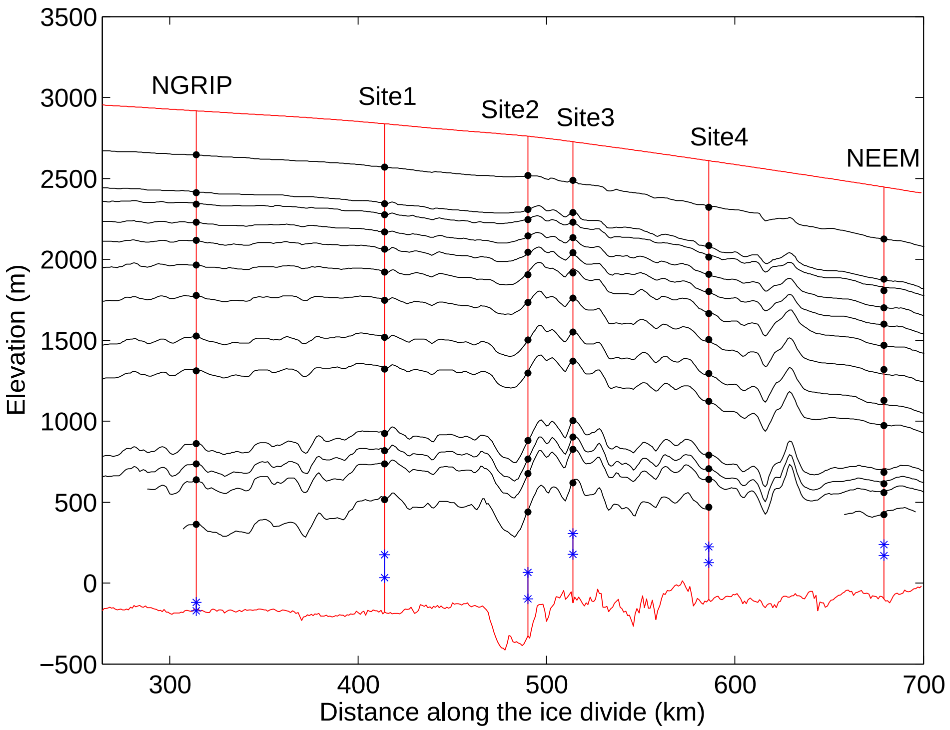

Figure 5.16: The location of the Eemian layer in the ice column (blue asterisks) at the different 1D sites calculated from the accepted model parameters obtained from the Monte Carlo solution to the 1D inverse problem at the different sites. At NorthGRIP only part of the Eemian ice is still present. The 13 observed isochones are shown as black lines, and the modelled depths of the isochrones are shown as black dots.

the layer to be located well above bedrock. However, at all these sites, the topography of the bedrock upstream from the sites is so uneven that there is a high risk that the stratigraphy of the ice has been broken in the lower part of the ice column due to the ice having flowed over the hilly bedrock. This is not a concern at Site 1 or at NEEM where the bedrock is considerably smoother. This study indicates that both these locations would be good places to drill for Eemian ice. Comparing the two sites, the Eemian layer is predicted to be thicker at Site 1 than at NEEM (131 m at Site 1 vs. 66 m at NEEM), but at NEEM the Eemian ice is expected to be found 50 m further above bedrock than at Site 1, and thus we expect to find significantly older ice at NEEM than at Site 1 - both due to the thicker layer beneath the Eemian ice and because the smaller thickness of the Eemian layer indicate a smaller annual layer thickness at NEEM. Thus the results from the present study support the choice of NEEM as the new deep ice core drill site.

5.1.6 The validity of using k_h and k_F in the 2D model

In the 2D model we assume that the ratios $k_h = h/H$ and $k_F = F_B/w_b$ are constant in time and space (cf. Eqs. (3.50) and (3.51)). By calculating these ratios from the accepted values of h, F_B, and w_b at the 1D sites we can get an indication of the validity of these assumptions. The values of k_h and k_F calculated from the parameter values at each 1D site are given in Table 5.5.

For all sites except NEEM the value of k_h is between 0.6 and 0.7, which indicates that the assumption holds for these areas. At NEEM the value is considerably higher: 0.94. However, NEEM is located quite far from the summit of the ice cap, and we would expect the value of k_h to grow when moving further down a flow line.

Histograms of the values of k_F calculated from the accepted values of F_B and w_b at each site are shown in Fig. 5.17. It is seen that the histograms are generally quite broad indicating that the value of k_F is not well determined. For Site 3, Site 4, and NEEM the distributions clearly indicate a best value of 0. Even though the distributions of k_F are broad, the best values do not differ much along the line, so the assumption of a linear relationship between F_B and w_b in the 2D model may still be a reasonable assumption, especially, when the 2D model is run for shorter parts of the line at a time rather than for the whole line at once.

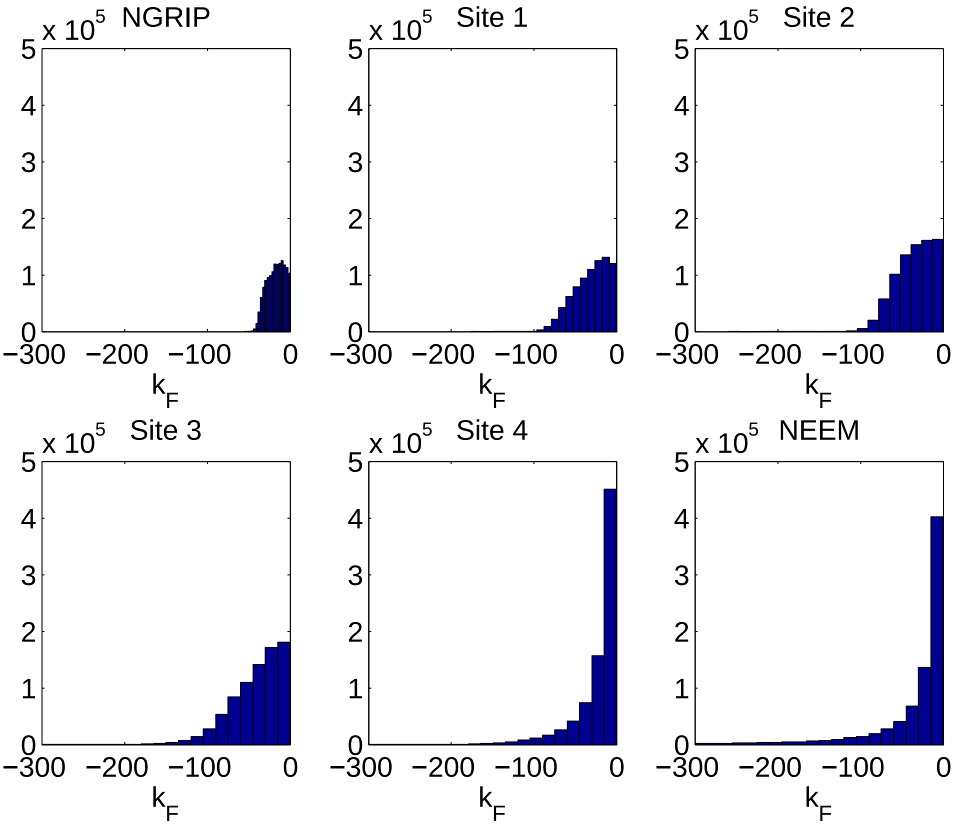

Figure 5.17: Histograms of the values of k_F calculated from the accepted values of F_B and w_b at the 1D sites.

5.1.7 Stability of solution for different values of *dt*

In order to check that the results are not dependent on the choice of dt, we solve the inverse problem with the 1D model for NorthGRIP using dt=25 yrs, half the value that was used above. A total of $1.2 \cdot 10^6$ accepted models were collected. The accepted values of the Monte Carlo-determined parameters and the histograms of accepted values are found in Appendix A (Figs. A.13 and A.14, respectively). The random walk was started at the values found from solving the inverse problem using dt=50 yrs in the forward model, and thus there is no significant burn-in period. Table 5.7 shows the obtained values for the Monte Carlo-determined parameters. The values from the solution to the problem with dt=50 yrs are shown for comparison. No significant difference is seen. The obtained values for p_1, p_2, and p_3 differ slightly more than within the uncertainties. However, due to the high correlation between these three parameters the effect on the accumulation rate is negligible, since the difference between the accumulation histories obtained with

dt	25	50
p_1 (m/yr ‰$^{-2}$)	$(6.6 \pm 0.3) \cdot 10^{-4}$	$(7.1 \pm 0.2) \cdot 10^{-4}$
p_2 (m/yr ‰$^{-1}$)	$(6.7 \pm 0.2) \cdot 10^{-2}$	$(7.1 \pm 0.2) \cdot 10^{-2}$
p_3 (m/yr)	1.75 ± 0.04	1.83 ± 0.03
A_0 (m/yr)	0.197 ± 0.002	0.197 ± 0.002
h (m)	1870 ± 190	1840 ± 160
F_B	0.18 ± 0.06	0.14 ± 0.06
w_b (mm/yr)	-7.4 ± 1.2	-7.5 ± 1.3

Table 5.7: Comparison of best estimates for the Monte Carlo-determined parameters at NorthGRIP for $dt = 25$ and dt=50. The 1D model with $\frac{\partial H}{\partial t}$=0 was used. The value and uncertainty of A_0 calculated from the accepted values of p_1, p_2, and p_3 is also shown.

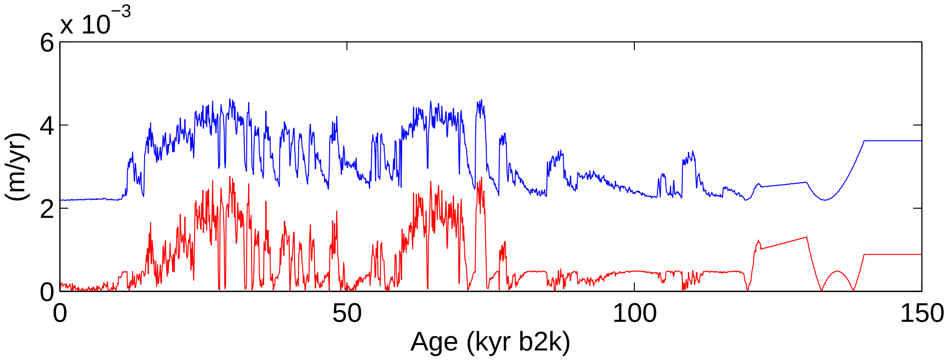

Figure 5.18: The absolute difference between the accumulation history calculated with dt=25 yrs and that calculated with dt=50 yrs (red) and the uncertainty on the accumulation history from dt=50 yrs (blue).

the two values of dt is smaller than the uncertainty on the accumulation history obtained with dt=50 yrs (cf. Fig. 5.18). Thus we feel confident that the choice of dt does not reduce the credibility of the results.

5.2 1D modelling - including ice thickness changes

The above calculations were done for an ice thickness constant in time. In this section, the two ice thickness histories described in Section 3.1.4 are used to account for the temporal changes in ice thickness at NorthGRIP and NEEM.

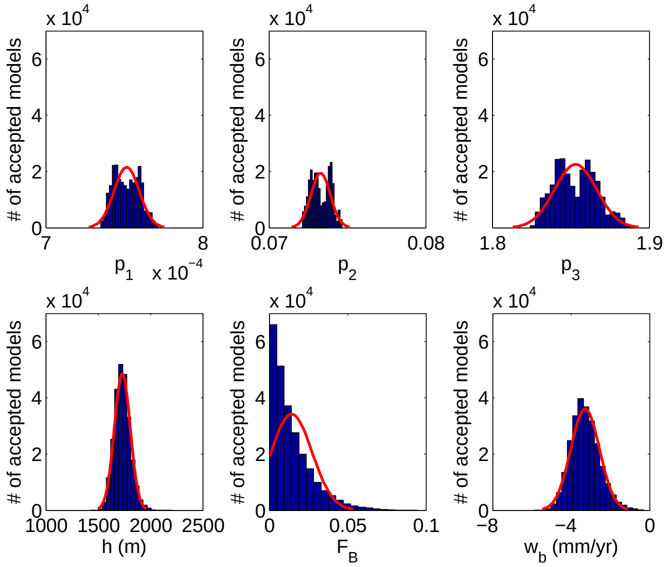

Figure 5.19: histograms for the accepted values of the Monte Carlo parameters after the burn-in period at NorthGRIP using the ice thickness history from Greve (2005) to account for past changes in ice thickness.

5.2.1 NorthGRIP

The two surface elevation histories used i this study are fundamentally different, so we would expect very different results from using the two ice thickness histories. A total of $4 \cdot 10^5$ and $1 \cdot 10^6$ accepted models were collected using the ice thickness histories from Greve (2005) and Vinther et al. (subm), respectively. Plots of the accepted model are found in Appendix A (Figs. A.15 and A.16). From the histogram of accepted values for the Monte Carlo-determined parameters from the model using the ice thickness history from Greve (2005) (see Fig. 5.19) it can be seen that the values of the accumulation model parameters p_1, p_2, and p_3 are not well determined from the Monte Carlo solution. All three histograms show double peaks of almost equal strength. However, due to the high correlation between these three parameters, the distribution of the values of A_0 calculated from the accepted values of p_1, p_2, and p_3 shows a strong single maximum (see Fig. 5.20), and since this is the only parameter dependant on p_1, p_2, and p_3, the double peaks do not lead to any major ambiguities in the results. The other three parameters are well determined. When using the ice thickness history from Vinther et al. (subm) all six Monte Carlo parameters are well determined from the Monte Carlo solution (cf. Fig. 5.21). Though there is a small hint of a double peak for p_2, one peak is much stronger than the other. Table 5.8 shows the best values for the model parameters for the case of each ice thickness history.

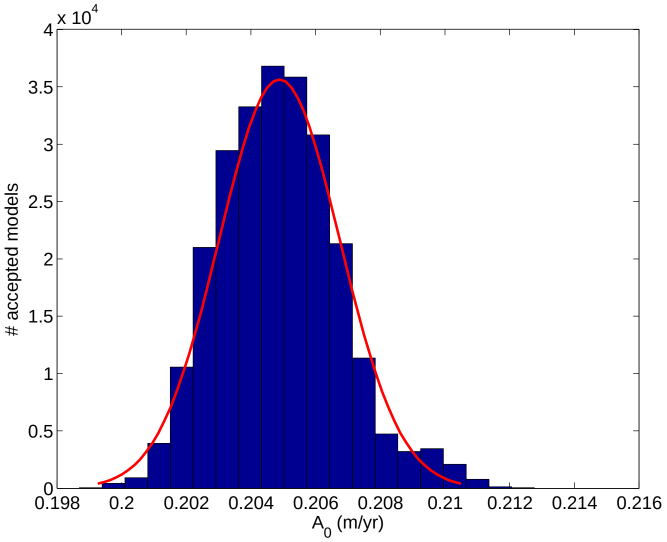

Figure 5.20: Values of A_0 at NorthGRIP calculated from the accepted values of p_1, p_2, and p_3 from the 1D model using the ice thickness history from Greve (2005) to account for changes in ice thickness.

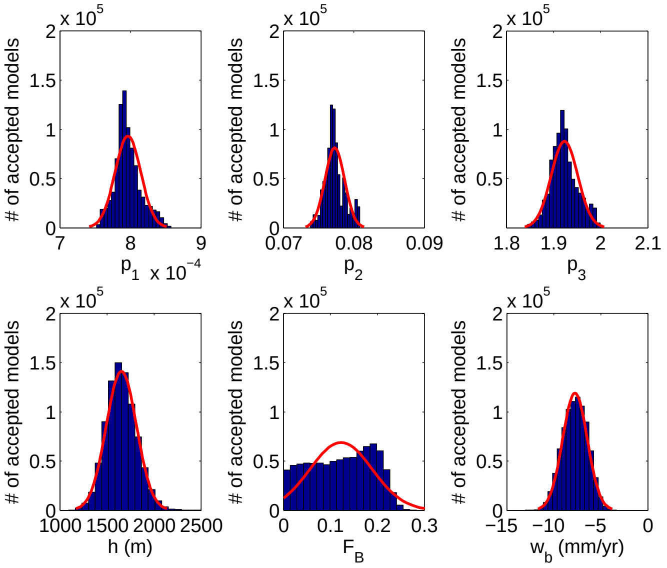

Figure 5.21: histograms for the accepted values of the Monte Carlo parameters after the burn-in period at NorthGRIP using the ice thickness history from Vinther et al. (subm) to account for past changes in ice thickness.

	Greve (2005)		Vinther et al. (subm)	
Parameter	Value	σ_{std}	Value	σ_{std}
p_1 (m/yr ‰$^{-2}$)	$7.5 \cdot 10^{-4}$	$0.1 \cdot 10^{-4}$	$7.9 \cdot 10^{-4}$	$0.2 \cdot 10^{-4}$
p_2 (m/yr ‰$^{-1}$)	$7.3 \cdot 10^{-2}$	$0.1 \cdot 10^{-2}$	$7.7 \cdot 10^{-2}$	$0.1 \cdot 10^{-2}$
p_3 (m/yr)	1.85	0.01	1.92	0.03
A_0 (m/yr)	0.205	0.002	0.189	0.002
h (m)	1730	80	1620	160
F_B	0	0.01	0.19	0.07
w_b (mm/yr)	-3.3	0.7	-7.5	1.3

Table 5.8: Best estimates and standard deviations for the six Monte Carlo parameters for the 1D model at NorthGRIP including past ice thickness changes. The value and uncertainty of the present accumulation rate, A_0, as calculated from the accepted values of p_1, p_2, and p_3 are also given. For comparison, the results from the 1D model with $\frac{\partial H}{\partial t} = 0$ can be found in Table 5.1.

The main differences between the results for the two ice thickness histories are the values of A_0 and w_b. Where the values of both these parameters obtained using the ice thickness history from Vinther et al. (subm) (0.189±0.002 m/yr and -7.5±1.3 mm/yr, respectively) are in agreement with observed values at the site, the present accumulation rate obtained using the ice thickness history from Greve (2005) is a little higher than the observed value (0.205±0.002 m/yr vs. 0.193±0.005 m/yr), and the obtained vertical velocity at the base is only -3.3±0.7 mm/yr, which is significantly lower than the value of -7 mm/yr found from ice core studies (North Greenland Ice Core Project members, 2004). Furthermore, as can be seen from Table 5.9, the model using the ice thickness history from Greve (2005) does not match the observed depth-age horizons as well as the model using the ice thickness history from Vinther et al. (subm) or the model not accounting for past changes in ice thickness.

The accumulation histories obtained from the three different 1D models used for the NorthGRIP site are shown in Fig. 5.22. The results from the model using the ice thickness history from Greve (2005) generally indicates higher accumulation rates than the results from the other two models.

5.2.2 NEEM

Due to the bad fit between observed and modelled depth-age horizons at NorthGRIP using the ice thickness history from Greve (2005) it was decided not to use this ice thickness history at NEEM. Thus the 1D inverse problem for NEEM was solved using only the ice thickness history from Vinther et al. (subm) to account for past changes in ice thickness. A total of $2 \cdot 10^5$ accepted

		$d_{\text{obs}} - d_{\text{model}}$ (m)		
Age (kyr)	d_{obs} (m)	$\frac{\partial H}{\partial t} = 0$	Greve (2005)	Vinther et al. (subm)
1.4	273	1	-12	-6
2.7	501	-4	-24	7
3.2	571	-6	-26	-1
4.0	689	0	-20	-9
4.8	802	0	-18	4
5.9	955	2	-12	5
7.5	1146	6	3	1
10.2	1396	5	46	-19
14.6	1600	-8	51	16
37.7	2055	-2	-43	-4
45.0	2182	1	-35	0
51.0	2284	4	-7	1
74.6	2553	-2	32	0

Table 5.9: The difference between observed (d_{obs}) and modelled (d_{model}) depths of the isochrones at NorthGRIP. The modelled isochrones are calculated using $\frac{\partial H}{\partial t} = 0$, and the surface elevation histories from Greve (2005), and Vinther et al. (subm), respectively.

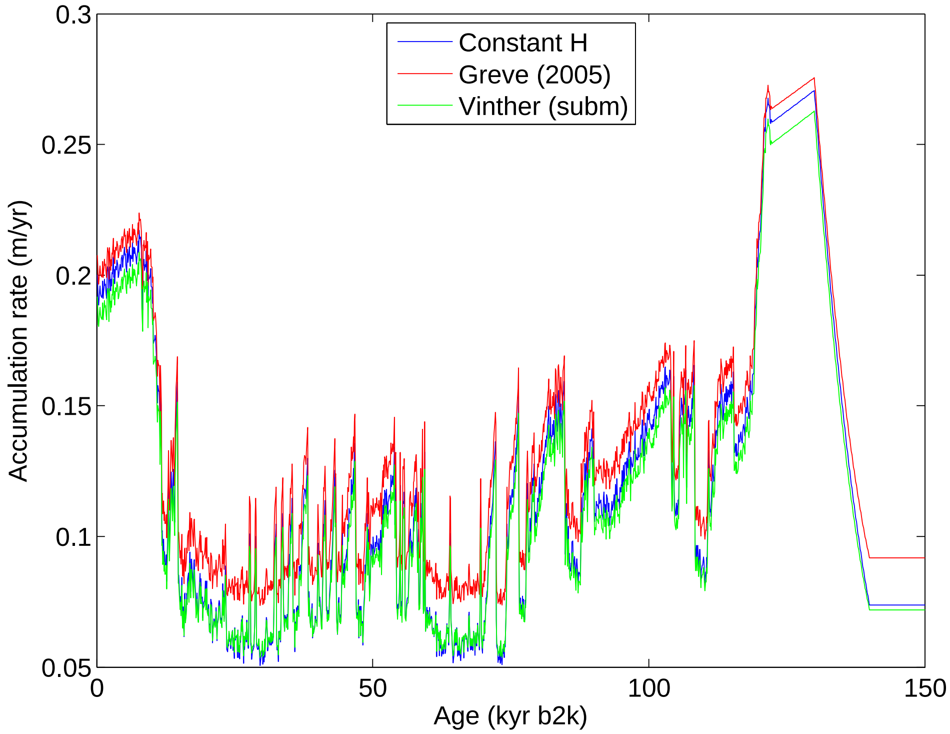

Figure 5.22: The accumulation histories determined with $\frac{\partial H}{\partial t}$=0 and the two ice thickness histories.

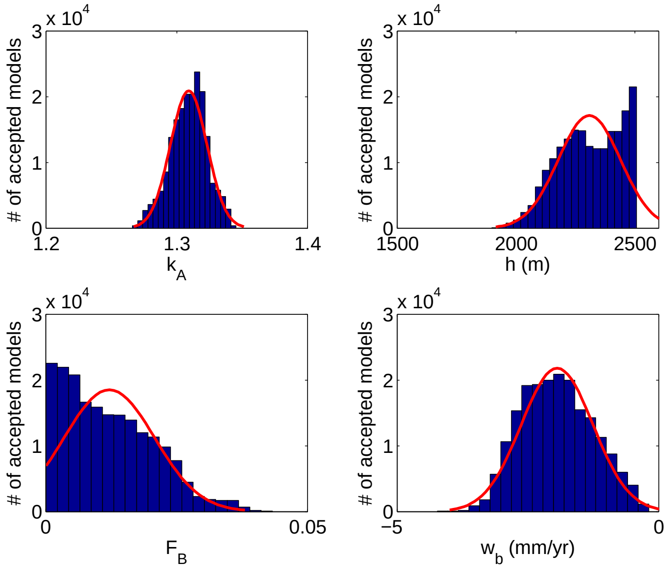

Figure 5.23: histograms for the accepted values of the Monte Carlo parameters after the burn-in period at NEEM using the ice thickness history from Vinther et al. (subm) to account for past changes in ice thickness.

models were collected. A plot of the accepted values for the four Monte Carlo parameters is found in Appendix A (Fig. A.17). Fig. 5.23 shows the histograms of accepted values after the burn-in period, and the best values for the Monte Carlo-determined parameters and the standard deviations from the corresponding histograms of accepted values are found in Table 5.10. The obtained values for the present accumulation rate is 0.253±0.003 m/yr, which is significantly higher than the value of 0.225±0.005 m/yr found from studies of shallow ice cores at the site. Also, the basal melt rate is estimated to 1.7±0.7 mm/yr indicating more basal melting than the model with constant ice thickness did.

The distribution for h shows a double peak (cf. Fig. 5.23). This could be caused by the proximity of the best value to the upper limit of allowed values. Regardless of the explanation, the double peak is not carried over to the location of the top and bottom of the Eemian layer, which are unambiguously determined (see Fig. 5.24).

The differences between observed and modelled locations of the 13 isochrones are shown in Table 5.11.

	Vinther et al. (subm)		$\frac{\partial H}{\partial t} = 0$	
Parameter	Value	σ_{std}	Value	σ_{std}
k_A	1.31	0.01	1.29	0.02
A_0 (m/yr)	0.253	0.003	0.254	0.005
h (m)	2500[a]	130	2370	170
F_B	0	0.01	0	0.002
w_b (mm/yr)	-1.7	0.7	0	0.1

---

[a] Double spike

Table 5.10: Best estimates and standard deviations for the four Monte Carlo-determined parameters for the 1D model at NEEM using $\frac{\partial H}{\partial t} = 0$ and the ice thickness history from Vinther et al. (subm) as stated. The value and uncertainty of the present accumulation rate, A_0, as calculated from the accepted values of k_A are also given.

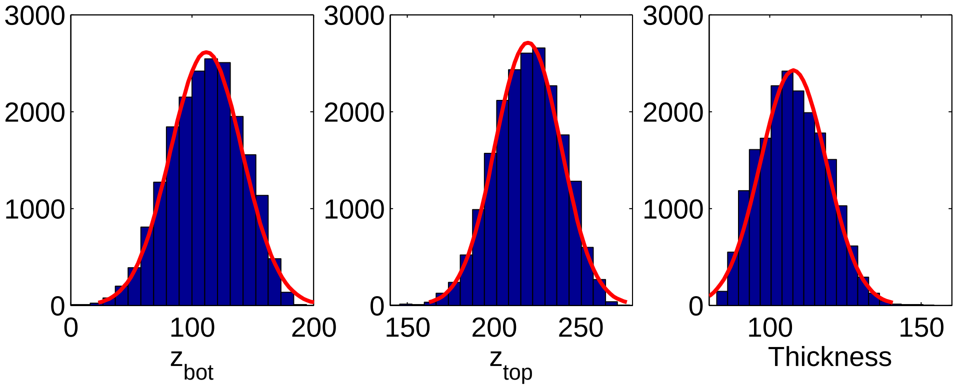

Figure 5.24: Histograms of the location of the bottom (z_{bot}), top (z_{top}), and thickness of the Eemian layer at NEEM as calculated from the accepted values for the 1D model using the ice thickness history from Vinther et al. (subm) to account for changes in ice thickness.

		$d_{\text{obs}} - d_{\text{model}}$ (m)	
Age (kyr)	d_{obs} (m)	$\frac{\partial H}{\partial t} = 0$	Vinther et al. (subm)
1.4	321	0	12
2.7	575	5	13
3.2	618	-21	-17
4.0	744	-2	2
4.8	854	7	14
5.9	983	6	3
7.5	1156	27	-2
10.2	1344	25	-14
14.6	1473	-1	-4
37.7	1739	-23	-9
45.0	1818	-15	1
51.0	1879	-9	4
74.6	2013	-11	3

Table 5.11: The difference in m between observed (d_{obs}) and modelled (d_{model}) depths of the isochrones at NEEM. The modelled isochrone depths are calculated using the accepted parameter values for the 1D model using $\frac{\partial H}{\partial t} = 0$ and the surface elevation historiy from Vinther et al. (subm), respectively.

5.2.3 Accumulation rates

The obtained estimate of the present accumulation rates for all the 1D sites and all the three ways of dealing with ice thickness changes are summarized in Fig. 5.25. It is worth noting, that accounting for past ice thickness changes using the ice thickness history from Vinther et al. (subm) does not lead to a modelled value for the present accumulation rate at NEEM that is in better agreement with the observations than the value found from the model not accounting for changes in ice thickness.

5.2.4 Eemian ice

The results from the 1D model investigations accounting for ice thickness changes are used to calculate the location of the Eemian layer at NorthGRIP and NEEM. The results are given in Table 5.12. The ice thickness history from Vinther et al. (subm) reaches back only to 123 kyr b2k. In order to start the forward run with the model at the beginning of the Eemian, the ice thickness estimate for 123 kyr b2k was just kept constant back to 130 kyr b2k. This is indeed a very crude estimate, but lacking better information, the simplest assumption was made. For comparison, the location of ice with the age of 123 kyr is estimated to be 177±23 m, which makes the layer of ice

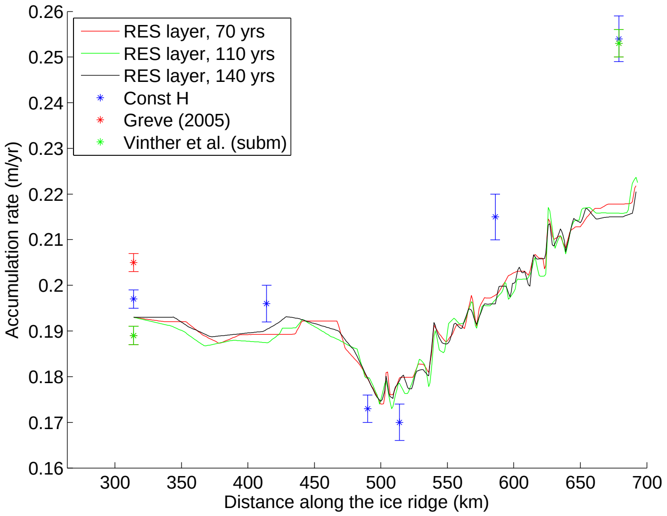

Figure 5.25: Comparison between the accumulation rate pattern obtained from shallow radar layers tuned to match the observed value at NorthGRIP (red, green, and black) and the results from solving the 1D inverse problem at the six sites (blue asterisks). Red and green asterisks indicate results obtained using the ice thickness histories from Greve (2005) and Vinther et al. (subm), respectively, to account for temporal changes in ice thickness. The error bars on the 1D results indicate the precision to which each value is determined from the Monte Carlo solution.

		z_{bot} (m)	z_{top} (m)	Thickness (m)
NGRIP	$\frac{\partial H}{\partial t} = 0$	-171[a]	-121±40	50±40[b]
	Greve (2005)	34±30	136±20	104±10
	Vinther et al. (subm)	-171[a]	-106±50	65±50[b]
NEEM	$\frac{\partial H}{\partial t} = 0$	169±7	238±6	66±2
	Vinther et al. (subm)	116[c]±30	226±20	106[c]±11

---

[a] All accepted models indicate that the early Eemian ice is lost.

[b] With the early Eemian ice being lost, the uncertainty on the thickness of the Eemian layer is given by the uncertainty on the position of the top of the layer.

[c] These numbers are calculating using a constant ice thickness from 123 kyr b2k and back to 130 kyr b2k.

Table 5.12: The location of the Eemian layer in the ice column at NorthGRIP and NEEM. Note that the full Eemian is not present at NorthGRIP. Thus, the given layer thickness is for the part of the period that is still present.

from 115 kyr to 130 kyr 48±5 m thick.

At NorthGRIP the results from the model with $\frac{\partial H}{\partial t} = 0$ and from that using the ice thickness history from Vinther et al. (subm) agree with each other and with observations from the ice core: The early part of the Eemian is removed by basal melting. The estimate of the top of the layer from the model using the Vinther et al. (subm) ice thickness history is best. The results from the model using the ice thickness history from Greve (2005) are not at all in agreement with the observations. According to these results the full Eemian record should still be located 200 m above bedrock. However, considering the bad fit between observed and modelled depth-age horizons, this is not surprising.

At NEEM there is a significant difference between the predicted thicknesses of the Eemian layer for the model disregarding ice thickness changes and the one using the ice thickness history from Vinther et al. (subm) to account for these changes. The predicted locations of the top of the Eemian layer does not differ much, but there is a significant difference in the predicted location of the bottom of the layer, leading to a difference of 40 m between the predicted thickness of the layer. This is the effect of the higher basal melt rate predicted from the study using the Vinther et al. (subm) data. This basal melt rate causes the bottom layers to be thicker but located deeper.

5.3 2D modelling - constant ice thickness

The 2D inverse problem is solved separately for three segments of the 435 km long section of the ice ridge studied in this thesis (cf. Section 4.2.1). In this section, the results obtained when assuming constant ice thickness with time are presented, while results obtained when including changes in ice thickness are presented in Section 5.4.

The number of accepted models collected for each segment falls between 70,000 and 510,000, and the burn-in periods are between 30,000 and 300,000 accepted steps. The NorthGRIP segment had a significantly longer burn-in period because the values of p_1, p_2, and p_3 from the accumulation model had to be determined.

5.3.1 Accumulation history at NorthGRIP

The distributions of accepted values for p_1, p_2, and p_3 are shown in Fig. 5.26. It is seen that these distributions show double peaks. However, the range of accepted values for each parameter is very small, and all accepted values

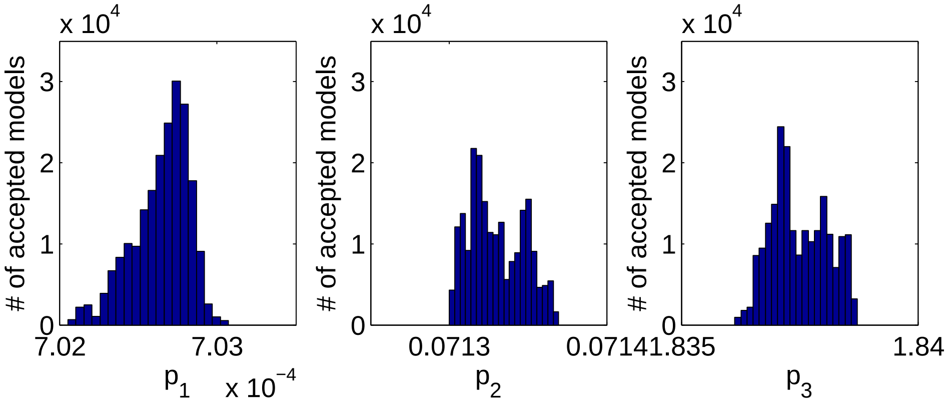

Figure 5.26: Histograms of values for the accumulation model parameters accepted after the burn-in period using the 2D model with $\frac{\partial H}{\partial t} = 0$.

fall within one standard deviation of the best value determined from the 1D model (cf. Table 5.1). The accumulation history obtained from solving the 2D inverse problem is well determined (the double peaks cancel out because p_2 and p_3 are highly correlated), and it is shown in Fig. 5.27, top panel, along with the accumulation history obtained with the 1D model. The main difference between the two is that the accumulation history obtained with the 2D model indicates lower accumulation rates during the stadials. This difference is of the same order as the standard deviation on the accumulation history from the 1D model (cf. Fig. 5.27, bottom panel). The accumulation history obtained from the 2D model was used when solving the 2D inverse problem for the other two segments.

5.3.2 Basal melt rates

Histograms of accepted values for w_b for each of the three segments are found in Figs. 5.28–5.30. Generally, the distributions for the first four melt rate intervals of a segment are broader than the others. The effect of basal melting on the internal layers increases with depth, so the deep isochrones are very important for the determination of the melt rates. Due to the horizontal movement of the ice, the modelled isochrones have moved out of the first couple of intervals before they have reached depths of more than ~1 km. As a consequence, there are only very weak constraints in the deep part of the ice for the first part of the line when solving the inverse problem, and the melt rate estimates obtained for that area are badly constrained. Furthermore, the distributions of accepted values of w_b for the last few melt rate intervals of the Middle segment are also broad (see Fig. 5.30). In this area the lowest isochrone is missing, and thus the solution to the inverse problem is not well

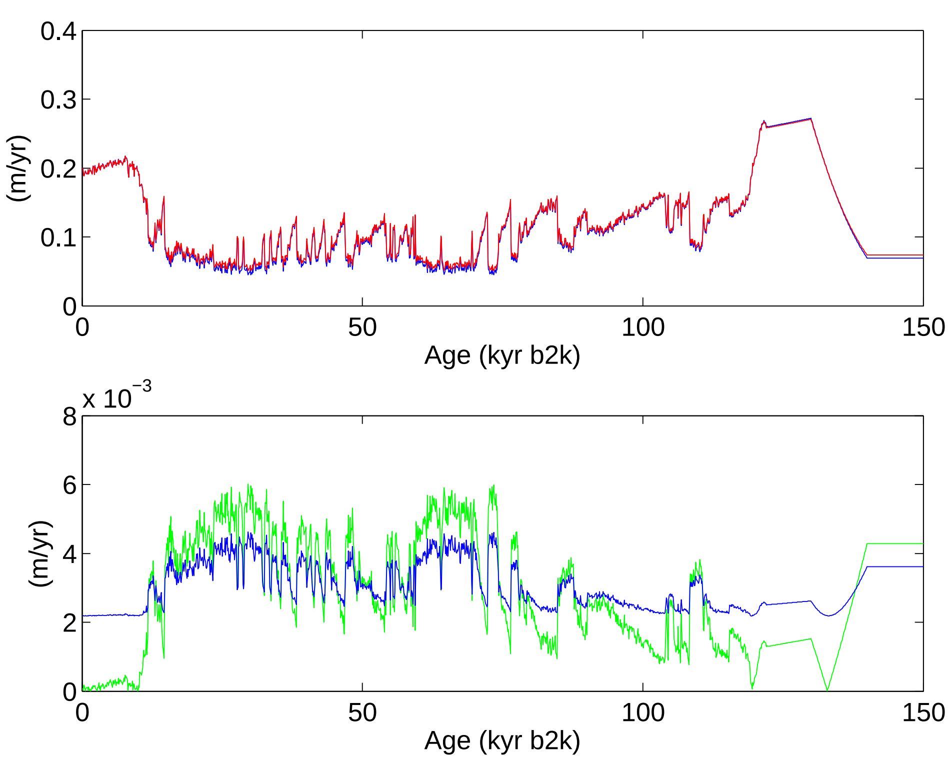

Figure 5.27: Above: The accumulation histories at NorthGRIP obtained from the 1D (red) and 2D (blue) models using $\frac{\partial H}{\partial t} = 0$. Below: The standard deviation on the accumulation history found from the 1D model (blue) and the difference between the accumulation histories obtained from the 1D and 2D models (green).

constrained here.

A step plot of the obtained basal melt rates along the line is shown in Fig. 5.31, middle panel. The areas, where the lowest isochrone is missing are shaded in grey. The melt rates determined from solving the 2D inverse problem for the NorthGRIP segment and those determined from the solution to the 2D inverse problem for the Middle segment agree fairly well in the overlap area (∼400–450 km from GRIP). The discrepancy could very well be caused by the lack of deep constraints in the solution for the Middle segment. The situation is quite different for the overlap section between the Middle and NEEM segments (∼520–640 km from GRIP), where a large discrepancy is seen between the melt rate estimate from the solutions to the two inverse problems. Several possible factors contributing to this can be identified. The largest differences are seen in the first part of the overlap. Here, the solution to the inverse problem for the NEEM segment is not well constrained due to the lack of modelled isochrones in the lower part of the ice sheet. Due to the higher velocity component parallel to the ice ridge here compared to further

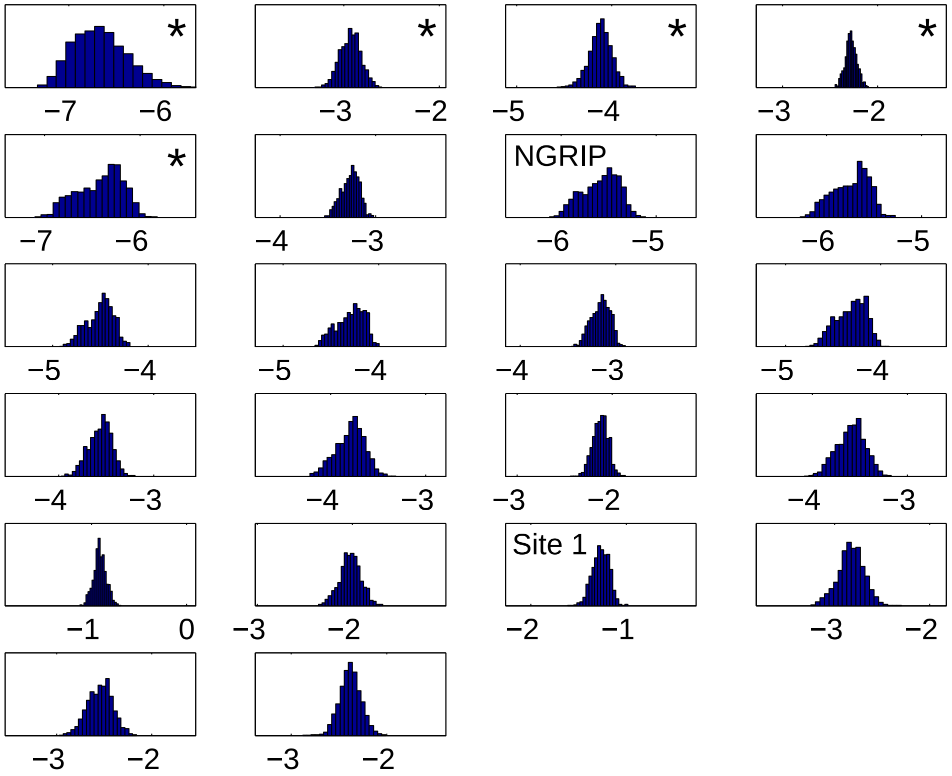

Figure 5.28: Histograms for the accepted values of w_b along the ice ridge for the North-GRIP segment (the sequence is to be read like a book from left to right). The units are mm/yr and the range of the x-axis for every histogram is the mean value ±1 mm/yr. The first melt rate interval is at the top left. Melt rate intervals, where the lowest isochrone is missing are marked with a black asterisk. The values were obtained using the 2D model with $\frac{\partial H}{\partial t} = 0$.

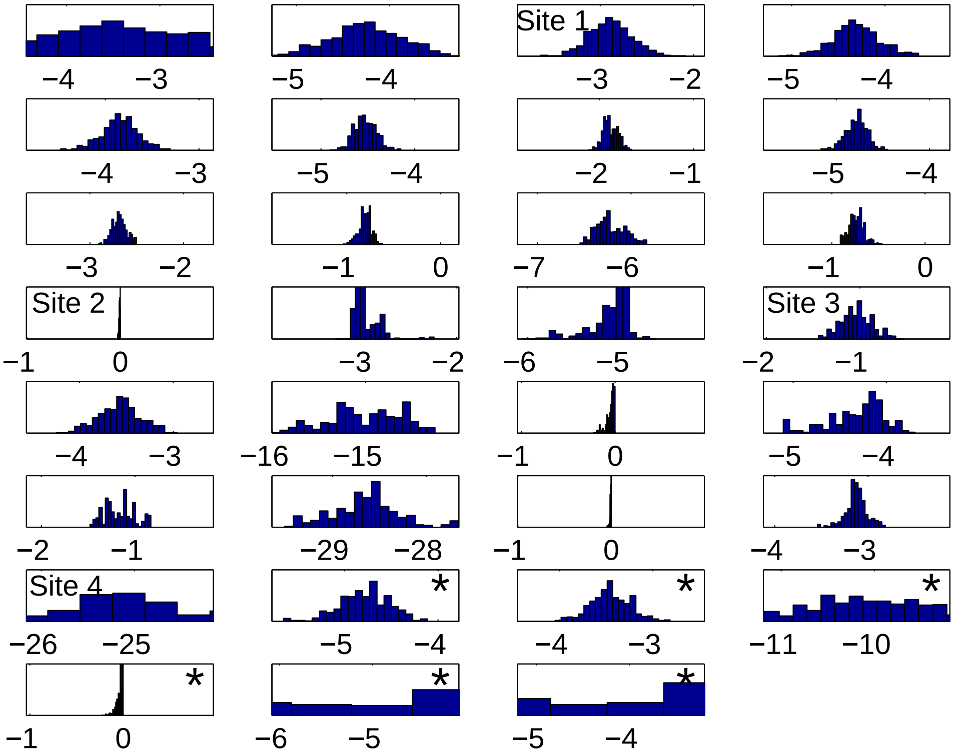

Figure 5.29: Histograms for the accepted values of w_b along the ice ridge for the Middle segment (the sequence is to be read like a book from left to right). The units are mm/yr and the range of the x-axis for every histogram is the mean value ± 1 mm/yr. The first melt rate interval is at the top left. Melt rate intervals, where the lowest isochrone is missing are marked with a black asterisk. The values were obtained using the 2D model with $\frac{\partial H}{\partial t} = 0$.

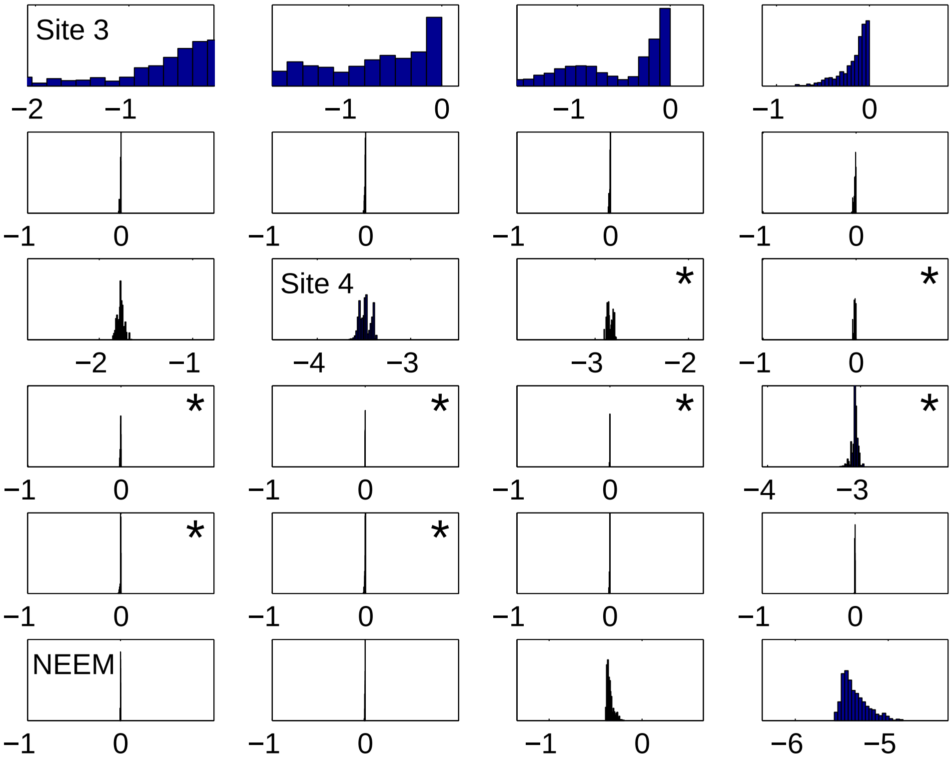

Figure 5.30: Histograms for the accepted values of w_b along the ice ridge for the NEEM segment (the sequence is to be read like a book from left to right). The units are mm/yr and the range of the x-axis for every histogram is the mean value ±1 mm/yr. The first melt rate interval is at the top left. Melt rate intervals, where the lowest isochrone is missing are marked with a black asterisk. The values were obtained using the 2D model with $\frac{\partial H}{\partial t} = 0$.

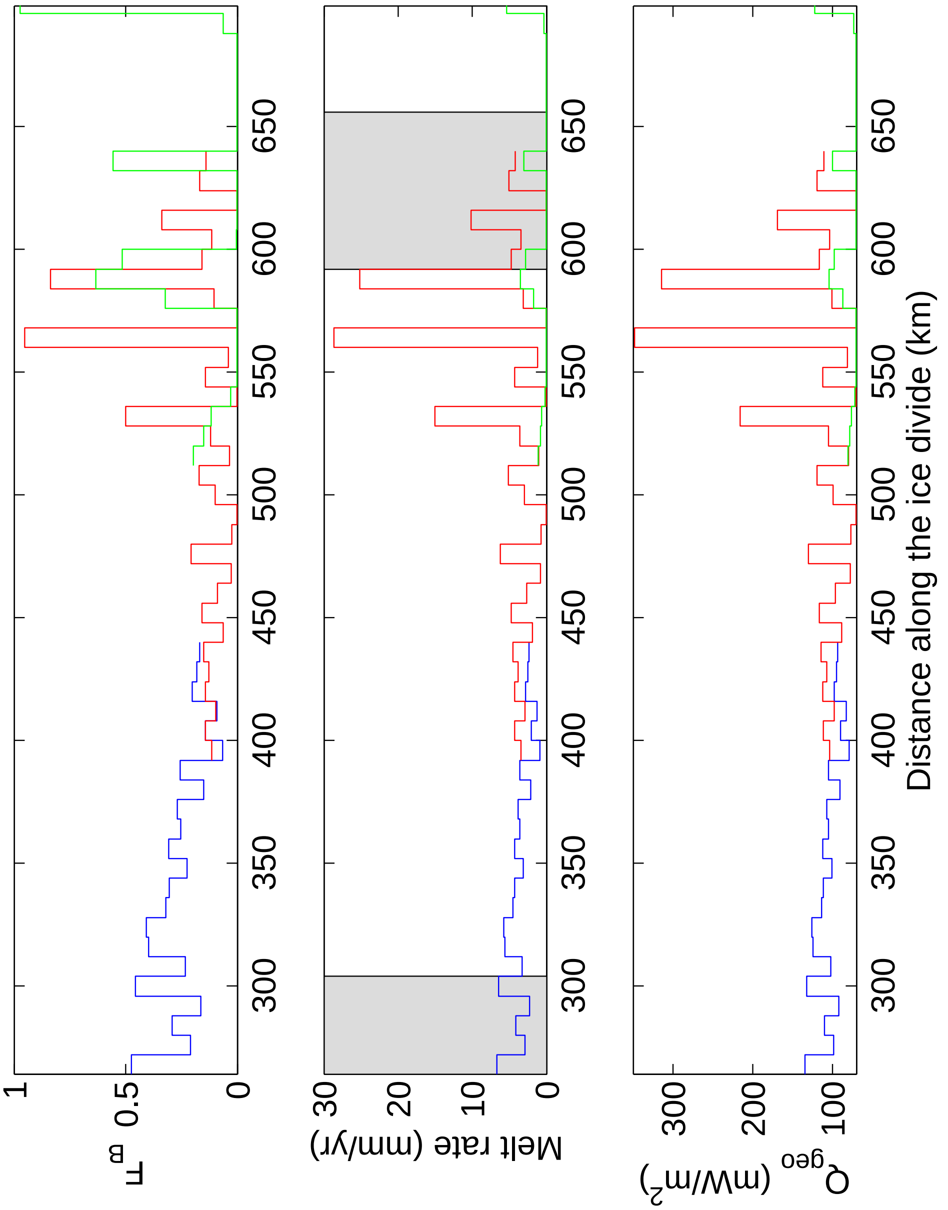

Figure 5.31: The values of F_B, w_b, and Q_{geo} along the ice divide. Results obtained from solving the 2D inverse problem for the NorthGRIP, Middle, and NEEM segments are shown in blue, red, and green, respectively. Areas where the lowest isochrone is not visible are shaded grey. The results were obtained assuming constant ice thickness with time.

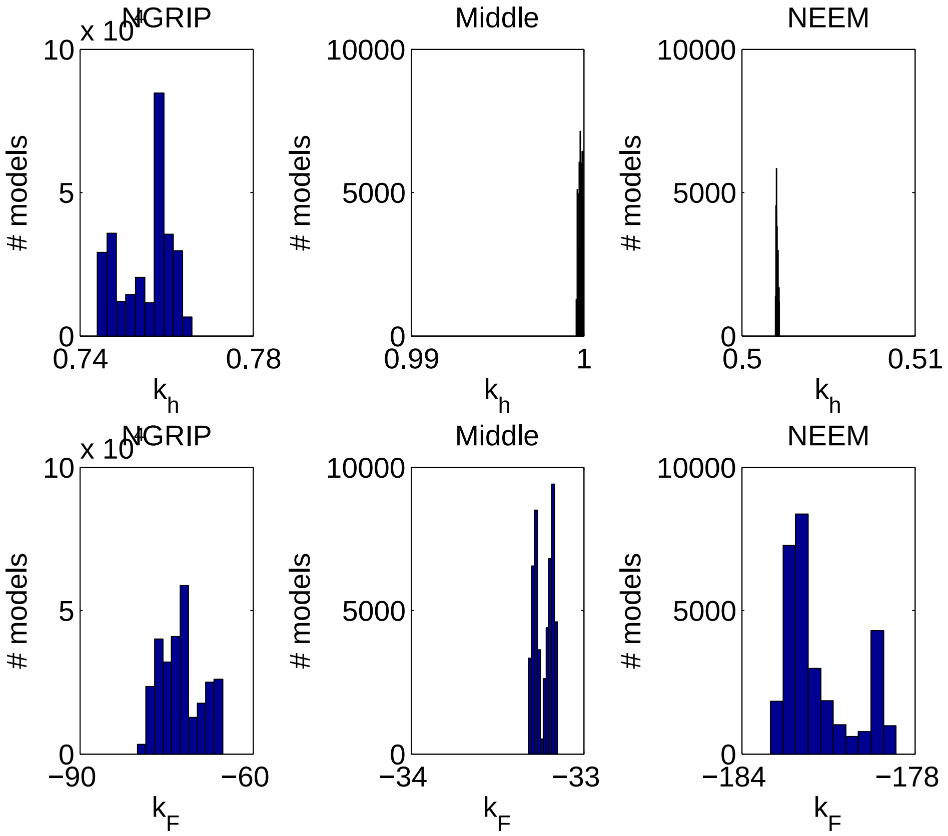

Figure 5.32: Histograms of accepted values for k_h and k_F for the three segments of the ice divide using the 2D model with $\frac{\partial H}{\partial t} = 0$.

upstream, there are no modelled isochrones in the lower half of the ice sheet for the first 10 melt rate intervals of the NEEM segment (cf. Fig. 5.36). The last part of the overlap falls within the region where the lowest isochrone is not visible. As mentioned above, this affects the determination of the basal melt rates.

5.3.3 Other flow parameters

Histograms of the accepted values for k_h and k_F for each of the three segments are shown in Fig. 5.32. None of the histograms shows the desired resemblance of a Gaussian distribution, and most of them have multiple peaks. However, the range of accepted values for each parameter in each segment is quite small, so a best value can still be estimated fairly well. In all cases, the step size had to be picked very small in order to maintain an accept rate of 30% or higher. Therefore, the model space was first investigated

	$\frac{\partial H}{\partial t} = 0$				Vinther et al. (subm)			
	k_h	σ_{kh}	k_F	σ_{kF}	k_h	σ_{kh}	k_F	σ_{kF}
NGRIP	0.76	0.006	-72	4	0.54	0.001	-83	2
Middle	1	$1 \cdot 10^{-4}$	-33	0.05	0.726	$1 \cdot 10^{-4}$	-38	0.1
NEEM	0.502	$1 \cdot 10^{-4}$	-182	1	0.402	0.001	-33	0.4

Table 5.13: Best estimates of the values of k_h and k_F for each of the three segments studied with the 2D model. The standard deviations of the distributions are also listed.

with a higher step size (and correspondingly lower accept rate). When the accepted values for the parameters settled around a level, the step size was decreased to obtain an accept rate of at least 30%. The range of accepted values for the two parameters in the Middle segment is particularly small. This segment is the longest one and the one with the largest variability in the basal melt rates. Thus it may be difficult to find values for k_h and k_F that give a good fit for all the different flow conditions represented in the segment. For the NEEM segment, the obtained basal melt rates are generally low, and the histogram for k_F also looks nicer than the one for the Middle segment. However, a very low range of accepted values for k_h is also seen in the NEEM segment. This segment covers the area where the direction of the ice ridge bends towards the NNW. This is the region, where the 1D results indicate the largest spatial variation in k_h (cf. Table 5.5), so this could also be a case of the model finding a narrow region of values for k_h that gives the best overall results for the whole segment. The obtained best estimates of k_h and k_F and the standard deviation on their distributions are found in Table 5.13.

The sets of accepted values for k_h, k_F, and w_b are used to calculate the kink height h, and the fraction of basal sliding, F_B. The values obtained for the six 1D sites are given in Table 5.14, and the values of F_B along the ice ridge are shown in Fig. 5.31. At Site 2 and NEEM the standard deviations on the histograms for accepted values of w_b are very small. This causes the distributions of F_B and Q_{geo} to also be very narrow, and the listed uncertainties are of course much lower than the true uncertainty on the estimate. In the case of h the very small uncertainties are caused by the narrow distribution for k_h for the Middle and NEEM segments. Histograms of the calculated values of F_B at NorthGRIP and NEEM are shown in Fig. 5.33. The distribution for F_B at NorthGRIP shows a well defined maximum, while the distribution for F_B at NEEM has no resemblance with a normal distribution. The fact that w_b was estimated to zero for many of the melt rate intervals in the NEEM segment complicates the determination of k_F and thus F_B.

		w_b (mm/yr)	F_B	h (m)	Q_{geo} (mW/m^2)
$\frac{\partial H}{\partial t} = 0$	NGRIP	-5.6±0.2	0.40±0.01	2310±20	124±2
	Site 1	-1.3±0.1	0.09±0.01	2260±20	82±1
	Site 2	$0\pm1\cdot10^{-5}$[a]	$0\pm2\cdot10^{-4}$[b]	3070±1	70±0.1
	Site 3	-1.0±0.2	0.03±0.01	2790±1	80±2
	Site 4[c]	-25±2	0.86±0.06	2690±1	310±20
	Site 4[d]	-3.5±0.1	0.63±0.01	1350±0.2	104±1
	NEEM	$0\pm2\cdot10^{-6}$[a]	$0\pm3\cdot10^{-4}$[b]	1270±0.2	70±0.02
Vinther et al. (subm)	NGRIP	-5.2±0.2	0.43±0.01	1650±3	120±2
	Site 1	-0.4±0.1	0.04±0.01	1620±2	74±1
	Site 2	$0\pm1\cdot10^{-5}$[a]	$0\pm2\cdot10^{-4}$[b]	2230±0.3	70±0.1
	Site 3	-1.1±0.4	0.04±0.01	2030±0.3	81±4
	Site 4[c]	-20±1	0.75±0.03	2026±0.3	260±7
	Site 4[d]	-25±1	0.82±0.03	1080±2	310±10
	NEEM	$0\pm1\cdot10^{-5}$[a]	$0\pm3\cdot10^{-4}$[b]	1010±1	70±0.1

---

[a] The parameter is strictly non-positive, so only the minus option applies.

[b] The parameter is strictly non-negative, so only the plus option applies.

[c] Results from Middle segment

[d] Results from NEEM segment

Table 5.14: Values of w_b, F_B, h, and Q_{geo} at the six 1D sites. The results were obtained using the 2D model with $\frac{\partial H}{\partial t} = 0$ or the ice thickness history from Vinther et al. (subm), as stated. The values at Site 4 obtained from the solutions to the Middle and NEEM segments are both given.

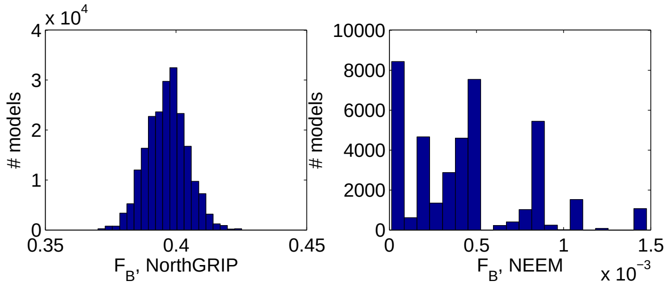

Figure 5.33: Histograms of values for F_B at NorthGRIP and NEEM calculated from the accepted values of k_F and w_b obtained with the 2D model with $\frac{\partial H}{\partial t}$=0.

When the basal melt rate is known, the amount of heat, Q_{melt}, used to melt the ice can be calculated using the relation

$$Q_{\text{melt}} = \rho w_b L,$$

where ρ and L are the density and latent heat of ice, respectively. The geothermal heat flux, Q_{geo}, is given by the sum of the amount of heat used to melt the ice and the amount of heat, Q_{ice}, conducted through the ice:

$$Q_{\text{geo}} = Q_{\text{melt}} + Q_{\text{ice}}.$$

Q_{ice} is determined from the gradient of the observed temperature profile $\frac{\partial T}{\partial z}$ at the base at NorthGRIP, i.e.

$$Q_{\text{ice}} = -K\frac{\partial T}{\partial z},$$

where K is the thermal conductivity of ice. Using Q_{ice}=70mW/m^2 (North Greenland Ice Core Project members, 2004), L=334 kJ/kg, and the basal melt rates found in this study, the geothermal flux along the ice ridge is calculated. The results are shown in Fig. 5.31, and the values obtained for the 1D sites are listed in Table 5.14.

5.3.4 Eemian ice

Figs. 5.34–5.36 show the observed and modelled isochrones for each segment along with the obtained basal melt rates. The differences between observed and modelled isochrones at the six 1D sites are listed in Table 5.15. Generally, the fit is better the closer to NorthGRIP. The worst fit is found in the region with large undulations on the observed isochrones upstream from NEEM. The modelled isochrones do not reproduce these undulations. The undulations happen over a very short distance, so maybe the resolution in the melt rate intervals is too low for the model to capture this feature. Furthermore, this region coincides with the area, where the lowest isochrone is not visible. It is also seen, that the modelled isochrones are too shallow in the upper part of the ice sheet at NEEM.

The modelled Eemian layer is shown in blue in Figs. 5.34–5.36. The model agrees well with the observations from the NorthGRIP ice core as it suggests that the lower part of the Eemian layer is missing at NorthGRIP. It is also seen, that the horizontal movement in the area around NEEM is so large, that the modelled Eemian isochrones have moved past NEEM. To get an estimate of the Eemian layer at NEEM we run the forward model for the Middle and NEEM segments combined. It was chosen to use the parameter values obtained from solving the inverse problem for the Middle segment up

Age (kyr)	NGRIP	Site 1	Site 2	Site 3	Site 4	NEEM
1.4	2	2	-18	-15	4	34
2.7	-2	-5	-29	-43	6	53
3.2	-2	2	-34	-39	20	27
4.0	5	5	-27	-34	22	46
4.8	8	7	-23	-37	6	53
5.9	12	8	-47	-78	28	47
7.5	21	9	-31	-46	32	60
10.2	21	15	-27	-42	31	44
14.6	7	6	-42	-40	31	9
37.7	12	24	-18	-22	10	-17
45.0	11	21	-17	-21	6	-15
51.0	10	28	-11	-26	2	-13
74.6	8	9	-34	-40	3	-21

Table 5.15: The difference in m between observed and modelled depths of the isochrones. The modelled depths are calculated from the accepted values of the model parameters of the 2D model with $\frac{\partial H}{\partial t} = 0$.

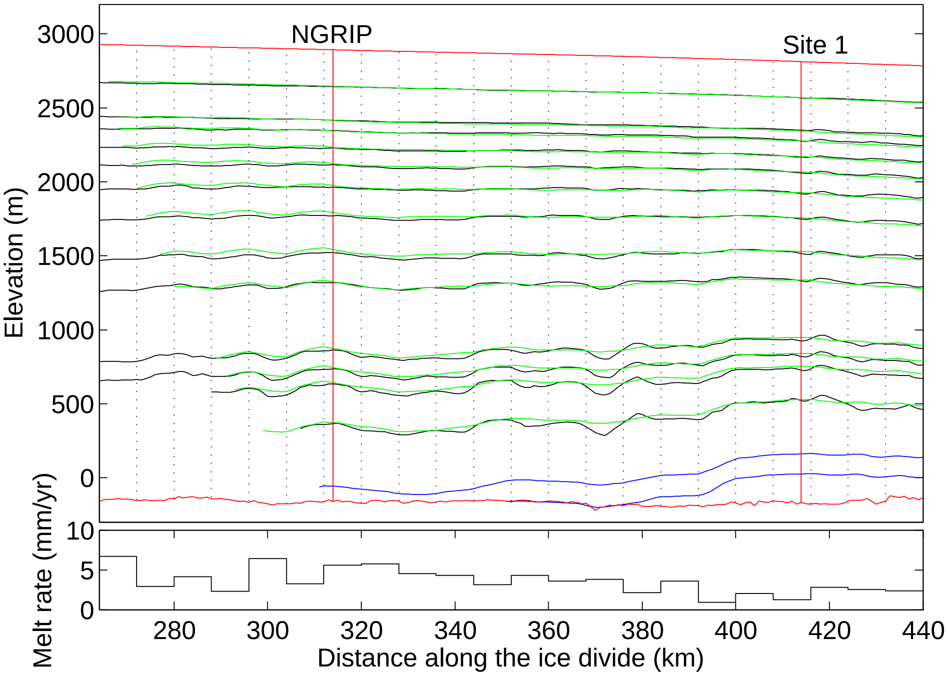

Figure 5.34: Top panel: Observed (black) and modelled (green) isochrones for the NorthGRIP segment. The modelled Eemain layer is shown in blue. The surface of the ice and the ice-bedrock interface are marked in red, NorthGRIP and Site 1 are marked by red vertical lines, and the dotted vertical lines indicate the melt rate intervals. Bottom panel: The obtained basal melt rates for the same area. These results were obtained from the 2D model using $\frac{\partial H}{\partial t} = 0$.

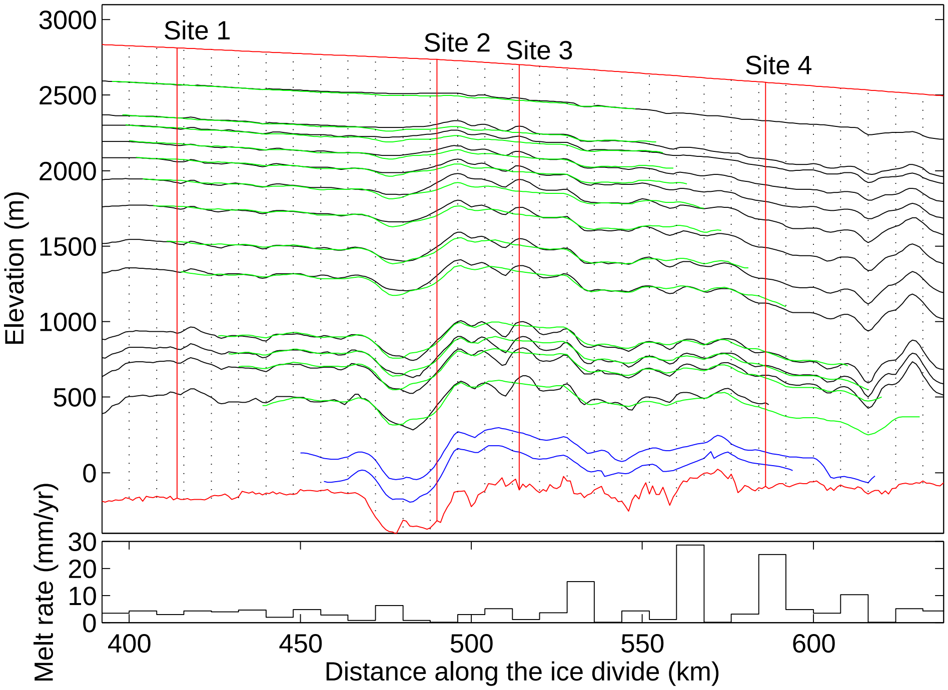

Figure 5.35: Observed (black) and modelled (green) isochrones for the Middle segment. The modelled Eemain layer is shown in blue. The surface of the ice and the ice-bedrock interface are marked in red, Sites 1–4 are marked by red vertical lines, and the dotted vertical lines indicate the melt rate intervals. Bottom panel: The obtained basal melt rates for the same area. These results were obtained from the 2D model using $\frac{\partial H}{\partial t} = 0$.

to 560 km from GRIP and the results from solving the inverse problem for the NEEM segment downstream from there. The obtained modelled Eemian layer is seen in Fig. 5.37. The location and thickness of the Eemian layer at the 1D sites calculated from the results from the 2D model with $\frac{\partial H}{\partial t} = 0$ are listed in Table 5.16. Histograms for the top, bottom, and thickness for the Eemian layer at NEEM are shown in Fig. 5.49. It is seen that the location and thickness of the layer is well determined.

The ice at the base at NorthGRIP originates $\sim$ 50 km upstream, while the early Eemian ice at NEEM was deposited $\sim$ 170 km upstream from the drill site according to the results obtained with the 2D model (cf. Fig. 5.37).

5.4 2D modelling - including ice thickness changes

Due to the bad performance of the 1D model when using the ice thickness history from Greve (2005) to account for past changes in ice thickness, the 2D inverse problem will not be solved using these data. The results from

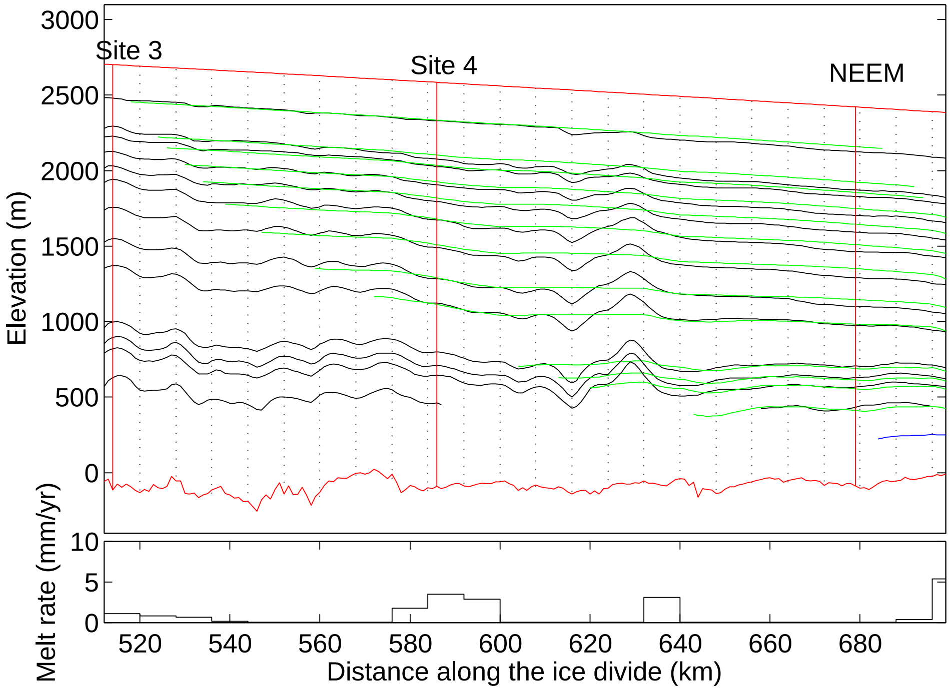

Figure 5.36: Top panel: Observed (black) and modelled (green) isochrones for the NEEM segment. The modelled Eemain layer is shown in blue. The surface of the ice and the ice-bedrock interface are marked in red, Site 4 and NEEM are marked by red vertical lines, and the dotted vertical lines indicate the melt rate intervals. Bottom panel: The obtained basal melt rates for the same area. These results were obtained from the 2D model using $\frac{\partial H}{\partial t} = 0$.

solving the 2D inverse problem using the ice thickness history from Vinther et al. (subm) to account for past changes in ice thickness are presented below.

The number of accepted models collected for each segment falls between 120,000 and 160,000, and the burn-in periods are between 70,000 and 120,000 accepted steps.

5.4.1 Accumulation history at NorthGRIP

The difference between the accumulation histories for NorthGRIP obtained with the 1D and 2D model for $\frac{\partial H}{\partial t} = 0$ was very little, and generally it requires many more accepted steps to reach equilibrium when p_1, p_2, and p_3 are determined compared to when they are not. Therefore, it was chosen to use the accumulation history obtained from the 1D model (cf. Fig. 5.22, green curve) when solving the 2D inverse problem.

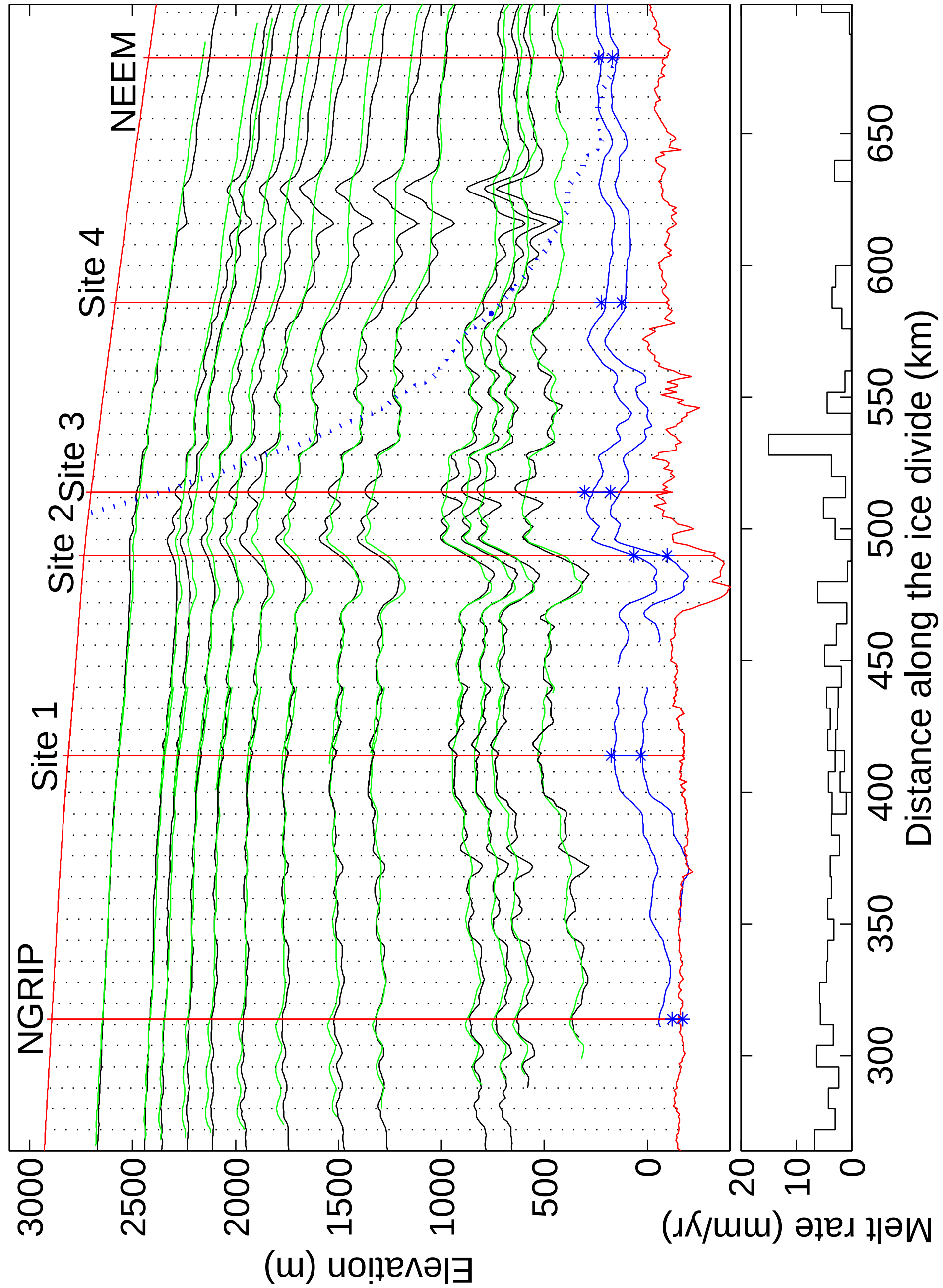

Figure 5.37: Top panel: Observed (black) and modelled (green) isochrones. The dotted vertical lines indicate the melt rate intervals. The modelled Eemain layer is shown in blue. The dotted blue line indicates the modelled path taken through the ice by the ice now found at the bottom of the Eemian at NEEM. The Eemian layer was modelled using the results from the Middle segment up to 560 km from GRIP and the results from the NEEM segment downstream from there. The blue asterisks indicate the top and bottom of the Eemian layer calculated using the 1D model with $\frac{\partial H}{\partial t} = 0$. Bottom panel: The obtained basal melt rates along the same section. The results were obtained from the 2D model with $\frac{\partial H}{\partial t} = 0$.

		z_{bot} (m)	z_{top} (m)	Thickness (m)
$\frac{\partial H}{\partial t} = 0$	NGRIP	-171[a]	-56±6	115±6[b]
	Site 1	25±5	160±5	135±1
	Site 2	-66±0.1	67±0.2	133±0.2
	Site 3	136±0.6	266±0.6	130±0.7
	Site 4	107±2	203±2	96±1
	NEEM	145±0.5	217±0.3	71±0.4
Vinther et al. (subm)	NGRIP	N/A	N/A	N/A
	Site 1	100±2[c]	219±2	119±0.2[c]
	Site 2	-54±0.2[c]	55±0.2	109±0.2[c]
	Site 3	202±0.6[c]	298±0.4	97±0.8[c]
	Site 4	57±6[c]	139±4	82±5[c]
	NEEM	146±0.4[c]	218±1	72±0.7[c]

---

[a] All accepted models indicate that the early Eemian ice is lost.

[b] With the early Eemian ice being lost, the uncertainty on the thickness of the Eemian layer is given by the uncertainty on the position of the top of the layer.

[c] These numbers are calculating using a constant ice thickness from 123 kyr b2k and back to 130 kyr b2k.

Table 5.16: The locations of the base and top of the Eemian layer and the thickness of the layer at the 1D sites obtained from the 2D model using $\frac{\partial H}{\partial t} = 0$ or the ice thickness history from Vinther et al. (subm) as stated. N/A means that no values was obtained. The modelled Eemian layer had moved past NorthGRIP. The location and thickness of the Eemian layer obtained with the 1D model are found in Tables 5.6 and 5.12.

5.4.2 Basal melt rates

Figs. 5.39–5.41 show histograms of the accepted values for the vertical velocity at the base. As was the case for the results from the 2D model not accounting for ice thickness changes, there is a great difference in how well determined the value of w_b is in the different melt rate intervals along the line. In many cases, the broad or double peaked distributions are coincident with the start of a segment, where the modelled isochrones have not reached great depths, or with regions where the lowest isochrone is missing. However, the double peaks in the distributions around Site 3 (cf. Fig. 5.40) can not be explained by this. In the area around Site 3 the isochrones show undulations with a wavelength of roughly the same size as the melt rate intervals and have a high amplitude compared to the isochrone shape upstream closer to NorthGRIP (cf. Fig. 5.46). Thus it may be impossible to get a good melt rate estimate here when using intervals of 8 km for the melt rate.

The obtained basal melt rates along the whole 435 km long section are shown in Fig. 5.42, middle panel. It is seen that there is still a disagreement between the melt rates obtained from solving the inverse problem for the Middle

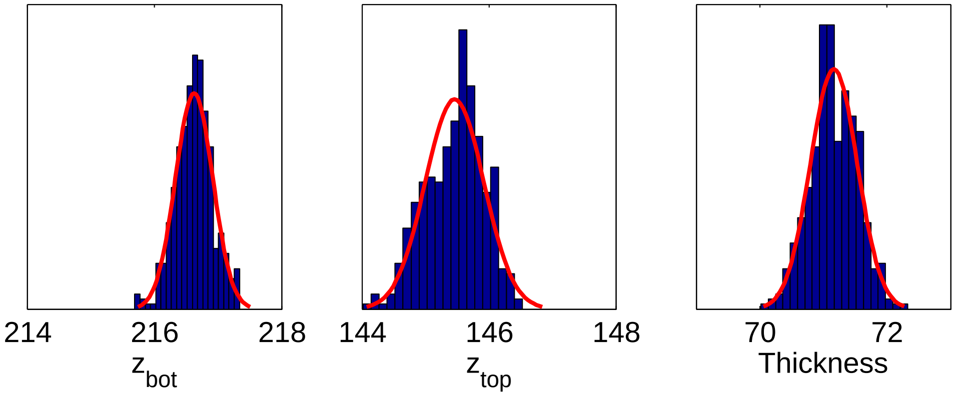

Figure 5.38: Histograms for the top, bottom, and thickness of the Eemian layer at NEEM as calculated from the 2D model with $\frac{\partial H}{\partial t} = 0$.

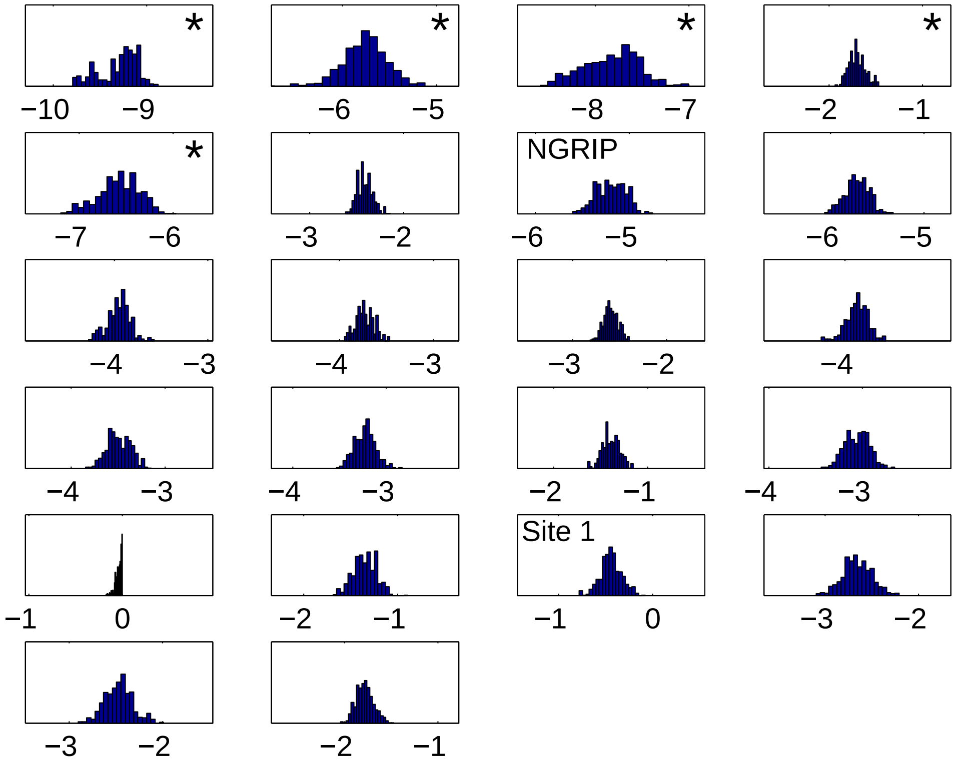

Figure 5.39: Histograms for the accepted values of w_b along the ice ridge for the NorthGRIP segment (the sequence is to be read like a book from left to right). The units are mm/yr and the range of the x-axis for every histogram is the mean value ±1 mm/yr. The first melt rate interval is at the top left. Melt rate intervals where the lowest isochrone is missing are marked by black asterisks. The values were obtained using the 2D model with the ice thickness history from Vinther et al. (subm).

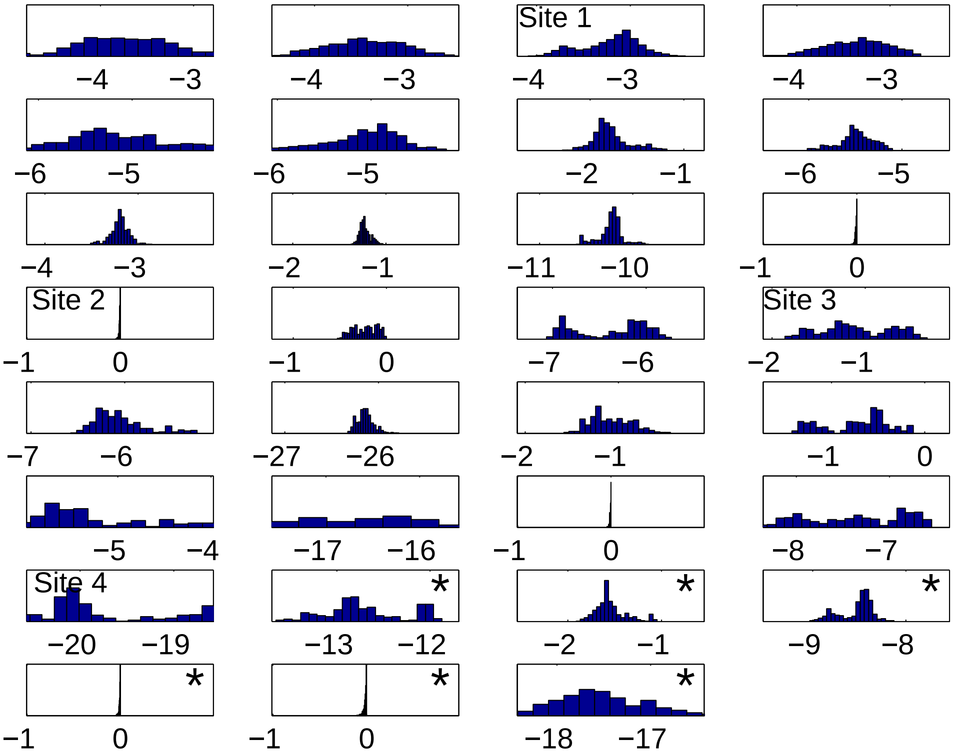

Figure 5.40: Histograms for the accepted values of w_b along the ice ridge for the Middle segment (the sequence is to be read like a book from left to right). The units are mm/yr and the range of the x-axis for every histogram is the mean value ±1 mm/yr. The first melt rate interval is at the top left. Melt rate intervals where the lowest isochrone is missing are marked by black asterisks. The values were obtained using the 2D model with the ice thickness history from Vinther et al. (subm).

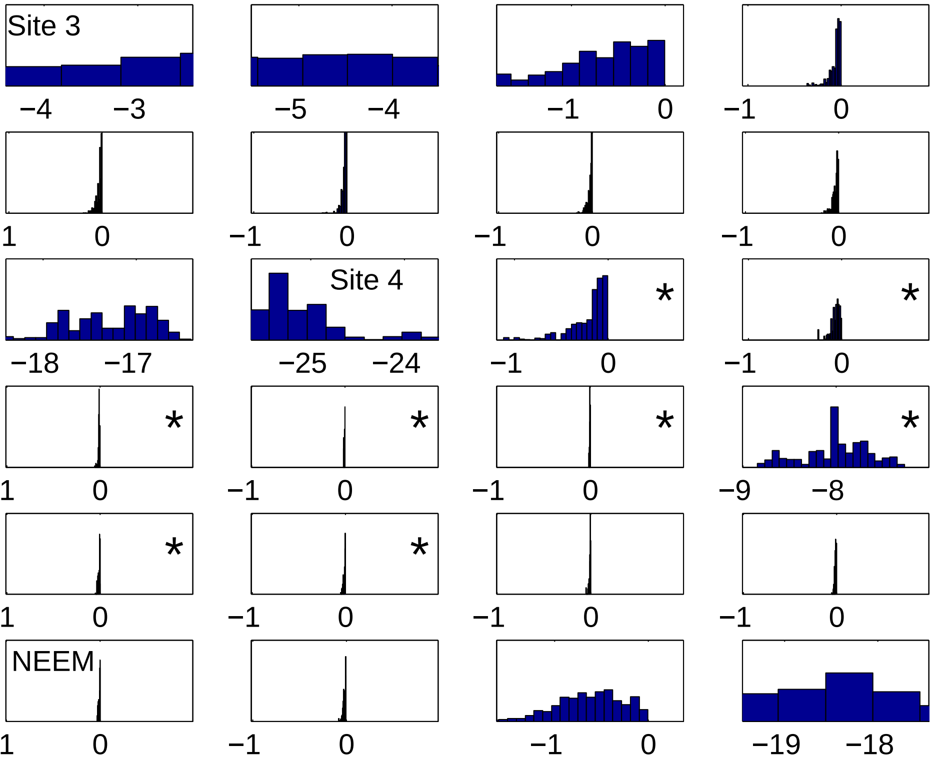

Figure 5.41: Histograms for the accepted values of w_b along the ice ridge for the NEEM segment (the sequence is to be read like a book from left to right). The units are mm/yr and the range of the x-axis for every histogram is the mean value ±1 mm/yr. The first melt rate interval is at the top left. Melt rate intervals where the lowest isochrone is missing are marked by black asterisks. The values were obtained using the 2D model with the ice thickness history from Vinther et al. (subm).

segment and those obtained from solving the inverse problem for the NEEM segment in the area of overlap (∼520–640 km from GRIP). However, the discrepancy seems to be a little smaller than for the model with $\frac{\partial H}{\partial t} = 0$.

5.4.3 Other flow parameters

Fig. 5.43 shows histograms of the accepted values for k_h and k_F for each of the three segments. Again, the range of accepted values for each parameter in each segment is very narrow. For the NorthGRIP and Middle segments, the distributions show a clear maximum, whereas the distributions for both parameters for the NEEM segment are less conclusive. The best values of the parameters in each segment are listed in Table 5.13 along with the standard deviation of the corresponding distribution.

The same way as described above, the accepted values for w_b, k_h, and k_F are used to calculate the geothermal heat flux, the kink height and the fraction of basal sliding. The values of these at the six 1D sites are listed in Table 5.14, and the variation of F_B and Q_{geo} along the whole section of the ice divide are shown in Fig. 5.42.

Histograms of values for F_B at NorthGRIP and NEEM as calculated from the accepted values of w_b, k_h, and k_F are shown in Fig. 5.44. The distribution of values for F_B at NorthGRIP looks very nice, while the histogram of values of F_B at NEEM is less convincing. However, there is a clear indication that the value is very close to zero.

5.4.4 Eemian ice

Figs. 5.45–5.47 show the observed and modelled isochrones for each segment, and the differences between them at the six 1D sites are listed in Table 5.17. As when using $\frac{\partial H}{\partial t} = 0$, the fit is good except for the region of large undulations upstream from NEEM and the too shallow modelled isochrones at NEEM.

As mentioned previously, the ice thickness history from Vinther et al. (subm) only reaches back to 123 kyr b2k. As was done in the 1D case, we assume constant ice thickness from 130 kyr b2k to 123 kyr b2k when modelling the Eemian layer. Because this is a crude assumption, the modelled layer of age 123 kyr is shown along with the modelled top and bottom of the Eemian layer in Figs. 5.45–5.47. The horizontal movement of the ice seems to be larger than for the model with $\frac{\partial H}{\partial t} = 0$, and the modelled Eemian isochrones have moved past NorthGRIP, and for the NEEM segment, they have moved

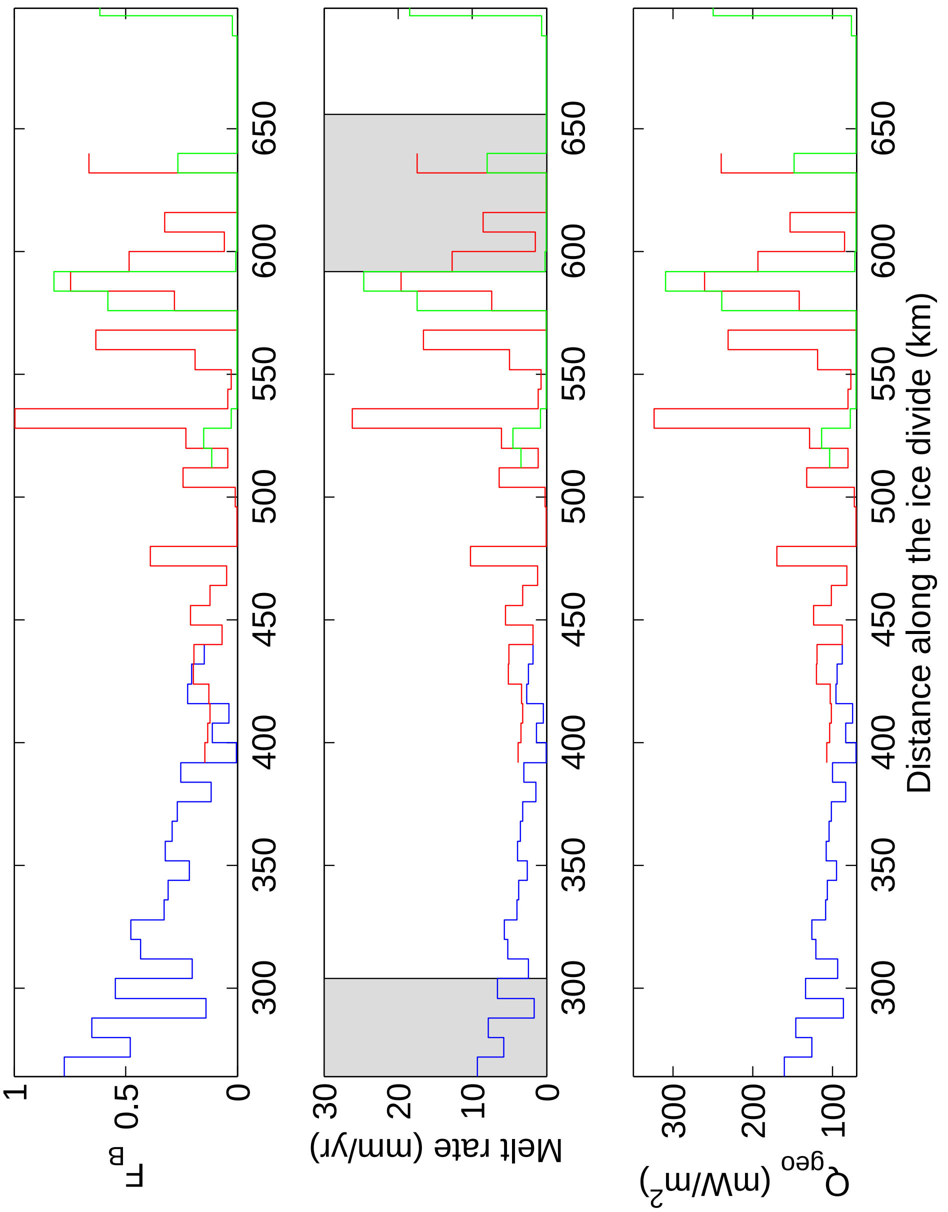

Figure 5.42: The obtained values for F_B, w_b, and Q_{geo} along the ice divide. Results obtained from solving the 2D inverse problem for the NorthGRIP, Middle, and NEEM segments are shown in blue, red, and green, respectively. Areas where the lowest isochrone is not visible are shaded grey. The ice thickness history from Vinther et al. (subm) was used to account for past changes in ice thickness.

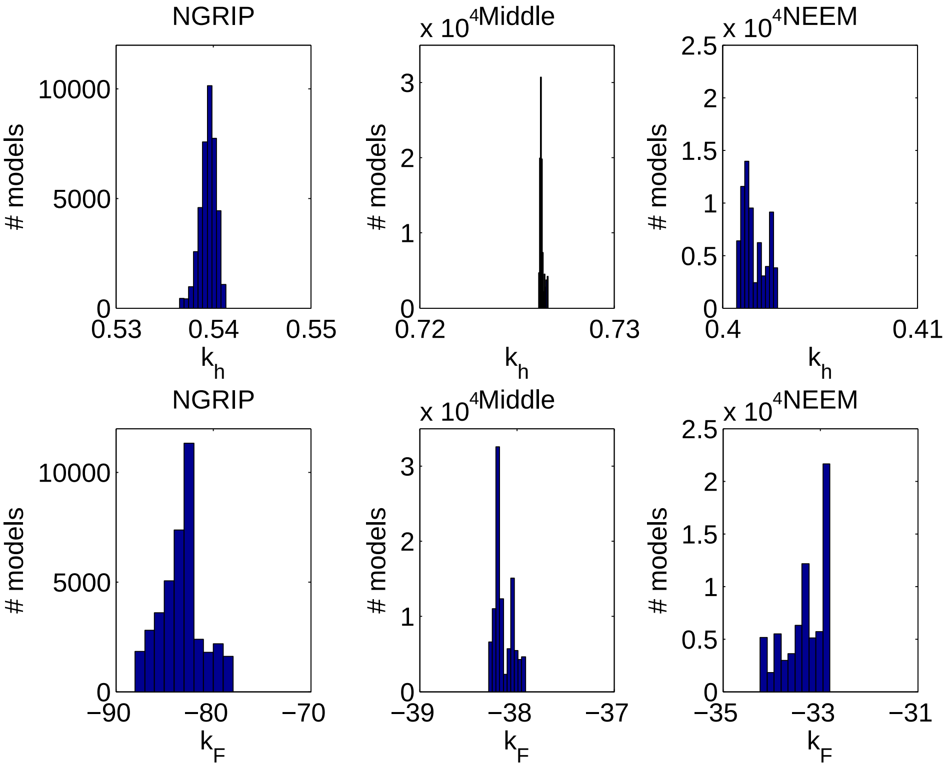

Figure 5.43: Histograms of accepted values for k_h and k_F for the three segments of the ice divide using the 2D model accounting for past changes in ice thickness using the ice thickness history from Vinther et al. (subm).

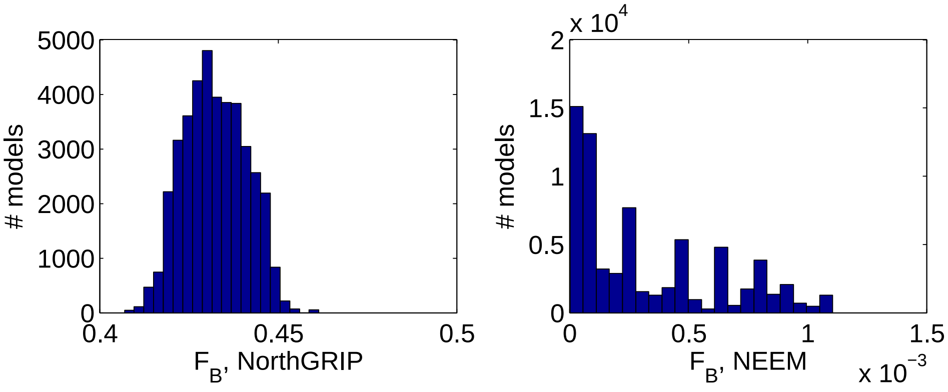

Figure 5.44: Histograms of values for F_B at NorthGRIP calculated from the accepted values of k_F and w_b obtained from the 2D model using the ice thickness history from Vinther et al. (subm).

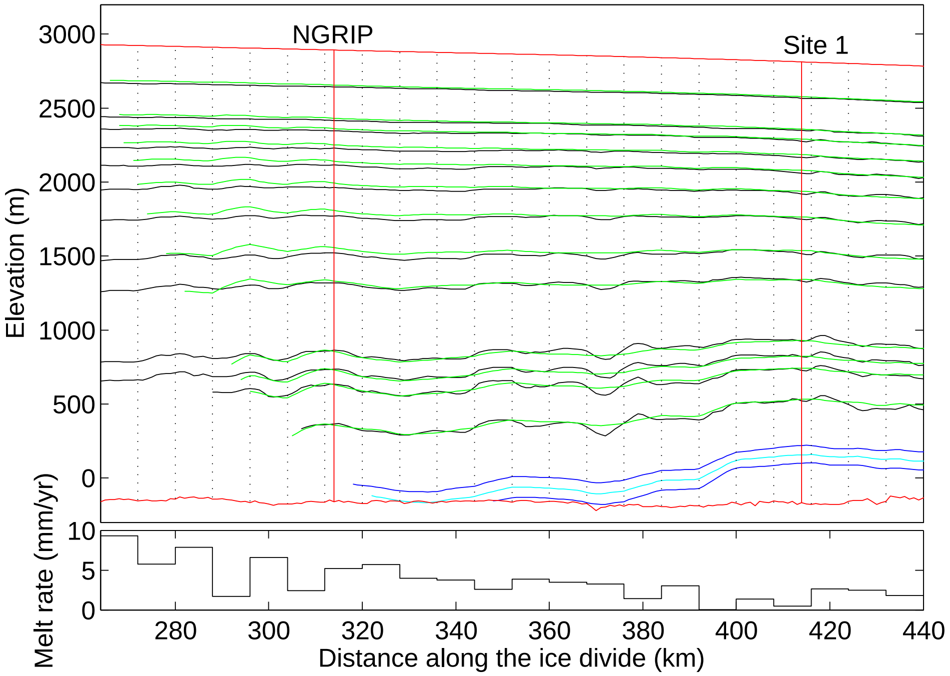

Figure 5.45: Top panel: Observed (black) and modelled (green) isochrones for the NorthGRIP segment. The modelled Eemain layer is shown in blue. The cyan line is the layer of age 123 kyr. The surface of the ice and the ice-bedrock interface are marked in red, NorthGRIP and Site 1 are marked by red vertical lines, and the dotted vertical lines indicate the melt rate intervals. Bottom panel: The obtained basal melt rates along the same segment. These results were obtained from the 2D model using the ice thickness history from Vinther et al. (subm).

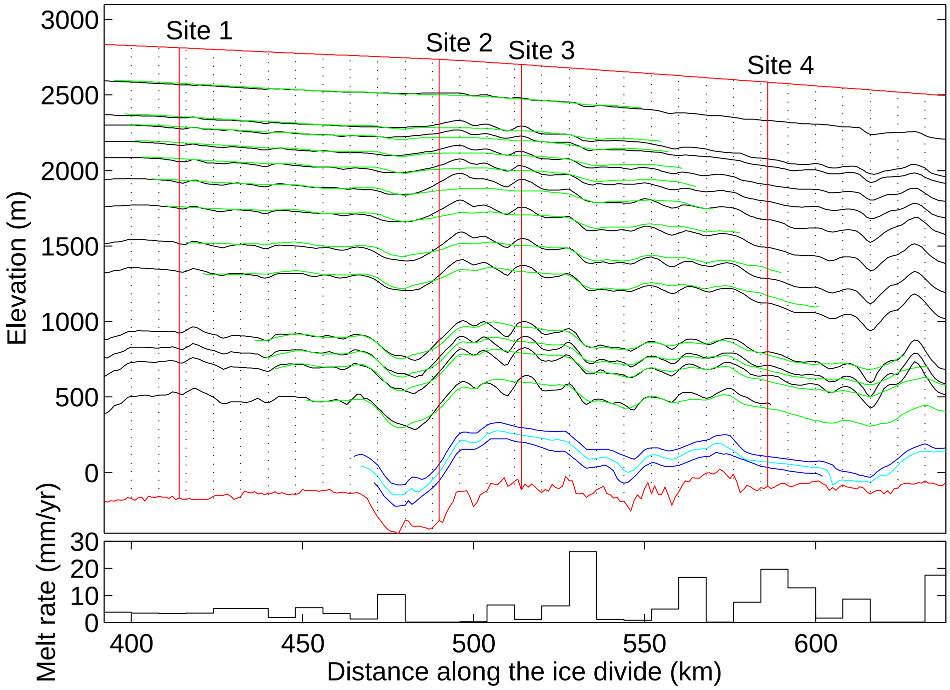

Figure 5.46: Top panel: Observed (black) and modelled (green) isochrones for the Middle segment. The modelled Eemain layer is shown in blue, and the cyan line is the 123 kyr modelled isochrone. The surface of the ice and the ice-bedrock interface are marked in red, Sites 1–4 are marked by red vertical lines, and the dotted vertical lines indicate the melt rate intervals. Bottom panel: The obtained basal melt rates along the same segment. These results were obtained from the 2D model using the ice thickness history from Vinther et al. (subm).

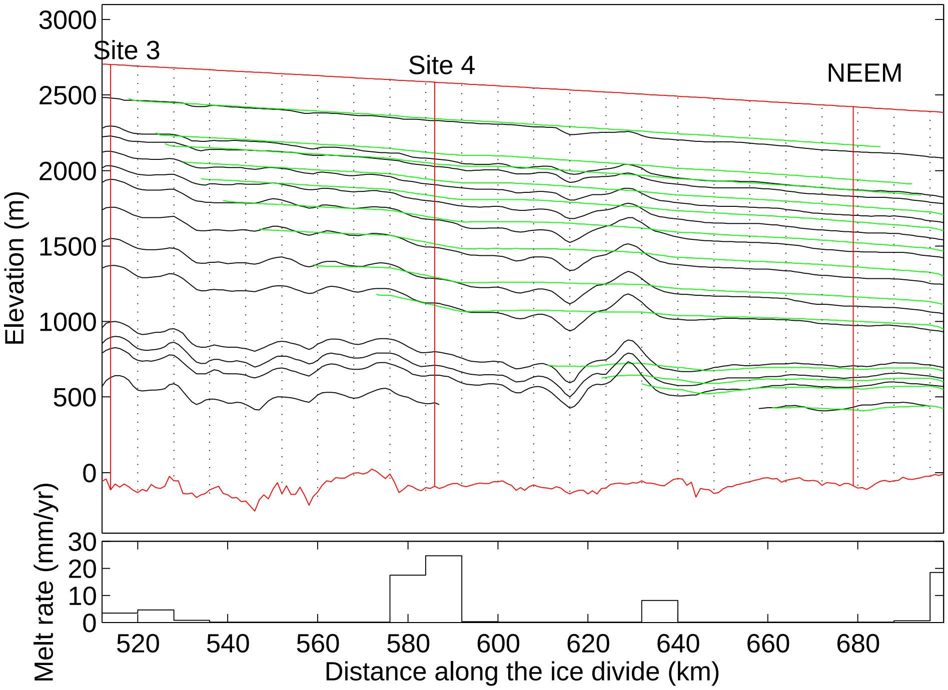

Figure 5.47: Top panel: Observed (black) and modelled (green) isochrones for the NEEM segment. The modelled Eemain layer is shown in blue, and the cyan line is the 123 kyr modelled isochrone. The surface of the ice and the ice-bedrock interface are marked in red, Sites 3 and 4 and NEEM are marked by red vertical lines, and the dotted vertical lines indicate the melt rate intervals. Bottom panel: The obtained basal melt rates along the same segment. These results were obtained from the 2D model using the ice thickness history from Vinther et al. (subm).

Age (kyr)	NGRIP	Site 1	Site 2	Site 3	Site 4	NEEM
1.4	12	11	-12	-7	12	51
2.7	14	9	-24	-34	37	69
3.2	14	15	-30	-32	10	38
4.0	24	19	-25	-29	16	56
4.8	26	20	-24	-33	24	67
5.9	30	18	-55	-76	-5	46
7.5	36	16	-42	-51	-21	20
10.2	36	22	-23	-47	-51	-28
14.6	14	11	-23	-42	-27	-26
37.7	-8	5	-35	-34	-70	-57
45.0	-4	5	-35	-27	-74	-47
51.0	-2	16	-22	-30	-85	-43
74.6	-7	10	-26	-30	-66	-39

Table 5.17: The difference in m between observed and modelled depths of the 13 isochrones. The modelled depths are calculated from the accepted values of the model parameters of the 2D model using the ice thickness history from Vinther et al. (subm) to account for changes in ice thickness.

past the end of the segment. As was done above, we combine the results obtained from the Middle and NEEM segments to get an estimate of the location of the Eemian layer along the ice divide. Again, we use results from the Middle segment upstream from 560 km from GRIP and results obtained from the NEEM segment downstream from here. The resulting Eemian layer is shown together with the Eemian layer from the NorthGRIP segment in Fig. 5.48. The location and thickness of the Eemian layer at the 1D sites are listed in Table 5.16. Fig. 5.49 shows histograms of the top, bottom, and thickness of the Eemian layer at NEEM. It is seen, that it is well determined.

According to the results obtained with the 2D model using the ice thickness history from Vinther et al. (subm) to account for past changes in ice thickness, the ice found at the beginning of the Eemian period at the NEEM site was deposited ~190 km upstream from the drill site.

5.5 Previously published results

Appendix B contains reprints of these papers

Buchardt, S. L. and Dahl-Jensen, D. (2007). Estimating the basal melt rate at NorthGRIP using a Monte Carlo technique. *Annals of Glaciology*, 45:137–142, doi:10.3189/172756407782282435 .

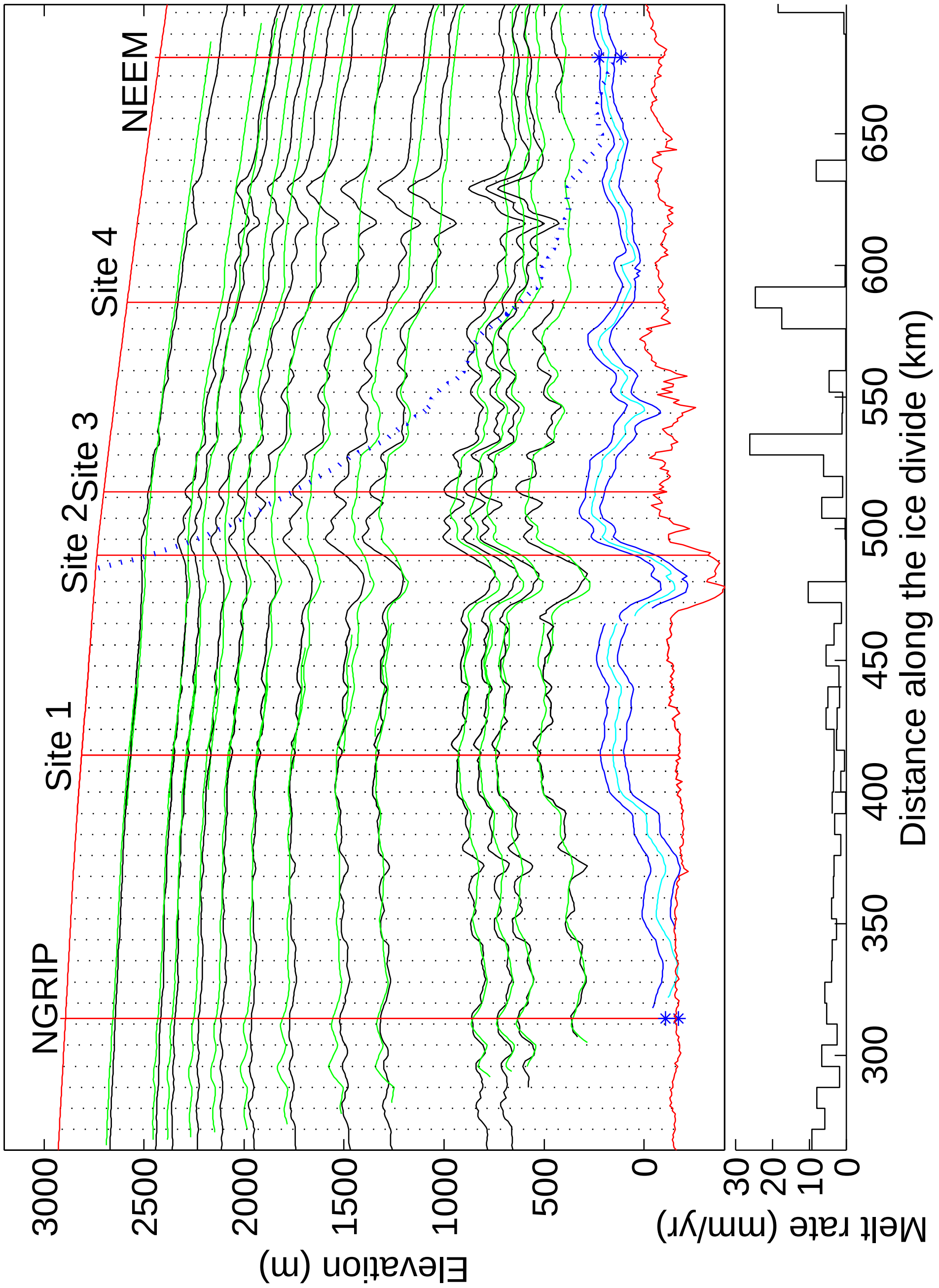

Figure 5.48: Observed (black) and modelled (green) isochrones. The dotted vertical lines indicate the melt rate intervals. The modelled Eemain layer is shown in blue, and the cyan line is the 123 kyr modelled isochrone. The dotted blue line indicates the modelled path the ice found at the beginning of the Eemian at NEEM has taken through the ice. The Eemian layer was modelled using the results from the Middle segment up to 560 km from GRIP and the results from the NEEM segment downstream from here. The blue asterisks indicate the top and bottom of the Eemian layer calculated from the 1D model using the ice thickness history from Vinther et al. (subm). Bottom panel: The obtained basal melt rates along the same segment. The results were obtained from the 2D model using the ice thickness history from Vinther et al. (subm) to account for changes in ice thickness.

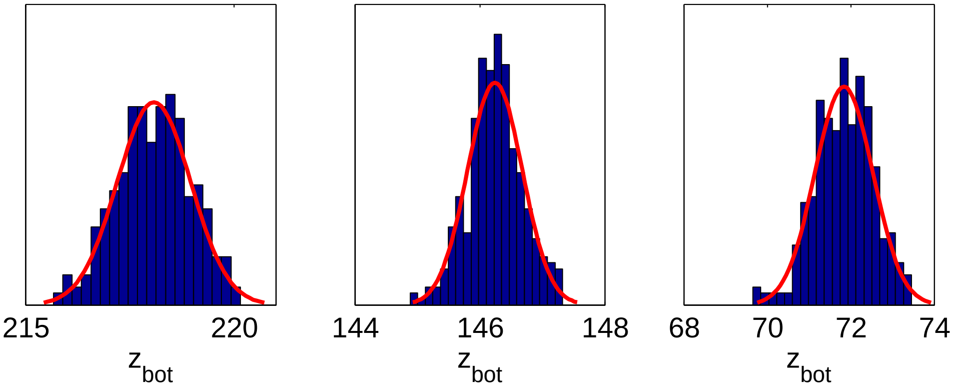

Figure 5.49: Histograms for the top, bottom, and thickness of the Eemian layer at NEEM as calculated from the 2D model using the ice thickness history from Vinther et al. (subm) to account for changes in ice thickness.

and

Buchardt, S. L. and Dahl-Jensen, D. (2008). At what depth is the Eemian layer expected to be found at NEEM? *Annals of Glaciology*, 48:100–102, doi:10.3189/172756408784700617.

These papers are based on studies similar to that presented in this thesis. Therefore, the main results from these papers are briefly summarized below.

Buchardt and Dahl-Jensen (2007)

In this paper the basal melt rates were calculated along the ice divide in the vicinity of the NorthGRIP drill site. As in this thesis 1D and 2D Dansgaard-Johnsen models were used to simulate the ice flow. There are some differences between the model used in this thesis and the one used by Buchardt and Dahl-Jensen (2007). These are summarized below:

- The accumulation model was given by Eq. (3.40)
- The accumulation pattern from Ohmura and Reeh (1991) modified to match the observed values at the drill sites was used
- The time step dt was 100 yrs
- The ice thickness was assumed constant in time
- In the 2D model the kink height h was tied linearly to the basal melt rate

	A_0 (m/yr)	h (m)	F_B	w_b (mm/yr)
1D	0.225±0.004	2420±250	0.07±0.03	-8.2±0.9
2D	0.219±0.0003	2280±50	0.09±0.01	-6.1±0.2

Table 5.18: The values of A_0, h, F_B, and w_b at NorthGRIP obtained from the 1D and 2D model studies by Buchardt and Dahl-Jensen (2007).

- The surface velocity was calculated as a linear function of the surface slope
- The basal melt rate intervals were 4 km long
- The velocity vectors were not rotated to be parallel to the bed at the ice-bedrock interface

The 1D and 2D inverse problems were solved using the Metropolis algorithm (cf. page 53) with 20 isochrones as constraints. These isochrones covered the age range 3.5–79.6 kyr b2k, and were collected by CreSIS in May 1999. The 1D problem was only solved for NorthGRIP and the 2D problem was solved for a section of the ice divide starting 82 km upstream from NorthGRIP and ending 22 km downstream from the drill site.

The obtained values for selected Monte Carlo-determined parameters at NorthGRIP are found in Table 5.18 for both the 1D and the 2D models. Fig. 5.50 shows a comparison between the shape of the lowest observed isochrone dated to 79.6 kyr b2k and the obtained basal melt rates along the ice divide. The two curves show very similar patterns, but the isochrone curve is shifted slightly to the right. The shift is caused by the horizontal flow velocity of the ice. The features created by the melt rate at a given place is carried with the ice along the line. This illustrates the advantage of using a two-dimensional model to simulate the ice flow.

Buchardt and Dahl-Jensen (2008)

The aim of the study presented in this paper is to estimate the location of the Eemian layer at NEEM using a 2D Dansgaard-Johnsen flow model and observed isochrones from RES images. The differences between the 2D ice flow model used by Buchardt and Dahl-Jensen (2008) and the one used in this thesis are summarized below:

- The accumulation model was given by Eq. (3.40)
- Prior to 123 kyr b2k the accumulation rates were calculated using the glacial index from Greve (2005)

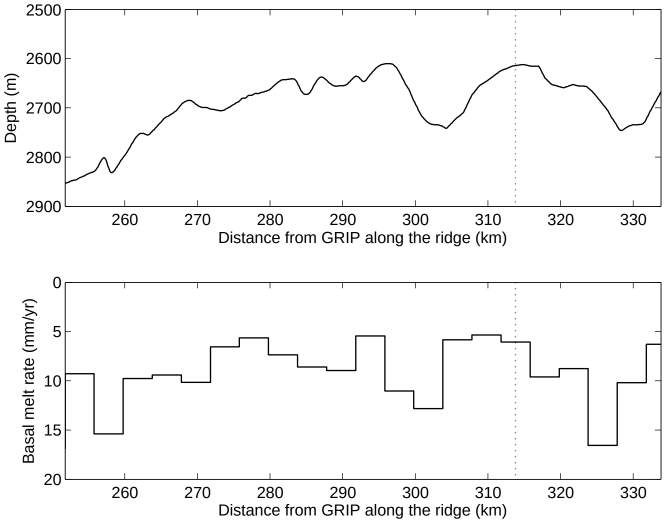

Figure 5.50: The isochrone dated to 79.6 kyr (above) and the basal melt rates (below) obtained from the 2D model study by Buchardt and Dahl-Jensen (2007).The length of each melt rate interval is 4 km. NorthGRIP is indicated by the dotted line. Figure from Buchardt and Dahl-Jensen (2007).

- The accumulation pattern from Ohmura and Reeh (1991) modified to match the observed values at the drill sites was used with the modification that the accumulation rate was allowed to grow faster and more when moving towards NEEM, than the data set indicates
- The kink height h was tied linearly to the basal melt rate
- The surface velocity was calculated as a linear function of the surface slope
- The model was run both for $\frac{\partial H}{\partial t} = 0$ and using the ice thickness history from Greve (2005) to account for past changes in ice thickness
- The time step dt was 100 yrs
- The velocity vectors were not rotated to be parallel to the bed at the ice-bedrock interface

A 224 km long section of the ice divide starting 204 km upstream from NEEM is studied. The 2D inverse problem is solved using the Metropolis algorithm (see page 53) constrained by 12 isochrones spanning the period 3.6–79.8 kyr b2k.

The main results of the study are summarized in Table 5.19. Fig. 5.51 shows the Eemian layer as calculated from the model accounting for temporal

	A_0 (m/yr)	w_b (mm/yr)	Eemian ice (m)	$z_{\rm bot}$ (m)
$\frac{\partial H}{\partial t}=0$	0.267±0.002	-1.0±0.5	75±10	50±40
Greve (2005)	0.257±0.002	-1.0±0.6	60±10	0±40

Table 5.19: Main results from the 2D study carried out by Buchardt and Dahl-Jensen (2008): Present accumulation rate at NEEM, vertical velocity at the base, thickness of the Eemian layer at NEEM, location of the bottom of the Eemian layer. For comparison, the bedrock is at -98 m at NEEM.

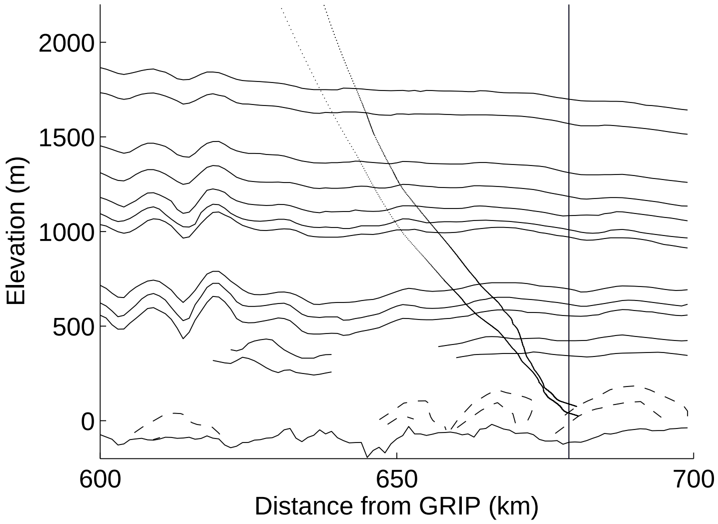

Figure 5.51: Observed isochrones (solid lines) and modelled top and base of the Eemian layer (dashed lines) calculated using the ice thickness history from Greve (2005) to account for changes in ice thickness. The dotted lines show the paths that the top and the base of the Eemian layer at NEEM have taken through the ice. The NEEM drill site is indicated by the vertical line.

changes in ice thickness. It also shows the paths that the top and base of the Eemian layer has taken through the ice. This indicates that the Eemian ice at NEEM originates some 50 km upstream from the drill site.

Chapter 6

Discussion

While some analysis and discussion was given as the results were presented in the previous chapter, this chapter is dedicated to a general discussion of what can be inferred from the results about accumulation, basal melting and Eemian ice in the region of study.

6.1 Accumulation and ice sheet evolution

The choice of accumulation model is crucial to the outcome of a model study like the one presented in this thesis. In this study it was chosen to use a different parameterization of the δ^{18}O-accumulation relationship than the one used by Johnsen et al. (1995) for the GRIP site, because this did not perform well on the NorthGRIP data (cf. Section 3.1.2). The new parameterization links the accumulation rate to the δ^{18}O values through a second degree polynomial (cf. Eq. (3.44)). However, there is no theoretical background for this choice. It was made merely because the relationship was simple and seemed to agree well with the distribution of points in a scatter plot of strain corrected observed annual layer thicknesses plotted vs. δ^{18}O value (cf. Fig. 5.8). Furthermore, the high correlation between the accepted values for the accumulation model parameters p_1, p_2, and p_3 (cf. Table 5.2) indicates, that the relationship is overparameterized.

The difference between observed and modelled isochrones at NorthGRIP obtained from the 1D model with and without including ice thickness changes are listed in Table 5.9. In all three cases the largest misfits are found for the Bølling (14.6 kyr) and early Holocene (10.2 kyr) isochrones, and when comparing observed and modelled annual layer thicknesses for this period (see Fig. 6.1) it is seen, that the modelled annual layers are too thick for

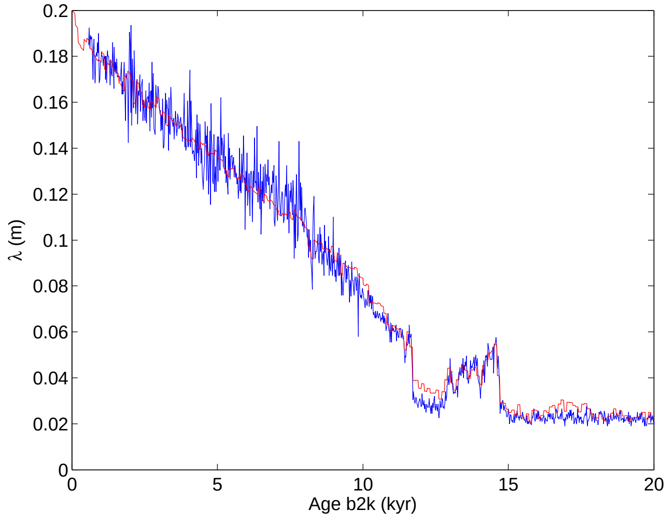

Figure 6.1: Observed (blue) and modelled (red) annual layer thicknesses at NorthGRIP for the last 20 kyr. The modelled layer thicknesses were obtained from the 1D model with constant ice thickness.

a large part of this period. Furthermore, comparing observed annual layer thicknesses from GRIP and NorthGRIP (Fig. 6.2) reveals another interesting feature. When the annual layer thicknesses are plotted against depth, the Holocene GRIP data follow a straight line (as predicted by the DJ model), but the NorthGRIP data show a kink around 1200 m's depth (corresponding to an age of ~8 kyr b2k), below which the layers at NorthGRIP are relatively thinner than at GRIP. This feature suggests lower accumulation rates in the period from Bølling to early Holocene than indicated by the isotopes (Sigfús Johnsen, personal communication 2008).

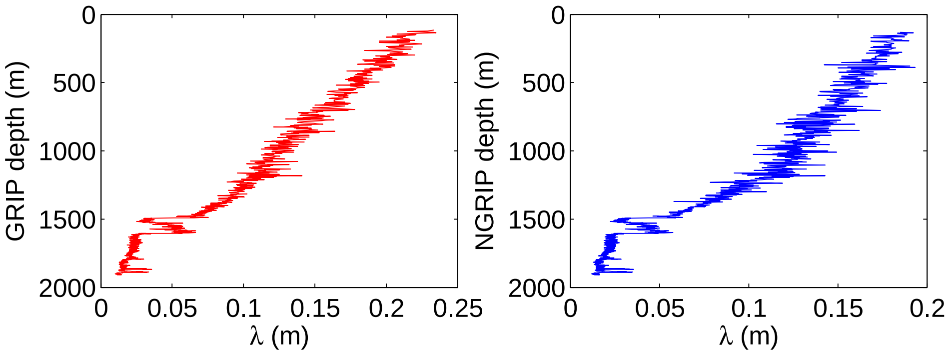

Figure 6.2: Observed annual layer thicknesses at GRIP (red) and NorthGRIP (blue).

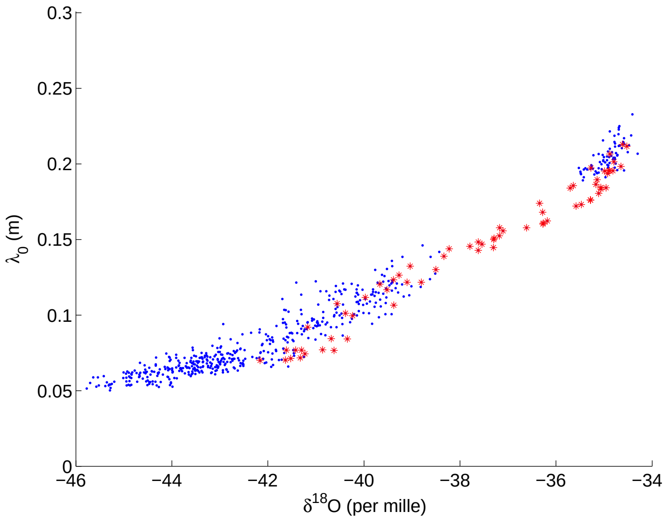

Figure 6.3: Strain corrected annual layer thicknesses versus δ^{18}O for the last 60 kyr at NorthGRIP. Data from the period 8–14.6 kyr b2k are marked in red.

One possible scenario that could explain this is that a connection existed between the Greenland ice sheet and the Innuitian ice sheet in Canada during the earliest part of the Holocene, causing the ice divide in the NorthGRIP area to be located west of its current position (Bo Vinther, personal communication 2009), meaning that the NorthGRIP drill site was located east of the ice divide instead of on the ice divide as at present. Observations show that there is a large gradient in accumulation rate across the ice divide with lower accumulation rates towards the north-east (Clausen et al., 1988; Ohmura and Reeh, 1991). A gradient in the δ^{18}O values is also seen, but it is relatively smaller (Clausen et al., 1988). The GRIP site is located at the Summit of the ice cap, where the connection of the two ice sheets would probably not change the geometry of the ice sheet significantly.

A consequence of this scenario would be a break down of the expected δ^{18}O-accumulation relation for the period where the ice divide was located west of NorthGRIP. In a plot of strain-corrected annual layer thicknesses versus $\delta^{18}O$ value, data points from this period would be located 'too low'. Such a plot is shown in Fig. 6.3, where the data points from the period 8–14.6 kyr b2k are marked in red. If these points were located slightly higher, the data set would take the same s-shaped form as seen for the GRIP data (cf. Fig. 3.3) and predicted by the accumulation model from Johnsen et al. (1995). Keeping this in mind, the best estimate of the accumulation history at NorthGRIP may be reached by using the accumulation model from Johnsen et al. (1995) (Eq. (3.40)) but adding a parameter that reduces the accumulation rate in the period 8–14.6 kyr b2k. In studies similar to the present work, such a parameter could be estimated from a Monte Carlo solution to the inverse problem.

The ice thickness data from Vinther et al. (subm) support the existence of a connection between the Greenland and Innuitian ice sheets in the early Holocene, and for the 1D model at NEEM, the best fit between observed and modelled isochrones was obtained using this data set (cf. Table 5.11). For the 2D model, the best fit was obtained when assuming constant ice thickness in time. The ice thickness data from Vinther et al. (subm) along the line were obtained simply from a linear interpolation between the ice thickness histories obtained for Camp Century and NorthGRIP. Still, using the Vinther et al. (subm) data leads to smaller misfits and result in better agreement with observed values than using the data set from Greve (2005).

The spatial changes in the accumulation rate along the ice divide was investigated from shallow RES layers and 1D model studies (cf. Section 3.2.1 and Fig. 5.25). The accumulation pattern derived from the shallow RES layers shows low accumulation rates in the area ∼500 km from GRIP. This is supported by the present accumulation rates obtained from the 1D studies. For Site 4 and NEEM there is a larger discrepancy between the accumulation rates obtained with the two methods. The value obtained at NEEM from the shallow RES layers agrees well with the value found from studies of a shallow ice core at the site, while the 1D model indicates a higher accumulation rate. A larger discrepancy between observations and results from 1D model studies at these two sites compared to sites closer to NorthGRIP is not surprising, as assumptions of constant ice thickness and constant accumulation pattern in time get less valid with distance from NorthGRIP. In this context it is interesting that the obtained values for the present accumulation rate at NEEM are very similar for the 1D models with and without including temporal changes in ice thickness (cf. Table 5.10). Furthermore, for both versions of the 2D model in the NEEM segment, the modelled isochrones were too shallow in the upper part of the ice sheet indicating that a higher accumulation rate during the last couple of thousand years would have made a better fit possible. The assumption of constant accumulation pattern or the parameterization of the surface velocity are likely to cause the discrepancy.

We know that the assumption of constant accumulation pattern does not hold good. At present, the ratio of the accumulation at NorthGRIP to that at GRIP is 83% but Grinsted and Dahl-Jensen (2002) found that it was 66% during the glacial period. The changes in the difference in surface altitude between NorthGRIP and NEEM have probably been larger than those between GRIP and NorthGRIP, and thus even larger differences are expected here.

	$\frac{\partial H}{\partial t} = 0$		Vinther et al. (subm)		Greve
	1D	2D	1D	2D	1D
NGRIP	7.5±1.3	5.6±0.2	7.5±1.3	5.2±0.2	3.3±0.7
Site 1	2.0±0.9	1.3±0.1	N/A	0.4±0.1	N/A
Site 2	2.2±1	$0\pm<0.1^a$	N/A	$0\pm<0.1^a$	N/A
Site 3	1.2±0.7	1.0±0.2	N/A	1.1±0.4	N/A
Site 4	1.5±0.7	$25^b/3.5^c\pm2^b/0.1^c$	N/A	$20^a/25^c\pm1^b/1^c$	N/A
NEEM	0 ± 0.1^a	$0\pm<0.1^a$	1.7±0.7	$0\pm<0.1^a$	N/A

---

[a] Value is strictly non-negative - only plus option applies.

[b] Results from Middle segment.

[c] Results from NEEM segment.

Table 6.1: The basal melt rate estimates obtained for the six 1D sites in the present study. All values are given in mm/yr. The listed uncertainties are the standard deviation the distribution of accepted model values and not the true uncertainties, which are larger.

6.2 Basal melt rates and geothermal flux

This study aims to estimate the basal melt rates along the ice divide in northern Greenland, yet a non-thermal model is used. This can be done because the basal melt rate equals minus the vertical velocity at the base of the ice sheet and thus can be treated as a flow parameter. However, the melt rate depends on the temperature gradient at the base, which changes with time because the surface climate and therefore the temperature of the ice changes with time. Thus the melt rates found in this study may be considered as average values for the past 74.6 kyr.

The results for the basal melt rates at the six 1D sites are summarized in Table 6.1 and the obtained basal melt rates along the full section obtained from the 2D model are shown in Figs. 5.37 and 5.48. The obtained values in the area of study range from zero up to more than 25 mm/yr, and though there are significant differences between the amplitude of the spatial changes in the area of high undulations upstream from NEEM, the melt rate patterns obtained from the 2D models assuming constant ice thickness and using the data set from Vinther et al. (subm) are similar. In the NorthGRIP end of the section, the results indicate a generally decreasing melt rate from ∼5–8 mm/yr around NorthGRIP to ∼2–3 mm/yr about 100 km downstream from the drill site. The results from all the model investigations done in this study indicate that there is basal melting everywhere in this part of the section, and the results from 1D and 2D studies at NorthGRIP and Site 1 are consistent. The 2D estimates are somewhat lower than the 1D estimates, which can be explained by the higher melt rates upstream from these sites. The one-dimensional model compensates for the upstream effect by finding a higher melt rate at the site. The basal melt rate estimates for NorthGRIP are all in agreement with the value of 7 mm/yr found from ice core studies (North Greenland Ice Core Project members, 2004) and the results from Buchardt and Dahl-Jensen (2007) (cf. Table 5.18), except for the very low melt rate estimate found when using the Greve (2005) data set in the 1D model. Using this data set also results in a high misfit between observed and modelled isochrones (cf. Table 5.9) lending little credibility to this result.

At Site 2 the 1D model indicates a small basal melt rate of 2.2 mm/yr, whereas both versions of the 2D model estimate no basal melting. Though the results are not inconsistent, the fact that the site is located on a steep slope could contribute to making the 2D estimate lower. The observed isochrones rise steeply here, and the modelled isochrones (2D) tend to be located a little too deep, so perhaps the 2D model needs 'help' to reproduce the steep rise and thus prefers no basal melting.

The 1D and 2D estimates for the basal melt rate at Site 3 are consistent. Downstream from Site 3 the findings from this study indicate a high spatial variability in the basal melt rate. The agreement between melt rate estimates obtained from the Middle and NEEM segments is not good in the overlap zone. This may be attributed to a combination of things. The horizontal movement of the modelled isochrones is very large, so the results from the first 10–12 melt rate intervals of the NEEM segment were obtained with no modelled isochrones in the lower half of the ice sheet. In the downstream part of the overlap zone, we find the area with large undulations of the observed isochrones that the modelled isochrones are not able to reproduce, and where the lowest isochrone is not visible. Given these circumstances it is difficult to assess which estimates have more credibility and should be used to estimate the position of the Eemian layer. From the position of the modelled isochrones it was decided to use the results obtained from the Middle segment up to 560 km from GRIP and the results from the NEEM segment downstream from there (upstream from 560 km there are no deep modelled isochrones for the NEEM segment).

The large discrepancy between the 1D and 2D results at Site 4 may be caused by the 2D model trying to fit the highly undulating observed isochrones downstream from the site. As mentioned above, the modelled isochrones cannot reproduce these undulations. Several factors contributing to this can be identified. Firstly, the undulations happen over too short distances for it to be possible to reproduce them using a model with a melt rate interval of 8 km. This is further complicated by the deepest trough being located right on the border between two melt rate intervals. Secondly, better results could possibly be obtained if the model was run for a segment such that all 13 modelled isochrones would be present in the area of high undulations and not just the upper or lower half as was the case in this study because of the choice of segments.

At NEEM all estimates indicate no basal melting except the one obtained from the 1D model using the data set from Vinther et al. (subm), which indicates a small basal melt rate of 1.7 mm/yr.

As mentioned previously, the uncertainties given on the results are a measure of how well determined the parameter is from the Monte Carlo solution to the inverse problem and not the true uncertainty, which is hard to determine. A rough estimate could be a few mm on the moderate melt rate values and more on the higher melt rate values.

From this study we have found a pattern of changing basal melt rates along the ice divide. The results indicate that conditions may change between a high basal melt rate and frozen conditions over short distances. This is in agreement with the findings of Oswald and Gogineni (2008), who used a method of narrowing the spread of measured echo intensities in RES data to distinguish between frozen and wet interfaces at the base if the ice. Their results agree with observations at GRIP and NorthGRIP, and the areas where their results indicate wet conditions often coincide with areas where the isochrones show undulations that can not be explained by bedrock topography.

A crude estimate of the total amount of water created by the basal melting is obtained by assuming that the average basal melt rate found in the area of study is representative for the whole region with basal melting. The average values of the basal melt rates along the ice divide are ∼3 mm/yr and ∼4 mm/yr using $\frac{\partial H}{\partial t} = 0$ and the data set from Vinther et al. (subm), respectively. Assuming that the area of basal melting is $4{\cdot}10^5$ km^2 (Dorthe Dahl-Jensen, personal communication 2005) we arrive at a total basal melt water production of ∼1–2 km^3/yr.

The basal melt rates were used to calculate the geothermal flux along the line (cf. Figs. 5.31 and 5.42). The geothermal flux is calculated as a linear function of the basal melt rate, and thus shows the same spatial variability. The obtained values vary by more than 100 mW/m^2 over distances of 10 km. Such a variability can exist only if the heat source is located near the surface. Large spatial variations in the geothermal flux have also been reported by Näslund et al. (2005). From studies of the Fennoscandian ice sheet during the Last Glacial Maximum, they found significant local changes in the geothermal flux in Sweden and Finland. The values of the geothermal flux found in the present study are, however, quite high.

Unlike in Antarctica, no subglacial lakes have been found in Greenland, and the drainage system of the meltwater created under the Greenland Ice Sheet is not well known. The water may be transported through small valleys observed in the bedrock topography. The presence of such canals may cause rapid spatial variations in the melt rate and is an alternative way of producing high local melt rates without strong changes in the geothermal heat flux. This is supported by the fact that dips in the isochrones are often observed over the small valleys in the bedrock. One such example could be the small dip in the bedrock around 370 km from GRIP. The isochrones dip quite deep above this feature possibly caused by melt water in the valley. However, this is just a speculation.

6.3 Eemian ice

Figs. 5.37 and 5.48 show the Eemian layers obtained from the results to the 1D and 2D models for constant ice thickness and accounting for changes in ice thickness using the data set from Vinther et al. (subm), respectively. All findings indicate that a full Eemian record is likely to be found well above bedrock at NEEM. Generally, there is little difference in the estimates obtained with 1D and 2D models except for the 1D model at NEEM using the data set from Vinther et al. (subm), which predicts a thicker Eemian layer located a little closer to bedrock. This is the effect of this model predicting a basal melt rate of 1.7 mm/yr. A basal melt rate increases the layer thickness and pulls the layers down. However, even with this melt rate, the Eemian layer is located well above bedrock.

Both versions of the 2D model predict the Eemian layer to be ~70 m thick and found in the depth range 2230–2300 m. A comparison of the Eemian layers obtained with and without including changes in ice thickness is shown in Fig. 6.4. Except for the overlap region between the NorthGRIP and Middle segments there is little difference between the results. These results for the Eemian layer are different from the results obtained by Buchardt and Dahl-Jensen (2008), which indicated an Eemian layer of ~60 m located ~100 m above bedrock. Furthermore, their modelled Eemian layer has a very different shape, and the Eemian ice was predicted to originate only ~50 km upstream (compared to 170–190 km found from the present study). This difference probably arises because of the different parameterizations of the surface velocity used in the two studies. The surface velocities used in this thesis are consistently higher than those used by Buchardt and Dahl-Jensen (2008). The differences in shape between the modelled Eemian layers probably arise because of differences in the parameterization of h and the fact that the velocity vector was not rotated to become parallel to the bedrock at

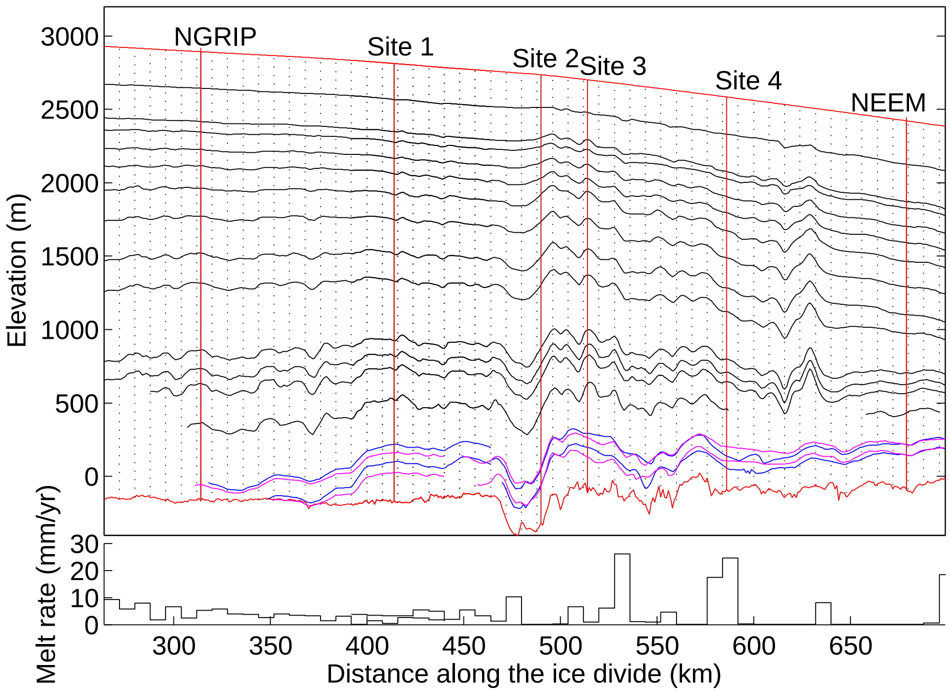

Figure 6.4: The modelled Eemian layer as calculated from the results of the 2D inverse problem assuming constant ice thickness (magenta) and using the data set from Vinther et al. (subm) to account for changes in ice thickness (blue). The observed isochrones are shown in black.

the base of the ice sheet in the study by Buchardt and Dahl-Jensen (2008). Furthermore, the radar data used to constrain the Monte Carlo solution in the study by Buchardt and Dahl-Jensen (2008) were not collected parallel to the ice ridge but at angles to it and were projected onto the ice divide.

Fig. 6.5 shows a RES image collected by CReSIS at NEEM in the summer of 2008. At depths of ∼2200–2300 m there is a layer (indicated by the arrow) with a thickness of a little less than 100 m. This coincides with the depth interval and thickness of the modelled layer from this study, so perhaps this is the Eemian layer showing up in the RES image. It is also worth noting that layers are visible even below the supposed Eemian layer, and they show no sign of disturbed stratigraphy.

6.4 Suggested improvements

From the lessons learned during this study, some improvements of the method used in this thesis can be suggested.

- As mentioned above, it is suggested to use the accumulation model from Johnsen et al. (1995) with an extra parameter lowering the accumulation rate in the early Holocene.

- It was not possible to capture the severe undulations of the observed isochrones upstream from NEEM. This is an area suspected of high basal melt rates, and as the old ice found in the NEEM ice core has flowed through this area, it would be nice to obtain better estimates in this area. Therefore, it is suggested to use smaller melt rate intervals. However, this increases the number of unknowns to be determined from the Monte Carlo solution to the inverse problem, so a balance between resolution and the number of parameters to be determined needs to be reached.

- To further improve the basal melt rate estimates in the area upstream from NEEM it is suggested to make sure to choose the segments so that modelled isochrones will be represented in this area throughout the period that the forward model is run for (in this study the last 74.6 kyr).

- The parameterizations of the kink height and the fraction of basal sliding in the 2D model work well in the NorthGRIP area, but further downstream, the range of accepted values for the parameters k_h and k_F became suspiciously narrow. A possible explanation to this could be the changing conditions within one segment. Determining one value

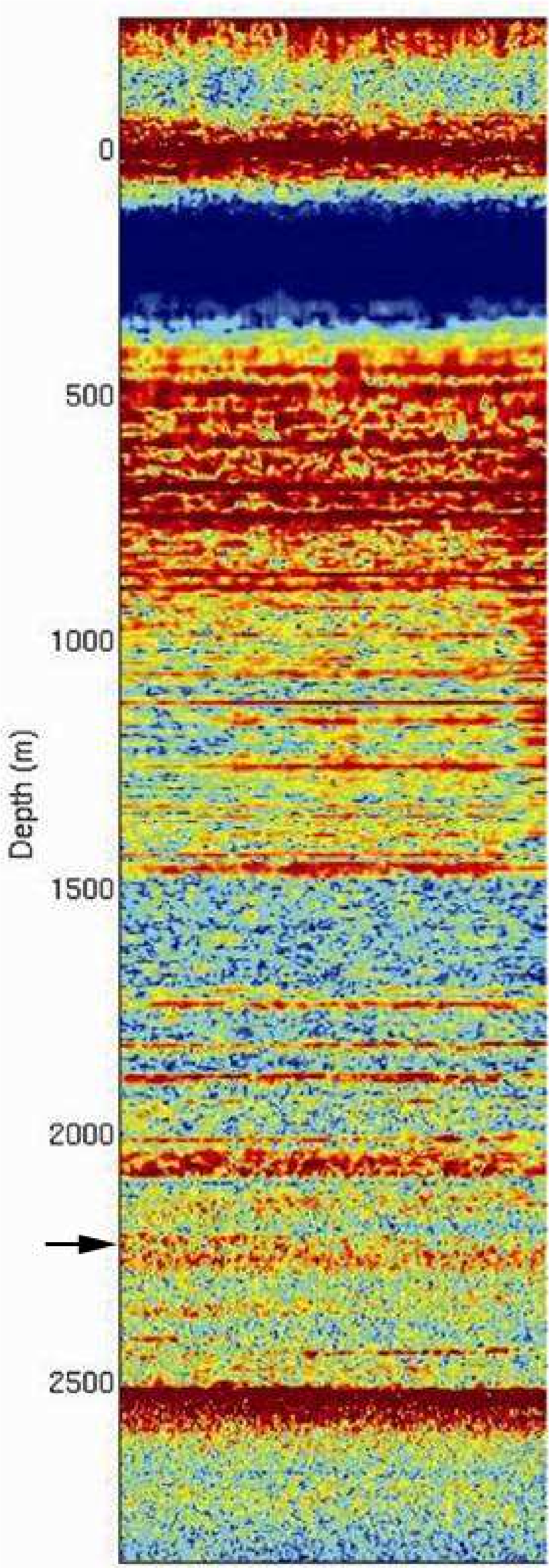

Figure 6.5: Ground based RES image collected at NEEM in 2008 (data, courtesy Prasad Gogineni). The reddish layer at a depth of ∼2200–2300 m indicated by the arrow is consistent with the depth range for the Eemian layer at NEEM obtained in this study. The horizontal scale of the image is a few hundred m.

for each of the two parameters that is good for the whole segment could be impossible. The easy way of testing this would be to allow spatial changes in k_h and k_F. Again, this would increase the number of parameters to be determined. It is suggested to keep the values of k_h and k_F constant over intervals of 50 km.

Chapter 7

Conclusion and outlook

The basal conditions along the northern part of the main ice ridge in Greenland were investigated using a Dansgaard-Johnsen ice flow model and Monte Carlo inversion. Combining ice core data and remote sensing radio-echo sounding data made it possible to obtain interesting information on the basal melt rate pattern under the ice sheet. A set of radio-echo sounding layers dated from their depths at the ice core drill sites was used to constrain the inversion. Using this data set, a melt rate profile that shows high spatial variability as well as generally high values for the basal melt rates in northern Greenland was obtained. The high spatial variability indicates a shallow source for the heat causing the melting, since a deeper source would provide a smoother pattern. The obtained melt rate pattern may prove useful when trying to determine the mineralogical composition of the bedrock in Greenland (Mygind, 2009), which is difficult to determine due to the thick ice sheet covering most of the island. The melt rate pattern and the deduced pattern of geothermal fluxes could supplement the seismic data and the point measurements at the ice core drill sites in providing insight into the Greenlandic underground.

From the obtained melt rates the total volume of water created every year from basal melting was estimated to be of the order 2 km^3. This estimate is by no means accurate, since it is calculated from only the basal melt rates along the main ice ridge. As concluded from this study, the basal melt rates are highly variable and the values along the main ice ridge may not be representative for all of the area where basal melting is indicated by the RES layers. However, the 1–2 km^3/year should be correct to the order of magnitude.

The two-dimensional model presented in Chapter 3 is well suited for well studied areas as e.g. in the vicinity of ice core drill sites where parameters like surface velocity and present accumulation rate are known. In these areas the model provides good estimates for the basal melt rate and constitutes a useful tool when correcting ice core profiles for upstream effects. In areas where less is known about the ice flow, the one-dimensional model described in Chapter 3 may be used to estimate the basal melt rate at different points. This could be used to create a map of basal melt rates in northern Greenland including features of much smaller scale than previously possible. Such a map would be valuable as input to large three-dimensional models of the ice sheet, e.g. (Greve, 2005), used to model the previous and the future state of the Greenland ice sheet. An optimized way of obtaining such a map could be to use the method developed by Oswald and Gogineni (2008) to identify areas with a wet base and then use a 1D model and a Monte Carlo method similar to those described in this thesis to infer basal melt rates. The Monte Carlo solution could be constrained by RES layers that are easily recognized and thus do not need to be traced to an ice core drill site to be dated (e.g. the Bølling isochrone an the three glacial isochrones used in this study).

The results of the inversion for the area around the new ice core drill site NEEM were used to predict the depth and thickness of the Eemian layer in the NEEM ice core. The results predict the layer to be located in the depth interval 2230–2300 m (∼200 m above bedrock) which is a good indicator that an undisturbed Eemian record may be retrieved at NEEM. The Eemian layer is predicted to span 70 m of the ice core. The basal ice at NEEM is estimated to be well above 150 kyr old.

Bibliography

Andersen, K. k., Svensson, A., Johnsen, S. J., Rasmussen, S. O., Bigler, M., Röthlisberger, R., Ruth, U., Siggaard-Andersen, M.-L., Steffensen, J. P., Dahl-Jensen, D., Vinther, B. M., and Clausen, H. B. (2006). The Greenland ice core chronology 2005, 15-42 ka. part 1: Constructing the time scale. *Quaternary Science Reviews*, 25:3246–3257. doi:10.1016/j.quascirev.2006.08.002.

Bogorodsky, V. V., Bentley, C. R., and Gudmandsen, P. E. (1985). *Radioglaciology*. D. Reidel Publishing Company.

Buchardt, S. L. and Dahl-Jensen, D. (2007). Estimating the basal melt rate at NorthGRIP using a Monte Carlo technique. *Annals of Glaciology*, 45:137–142. doi:10.3189/172756407782282435.

Buchardt, S. L. and Dahl-Jensen, D. (2008). At what depth is the Eemian layer expected to be found at NEEM? *Annals of Glaciology*, 48:100–102. doi:10.3189/172756408784700617.

Chen, J. L., Wilson, C. R., and Tapley, B. D. (2006). Satellite gravity measurements confirm accelerated melting of Greenland ice sheet. *Science*, 313:1958–1960.

Clausen, H. B., Gundestrup, N. S., Johnsen, S. J., Bindschadler, R., and Zwally, J. (1988). Glaciological investigations in the Crête area, Central Greenland: A search for a new deep-drilling site. *Annals of Glaciology*, 10:10–15.

Clough, J. W. (1977). Reflections from internal layers in ice sheets. *Journal of Glaciology*, 18(78):3–14.

CReSIS (2007). https://www.cresis.ku.edu/research/data/datafiles/greenland/2007/pdf/20070917.pdf.

Dahl-Jensen, D., Gundestrup, N. S., Gogineni, P., and Miller, H. (2003). Basal melt at NorthGRIP modeled from borehole, ice-core and radio-echo sounder observations. *Annals of Glaciology*, 37:207–212.

Dahl-Jensen, D., Gundestrup, N. S., Keller, K., Johnsen, S. J., Gogeneni, P., Allen, C. T., Chuah, T. S., Miller, H., Kipfstuhl, S., and Waddington, E. D. (1997). A search in north Greenland for a new ice-core drill site. *Journal of Glaciology*, 43(144):300–306.

Dahl-Jensen, D., Johnsen, S. J., Hammer, C. U., and Jouzel, J. (1993). Past accumulation rates derived from observed annual layers in the GRIP ice core from Summit, Central Greenland. In Peltier, W. R., editor, *NATO ASI Series, Vol. I, 12, Ice in the Climate System*, pages 517–532. Springer-Verlag, Berlin.

Dansgaard, W. and Johnsen, S. J. (1969). A flow model and a time scale for the ice core from Camp Century, Greenland. *Journal of Glaciology*, 8(53):215–223.

Dowdeswell, J. A. and Evans, S. (2004). Investigations of the form and flow of ice sheets and glaciers using radio-echo sounding. *Reports on Progress in Physics*, 67:1821–1861.

Drewry, D. J. (1975). Comparison of electromagnetic and seismic-gravity ice thickness measurements in East Antarctica. *Journal of Glaciology*, 15(73):137–150.

Evans, S. (1965). Dielectric properties of ice and snow – a review. *Journal of Glaciology*, 5(42):773–792.

Fahnestock, M., Abdalati, W., Joughin, I., Brozena, J., and Gogineni, P. (2001a). High geothermal heat flow, basal melt, and the origin of rapid ice flow in central Greenland. *Science*, 294(5550):2338–2342.

Fahnestock, M., Abdalati, W., Luo, S., and Gogineni, S. (2001b). Internal layer tracing and age-depth-accumulation relations for the northern Greenland ice sheet. *Journal of Geophysical Research*, 106(D24):33789–33797.

Feller, W. (1970). *An Introduction to Probability Theory and Its Applications*. John Wiley.

Fujita, S. and Mae, S. (1994). Causes and nature of ice-sheet radio-echo internal reflections estimated from the dielectric properties of ice. *Annals of Glaciology*, 20:80–86.

Fujita, S., Maeno, H., Uratsuka, S., Furukawa, T., Mae, S., Fujii, Y., and Watanabe, O. (1999). Nature of radio echo layering in the Antarctic ice sheet detected by a two-frequency experiment. *Journal of Geophysical Research*, 104(B6):13013–13024.

Glen, J. W. (1955). The creep of ploycrystalline ice. In *Proceedings of the Royal Society of London*, volume 228 of *Series A*, pages 519–538.

Gogineni, S., Chuah, T., Allen, C., Jezek, K., and Moore, R. K. (1998). An improved coherent radar depth sounder. *Journal of Glaciology*, 44(148):659–669.

Gogineni, S., Tammana, D., Braaten, D., Leuschen, C., Akins, T., Legarsky, J., Kanagaratnam, P., Stiles, J., Allen, C., and Jezek, K. (2001). Coherent radar ice thickness measurements over the Greenland ice sheet. *Journal of Geophysical Research*, 106(D24):33761–33772.

Göktas, F. (1999). Ergebnisse der Untersuchung des grönländischen Inlandeises mit dem elektromagnetischen Reflexionsverfahren in der Umgebung von GRIP. *Berichte zur Polarforschung*, 336.

Greve, R. (2005). Relation of measured basal temperatures and the spatial distribution of the geothermal heat flux for the Greenland ice sheet. *Annals of Glaciology*, 42:424–432.

Grinsted, A. and Dahl-Jensen, D. (2002). A Monte Carlo-tuned model of the flow in the NorthGRIP area. *Annals of Glaciology*, 35:527–530.

Gudmandsen, P. (1975). Layer echoes in polar ice sheets. *Journal of Glaciology*, 15(73):95–101.

Gundestrup, N. S., Clausen, H. B., Hansen, B. L., and Rand, J. (1987). Camp Century survey 1986. *Cold Regions Science and Technology*, 14:281–288.

Hamilton, R. A., Brooke, F. R., Peacock, J. D., Arnold, K., Bowater, S., Bull, C., and Lister, H. (1956). British north greenland expedition 1952-4: Scientific results. *The Geographical Journal*, 122(2):203–237.

Hammer, C. U. (1980). Acidity of polar ice cores in relation to absolute dating, past volcanism, and radio-echos. *Journal of Glaciology*, 25(93):359–372.

Harrison, C. H. (1973). Radio echo sounding of horizontal layers in ice. *Journal of Glaciology*, 12(66):383–397.

Hastings, W. K. (1970). Monte Carlo sampling methods using Markov chains and their applications. *Biometrika*, 57(1):97–109. doi:10.1093/biomet/57.1.97.

Hempel, L., Thyssen, F., Gundestrup, N., Clausen, H. B., and Miller, H. (2000). A comparison of radio-echo sounding data and electrical conductivity of the GRIP ice core. *Journal of Glaciology*, 46(154):369–374.

Hvidberg, C. S., Keller, K., and Gundestrup, N. S. (2002). Mass balance and ice flow along the north-northwest ridge of the Greenland ice sheet at NorthGRIP. *Annals of Glaciology*, 35:521–526.

Jezek, K., Gogineni, S., Rodriguez, F., Hoch, A., and Sonntag, J. (2007). GISMO: Arctic '07 - fall deployment of the NASA P-3 to Greenland. Technical report, CReSIS, University of Kansas.

Johnsen, S. J., Dahl-Jensen, D., Dansgaard, W., and Gundestrup, N. (1995). Greenland palaeotemperatures derived from GRIP bore hole temperature and ice core isotope profiles. *Tellus*, 47B(5):624–629.

Johnsen, S. J., Dahl-Jensen, D., Gundestrup, N., Steffensen, J. P., Clausen, H. B., Miller, H., Masson-Delmotte, V., Sveinbjörnsdóttir, A., and White, J. (2001). Oxygen isotope and palaeotemperature records from six Greenland ice-core stations: Camp Century, Dye-3, GRIP, GISP2, Renland and NorthGRIP. *Journal of Quarternary Science*, 16(4):299–307.

Johnsen, S. J. and Dansgaard, W. (1992). On flow model dating of stable isotope records from Greenland ice cores. In Bard, E. and Broecker, W. S., editors, *NATO ASI Series, Vol. I, 2, The Last Deglaciation: Absolute and Radiocarbon Chronologies*, pages 13–24. Springer-Verlag, Berlin.

Johnsen, S. J., Dansgaard, W., and White, J. W. C. (1989). The origin of arctic precipitation under present and glacial conditions. *Tellus*, 41B(4):452–468.

Leysinger Vieli, G. J.-M. C., Hindmarsh, R. C. A., and Siegert, M. J. (2007). Three-dimensional flow influences on radar layer stratigraphy. *Annals of Glaciology*, 46:22–28.

Marshall, S. J. and Cuffey, K. M. (2000). Peregrinations of the Greenland ice sheet divide in the last glacial cycle: implications for central Greenland ice cores. *Earth and Planetary Letters*, 179(1):73–90.

Menke, W. (1989). *Geophysical Data Analysis: Discrete Inverse Theory.* Academic Press.

Metropolis, N., Rosenbluth, A. W., Rosenbluth, M. N., Teller, A. H., and Teller, E. (1953). Equation of state calculations by fast computing machines. *The Journal of Chemical Physics*, 21(6):1087–1092.

Metropolis, N. and Ulam, S. (1949). The Monte Carlo method. *Journal of the American Statistical Association*, 44(247):335–341.

Millar, D. H. M. (1981). Radio-echo layering in polar ice sheets and past volcanic activity. *Nature*, 292(5822):441–443.

Miners, W. D., Wolff, E. W., Moore, J. C., Jacobel, R., and Hempel, L. (2002). Modeling the radio echo reflections inside the ice sheet at Summit, Greenland. *Journal of Geophysical Research*, 107(B8, 2172):EPM 6–1–EPM 6–11.

Mosegaard, K. (1998). Resolution analysis of general inverse problems through inverse Monte Carlo sampling. *Inverse Problems*, 14:405–426.

Mosegaard, K. (2006). *Monte Carlo analysis of inverse problems.* Doctoral thesis, University of Copenhagen, Denmark.

Mosegaard, K. and Tarantola, A. (1995). Monte Carlo sampling of solutions to inverse problems. *Journal of Geophysical Research*, 100(B7):12431–12447.

Mygind, M. (2009). Modelling of geothermal heat under the Greenland ice sheet by inversion of basal melt rates. Master's thesis, Centre for Ice and Climate, Niels Bohr Institute, University of Copenhagen.

Näslund, J.-O., Jansson, P., Fastook, J. L., Johnson, J., and Andersson, L. (2005). Detailed spatially distributed geothermal heat-flow data for modeling of basal temperatures and meltwater production beneath the Fennoscandian ice sheet. *Annals of Glaciology*, 40:95–101.

North Greenland Ice Core Project members (2004). High-resolution record of Northern Hemisphere climate extending into the last interglacial period. *Nature*, 431(7007):147–151.

Ohmura, A. and Reeh, N. (1991). New precipitation and accumulation maps for Greenland. *Journal of Glaciology*, 37(125):140–148.

Oswald, G. K. A. and Gogineni, S. P. (2008). Recovery of subglacial water extent from Greenland radar survey data. *Journal of Glaciology*, 54(184):94–106.

Paren, J. G. and Robin, G. d. Q. (1975). Internal reflections in polar ice sheets. *Journal of Glaciology*, 14(71):251–259.

Parrenin, F., Hindmarsh, R. C. A., and Rémy, F. (2006). Analytical solutions for the effect of topography, accumulation rate and lateral flow divergence on isochrone layer geometry. *Journal of Glaciology*, 52(177):191–202.

Pollack, H. N., Hurter, S. J., and Johnson, J. R. (1993). Heat flow from the Earth's interior: analysis of the global data set. *Reviews of Geophysics*, 31(3):267–280.

Rasmussen, S. O., Andersen, K. K., Svensson, A. M., Steffensen, J. P., Vinther, B. M., Clausen, H. B., Siggaard-Andersen, M.-L., Johnsen, S. J., Larsen, L. B., Dahl-Jensen, D., Bigler, M., Röthlisberger, R., Fischer, H., Goto-Azuma, K., Hansson, M. E., and Ruth, U. (2006). A new Greenland ice core chronology for the last glacial termination. *Journal of Geophysical Research*, 111(D06102). doi:10.1029/2005JD006079.

Rignot, E. and Kanagaratnam, P. (2006). Changes in the velocity structure of the Greenland ice sheet. *Science*, 311:986–990.

Shepherd, A. and Wingham, D. (2007). Recent sea-level contributions of the Antarctic and Greenland ice sheets. *Science*, 315:1529–1532. doi:10.1126/science.1136776.

Svensson, A., Andersen, K. K., Bigler, M., Clausen, H. B., Dahl-Jensen, D., Davies, S. M., Johnsen, S. J., Muscheler, R., Parrenin, F., Rasmussen, S. O., Röthlisberger, R., Seierstad, I., Steffensen, J. P., and Vinther, B. M. (2008). A 60 000 year Greenland stratigraphic ice core chronology. *Climate of the Past*, 4:47–57.

Svensson, A., Andersen, K. K., Bigler, M., Clausen, H. B., Dahl-Jensen, D., Davies, S. M., Johnsen, S. J., Muscheler, R., Parrenin, F., Rasmussen, S. O., Röthlisberger, R., Steffensen, J. P., and Vinther, B. M. (2006). The Greenland ice core chronology 2005, 15-42 ka. part 2: Comparison to other records. *Quaternary Science Reviews*, 25:3258–3267. doi:10.1016/j.quascirev.2006.08.003.

Tarantola, A. (2005). *Inverse Problem Theory and Methods for Model Parameter Estimation*. SIAM, Philadelphia.

Tarantola, A. and Mosegaard, K. (2000). Mathematical basis for physical inference. *arXiv:math-ph/0009020 v1*, pages 1–24.

Tarantola, A. and Valette, B. (1982). Inverse problems=quest for information. *Journal of Geophysics*, 50(3):159–170.

Vaughan, D. G., Anderson, P. S., King, J. C., Mann, G. W., Mobbs, S. D., and Ladkin, R. S. (2004). Imaging of firn isochrones across an Antarctic ice rise and implications for patterns of snow accumulation rate. *Journal of Glaciology*, 50(170):413–418.

Vinther, B. M., Buchardt, S. L., Clausen, H. B., Dahl-Jensen, D., Johnsen, S. J., Fisher, D. A., Koerner, R. M., Raynaud, D., Lipenkov, V., Andersen, K. K., Blunier, T., Rasmussen, S. O., Steffensen, J. P., and Svensson, A. (subm). Significant Holocene thinning if the Greenland ice sheet. Submitted for publication.

Vinther, B. M., Clausen, H. B., Johnsen, S. J., Rasmussen, S. O., Andersen, K. K., Buchardt, S. L., Dahl-Jensen, D., Seierstad, I. K., Siggaard-Andersen, M.-L., Steffensen, J. P., Svensson, A. M., Olsen, J., and Heinemeier, J. (2006). A synchronized dating of three Greenland ice cores throughout the Holocene. *Journal of Geophysical Research*, 111(D13102). doi:10.1029/2005JD006921.

Waelbroeck, C., Labeyrie, L., Michel, E., Duplessy, J. C., McManus, J. F., Lambeck, K., Balbon, E., and Labracherie, M. (2002). Sea-level and deep water temperature changes derived from benthic foraminifera isotopic records. *Quaternary Science Reviews*, 21:295–305.

Waite, A. H. (1959). Ice depth soundings with UHF radio waves in the Arctic and Antarctic and some observed over-ice altimeter errors. Technical Report 2092, US Army SRDL, Signals Research and Development Laboratory, Fort Monmouth, NJ.

Waite, A. H. and Schmidt, V. (1962). Gross errors in height indication from pulsed radar altimeters operating over thick ice or snow. *Proc. Inst. Radio Engineers*, 50(6):1515–1520.

Weertman, J. (1976). Sliding-no sliding zone effect and age determination of ice cores. *Quaternary Research*, 6(2):203–207.

Appendix A

Supplementary 1D modelling results

A.1 Site 1

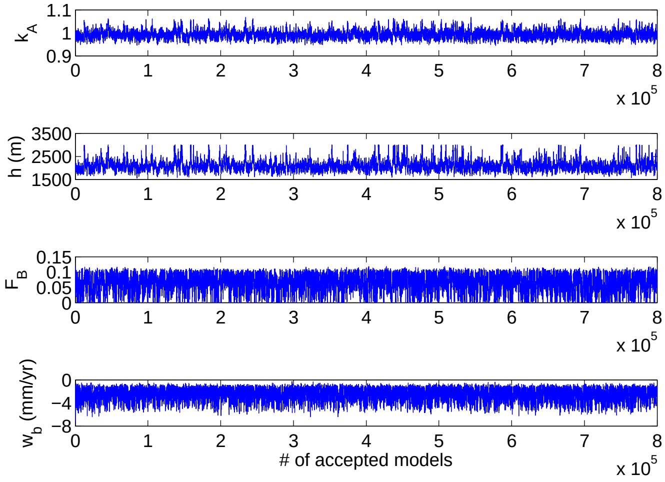

Figure A.1: Accepted values for the four unknown parameters for the 1D model at Site 1. The results were obtained using $\frac{\partial H}{\partial t} = 0$.

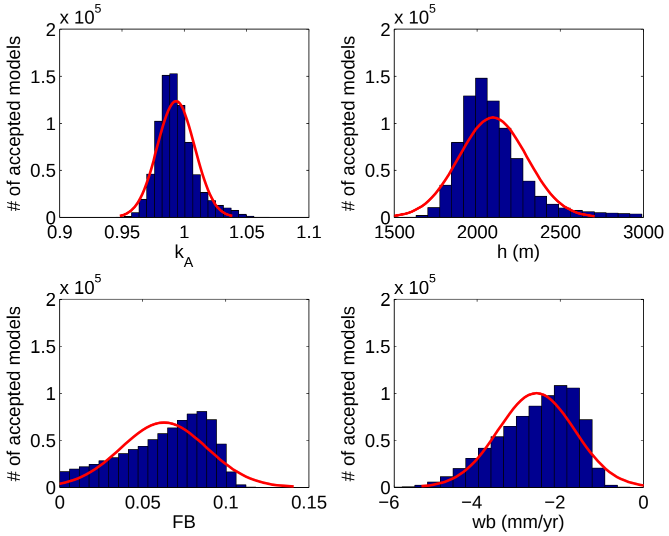

Figure A.2: Blue: Histogram of the parameter values for the accepted models at Site 1 after the burn-in period. Red: Gaussian distribution fitted to the accepted model parameters. These results were obtained using the 1D model with $\frac{\partial H}{\partial t} = 0$.

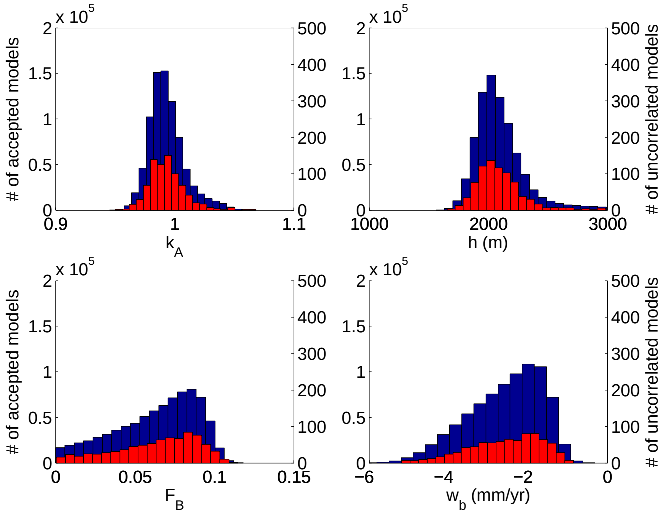

Figure A.3: Comparison of histograms for the parameter values for Site 1 for all the accepted models after the burn-in period (blue, left hand vertical axis) and those for only uncorrelated models (red, right hand vertical axis).

A.2 Site 2

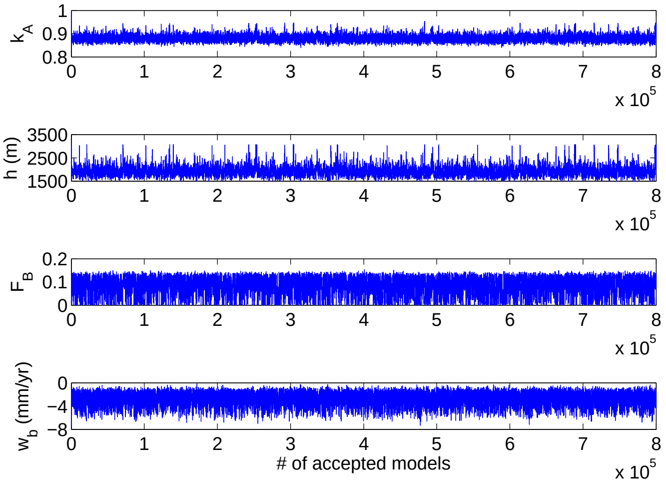

Figure A.4: Accepted values for the four unknown parameters for the 1D model at Site 2. The results were obtained using $\frac{\partial H}{\partial t} = 0$.

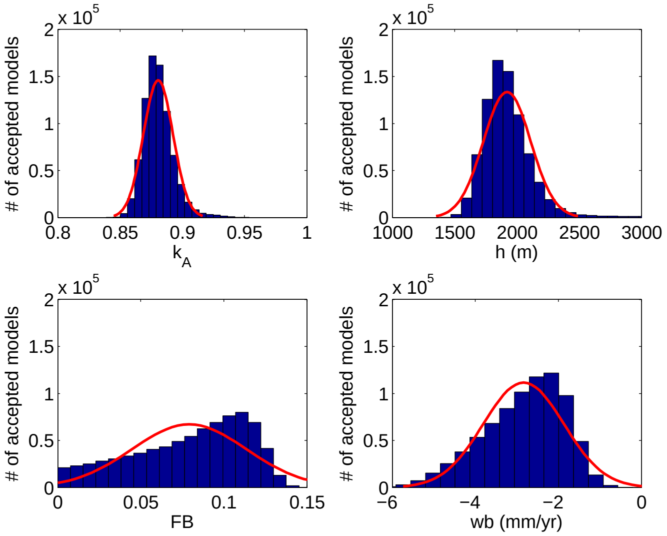

Figure A.5: Blue: Histogram of the parameter values for the accepted models at Site 2 after the burn-in period. Red: Gaussian distribution fitted to the accepted model parameters. These results were obtained using the 1D model with $\frac{\partial H}{\partial t} = 0$.

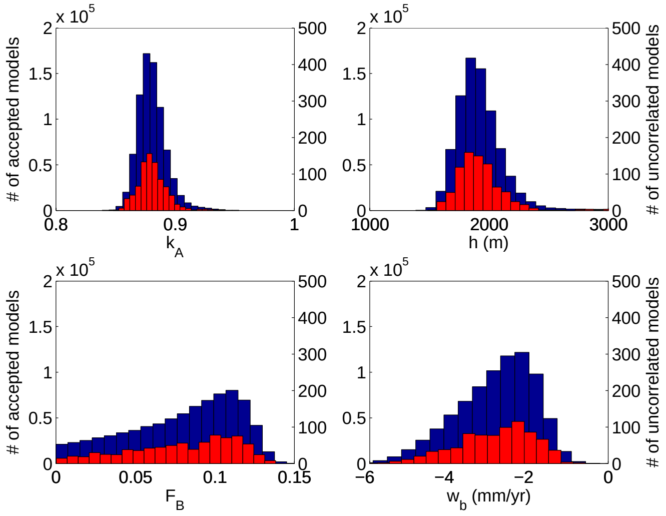

Figure A.6: Comparison of histograms for the parameter values for Site 2 for all the accepted models after the burn-in period (blue, left hand vertical axis) and those for only uncorrelated models (red, right hand vertical axis).

A.3 Site 3

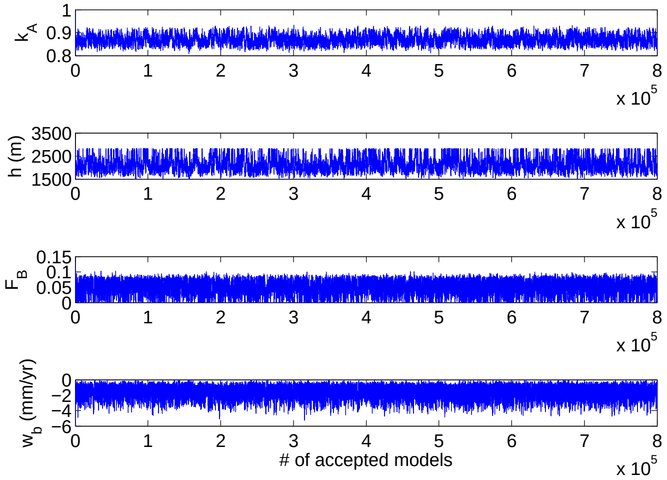

Figure A.7: Accepted values for the four unknown parameters for Site 3. These results were obtained using the 1D model with $\frac{\partial H}{\partial t} = 0$.

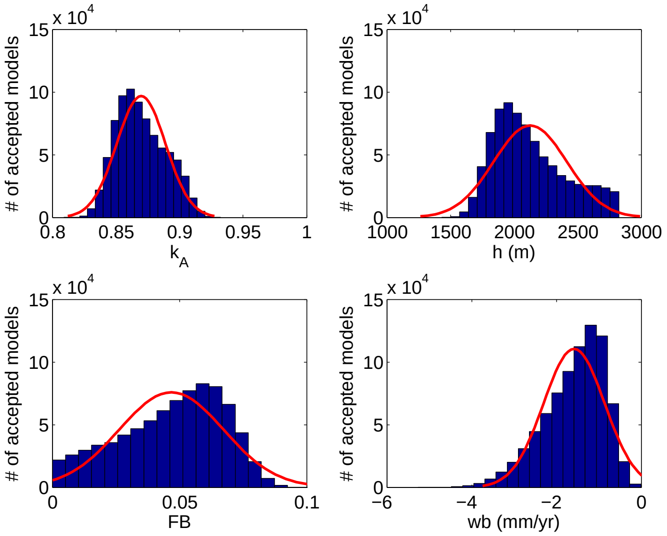

Figure A.8: Blue: Histogram of the parameter values for the accepted models at Site 3 after the burn-in period. Red: Gaussian distribution fitted to the accepted model parameters. These results were obtained using the 1D model with $\frac{\partial H}{\partial t} = 0$.

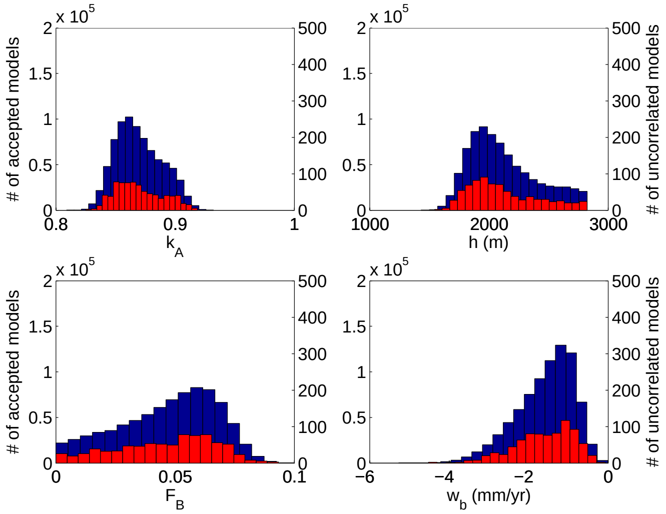

Figure A.9: Comparison of histograms for the parameter values for Site 3 for all the accepted models after the burn-in period (blue, left hand vertical axis) and those for only uncorrelated models (red, right hand vertical axis).

A.4 Site 4

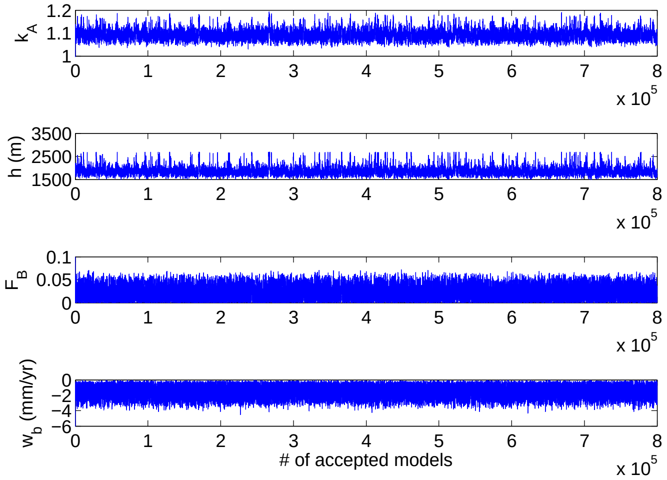

Figure A.10: Accepted values for the four unknown parameters for Site 4. These results were obtained using the 1D model with $\frac{\partial H}{\partial t} = 0$.

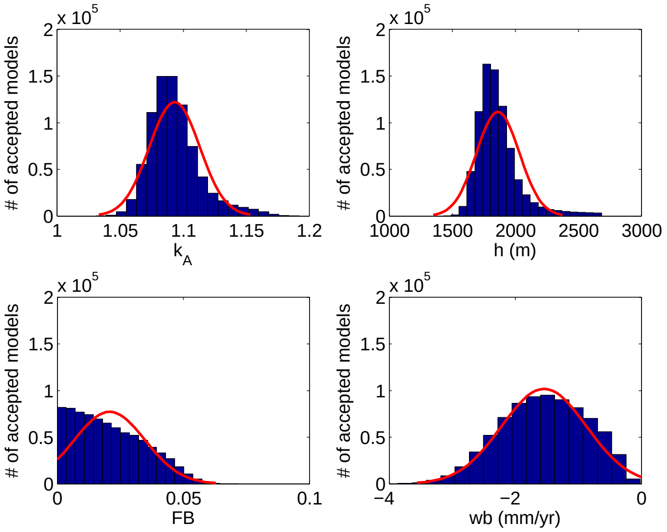

Figure A.11: Blue: Histogram of the parameter values for the accepted models at Site 4 after the burn-in period. Red: Gaussian distribution fitted to the accepted model parameters. These results were obtained using the 1D model with $\frac{\partial H}{\partial t} = 0$.

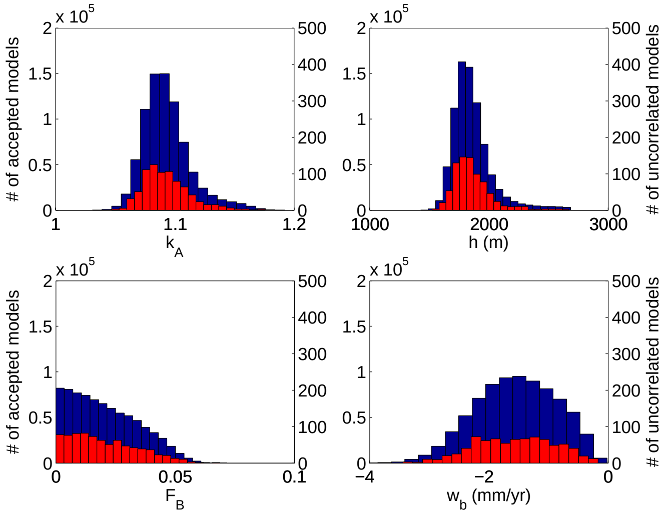

Figure A.12: Comparison of histograms for the parameter values for Site 4 for all the accepted models after the burn-in period (blue, left hand vertical axis) and those for only uncorrelated models (red, right hand vertical axis).

A.5 *dt*=25 yrs

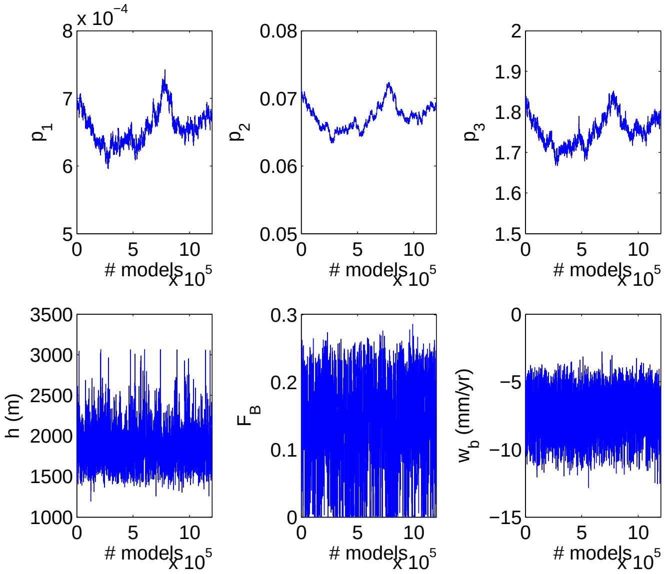

Figure A.13: Accepted values for the six unknown parameters for NorthGRIP using *dt*=25 yrs.

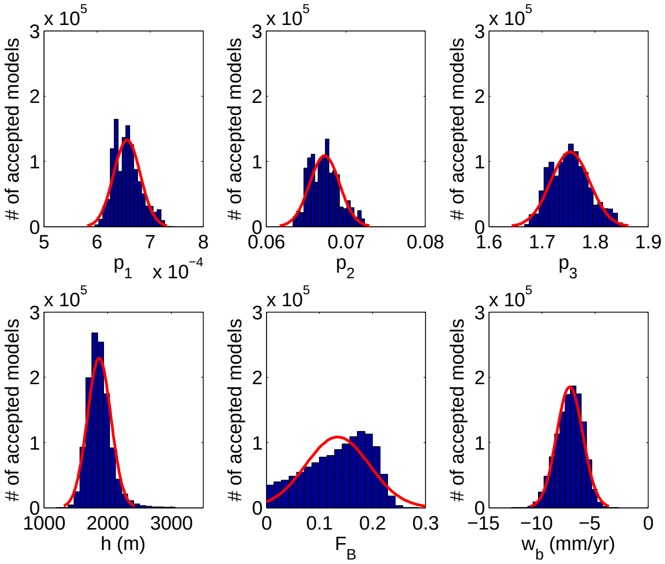

Figure A.14: Histograms for the accepted values after the burn-in period for *dt*=25 yrs in the forward model and a fitted normal distribution (red).

A.6 Including temporal changes in H

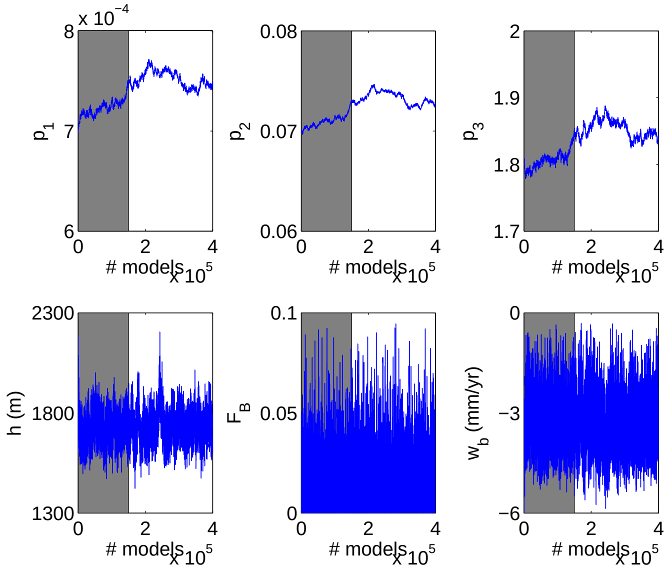

Figure A.15: Accepted values for the Monte Carlo parameters when using the data set from Greve (2005) to account for past changes in ice thickness. The burn-in period was determined to 150,000 accepted steps and is indicated in grey.

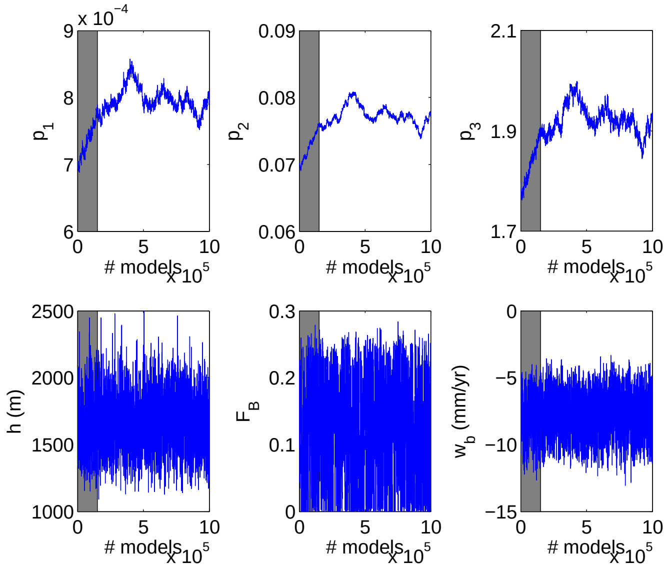

Figure A.16: Accepted values for the Monte Carlo parameters when using the data set from Vinther et al. (subm) to account for past changes in ice thickness. The burn-in period was determined to be 150,000 accepted steps and is indicated in grey.

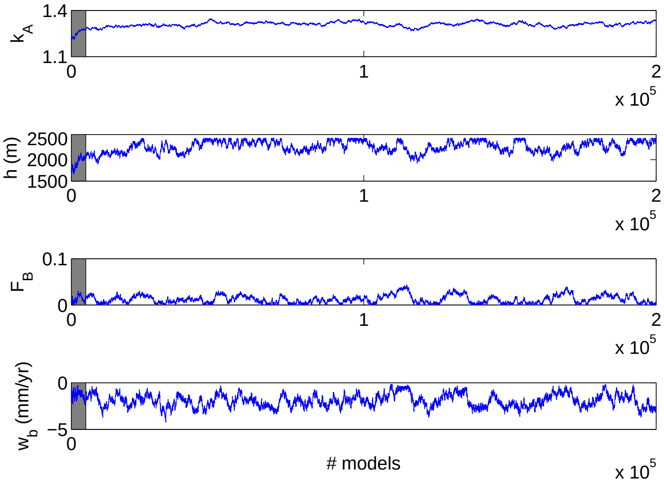

Figure A.17: Accepted values for the Monte Carlo parameters at NEEM when using the data set from Vinther et al. (subm) to account for past changes in ice thickness. The burn-in period of 5,000 accepted steps is indicated in grey.

Appendix B

Papers and manuscripts

Three papers that were prepared during the course of the PhD study are reproduced below. The first two are based on modelling studies similar to what is presented in this thesis, though a different accumulation model was used, and the inverse problem was constrain with different radar data. In the first paper, basal melt rates are inferred from radio-echo layers in the area upstream from NorthGRIP, while the second paper deals with the position of the Eemian at NEEM. Both papers are published in Annals of Glaciology:

Buchardt, S. L. and Dahl-Jensen, D. (2007). Estimating the basal melt rate at NorthGRIP using a Monte Carlo technique. *Annals of Glaciology*, 45:137–142. doi:10.3189/172756407782282435.

Buchardt, S. L. and Dahl-Jensen, D. (2008). At what depth is the Eemian layer expected to be found at NEEM? *Annals of Glaciology*, 48:100–102. doi:10.3189/172756408784700617.

The last paper infers past surface elevation changes at four drill sites in Greenland from isotopic studies. This paper has been submitted for publication:

Vinther, B. M., Buchardt, S. L., Clausen, H. B., Dahl-Jensen, D., Johnsen, S. J., Fisher, D. A., Koerner, R. M., Raynaud, D., Lipenkov, V., Andersen, K. K., Blunier, T., Rasmussen, S. O., Steffensen, J. P. and Svensson, A. (submitted). Significant Holocene thinning of the Greenland ice sheet.

Estimating the basal melt rate at NorthGRIP using a Monte Carlo technique

Susanne L. BUCHARDT, Dorthe DAHL-JENSEN

Ice and Climate, Niels Bohr Institute, University of Copenhagen, Juliane Maries vej 30, DK-2100 Copenhagen OE, Denmark
E-mail: lilja@gfy.ku.dk

ABSTRACT. From radio-echo sounding (RES) surveys and ice core data it can be seen that the ice sheet is melting at the base in a large area in Northern Greenland. The RES images reveal internal layers in the ice. The layers are former deposition surfaces and are thus isochrones. Undulations of the isochrones in regions where the base is smooth suggest that the basal melt rate changes over short distances. This indicates that the geothermal heat flux is very high and has large spatial variability in Northern Greenland. In this study, the basal melt rate at the NorthGRIP drill site in North-Central Greenland is calculated by inverse modelling. We use simple one- and two-dimensional flow models to simulate the ice flow along the NNW-trending ice ridge leading to NorthGRIP. The accumulation is calculated from a dynamical model. Several ice flow parameters are unknown and must be estimated along with the basal melt rate using a Monte Carlo method. The Monte Carlo inversion is constrained by the observed isochrones, dated from the timescale established for the NorthGRIP ice core. The estimates of the basal melt rates around NorthGRIP are obtained from both the one- and two-dimensional models. Combining the estimated basal melt rates with the observed borehole temperatures allows us to convert the basal melt rates to geothermal heat flow values. From the two-dimensional model we find the basal melt rate and geothermal heat flux at NorthGRIP to be 6.1 mm a^{-1} and 129 mW m^{-2}, respectively.

INTRODUCTION

The NorthGRIP (North Greenland Ice Core Project) ice core was drilled during 1996–2004 at 75.10° N, 42.32° W, 316 km NNW of the GRIP drill site in Central Greenland. The ice in the area flows along a NNW-trending ice ridge from GRIP towards NorthGRIP. The surface velocity at NorthGRIP is 1.3 m a^{-1} (Hvidberg and others, 2002), the ice thickness is 3090 m and the present mean annual temperature is –31.5°C. The aim of the drilling was to retrieve ice from the Eemian interglacial period 130–115 kyr ago. Before drilling was initiated, it was predicted that the Eemian layer would be found at depths of 2750–2850 m (Dahl-Jensen and others, 1997). However, as bedrock was approached it became evident that the ice was melting at the bottom. The basal layers did not thin as fast as was expected, and Eemian ice was not encountered until 80 m above bedrock (North Greenland Ice Core Project members, 2004). When it had been established that there is basal melting at NorthGRIP, it was concluded from radio-echo sounding (RES) images that the ice must be melting at the base in a large area in Northern Greenland. As the geothermal heat flux in the area is unknown, it is not straightforward to calculate the melt rate at NorthGRIP. Furthermore, the shape of the RES layers suggests that the melt rate varies significantly over short distances in the area (Dahl-Jensen and others, 2003). Using a Monte Carlo method to invert an ice flow model for the flow line from GRIP to NorthGRIP allows us to estimate the melt rates in the area around NorthGRIP.

MODELLING THE ICEFLOW

A Dansgaard-Johnsen model (Dansgaard and Johnsen, 1969) is used to simulate the ice flow along the flowline from GRIP to NorthGRIP. Both one- and two-dimensional approaches are used. For this purpose, a coordinate system is adopted with a horizontal x axis along the NNW-trending ice ridge in the direction of the flow at NorthGRIP, and a vertical z axis pointing upwards. The origin of this coordinate system is located at GRIP at sea level. This study has been concerned with a 104 km long section of the ridge starting 82 km upstream from NorthGRIP and ending 22 km downstream. Accounting for melting and sliding at the base, and assuming constant ice thickness with time, the horizontal velocity u and the vertical velocity w are given by

$$u = \begin{cases} u_{\mathrm{sur}} & z \in [h, H] \\ u_{\mathrm{sur}}\left(F_{\mathrm{B}} + (1 - F_{\mathrm{B}})\frac{z}{h}\right) & z \in [0, h], \end{cases} \tag{1}$$

and

$$w = \begin{cases} w_0 + \frac{\partial w_{\mathrm{sur}}}{\partial z}\left(z - \frac{1}{2}h(1 - F_{\mathrm{B}})\right) & z \in [h, H] \\ w_0 + \frac{\partial w_{\mathrm{sur}}}{\partial z}\left(F_{\mathrm{B}}z + \frac{1}{2}(1 - F_{\mathrm{B}})\frac{z^2}{h}\right) & z \in [0, h], \end{cases} \tag{2}$$

respectively. Here u_{sur} is the horizontal surface velocity, z the ice equivalent height above bedrock, $F_{\mathrm{B}} = u_{\mathrm{bed}}/u_{\mathrm{sur}}$ the fraction of basal sliding, H the ice thickness in ice equivalent and h is called the kink height. The vertical velocity at the base is w_0, and

$$\frac{\partial w_{\mathrm{sur}}}{\partial z} = -\frac{a + w_0}{H - \frac{1}{2}h(1 - F_{\mathrm{B}})} \tag{3}$$

where a is the annual ice equivalent accumulation. The basal melt rate w_{b} is given by $w_{\mathrm{b}} = -w_0$. The one-dimensional model is obtained by disregarding the horizontal movement, $u = 0$.

In the two-dimensional model, the basal melt rate is allowed to vary along the flowline, changing value every 4 km. The melt rate is considered constant within each of these 4 km intervals. In order to limit the number of parameters to be determined by the Monte Carlo inversion, the kink height h and the fraction of basal sliding F_{B} are

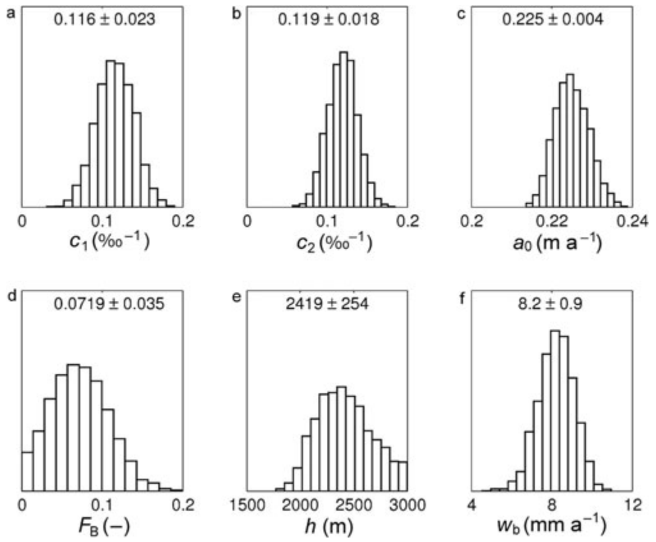

Fig. 1. Histograms of accepted values for parameters of the one-dimensional model; mean and standard deviation are displayed above each distribution. (a), (b) The relative slopes of the accumulation rate in warm (c_1) and cold (c_2) climate, respectively (Equation (8)). (c) The present ice equivalent accumulation rate at NorthGRIP a_0. (d) The fraction of basal sliding, F_B. (e) The kink height h from the Dansgaard-Johnsen model (Equations (1) and (2)). (f) The basal melt rate at NorthGRIP, w_b.

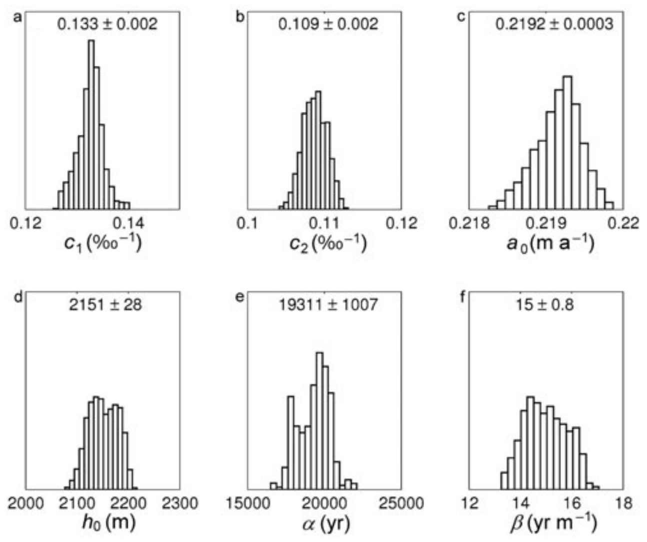

Fig. 2. Histograms of accepted values for parameters of the two-dimensional model (see Fig. 3 for the melt rates); mean and standard deviation are displayed above each distribution. (a), (b) The relative slopes of the accumulation rate in warm (c_1) and cold (c_2) climate, respectively. (c) The present ice equivalent accumulation rate at NorthGRIP a_0. (d), (e) The parameters h_0 and α linking the kink height to the melt rate (Equation (4)). (f) The link β between the fraction of bottom sliding and the basal melt rate (Equation (5)).

considered linear functions of the melt rate:

$$h = \alpha w_b + h_0 \tag{4}$$

$$F_B = \beta w_b. \tag{5}$$

Thus h and F_B also vary from one 4 km interval to another. Dahl-Jensen and others (1997) obtained estimates for the present accumulation rates along the flow line from shallow ice core studies. In the present work, it is assumed that the ratio of the accumulation rate at any point along the line to that at NorthGRIP is constant in time. Thus, the accumulation history at any point along the line can be inferred from the accumulation history at NorthGRIP $a(t)$ which is calculated from the accumulation model presented below.

The ice thickness at NorthGRIP is assumed to be constant in time in agreement with model results (Letréguilley and others, 1991; Marshall and Cuffey, 2000). All the parameters of the flow model except the accumulation rate a are thus assumed to be constant in time. α, β, h_0 and the value of w_b within each 4 km interval are unknown and will be estimated using a Monte Carlo inversion of the flow model.

THE ACCUMULATION MODEL

The accumulation history at the NorthGRIP drill site is calculated using a model of the same type as that used by Johnsen and others (1995) to date the GRIP ice core. The time-dependent ice equivalent accumulation rate $a(t)$ is calculated from the measured δ^{18}O values:

$$a(t) = a_0 \exp(R)$$

$$R = k_2\left(\delta^{18}\mathrm{O}(t) - \delta^{18}\mathrm{O_w}\right) + \frac{1}{2}k_1\left(\delta^{18}\mathrm{O}(t)^2 - \delta^{18}\mathrm{O_w^2}\right) \tag{6}$$

$$k_1 = \frac{c_1 - c_2}{\delta^{18}\mathrm{O_w} - \delta^{18}\mathrm{O_c}}; \qquad k_2 = c_1 - \delta^{18}\mathrm{O_w} k_1 \tag{7}$$

where a_0 is the present ice equivalent accumulation rate at NorthGRIP and $\delta^{18}\mathrm{O_w} = -35.2$‰ and $\delta^{18}\mathrm{O_c} = -42$‰ are typical δ^{18}O values for warm and cold climate at NorthGRIP, respectively. c_1 and c_2 denote the relative slopes of a in warm and cold climate, respectively, and are defined as

$$c_1 = \frac{1}{a}\frac{\partial a}{\partial \delta^{18}\mathrm{O}}\bigg|_{\delta^{18}\mathrm{O_w}}; \qquad c_2 = \frac{1}{a}\frac{\partial a}{\partial \delta^{18}\mathrm{O}}\bigg|_{\delta^{18}\mathrm{O_c}}. \tag{8}$$

The parameters a_0, c_1 and c_2 are found from the Monte Carlo inversion. The GICC05 timescale (Rasmussen and others, 2005; Vinther and others, 2006) is used for the δ^{18}O curve back to 42 kyr b2k (before 2000 AD), and further back in time the ss09sea timescale (Johnsen and others, 2001) is used. However, the ss09sea timescale has been shifted to agree with the GICC05 at 42 kyr b2k. The measured δ^{18}O values have been corrected for the changes in the isotopic composition of seawater due to the build up of ice on the continents during the glacial period (Waelbroeck and others, 2002).

MONTE CARLO INVERSION

In the one-dimensional model, the horizontal velocity is $u = 0$ and only the basal melt rate at NorthGRIP is included. Thus the kink height h and the fraction of basal sliding F_B are included directly as model parameters instead of α, h_0 and β (see Equations (4) and (5)). This reduces the number of model parameters to be determined by the Monte Carlo inversion to 6: c_1, c_2, a_0, F_B, h and w_b.

In the two-dimensional model, the basal melt rate w_b has 26 unknown values, one for each 4 km along the 104 km long flowline. Together with α, h_0 and β from Equations (4) and (5) and c_1, c_2 and a_0 of the accumulation model it adds up to a total of 32 unknown model parameters.

An observed data set exists $\boldsymbol{d}^{\mathrm{obs}}$ consisting of 20 internal layers identified in the RES images (Chuah and others, 1996; Dahl-Jensen and others, 1997; Gogineni and others, 1998,

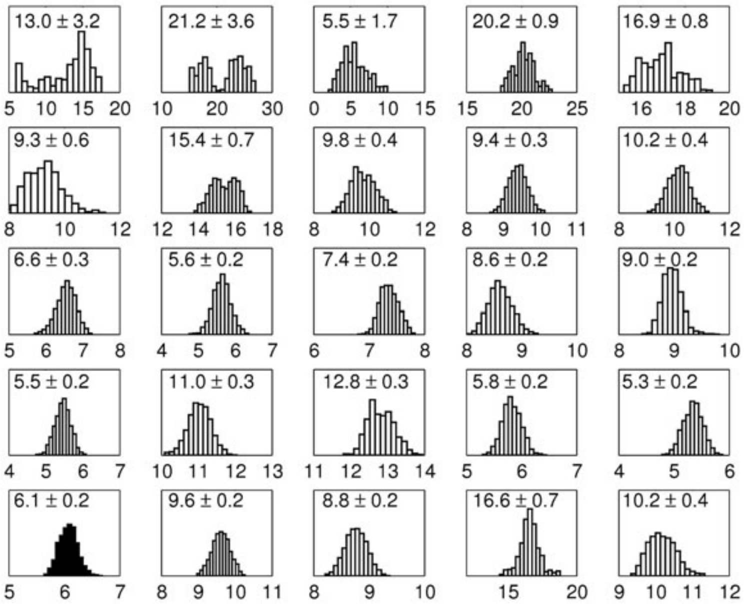

Fig. 3. Histograms of accepted values of the basal melt rate at 4 km intervals along the flow line. The measurements closest to GRIP are displayed at the top left, and those furthest from GRIP are at the lower right. The histogram for the interval containing NorthGRIP is shown in black. The units are mm a^{-1}.

2001; Fahnestock and others, 2001; Kanagaratnam and others, 2001). The layers are generally accepted to be isochrones. They have been dated from their depths (600–2700 m) in the NorthGRIP ice core using the same timescale as for the δ^{18}O record. This gives isochrone ages from 3.5–79.6 kyr. We will now use the ice flow model and the observed data to calculate the unknown model parameters as an inverse problem. Since the problem is highly nonlinear we turn to a Monte Carlo method in order to solve it. The model space is investigated through a random walk. For each step in the random walk, a modelled data set ***d(m)*** is created by running the forward flow model with the combination ***m*** of unknown model parameters. This is compared to the observed data set by calculating the misfit function *S*:

$$S(\boldsymbol{m}) = \frac{1}{2}\sum_i \sum_j \frac{\left(d_{ij}^{\mathrm{obs}} - d_{ij}\right)^2}{s_{ij}^2} \qquad (9)$$

where $i = 1$–20 as there are 20 isochrones and j runs through the 81 data points followed on each isochrone. s_{ij} denotes the uncertainty in a data point d_{ij}^{obs}. This uncertainty is given by the vertical resolution of the radar used to measure data. The starting point of the forward model is 79.6 kyr ago, since we do not have older isochrones to compare. The model is run to the present time in steps of 100 years. The likelihood function L is given by

$$L(\boldsymbol{m}) = k \exp\left(-S(\boldsymbol{m})\right) \qquad (10)$$

where k is a normalization constant. Each step of the random walk is accepted or rejected according to the Metropolis criterion

$$P_{\mathrm{accept}} = \min\left(1, \frac{L(\boldsymbol{m}_{\mathrm{test}})}{L(\boldsymbol{m}_{\mathrm{current}})}\right) \qquad (11)$$

where $\boldsymbol{m}_{\mathrm{current}}$ is the most recently accepted model and $\boldsymbol{m}_{\mathrm{test}}$ is the model being tested. It can be shown that this random walk samples the posterior probability density in the model space (Mosegaard and Tarantola, 1995). The final result is independent of the choice of initial values for the unknown model parameters.

RESULTS

One-dimensional inversion

The random walk in the model space was continued until a reasonable statistic was obtained. In the results presented here, 300 000 models were accepted. The distributions of the accepted values for each model parameter are shown in Figure 1. The mean and standard deviation for each distribution are displayed above the histograms. All distributions are seen to resemble Gaussian distributions, with strong single maxima. This means that the parameters are well defined by the Monte Carlo inversion.

The result for the melt rate at NorthGRIP is found to be 8.2 ± 0.9 mm a^{-1}. When the melt rate is known, the amount of heat used to melt the ice Q_{melt} can be calculated using the relation

$$Q_{\mathrm{melt}} = \rho w_{\mathrm{b}} L_{\mathrm{ice}} \qquad (12)$$

where ρ and L_{ice} are the density and latent heat of ice, respectively. The geothermal heat flux Q_{geo} is given by the sum of the amount of heat used to melt the ice and the amount of heat conducted through the ice Q_{ice}:

$$Q_{\mathrm{geo}} = Q_{\mathrm{melt}} + Q_{\mathrm{ice}}\,. \qquad (13)$$

Q_{ice} is determined from the gradient of the observed temperature profile $\partial T/\partial z$ at the base at NorthGRIP, i.e.

$$Q_{\mathrm{ice}} = -K\frac{\partial T}{\partial z} \qquad (14)$$

where K is the thermal conductivity of ice. Using $Q_{\mathrm{ice}} = 70\,\mathrm{mW\,m^{-2}}$ (North Greenland Ice Core Project members, 2004) and the basal melt rate found in this study, the geothermal heat flux at NorthGRIP is calculated to be 150 ± 12 mW m^{-2}.

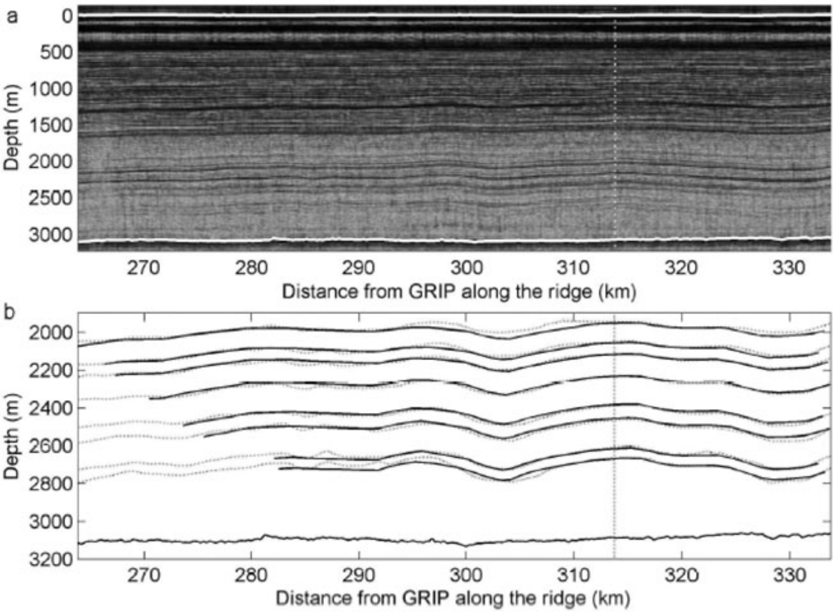

Fig. 4. (a) RES image collected along the ice ridge between GRIP and NorthGRIP. The surface and bedrock are shown in white. NorthGRIP is indicated by the vertical dotted line. (b) Comparison between observed (dotted) and modelled (solid) isochrones in the lower part of the ice sheet. The shown isochrones have been dated to 28.6, 34.6, 37.6, 44.7, 53.8, 59.7, 75.2 and 79.6 kyr b2k, respectively. The bedrock is shown in the bottom of the plot. The modelled isochrones are seen to reproduce the large-scale undulations of the observed isochrones. Higher accumulation rate and higher melt rate cause the isochrones to be located deeper in the ice sheet upstream (left) from the drill site.

Two-dimensional inversion

In this inversion, the full suite of 32 model parameters was determined. The random walk in the model space was continued until a reasonable statistic was obtained. In the results presented here, 250 000 models were accepted. The distributions of the accepted values for the model parameters are shown in Figures 2 and 3. The three parameters from the accumulation model (c_1, c_2 and a_0) are all well determined by the Monte Carlo inversion (Figs 2a–c), while the distributions for α and h_0 both show a double peak. The consequence is that the kink height h calculated from Equation (4) is not well determined by the inversion. However, the peaks are close together so the effect on the determination of the basal melt rates is small.

The basal melt rates are well determined for all the 4 km long intervals except the first five (see Fig. 3). The effect of basal melting on the internal layers increases with depth, so the deep layers are very important for the determination of the melt rates. Due to the horizontal movement of the ice, the modelled isochrones have moved out of the first intervals before they have reached great depths. As a consequence, the inversion has not had any constraints in the deep part of the ice for the first part of the line, and the melt rate estimates obtained for that area are badly constrained. The melt rate is seen to vary between $5.3 \pm 0.2\,\mathrm{mm\,a^{-1}}$ and $21.2 \pm 3.6\,\mathrm{mm\,a^{-1}}$ with the smallest value just upstream from the NorthGRIP drill site. The melt rate at NorthGRIP is found to be $6.1 \pm 0.2\,\mathrm{mm\,a^{-1}}$. This is considerably lower than the estimate obtained from the one-dimensional model. The higher melt rates upstream from the drill site pull the internal layers down before the ice reaches the NorthGRIP drill site. The one-dimensional model thus compensates for the upstream effect by over-estimating the melt rate.

Figure 4 shows a comparison between observed and modelled isochrones in the lower part of the ice sheet. It can be seen that the modelled isochrones successfully reproduce the large-scale variations of the observed isochrones.

Figure 5 shows a comparison between the shape of the lowest observed isochrone dated to 79.6 kyr b2k and the variation of the melt rate along the line. The two curves show very similar patterns, but the isochrone curve is shifted slightly to the right. The shift is caused by the horizontal flow velocity of the ice. The features created by the melt rate at a given place is carried with the ice along the line. This illustrates the advantage of using a two-dimensional model to simulate the ice flow.

Using Equations (12) and (13) and $Q_{\mathrm{ice}} = 70\,\mathrm{mW\,m^{-2}}$, the geothermal heat flux at NorthGRIP is determined to be $129 \pm 2\,\mathrm{mW\,m^{-2}}$. Both upstream and downstream from the drill site, significantly higher values of the geothermal heat flux are found.

DISCUSSION

The above stated uncertainties are the standard deviations of the histograms of accepted model values. They only reflect the precision with which the Monte Carlo inversion is able to determine the value of the parameters and do not include uncertainties arising from model deficiencies and assumptions. The total uncertainties of the parameters are therefore believed to be larger than the stated standard deviations.

The ratio between the accumulation rate at NorthGRIP and at other locations along the flow line was assumed constant in time. At present the ratio of the accumulation at NorthGRIP to that at GRIP is 83%, but Grinsted and Dahl-Jensen (2002) found that this ratio was as low as 66% during the glacial period. This indicates that the accumulation ratio at other places along the line may also have changed in time. Consequently, the assumption of unchanged accumulation pattern along the line with time may be poor. The

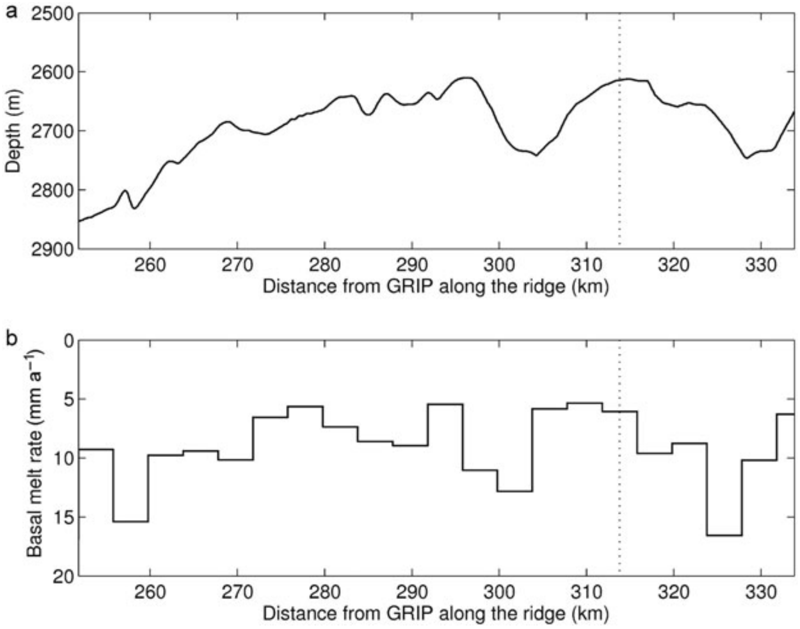

Fig. 5. (a) The lowest isochrone from the radar data set used in this study. (b) The melt rates along the line found from the Monte Carlo inversion. Notice the reversed melt rate axis. NorthGRIP is indicated by the dotted line.

results from Grinsted and Dahl-Jensen (2002) indicate that the accumulation pattern seen today in the area between GRIP and NorthGRIP was more pronounced during the glacial period. If this is the case, the accumulation rates used upstream from NorthGRIP in this model are slightly overestimated for the glacial period, resulting in an underestimation of the melt rates.

The fraction of basal sliding was assumed to be linearly related to the melt rate (Equation (5)). This is based on the premise that a higher melt rate will provide a larger amount of water to lubricate the bed and thus result in a larger sliding velocity. However, this assumption may not hold if the meltwater is drained from the area where it is produced e.g. through valleys or channels. Thus, in assuming Equation (5) is correct, we also assume that the meltwater does not move far from where it is produced.

This study aims to estimate the basal melt rate at NorthGRIP, yet we use a non-thermal model. This can be done because the basal melt rate equals minus the vertical velocity at the base of the ice sheet and thus can be treated as a flow law parameter. However, the melt rate depends on the temperature gradient at the base, which changes with time because the surface climate and therefore the temperature of the ice changes with time. Thus the melt rates found in this study may be considered as average values for the past 79.6 kyr.

Ice core studies have found values of 7 mm a^{-1} and 140 mW m^{-2} for the basal melt rate and geothermal heat flux at NorthGRIP (North Greenland Ice Core Project members, 2004). These values fall in between the values found from the two- and one-dimensional models, and considering the assumptions made in the model, the results found in this study do not disagree with those obtained from ice core studies.

CONCLUSIONS

The basal melt rate at NorthGRIP is found to be 8.2 mm a^{-1} using the one-dimensional model and 6.1 mm a^{-1} using the two-dimensional model. The difference between the two numbers illustrates the importance of using a two-dimensional model even though the computational time is significantly larger.

The basal melt rate is found to vary between 5.3 mm a^{-1} and 21.2 mm a^{-1} along the flowline. Assuming the variation is caused by geothermal heat flux variations, Q_{geo} varies between 121 mW m^{-2} and 231 mW m^{-2} over scales of 10 km. This requires the sources for the changes in geothermal heat flux to be located near the surface. Large spatial variations in the geothermal heat flux have also been reported by Näslund and others (2005). From studies of the Fennoscandian ice sheet during the Last Glacial Maximum they found significant local changes in the geothermal heat flux in Sweden and Finland. The values of the geothermal heat flux found in the present study are, however, quite high.

The drainage system of the meltwater created under the Greenland Ice Sheet is not well known. The water may be transported through small valleys observed in the bedrock topography. The presence of such canals may cause rapid spatial variations in the melt rate and is an alternative way of producing high local melt rates without strong changes in the geothermal heat flux. This is supported by the fact that dips in the isochrones are often observed over the small valleys in the bedrock.

REFERENCES

Chuah, T.S., S.P. Gogineni, C. Allen and B. Wohletz. 1996. *Radar thickness measurements over the northern part of the Greenland ice sheet. Technical Report.* 10470–3. Lawrence, KS, University of Kansas Center for Research Inc. Radar Systems and Remote Sensing Laboratory.

Dahl-Jensen, D. *and 9 others*. 1997. A search in north Greenland for a new ice-core drill site. *J. Glaciol.*, **43**(144), 300–306.

Dahl-Jensen, D., N. Gundestrup, S.P. Gogineni and H. Miller. 2003. Basal melt at NorthGRIP modeled from borehole, ice-core and radio-echo sounder observations. *Ann. Glaciol.*, **37**, 207–212.

Dansgaard, W. and S.J. Johnsen. 1969. A flow model and a time scale for the ice core from Camp Century, Greenland. *J. Glaciol.,* **8**(53), 215–223.

Fahnestock, M., W. Abdalati, I. Joughin, J. Brozena and P. Gogineni. 2001. High geothermal heat flow, basal melt, and the origin of rapid ice flow in central Greenland. *Science,* **294**(5550), 2338–2342.

Gogineni, S., T. Chuah, C. Allen, K. Jezek and R.K. Moore. 1998. An improved coherent radar depth sounder. *J. Glaciol.,* **44**(148), 659–669.

Gogineni, S. *and 9 others*. 2001. Coherent radar ice thickness measurements over the Greenland ice sheet. *J. Geophys. Res.,* **106**(D24), 33,761–33,772.

Grinsted, A. and D. Dahl-Jensen. 2002. A Monte Carlo-tuned model of the flow in the NorthGRIP area. *Ann. Glaciol.,* **35**, 527–530.

Hvidberg, C.S., K. Keller and N.S. Gundestrup. 2002. Mass balance and ice flow along the north-northwest ridge of the Greenland ice sheet at NorthGRIP. *Ann. Glaciol.,* **35**, 521–526.

Johnsen, S.J., D. Dahl-Jensen, W. Dansgaard and N.S. Gundestrup. 1995. Greenland paleotemperatures derived from GRIP borehole temperature and ice core isotope profiles. *Tellus,* **47B**(5), 624–629.

Johnsen, S.J. *and 8 others*. 2001. Oxygen isotope and palaeotemperature records from six Greenland ice-core stations: Camp Century, Dye-3, GRIP, GISP2, Renland and NorthGRIP. *J. Quat. Sci.,* **16**(4), 299–307.

Kanagaratnam, P., S.P. Gogineni, N. Gundestrup and L. Larsen. 2001. High-resolution radar mapping of internal layers at the North Greenland Ice Core Project. *J. Geophys. Res.,* **106**(D24), 33,799–33,811.

Letréguilly, A., N. Reeh and P. Huybrechts. 1991. The Greenland ice sheet through the last glacial-interglacial cycle. *Palaeogeogr., Palaeoclimatol., Palaeoecol.,* **90**(4), 385–394.

Marshall, S.J. and K.M. Cuffey. 2000. Peregrinations of the Greenland ice sheet divide in the last glacial cycle: implications for central Greenland ice cores. *Earth Planet Sci. Lett.,* **179**(1), 73–90.

Mosegaard, K. and A. Tarantola. 1995. Monte Carlo sampling of solutions to inverse problems. *J. Geophys. Res.,* **100**(B7), 12,431–12,447.

North Greenland Ice Core Project members. 2004. High-resolution record of Northern Hemisphere climate extending into the last interglacial period. *Nature,* **431**, 147–151.

Näslund, J.-O., P. Jansson, J.L. Fastook, J. Johnson and L. Andersson. 2005. Detailed spatially distributed geothermal heat-flow data for modeling of basal temperatures and meltwater production beneath the Fennoscandian ice sheet. *Ann. Glaciol.,* **40**, 95–101.

Rasmussen, S.O. *and 15 others*. 2006. A new Greenland ice core chronology for the last glacial termination. *J. Geophys. Res.,* **111**, D06102. (10.1029/2005JD006079.)

Vinther, B.M. *and 12 others*. 2006. A synchronized dating of three Greenland ice cores throughout the Holocene. *J. Geophys. Res.,* **111**, D13102. (10.1029/2005JD006921.)

Waelbroeck, C. *and 7 others*. 2002. Sea-level and deep water temperature changes derived from benthic foraminifera isotopic records. *Quat. Sci. Rev.,* **21**(1–3), 295–305.

At what depth is the Eemian layer expected to be found at NEEM?

Susanne L. BUCHARDT, Dorthe DAHL-JENSEN

Ice and Climate, Niels Bohr Institute, University of Copenhagen, Juliane Maries Vej 30, DK-2100 Copenhagen, Denmark
E-mail: lilja@gfy.ku.dk

ABSTRACT. No continuous record from Greenland of the Eemian interglacial period (130–115 ka BP) currently exists. However, a new ice-core drill site has been suggested at 77.449° N, 51.056° W in northwest Greenland (North Eemian or NEEM). Radio-echo sounding images and flow model investigations indicate that an undisturbed Eemian record may be obtained at NEEM. In this work, a two-dimensional ice flow model with time-dependent accumulation rate and ice thickness is used to estimate the location of the Eemian layer at the new drill site. The model is used to simulate the ice flow along the ice ridge leading to the drill site. Unknown flow parameters are found through a Monte Carlo analysis of the flow model constrained by observed isochrones in the ice. The results indicate that the Eemian layer is approximately 60 m thick and that its base is located approximately 100 m above bedrock.

INTRODUCTION

Ice from the Eemian period (130–115 ka BP) was found in the central Greenland ice cores (GRIP (Greenland Icecore Project) and GISP2 (Greenland Ice Sheet Project 2)) as well as in the NorthGRIP (North Greenland Icecore Project) ice core. The early part of the Eemian layer was, however, gone in the latter due to a high basal melt rate, and in the central Greenland cores the stratigraphy was broken in the bottom 10% of the cores due to flow over an uneven bed. An undisturbed record of the full Eemian period has therefore not yet been obtained from Greenland. A new ice-core drill site, NEEM (North Eemian), has been suggested at 77.449° N, 51.056° W in northwest Greenland, and drilling is planned to begin in 2008. The NEEM drilling project is an international effort with 14 participating nations, and its main purpose is to retrieve a continuous record of the whole Eemian interglacial.

The new drill site is located 365 km downstream from NorthGRIP on the ice ridge that runs north-northwest from GRIP via NorthGRIP towards Camp Century (see Fig. 1). The altitude at NEEM is 2447 m and radar investigations indicate an ice thickness of 2561 m. The accumulation rate and surface velocity are not well known but they are expected to be somewhat larger than at NorthGRIP since NEEM is located further out on the flank at lower altitude and with steeper surface slope. From radio-echo sounding (RES) images it is seen that the very smooth bed found around NorthGRIP does not extend all the way to the NEEM drill site. However, the bedrock undulations at NEEM are on a much smaller scale than at GRIP, so there is no immediate reason to suspect folding of the deep layers. The location of the drill site for the new ice core was selected from studies of the internal structure of the ice, as seen on RES images. The Eemian layer is located too deep in the ice to show up in the existing RES images, but the shape of the younger internal layers indicates that Eemian ice is located relatively high above the bed at NEEM. A modelling effort is needed in order to predict the depth and thickness of the Eemian layer.

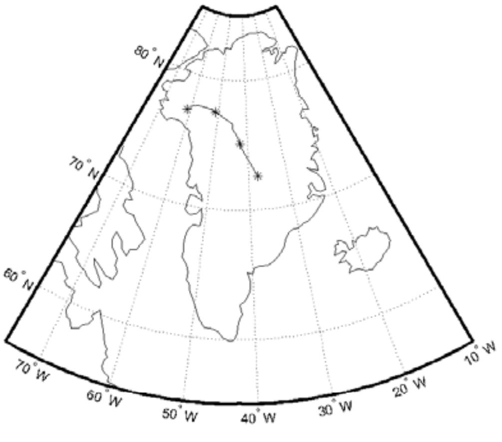

Fig. 1. Map of Greenland with indicated drill sites along the ice ridge in northwest Greenland. Starting from the south and moving along the flowline the drill sites are: GRIP, NorthGRIP, NEEM and Camp Century.

RADAR DATA

Large parts of the Greenland ice sheet have been investigated with airborne radio-echo sounders by the Center for Remote Sensing of Ice Sheets, University of Kansas, USA (Chuah and others, 1996). The RES images show the ice surface, the ice–bedrock interface and internal layers in the ice. Individual internal layers can be followed over hundreds of kilometres and are generally accepted as isochrones. The shape of the isochrones reveals information about the ice dynamics, especially the basal melt rate. Undulations which increase with depth are an indication of spatially changing basal melt rates. In an area with a high basal melt rate, the isochrones will be pulled down faster than in areas with low or no basal melting.

In order to constrain a Monte Carlo analysis of the inverse problem presented below, we need a dated set of observed isochrones. Twelve layers have been traced from NorthGRIP to NEEM in the RES images. The layers are dated from their depths in the NorthGRIP ice core, and their ages fall between 3.6 and 79.8 ka. The two deepest isochrones are very faint in the RES images, and in some areas they are impossible to trace. However, the visible parts of these two layers are included, as it is crucial to have deep constraints on the Monte Carlo analysis.

MODELLING

Forward model

A 224 km long section along the north-northwest-trending ice ridge is considered, and a model approach similar to that used by Buchardt and Dahl-Jensen (2007) is taken. The ice flow along the ice ridge is therefore simulated using a two-dimensional Dansgaard–Johnsen model (Dansgaard and Johnsen, 1969) that accounts for basal melting and sliding. The model requires surface velocity u_{sur}, ice thickness H, accumulation rate a, basal melt rate w_{b}, kink height h and the ratio of basal sliding velocity to surface velocity F_{B} as input. The horizontal velocity u and the vertical velocity w are calculated as

$$u = \begin{cases} u_{\mathrm{sur}} & z \in [h, H] \\ u_{\mathrm{sur}}\left(F_{\mathrm{B}} + (1 - F_{\mathrm{B}})\dfrac{z}{h}\right) & z \in [0, h] \end{cases} \tag{1}$$

and

$$w = \begin{cases} \dfrac{\partial w_{\mathrm{sur}}}{\partial z}\left(z - \dfrac{1}{2}h(1 - F_{B})\right) - w_{\mathrm{b}} & z \in [h, H] \\ \dfrac{\partial w_{\mathrm{sur}}}{\partial z}\left(F_{\mathrm{B}}z + \dfrac{1}{2}(1 - F_{\mathrm{B}})\dfrac{z^2}{h}\right) - w_{\mathrm{b}} & z \in [0, h] \end{cases}, \tag{2}$$

where z is the ice equivalent height above bedrock and

$$\frac{\partial w_{\mathrm{sur}}}{\partial z} = \frac{w_{\mathrm{b}} - a}{H - \frac{1}{2}h(1 - F_{\mathrm{B}})}. \tag{3}$$

All parameters are allowed to vary horizontally, whereas temporal changes are only considered for H and a.

The spatial variation in H is known from radar surveys (Chuah and others, 1996), and the temporal changes are calculated using the SICOPOLIS (SImulation COde for POLythermal Ice Sheets) ice-sheet model for Greenland (Greve, 2005). The accumulation rates in the area are not well known. Accumulation rate values along the ice ridge are inferred from Ohmura and Reeh (1991) but tuned to match the known values at the drill sites. The accumulation maps from Ohmura and Reeh (1991) are based on interpolations between measurements with a coarser resolution than optimal for use in this study. We therefore wish to allow for the possibility that the overall pattern with low values in the centre of the ice sheet and higher values closer to the coast is more pronounced in the area of study than suggested by the current dataset. This is done by adding to the data a contribution that grows linearly with the distance from NorthGRIP (where the accumulation rate is well determined). The speed γ with which the contribution grows with distance is left to be determined from the Monte Carlo analysis.

The accumulation history is calculated from the dated δ^{18}O record from NorthGRIP using a model similar to that developed by Johnsen and others (1995). We therefore have high accumulation in warm periods and low in cold periods. It is assumed that the ratio of the accumulation rate at any point along the line to that at NorthGRIP is constant in time. The oldest ice found in the NorthGRIP ice core has been dated to 123 ka. When starting the forward model before this time, the glacial index from Greve (2005) is used to scale the accumulation further back in time.

The surface velocities in the area around NEEM are not known. However, from empirical studies of the area around NorthGRIP where a strain net was established, a linear relationship between surface slope and along-ridge surface velocities has been found. Therefore, the value of u_{sur} is in this work calculated as a linear function of the observed surface slope, i.e.

$$u_{\mathrm{sur}} = C\frac{\mathrm{d}S}{\mathrm{d}x}, \tag{4}$$

where C is a constant and $\mathrm{d}S/\mathrm{d}x$ is the surface slope. The value of C is chosen so that the calculated surface velocity at NorthGRIP matches the observed value of 1.3 m a^{-1} (Hvidberg and others, 2002). At all times, the value of u_{sur} calculated as above is scaled with the factor $a(t)/a_0$ to compensate for the changes in accumulation rate.

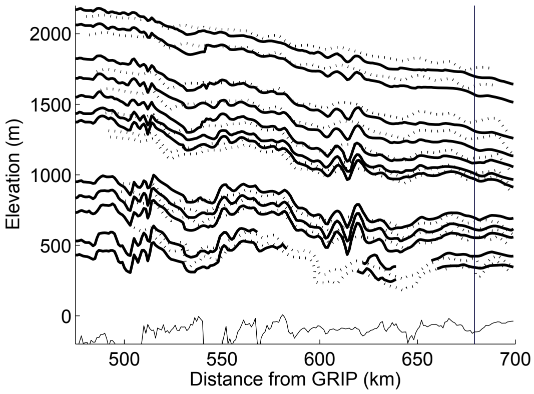

Fig. 2. Observed (solid lines) and modelled (dotted lines) isochrones. The NEEM drill site is indicated by the vertical line.

The value of w_{b} is allowed to change for every 8 km, giving rise to 28 different unknown values along the section. The kink height h and the fraction of basal sliding F_{B} are tied linearly to the melt rate to restrict the number of unknowns (Buchardt and Dahl-Jensen, 2007).

To investigate the importance of including the temporal changes of H, the model is also run with $\mathrm{d}H/\mathrm{d}t = 0$ for comparison.

Solving the inverse problem

Thirty-four parameters from the forward model are unknown and must be determined from a Monte Carlo analysis. The forward model is run several hundred thousand times with various combinations of values for the model parameters. After each run, the fit between observed isochrones and isochrones calculated by the forward model is used to decide whether the used model parameters should be accepted or rejected. The values of the model parameters are changed between each run by using random numbers (a random walk in the model space). By examining the statistical properties of the accepted values for the model parameters, best estimates for these 34 unknown parameters can be inferred. A more thorough description of the Metropolis algorithm used to solve this problem is given by Buchardt and Dahl-Jensen (2007).

RESULTS AND DISCUSSION

Time-dependent ice thickness

The fit between the observed and the modelled isochrones is satisfactory. The modelled isochrones recreate the overall shape of those observed (Fig. 2). About 50 km upstream from NEEM, the observed isochrones display high-amplitude undulations. These variations happen over too short a distance

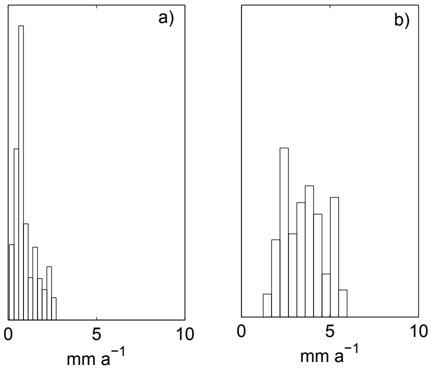

Fig. 3. Histogram of accepted values for the melt rate (a) in the interval at NEEM and (b) 75 km upstream from NEEM, where there are no data for the lowest two isochrones. In (a), the histogram shows a single maximum, so the melt rate in this interval is well defined by the solution. However, it can be seen that the solution in (b) does not provide a well-defined value for the melt rate.

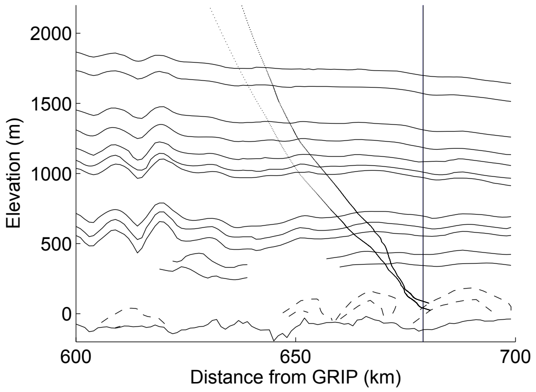

Fig. 4. Observed isochrones (solid lines) and modelled top and base of the Eemian layer (dashed lines) calculated from the model with time-dependent ice thickness. The dotted lines show the paths that the top and the base of the Eemian layer at NEEM have taken through the ice. The NEEM drill site is indicated by the vertical line.

to be resolved by the model, which has melt rate intervals 8 km long.

Most model parameters are well defined by the Monte Carlo analysis, i.e. the histograms of the accepted values for the parameters resemble Gaussian distributions. Only the melt rate values in the intervals where there are no data for the two deepest isochrones are not well defined. In these intervals, the distributions for the accepted values for the melt rate are broader and do not show a clear single maximum (Fig. 3). This illustrates the importance of including deep isochrones if information on the melt rate is required.

The melt rate at NEEM is found to be $1.0 \pm 0.6\,\mathrm{mm\,a^{-1}}$. However, about 50 km upstream from the drill site where the observed layers show undulations of a very high amplitude, values of almost $11\,\mathrm{mm\,a^{-1}}$ are found. Using the value of γ found from the Monte Carlo analysis, we find the accumulation rate at NEEM to be $0.26\,\mathrm{m\,a^{-1}}$.

Running the forward model with the parameter estimates found from this analysis results in a modelled Eemian layer of 60 ± 10 m thickness located 100 ± 40 m above bedrock at NEEM (Fig. 4). The age of the ice at the base is estimated to be around 200 ka. Eemian ice has been transported approximately 50 km along the ice ridge since deposition. It is therefore not likely that the Eemian layer has been significantly affected by the higher melt rates in the previously mentioned area with large undulations of the isochrones.

Constant ice thickness

The general observations regarding fit and well-determined parameters for the model with constant ice thickness are the same as for the analysis of the model with time-dependent ice thickness. The thickness of the Eemian layer is found to be 75 ± 10 m and the base of the layer is found to be located 150 ± 40 m above bedrock. The accumulation rate in this case is found to be $0.27\,\mathrm{m\,a^{-1}}$ and the melt rate is $1.0 \pm 0.5\,\mathrm{mm\,a^{-1}}$.

In the upper part of the ice sheet, solving both inverse problems results in modelled isochrones that are too shallow close to NEEM and too deep upstream from the drill site (Fig. 2). A possible cause for this is that the accumulation pattern used in the model may not be a good estimate of the true accumulation pattern. Furthermore, changes over time in the accumulation pattern are not accounted for in the model but may have significantly influenced the shape of the observed isochrones.

CONCLUSION

Both models indicate that a full record of the Eemian period can be obtained at NEEM, and both models predict the layer to be located well above bedrock. The model with time-dependent ice thickness predicts an Eemian layer of 60 ± 10 m; the model with constant ice thickness over time predicts a thickness of 75 ± 10 m. Both solutions indicate basal ice of an age of at least 200 ka. The melt rate at NEEM is estimated to be 1 mm with an uncertainty of around 0.5 mm. This is good news for the drilling project, since a small melt rate keeps the layer thickness at the base larger than if there is no melting.

REFERENCES

Buchardt, S.L. and D. Dahl-Jensen. 2007. Estimating the basal melt rate at NorthGRIP using a Monte Carlo technique. *Ann. Glaciol.*, **45**, 137–142.

Chuah, T.S., S.P. Gogineni, C. Allen and B. Wohletz. 1996. Radar thickness measurements over the northern part of the Greenland ice sheet. Lawrence, KS. University of Kansas Center for Research Inc. Radar Systems and Remote Sensing Laboratory. (Technical Report. 10470-3.)

Dansgaard, W. and S.J. Johnsen. 1969. A flow model and a time scale for the ice core from Camp Century, Greenland. *J. Glaciol.*, **8**(53), 215–223.

Greve, R. 2005. Relation of measured basal temperatures and the spatial distribution of the geothermal heat flux for the Greenland ice sheet. *Ann. Glaciol.*, **42**, 424–432.

Hvidberg, C.S., K. Keller and N.S. Gundestrup. 2002. Mass balance and ice flow along the north-northwest ridge of the Greenland ice sheet at NorthGRIP. *Ann. Glaciol.*, **35**, 521–526.

Johnsen, S.J., D. Dahl-Jensen, W. Dansgaard and N.S. Gundestrup. 1995. Greenland paleotemperatures derived from GRIP borehole temperature and ice core isotope profiles. *Tellus B*, **47**(5), 624–629.

Ohmura, A. and N. Reeh. 1991. New precipitation and accumulation maps for Greenland. *J. Glaciol.*, **37**(125), 140–148.

Significant Holocene thinning of the Greenland ice sheet

B. M. Vinther[1], S. L. Buchardt[1], H. B. Clausen[1], D. Dahl-Jensen[1], S. J. Johnsen[1], D. A. Fisher[2], R. M. Koerner[2*], D. Raynaud[3], V. Lipenkov[4], K. K. Andersen[1], T. Blunier[1], S. O. Rasmussen[1], J. P. Steffensen[1] and A. M. Svensson[1]

[1] *Centre for Ice and Climate, Niels Bohr Institute, University of Copenhagen, Juliane Maries Vej 30, DK-2100 Copenhagen Oe, Denmark.*

[2] *Glaciology Section, Terrain Sciences Division, Geological Survey of Canada, 601 Booth Street, Ottawa, ON, Canada K1A 0E8.*

[3] *Laboratoire de Glaciologie et Géophysique de l'Environnement, CNRS/UJF, BP 96, 38402 Saint-Martin-d'Hères, France.*

[4] *Arctic and Antarctic Research Institute, 38 Bering street, St. Petersburg 199397, Russia.*

[*] Deceased.

Entering an era of global warming, the stability of the Greenland ice sheet (GIS) is a major concern[1], especially in the light of new evidence of rapidly changing flow and melt conditions at the GIS margins[2]. Hence it is imperative to advance our understanding of GIS dynamics by studying the response of the GIS to past climatic change. In this study we extract both the Holocene Greenland temperature history and the evolution of GIS surface elevation at four GIS locations. We achieve this by comparing water stable isotope data ($\delta^{18}O$) from GIS

ice cores[3,4] to ice core data from small marginal ice caps. Results are corroborated by ice core air content, a proxy for surface elevation[5]. Contrary to existing temperature estimates derived from GIS ice core stable isotope records only[6], the new temperature history reveals a pronounced Greenland Holocene climatic optimum coinciding with maximum thinning near the GIS margins. State of the art ice sheet models are generally found to be lacking in their ability to reproduce GIS response to the Holocene climate.

Ice cores from six locations[3,7] have now been synchronized to the Greenland Ice Core Chronology 2005 (GICC05) throughout the Holocene (see Fig. 1a). The GICC05 annual layer counting was performed simultaneously on the DYE-3, GRIP and NGRIP ice cores for the entire Holocene[8,9]. For the Agassiz[10], Renland[10] and the Camp Century ice cores the time scale has been transferred using volcanic markers identifiable in Electrical Conductivity Measurements[11] (see supplementary information). The six synchronized Holocene $\delta^{18}O$ records show large differences in millennial scale trends (Fig 1b). All $\delta^{18}O$ records have been obtained in the same laboratory (Copenhagen Isotope Laboratory), assuring maximum confidence in the homogeneity of the data sets. The differences are thus real features that need to be understood and explained before firm conclusions about the evolution of Greenland climate during the Holocene can be supported by these data.

Changes in regional temperatures, moisture source regions, moisture transport and precipitation seasonality affect the $\delta^{18}O$ of precipitation[6]. All these parameters are, however, expected to produce regional patterns of change, implying that trends in nearby $\delta^{18}O$ records should always be similar, except where the records are heavily influenced by a combination of ice flow and post-deposition phenomena, such as wind-scouring. Ice cores from Agassiz and Renland are retrieved from ice cap domes and are thus not influenced by ice flow. The Camp Century site is only slightly affected by a steady ice flow, and yet the trends in the neighbouring Agassiz and Camp Century cores are dissimilar, in fact Agassiz δ^{18}O is much more similar to the signal recorded at Renland on the other side of the GIS.

Given the dissimilarity of some neighboring δ^{18}O records, a more likely cause of the differences in δ^{18}O trends is past changes in the elevation of the GIS. Elevation change will influence trends in the δ^{18}O records (see supplementary information), and the differences in the long term δ^{18}O trends do appear to be related to changing GIS elevation: The records from the centre of the ice sheet (GRIP and NGRIP), the records closer to the margin of the ice sheet (DYE-3 and Camp Century), and the records from the small ice caps close to the GIS (Agassiz and Renland) are all pair wise similar.

For the GIS ice core records, the hypothesis that elevation change affected the δ^{18}O of the past is difficult to evaluate, as little is known of the GIS elevation history. Ice sheet modelling is of little help because modelled elevation histories for GIS are highly dependent on poorly known boundary conditions, such as the past positions of the GIS margin[12]. For the small Agassiz and Renland ice caps, it is, however, possible to reconstruct past elevation histories with some confidence. Neither of these ice caps are believed to have experienced significant changes in ice sheet thickness during most of the Holocene due to topographical constraints and the limited thickness of the ice caps[7,13] (see supplementary information). Both the Renland and the Agassiz bedrocks have experienced a significant post-glacial uplift. For Renland the uplift resulted from the retreat of the GIS, whereas the Agassiz uplift was caused by the disintegration of the

Innuitian ice sheet that covered most of the Queen Elizabeth Islands (QEI) during the last glaciation[14]. For both locations robust estimates of bedrock elevation have been obtained through studies of past sea level changes in nearby fiords[14,15]. The Renland bedrock elevation history is based on such studies throughout the Holocene, whereas the Agassiz bedrock elevation history is based on data sets back to 9.5 ka. For the period from 9.5 ka back to 11.7 ka Agassiz bedrock elevation can be estimated by extrapolation, using the observed exponential half-life for the bedrock elevation change in the 0-9.5 ka period[16]. Assuming that Agassiz and Renland δ^{18}O records have not been significantly influenced by changes in ice thickness during the Holocene, it is possible to correct the δ^{18}O records for past elevation changes, simply by using their respective bedrock elevation histories and the observed Greenland δ^{18}O-height relationship (see Fig. 1c, 1d and supplementary information).

The similarity between the uplift corrected Agassiz and Renland δ^{18}O records is astounding given that the two ice caps are separated by some 1500 kilometres and by the entire GIS. The similarity suggests that Greenland climate during the Holocene was homogenous with the same millennial scale δ^{18}O evolution both east and north-west of the ice sheet. The homogeneous climatic history for the Greenlandic region is probably related to the regional change in solar insolation[17], at least for the past 10 ka.

Given the similarity of the Agassiz and Renland elevation-corrected δ^{18}O records, we assume that their common millennial scale δ^{18}O trends would have been present in the ice cores from the GIS, if the GIS had not changed surface elevation. The elevation histories for the four drill sites on the GIS (see Fig. 2a) can then be estimated from the changes in difference between δ^{18}O records from the GIS sites and elevation corrected δ^{18}O records from the two adjacent ice caps. The elevation changes seen in Fig. 2a are corrected for upstream effects due to ice flow at the drill sites[18,19] (see supplementary information), thus showing GIS elevation changes at the four drill site locations. The derivation of the GIS elevation change uncertainty bands shown in Fig. 2a is discussed in the supplementary information.

From Fig. 2a it is seen that the initial response of the GIS to Holocene climatic conditions was a slight increase in elevation at all locations right after the onset of the Holocene (most likely in response to increased precipitation and bedrock uplift). Secondly, the GIS responded to the effects of increased melt at the margins and ice break-off because of rising sea level. The melt and ice break-off induced rapid thinning at the Camp Century and DYE-3 sites, located relatively near the margin. Thirdly the thinning process propagated slowly towards the centre of the GIS, reaching GRIP at the present summit some 4000 years after the onset of the Holocene.

The total gas content of air bubbles trapped in the ice is the only other known parameter in ice cores that is significantly and directly influenced by elevation change. A comparison between the elevation histories for GRIP and Camp Century and their total gas content records[5,20] (Fig. 2b) shows an excellent qualitative agreement between past elevation change and change in total gas content. A detailed quantitative study of the differences between Camp Century and GRIP elevation and total gas content histories also yields strong support for the isotope-based elevation histories (see supplementary information).

Fig. 2c shows a reconstruction of the evolution of Greenland temperatures during the Holocene. This temperature reconstruction is based on Agassiz and Renland average $\delta^{18}O$ corrected for uplift and changes in $\delta^{18}O$ content of the ocean[21]. The conversion from $\delta^{18}O$ to temperature has been obtained through a calibration with borehole temperatures from Camp Century, DYE-3, GRIP and NGRIP[22]. It is noteworthy that the borehole temperature profiles are fully consistent with the Agassiz and Renland average $\delta^{18}O$ record, supporting our assertion that climate in and around Greenland has been homogeneous during the Holocene (see supplementary information).

The average rate of elevation change at the Camp Century and DYE-3 drill sites is also shown in Fig. 2c. It can be inferred that elevations at these two sites near the margin of the GIS respond rapidly to Greenland temperature change. The most significant periods of elevation loss coincided with the climatic optimum 7-10 kyrs ago. This suggests that the GIS responds significantly to a temperature increase of a few degrees Celsius, even though part of the GIS response in the early Holocene also was associated with ice break-off resulting from rising sea level. The colder climate prevailing during the past two millennia induced a slight increase in elevation of the GIS at these sites.

The 600 m decrease in surface elevation observed at Camp Century in the period from 11 ka to 6 ka can be taken as strong support for the finding that the Hall Basin, Kennedy Channel and Kane Basin were completely covered by ice sheet ice during the earliest Holocene, thereby connecting Greenland to the Innuitian ice sheet on Ellesmere Island[14,23]. The breakdown of this interconnection and the retreat of the GIS from the continental shelf edge in Melville Bay then led to a significant decrease in surface elevation at Camp Century. At DYE-3, GIS elevation was reduced by some 400 meters as the width of the southern GIS probably decreased by a third during the transition from glacial to Holocene climatic conditions[24,25].

The novel concept of using the combined evidence from Greenland and Canadian ice cores to extract both a Holocene temperature history (Fig. 2c) and Holocene elevation histories (Fig. 2a) for the GIS is essential for validating efforts to model GIS evolution. Comparing the results of two conceptual modelling efforts[12,26] with the new GRIP Holocene elevation curve, it is possible to give a semi-emperical estimate of the position of the GIS margin during the last glaciation, as only a marginal position at the continental shelf edge is consistent with the observed GRIP elevation history (see Fig. 3a). A comparison of the GRIP elevation change with more recent state-of-the-art 3-D thermomechanical ice sheet models[27,28,29,30], strongly suggests that none of these models capture the evolution in GRIP elevation during the Holocene (see Fig. 3b). The results of the conceptual modelling shown in Fig. 3a, indicate that the 3-D models fail to advance the GIS sufficiently far onto the continental shelf during the last glaciation, possibly due to insufficient understanding of ice sheet/ocean interactions. The poor 3-D model performance might also be a consequence of similarly simplified climatic forcing series being applied in all model runs, e.g. underestimating the amplitude of the Greenland Holocene climatic optimum.

The clear Greenland Holocene climatic optimum now unmasked in GIS ice core δ^{18}O records bring these records into line with borehole temperature data. This rehabilitates δ^{18}O as a reliable temperature proxy, thus paving the way for temperature reconstructions based on high resolution ice core δ^{18}O records. The GIS temperature and elevation histories presented here furthermore suggest that the GIS responds more vigorously to climatic change than indicated by the 3-D models used for GIS projections. Therefore it is entirely possible that a future Greenland temperature increase of a few degrees Celsius will result in GIS mass loss and sea level change contributions larger than hitherto projected.

[1] Witze, Losing Greenland, *Nature*, **452**, 798-802 (2008).

[2] Rignot and Kanagaratnam, Changes in the Velocity Structure of the Greenland Ice Sheet, *Science*, **311**, 986-990 (2006).

[3] Johnsen and Vinther, Stable isotope records from the Greenland Ice Cores, *Encyclopedia of Quat. Sci.*, **2**, 1250-1258 (2007)

[4] Fisher et al., Inter-comparison of Ice Core δ^{18}O and Precipitation Records from Sites in Canada and Greenland over the last 3500 years and over the last few Centuries in detail using EOF Techniques, *NATO ASI Series*, **141**, 297-328 (1996).

[5] Raynaud and Lorius, Climatic Implications of Total Gas Content in Ice at Camp Century, *Nature*, **243**, 283-284 (1973).

[6] Masson-Delmotte et al., Holocene climatic changes in Greenland: Different deuterium excess signals at Greenland Ice Core Project (GRIP) and NorthGRIP, *J. Geophys. Res.,* **110**, D14102 (2005).

[7] Koerner and Fisher., A record of Holocene summer climate from a Canadian high-Arctic ice core, *Nature*, **343**, 630-632, (1990).

[8] Rasmussen et al., A new Greenland ice core chronology for the last glacial termination, *J. Geophys. Res.*, **111**, D06102 doi:10.1029/2005JD006079 (2006).

[9] Vinther et al., A synchronized dating of three Greenland ice cores throughout the Holocene, *J. Geophys. Res.*, **111**, D13102, doi:10.1029/2005JD006921 (2006).

[10] Vinther et al., Synchronizing Ice Cores from the Renland and Agassiz Ice Caps to the Greenland Ice Core Chronology, *J. Geophys. Res.*, **113**, D08115, doi:10.1029/2007JD009143 (2008).

[11] Hammer, et al., Greenland ice sheet evidence of post-glacial volcanism and its climatic impact, *Nature*, **288**, 230-235 (1980).

[12] Cuffey and Clow, Temperature, accumulation, and ice sheet elevation in central Greenland through the last deglacial transition, *J. Geophys. Res.*, **102**, 26383-26396 (1997).

[13] Johnsen et al., A deep ice core from east Greenland, *Meddelelser om Grønland*, **29**, 3–29 (1992).

[14] Blake, Studies of glacial history in Arctic Canada. I. Pumice, radiocarbon dates and differential post-glacial uplift in the eastern Queen Elizabeth Islands, *Can. J. Earth Sci.*, **7**, 634-664 (1970).

[15] Funder, Holocene stratigraphy and vegetation history in the Scoresby Sund area, East Greenland, *Grønlands Geologiske Undersøgelse Bulletin*, **129** (1978).

[16] Dyke and Peltier, Forms, response times and variability of relative sea-level curves, glaciated North America, *Geomorphology*, **32**, 315-333, (2000).

[17] Laskar et al., A long term numerical solution for the insolation quantities of Earth, *Astronomy and Astrophysics*, **428**, 261-285, (2004).

[18] Buchardt and Dahl-Jensen., Estimating the basal melt rate at NorthGRIP using a Monte Carlo technique, *Ann. Glac.*, **45**, 137-142 (2007).

[19] Reeh et al., Dating the Dye-3 ice core by flow model calculations, *AGU Geophysical Monograph*, **33**, 57–65 (1985).

[20] Raynaud et al., Air content along the Greenland Ice Core Project core: A record of surface climatic parameters and elevation in central Greenland, *J. Geophys. Res.*, **102**, 26607-26613 (1997).

[21] Waelbroeck et al., Sea-level and deep water temperature changes derived from benthic foraminifera isotopic records, *Quat. Sci. Rev.*, **21**, 295-305 (2002).

[22] Dahl-Jensen et al., Past temperatures directly from the Greenland ice sheet, *Science*, **282**, 268–271 (1998).
[23] Blake, Glaciated landscapes along Smith Sound, Ellesmere Island, Canada and Greenland, *Ann. Glac.*, **28**, 40-46 (1999).
[24] Jennings et al., Freshwater forcing from the Greenland Ice Sheet during the Younger Dryas: evidence from southeastern Greenland shelf cores, *Quat. Sci. Rev.*, **25**, 282–298 (2006).
[25] Long et al., Late Weichselian relative sea-level changes and ice sheet history in southeast Greenland, *Earth & Plan. Sci. Lett.*, **272**, 8-18 (2008).
[26] Johnsen et al., Greenland palaeotemperatures derived from GRIP bore hole temperature and ice core isotope profiles, *Tellus B*, **47** (5), 624-629 (1995).
[27] Huybrechts, Sea-level changes at the LGM fromice-dynam ic reconstructions of the Greenland and Antarctic ice sheets during the glacial cycles, *Quat. Sci. Rev.*, **21**, 203–231 (2002).
[28] Tarasov and Peltier, Greenland glacial history, borehole constraints and Eemian extent, *J. Geophys. Res.*, **108**, B3, 2124-2143 (2003).
[29] Greve, Relation of measured basal temperatures and the spatial distribution of the geothermal heat flux for the Greenland ice sheet, *Ann. Glac.*, **42**, 424-432 (2005).
[30] Lhomme et al., Tracer transport in the Greenland Ice Sheet: constraints on ice cores and glacial history, *Quat. Sci. Rev.*, **24**, 173–194 (2005).

Supplementary Information accompanies the paper on **www.nature.com/nature**.

Acknowledgements A special acknowledgement is given to lab. tech. Anita Boas, who has meticulously carried out most of the stable isotope measurements presented in this paper during her 38 years at the Copenhagen stable isotope lab. Dr. Weston Blake Jr. from the Geological Survey of Canada is thanked for providing his insight, suggestions and corrections during the drafting of this paper. Two anonymous reviewers are thanked for their constructive comments and suggestions. Prof. Ralf Greve from the Institute of Low Temperature Science, Hokkaido University, Japan, is thanked for providing elevation data from his GIS modelling effort. B.M.V. thanks the Carlsberg Foundation for funding and the Climatic Research Unit at University of East Anglia for hosting his research during all of 2007. V.L and D.R. thank for support from the GDRE Vostok (INSU/CNRS funding and RFBR-CNRS grant 05-05-66801).

Author Information Correspondence and requests for materials should be addressed to B.M.V. (bo@gfy.ku.dk).

Figure 1: **Holocene δ^{18}O records**. **a**, Drill site locations for the ice cores which have been cross-dated to the GICC05 timescale. Site elevations are given in parenthesis. **b,** 20-year averages and millennial scale trends of δ^{18}O during the Holocene as observed in ice core records from six locations in Greenland and Canada. **c,** Uplift corrected Renland and Agassiz Holocene δ^{18}O. 20-year averages and millennial scale trends in the Agassiz and Renland Holocene δ^{18}O records. Annual average insolation at 75°N is shown in orange. **d**, Agassiz and Renland post-glacial bedrock uplift histories and corresponding δ^{18}O correction values.

Figure 2: **Holocene elevation change histories for Greenland ice sheet locations. a,** Elevation changes at the drill sites, after correction for ice-flow-related upstream effects. The shaded bands show the 1σ uncertainties on the elevation histories. **b,** Depositional elevation histories at GRIP and Camp Century compared to total gas measurements carried out on the two ice cores. **c,** Average ice sheet rate of elevation change at DYE-3 and Camp Century compared to Greenland temperature change derived from Agassiz and Renland δ^{18}O records.

Figure 3: Empirical and modelled Holocene elevation change histories for the summit of the Greenland Ice Sheet. a, Elevation change at the GRIP drill site compared to four different estimates from two different simple ice sheet models. The modelled estimates are based on three different assumed maximum advances (ΔL) of the margin of the Greenland Ice Sheet during the Last Glacial Maximum. **b,** Elevation change at the GRIP drill site compared to elevation estimates from four different complex 3-D thermomechanical ice sheet models.


a
80°N
70°N
60°N
50°W
40°W
30°W
Agassiz (1730 m)
Camp Century (1890 m)
NGRIP (2920 m)
GRIP (3230 m)
Renland (2350 m)
DYE-3 (2490 m)
b
-25
-27
-29
-28
-30
-32
-34
-36
-38
-34
-36
-38
-26
-28
-30
-27
-29
-31
-33
Agassiz (1984/87)
Camp Century
NGRIP
GRIP
Renland
DYE-3
$\delta^{18}O$ (‰)
0
2000
4000
6000
8000
10000
Age b2k (years)
c
75°N Annual Average Insolation
Renland
Agassiz (1984/87)
-26
-27
-28
-29
-30
$\delta^{18}O$ (‰)
195
190
185
Insolation (W/m^2)
d
Renland uplift correction
Agassiz uplift correction
0.6
0
-0.6
-1.2
-1.8
$\delta^{18}O$ (‰)
-100
0
100
200
300
Past depression (m)
0
2000
4000
6000
8000
10000
Age b2k (years)


a
Site elevation change (m)
700
600
500
400
300
200
100
0
-100
-200
Camp Century
DYE-3
GRIP
NGRIP
0
2000
4000
6000
8000
10000
Age b2k (years)
b
Change in depositional elevation (m)
300
200
100
0
600
400
200
0
-200
GRIP elevation
GRIP total gas content
Camp Century elevation
Camp Century total gas content
Total gas content (cm^3/kg)
80
85
90
95
100
105
110
115
120
125
0
5000
10000
Age b2k (years)
c
Camp Century & DYE-3 average rate of elevation change
Agassiz & Renland average temperature change
Temperature change (°C)
4
2
0
-2
-4
-6
Rate of ice sheet elevation change (m/century)
-20
-15
-10
-5
0
5
10
15
0
5000
10000
Age b2k (years)

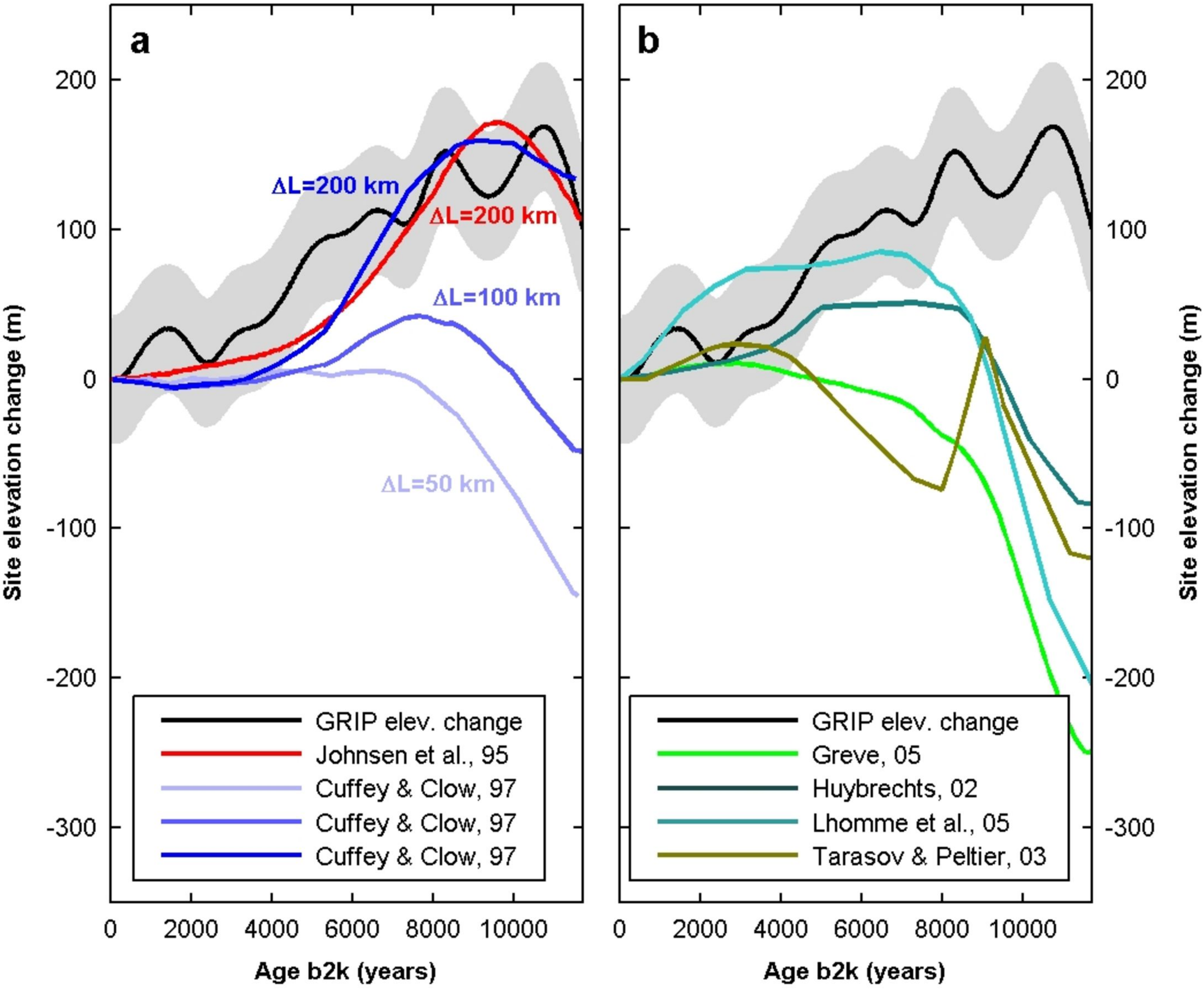
a
b
ΔL=200 km
ΔL=200 km
ΔL=100 km
ΔL=50 km
200
100
0
-100
-200
-300
Site elevation change (m)
0
2000
4000
6000
8000
10000
Age b2k (years)
GRIP elev. change
Johnsen et al., 95
Cuffey & Clow, 97
Cuffey & Clow, 97
Cuffey & Clow, 97
GRIP elev. change
Greve, 05
Huybrechts, 02
Lhomme et al., 05
Tarasov & Peltier, 03

Significant Holocene thinning of the Greenland ice sheet: Supplementary Information

Transferring the GICC05 time scale to the Camp Century core. The GICC05 timescale, which is based on combined DYE-3, GRIP, and NGRIP data in the Holocene, was applied to the Camp Century core by matching prominent volcanic markers seen in electrical conductivity measurements in the Camp Century core to those detected in the other Greenland ice cores. Annual layer thicknesses in the synchronized Camp Century time scale were subsequently verified by annual layer counts across sections where detailed stable isotope data are available.

Renland and Agassiz ice cap stability. The Renland ice cap is situated on a high-elevation plateau on the Renland Peninsula in the Scoresbysund Fiord. The ice cap covers an area of just 1200 km^2 and has a thickness of a few hundred meters. The margins of the ice cap are constrained by the limits of the plateau, with steep descends of approximately 2 km down to the Fiord and the surrounding terrain. At present the Renland ice cap is overflowing the edges of the plateau at numerous locations along the perimeter. Hence the slightest increase/decrease in elevation of the ice sheet surface of the small ice cap will lead to a very significant increase/decrease in drainage, stabilizing the ice volume and making significant elevation change unlikely[1]. Indeed, a conceptual model[2,3] of the Renland ice cap shows that the glacial to Holocene warming and tripling of accumulation resulted in less than 30 meters of change in ice cap thickness.

The 325 m Renland ice core revealed that the ice cap contains a continuous stratigraphy covering the past 60,000 years[4], as well as a three meter layer of Eemian interglacial ice.

As the ice core was not drilled all the way to bedrock it is possible that even older ice exist at the deepest strata of the Renland ice cap. The evidence in the ice core of a well preserved stratigraphy and Eemian ice in the shallow Renland ice cap is testimony to its extraordinary stability.

The Agassiz ice cap is the northern part of a 16,000 km^2 ice field covering the central part of Ellesmere Island, Canada. The two ice cores drilled on the Agassiz ice cap in 1984 and 1987, were both retrieved from a local dome on the ice cap. The location of the dome is determined by an underlying maximum in bedrock elevation. The stability of the dome location has resulted in the formation of a Raymond bump in the internal layering of the ice cap[4]. The thickness of the ice cap is only 127 m at the dome[5], with ice from the Holocene down to a depth of approximately 117 m. The fact that all cores from Agassiz contain the entire Holocene, as well as glacial ice[4] makes it unlikely that the ice has been significantly shallower at the dome during the Holocene. A model study of ice flow between three boreholes in connection with scouring effects, furthermore suggested that the Agassiz ice cap has been stable for the past 8000 years[5]. A maximum in melt layer frequency is registered in the cores from 10,000 to 11,000 years ago according to the GICC05 time scale. Hence it is possible that the Agassiz ice cap thinned during this period. It is, however, important to note that this does not imply that Agassiz δ^{18}O was affected by this possible elevation change. As explained in the next section, the Agassiz ice cap is situated in an area without significant altitude effects on δ^{18}O.

Correcting δ^{18}O records for past changes in surface elevation. From studies of numerous Greenland ice core δ^{18}O records and of observations along the coasts of

Greenland it has been established that the average observed δ^{18}O level over and around the ice sheet can be almost completely described by two effects: An altitude effect (-0.6‰ per 100 m) and a latitude effect (-0.54‰ per degree N)[6,7].

The altitude effect is due to the moist-adiabatic cooling of an air mass forced to rise over the Greenland ice sheet. As the air mass cools, precipitation is formed and fractionation takes place[6].

Observations of snow and ice in the Queen Elizabeth Islands (QEI), Canada show that no significant altitude effects are observed in the QEI, except on the slopes facing Baffin Bay[8]. This observation implies that a precipitating air mass only responds with the well understood altitude effect to the first major topographic barrier it encounters after leaving Baffin Bay, whereas the topography further inland is not of sufficient significance to force the air mass to rise further.

As the post-glacial bedrock rebound observed at the Agassiz drill site is part of a rebound pattern affecting the whole QEI area (thereby also that part of Ellesmere Island facing Baffin Bay), it is to be expected that the usual altitude effect also applies for the post-glacial rebound of the Agassiz ice cap. Hence it is prudent to use the -0.6‰ per 100 m elevation correction, as long as the Agassiz bedrock elevation change is representative of a change affecting the entire QEI area. Had the Agassiz ice cap changed its elevation independently of the QEI area (i.e., by changing its ice thickness), no elevation correction would have been needed.

Correcting δ^{18}O records for upstream effects. A part of the long term isotope signal in ice cores from regions of the GIS with significant ice flow is due to upstream effects; i.e., ice found in the deeper layers at a given drill site originated from precipitation from higher elevation transported by the ice flow. Thus, over time, ice with lower $\delta^{18}O$ values from a higher upstream position flows down-slope to a drill site.

To derive the elevation change at a drill site, it is therefore necessary to correct the record for such upstream effects. Fig. S1a shows the elevation change estimates for the Camp Century, DYE-3, GRIP and NGRIP drill sites before upstream correction, whereas Fig. S1b shows the estimates after correction for upstream effects.

For the DYE-3 record, upstream effects were calculated from a detailed modelling effort performed as part of the Greenland Ice Sheet Program[9], while the NGRIP[10] and Camp Century upstream estimates are based on flow modelling tuned to internal layering in the ice sheet as recorded by radio echo soundings using a Monte Carlo approach.

Estimating uncertainties associated with the elevation histories. The uncertainty bands on the elevation histories shown in Fig S1 are based on two observations. Firstly, the average deviation between the millennial scale trends in Renland and Agassiz $\delta^{18}O$ converts into an uncertainty of ±24 meters. Secondly, the existence of two parallel records from the Agassiz ice cap (see Fig. S2a) can be used to estimate the uncertainty of the millennial scale trends in any given ice core record. The average deviation between Agassiz 1984 and 1987 $\delta^{18}O$ converts into an uncertainty of ±16 meters, yielding a total uncertainty of ±40 meters on the elevation histories. The older Camp Century and DYE-3 records have an additional uncertainty contribution from less precise $\delta^{18}O$ measurements of ±0.15 per mil that converts into an additional ±25 meters. An evaluation of the uncertainty estimates can be obtained from a comparison of GRIP and GISP2[11] ice core $\delta^{18}O$ records (see Fig. 2a). The GISP2 core was drilled just 30 km away from the GRIP drill site and the GISP2 elevation history should therefore be similar to the GRIP elevation history. It is reassuring that GISP2 and GRIP elevation estimates show agreement within the estimated 1σ errors (see Fig. 2b). Note that approximately 10 meters of the 10-40 meter difference 4000-10,000 years ago is due to upstream effects affecting only the GISP2 site. It should also be mentioned that the GISP2 time scale has not been synchronized to GICC05. This is, however, of minor importance as GISP2/GICC05 time scale differences are less than 50 years during the Holocene[12].

Elevation change and total gas content. The influence of elevation change on the total gas content is due to the altitude gradient of atmospheric pressure. Although the relationship between surface pressure and total gas content is relatively straightforward, surface melting can severely disturb the total gas record[13]. It is therefore only possible to use total gas records from ice cores drilled in areas with little or no melt. Total gas measurements have been carried out on two ice cores from such favourable Greenland locations: Camp Century[14,15] and GRIP[16]. A comparison between the total gas data from these cores and their elevation histories is shown in Fig. S3a and S3c. As the existing measurements of total gas content on the Camp Century ice core were rather scarce (purple crosses in Fig. S3c), new measurements on archived Camp Century ice were performed. The new measurements (black crosses in Fig. S3c) are generally lower than the existing data. A likely reason for this offset is gas loss due to diffusion in the ice matrix during the 35 years of storage of the ice core[17], but it is also possible that a systematic shift in absolute values exists between the old pioneering measurements and the new data obtained with a more sophisticated setup. The new Camp Century data are brought into agreement with the original measurements by adding a constant value of 10 cm^3/kg.

The elevation histories for GRIP and Camp Century and their respective total gas content records (Fig. S3a and S3c) agrees qualitatively. However, regressing the change in total gas content towards elevation change (see Fig. S3b and S3d) make it evident that the observed total gas content to elevation slope is steeper than the theoretically predicted total gas content to elevation slope[16] which is -0.015±0.001 cm^3/(kg·m) for the two drill sites. The theoretical value is derived from the temperature and pressure gradients with respect to altitude. The temperature gradient obtained from temperature measurements[18,19] at multiple Greenland automatic weather stations is -0.0070±0.0004 °C/m, whereas the pressure gradient is found to be -0.102±0.003 hPa/m.

The reason for the lack of quantitative agreement between elevation histories and past total gas content is that the total gas content is also affected by changes in summer insolation and surface temperature[20]. Comparing changes in total gas content and elevation change between two ice cores we are able to quantitatively compare theoretical and experimental values. In Fig. S3e the Camp Century to GRIP elevation and total gas content differences are presented. The corresponding regressions (both for old and new Camp Century data) are given in Fig. S3f. The total gas content to elevation slopes for the differential data are close to the theoretically predicted slope of -0.015±0.001 cm^3/(kg·m) for both the old and the new total gas content measurements. This excellent agreement strongly supports the elevation histories for the two sites. The quantitative agreement also indicates that the temperature histories are very similar for Camp Century and GRIP.

Deriving a temperature record from Agassiz and Renland δ^{18}O. In order to obtain an estimate of Holocene Greenland temperature conditions we decided to calibrate the uplift-corrected Agassiz and Renland average δ^{18}O using the borehole temperature profiles from Camp Century[21], DYE-3[22], GRIP[3,23] and NGRIP[24].

A forward modelling approach is applied, where it is assumed that the Agassiz/Renland ice core δ^{18}O profile (after being corrected for uplift and the changing δ^{18}O content of sea water[25]) can be translated into surface temperatures at the drill sites. As the calibration is restricted to the Holocene it is assumed that the δ^{18}O record can be translated into surface temperature using a linear relation to be determined by the calibration. Ice flow is calculated with a non-steady state Dansgaard-Johnsen model with a bottom sliding velocity scaled to be 15% of the horizontal surface velocity[24,26] and (for NGRIP) bottom melting (see Table S1). The non-steady state flow model is forced by the elevation histories for the drill sites (see Fig. S1a), and Holocene accumulation rates are then derived through an iterative approach to fit the Holocene annual layer thickness profiles found in the ice cores[12]. The temperature profile in the ice sheet is calculated by numerical integration of the differential equation for heat conduction in moving firn and ice[27].

Initialization of the ice flow model is carried out with a prescribed mean glacial accumulation rate for the 60.000 years preceding the Holocene[26,28] (see Table S1) and a mean glacial temperature to be determined by the calibration. Using these glacial climatic conditions a steady state temperature profile is calculated. For Camp Century, DYE-3 and GRIP a slab of bedrock with a thickness equal to the ice thickness is included in the steady state calculation and a geothermal heat flux is applied below the slab. The geothermal heat fluxes are determined by the calibration. For NGRIP a bottom melt rate of 6 mm ice per year is applied[10] and the ice temperature at bedrock is always at the pressure melting point.

For the four drill sites a total of 9 unknowns are to be determined by calibration: The difference between glacial and present temperature (1 unknown), the three geothermal heat fluxes (3 unknowns) and the linear temperature/δ^{18}O relation for the four drill sites (5 unknowns, as the temperature/δ^{18}O slope is the same for all four sites). The determination is carried out as follows: First a temperature/δ^{18}O slope is chosen. Secondly the NGRIP linear temperature/δ^{18}O relation (with fixed slope) and the difference between the glacial and the present temperature is determined by minimizing the misfit between NGRIP observed and modelled borehole temperatures. Thirdly the geothermal heat fluxes and the linear temperature/δ^{18}O relations (with fixed slope) are determined for Camp Century, DYE-3 and GRIP by minimizing their misfits. For all cores the misfit calculation is restricted to the part of the profile most affected by Holocene temperature conditions, i.e. the profile down to the depth where the amplitude of a temperature signal from the beginning of the Holocene presently has its maximum amplitude.

The average minimum misfits found by using the above procedure are listed in Table S2. It can be seen that a minimum misfit of 0.047°C is found for a temperature/δ^{18}O slope of 2.1°C/‰. The average misfit is comparable to the typical uncertainty of 0.03-0.05°C on borehole temperature profiles[21,22,24], but it should be noted that the most deviant profile has an average misfit of 0.066°C, which is somewhat larger than expected. However, the modelled and observed borehole temperature profiles in Fig. S4, show that most of the misfit for the four profiles is caused by centennial temperature oscillations in the upper 200 meters of the profiles. As only variations on millennial time scales are of importance for the elevation calculations, it is worth noting that the average misfit for the four profiles drops to 0.037°C, if the upper 200 meters are excluded from the calculations.

The small misfits for all profiles (especially related to millennial-scale temperature variations) is strong evidence that the average of the Agassiz and Renland $\delta^{18}O$ records is indeed a good proxy for the millennial scale variability in the Greenland temperature history during the Holocene, confirming the assertion that the Agassiz/Renland records are representative for climate in the entire Greenlandic region. This implies that the strongest signals in millennial scale Greenland Holocene $\delta^{18}O$ are due to temperature change and elevation change, whereas the many other potential factors proposed to influence precipitation $\delta^{18}O$[29,30] are of secondary importance.

Finally it should be noted that the Holocene temperature/$\delta^{18}O$ slope is estimated with a quantifiable uncertainty, as temperature/$\delta^{18}O$ slopes ranging from 1.9°C/‰ to 2.3°C/‰ all yield average misfits within the expected uncertainty range.

Table S1 Dansgaard-Johnsen ice flow model parameters

Parameter/Drill site	Camp Century	DYE-3	GRIP	NGRIP
Present Ice sheet thickness (m)	1389	2037	3029	3090
Present kink height (m)	500	300	1700	1200
Bottom melting rate (m ice eqv./yr)	-	-	-	0.006
Glacial accumulation rate (m ice eqv /yr)	0.076	0.142	0.107	0.073

Table S2 Borehole temperature modelling results

Temperature/$\delta^{18}O$ slope (°C/‰)	Glacial to present temperature change at present elevation (°C)	Average misfit, all cores (°C)	Average misfit, most deviant core (°C)	Geothermal heat fluxes for Camp Century, DYE-3, GRIP (mW/m^2)
1.7	13.5	0.058	0.108	49.2, 48.1, 48.4
1.8	13.6	0.053	0.092	49.2, 48.1, 48.5
1.9	13.7	0.049	0.076	49.3, 48.2, 48.7
2.0	13.8	0.048	0.064	49.3, 48.2, 48.8
2.1	13.9	0.047	0.066	49.4, 48.1, 48.9
2.2	13.9	0.048	0.074	49.5, 48.2, 48.9
2.3	14.0	0.050	0.082	49.6, 48.2, 49.2
2.4	14.1	0.056	0.091	49.6, 48.3, 49.2
2.5	14.2	0.064	0.099	49.7, 48.3, 49.4

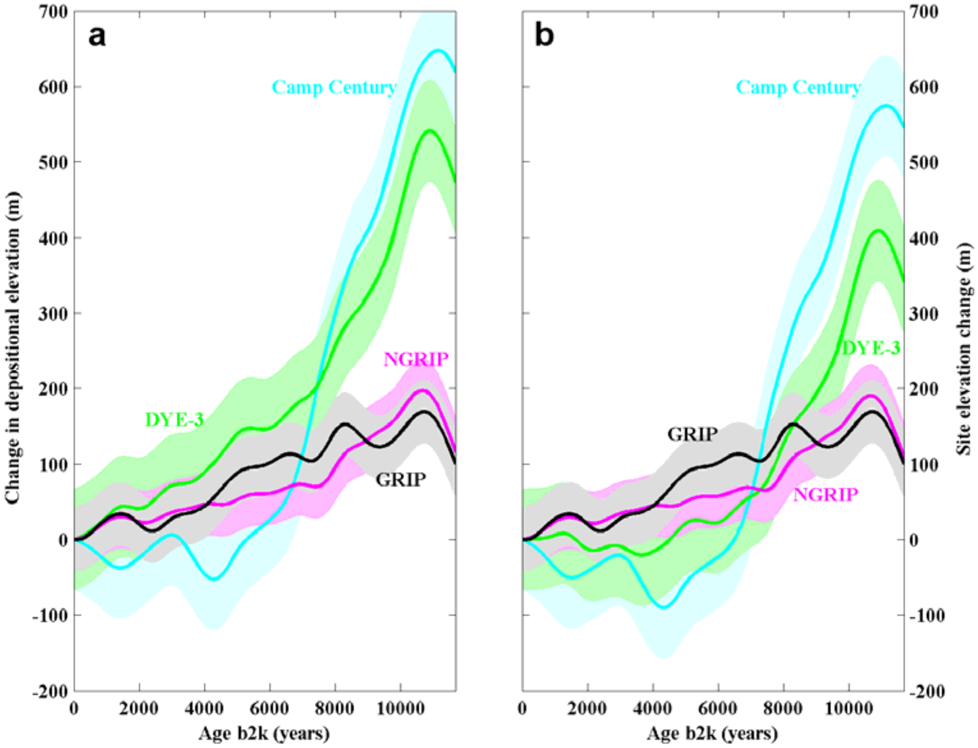

Figure S1: Holocene elevation change histories for four Greenland locations. a, Total change in depositional elevation necessary to explain the millennial scale trends in δ^{18}O seen in the four ice cores. **b,** Elevation changes at the drill sites, after correction for ice-flow related upstream effects. The shaded bands show the 1σ uncertainties on the elevation histories.

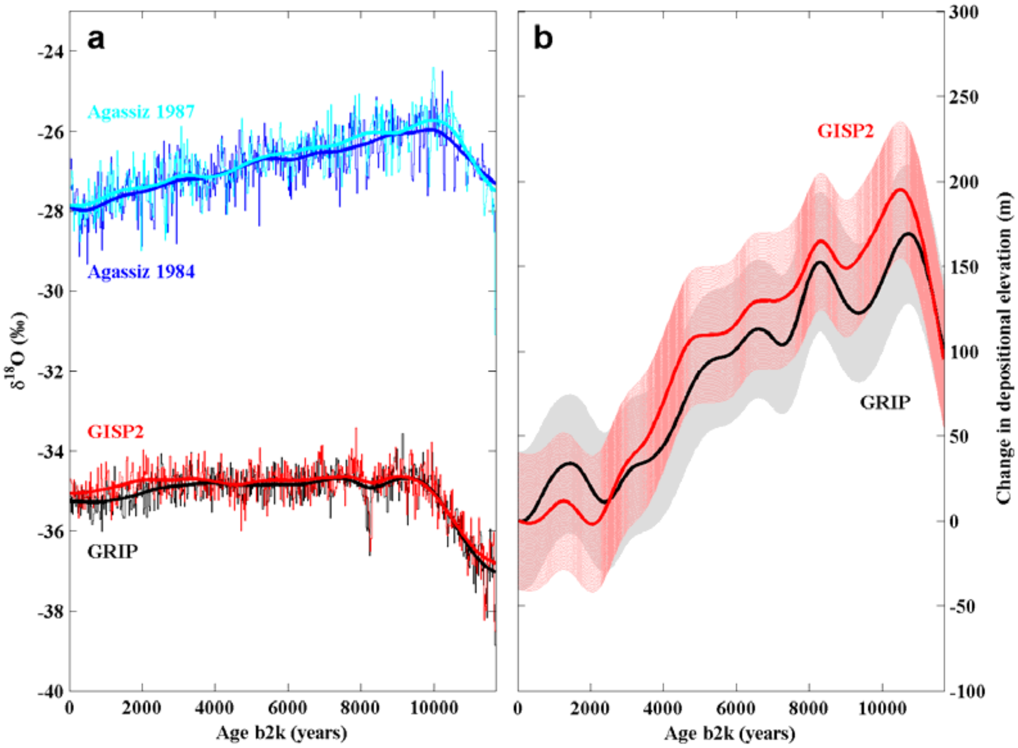

Figure S2: Trends in $\delta^{18}O$ records from ice cores drilled in close proximity to each other. a, Comparison of $\delta^{18}O$ records from two Agassiz ice cores, drilled 30 meters apart and from two central Greenland ice cores (GRIP and GISP2) drilled 30 km apart**. b,** Total change in depositional elevation necessary to explain the millennial scale trends in $\delta^{18}O$ seen in the GRIP and GISP2 ice cores.

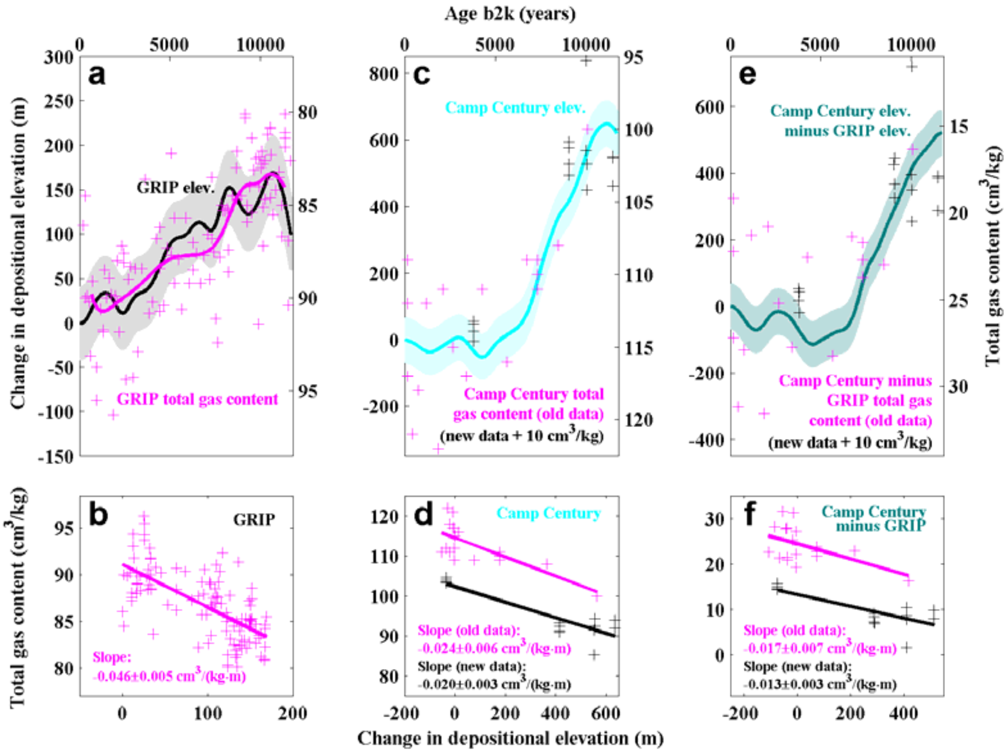

Figure S3: Total gas content compared to observed Holocene elevation change histories for GRIP and Camp Century. a, Elevation change at the GRIP drill site compared to change in total gas content, and **b**, the regression relationship between these parameters. **c, d,** The same for Camp Century. **e,** Difference in elevation change between Camp Century and GRIP drill sites compared to difference in total gas content change, and **f,** the regression relationship between these parameters.

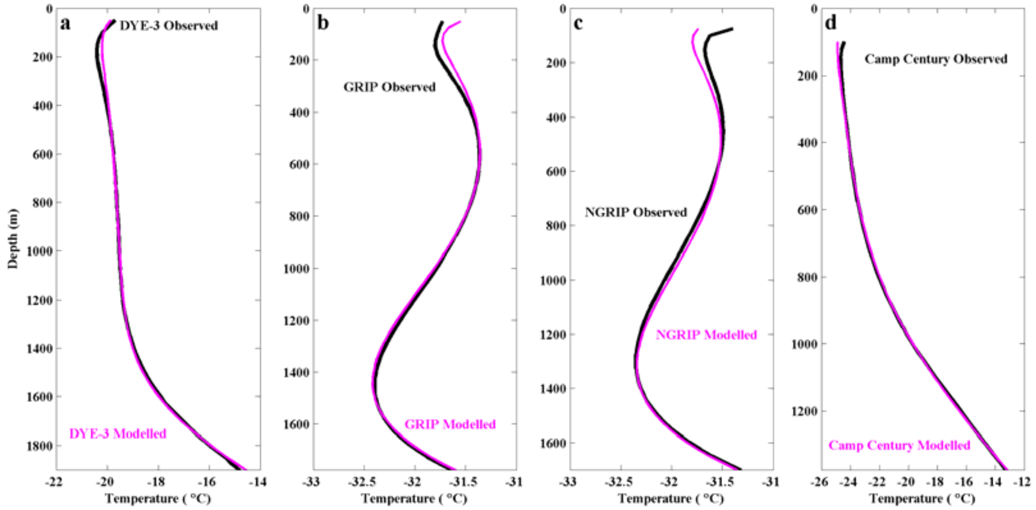

Figure S4: Temperature calibration of Agassiz and Renland average δ^{18}O. Observed borehole temperature profile and the optimal model fit for. **a,** DYE-3, **b,** GRIP, **c,** NGRIP and **d,** Camp Century.

---

[1] Johnsen et al., A deep ice core from east Greenland, *Meddelelser om Grønland*, **29**, 3–29 (1992).

[2] Vialov, Regularities of glacial ice shields movement and the theory of glaciers, I*nt. Ass. Hydrol. Sci. Pub.,* **47**, 266-275 (1958).

[3] Johnsen et al., Greenland palaeotemperatures derived from GRIP bore hole temperature and ice core isotope profiles, *Tellus B*, **47**(5), 624-629 (1995).

[3] Dahl-Jensen et al., Past temperatures directly from the Greenland ice sheet, *Science*, **282**, 268–271 (1998).

[4] Vinther et al., Synchronizing Ice Cores from the Renland and Agassiz Ice Caps to the Greenland Ice Core Chronology, *J. Geophys. Res.*, **113**, D08115 (2008).

[5] Fisher et al., Holocene climatic records from Agassiz Ice Cap, Ellesmere Island, NWT, Canada, Holocene, **5**, 19-24 (1995).

[6] Dansgaard, The isotopic composition of natural waters, *Meddelelser om Grønland*, **165**, 2 (1961).

[7] Johnsen et al., The origin of Arctic precipitation under present and glacial conditions, *Tellus*, **41B**, 452-468 (1989).

[8] Koerner, Accumulation, ablation, and oxygen isotope variations on the Queen Elizabeth Islands ice caps, Canada, *J. Glac.*, **22**, 86, 25-41 (1979).

[9] Reeh et al., Dating the Dye-3 ice core by flow model calculations, AGU *Geophysical Monograph*, **33**, 57–65 (1985).

[10] Buchardt and Dahl-Jensen., Estimating the basal melt rate at NorthGRIP using a Monte Carlo technique, *Ann. Glac.*, **45**, 137-142 (2007).

[11] Stuiver et al., Is there evidence for solar forcing of climate in the GISP2 oxygen isotope record?, *Quaternary Research*, **48**, 259-266 (1997).

[12] Vinther et al., A synchronized dating of three Greenland ice cores throughout the Holocene, *J. Geophys. Res.*, **111**, D13102, doi:10.1029/2005JD006921 (2006).

[13] Herron and Langway, Deriviation of paleoelevations from total air content of two deep Greenland ice cores, *IAHS*, **170**, 283-295 (1987).

[14] Raynaud and Lorius, Climatic Implications of Total Gas Content in Ice at Camp Century, *Nature*, **243**, 283-284 (1973).

[15] Raynaud and Lebel, Total gas content and surface elevation of polar ice sheets, *Nature*, **281**, 289-291 (1979).

[16] Raynaud et al., Air content along the Greenland Ice Core Project core: A record of surface climatic parameters and elevation in central Greenland, *J. Geophys. Res.*, **102**, 26607-26613 (1997).

[17] Ikeda-Fukazawa et al., Effects of molecular diffusion on trapped gas composition in polar ice cores, *Earth & Plan. Sci. Lett.*, **229**, 183-192 (2005).

[18] Box and Rinke., Evaluation of Greenland Ice Sheet Surface Climate in the HIRHAM Regional Climate Model Using Automatic Weather Station Data, *J. Clim.*, 16, 1302-1319 (2003).

[19] Steffen and Box, Surface climatology of the Greenland ice sheet: Greenland Climate Network 1995-1999, *J. Geophys. Res.*, **106**, D24, 33951-33964 (2001).

[20] Raynaud et al., The local insolation signature of air content in Antarctic ice. A new step toward an absolute dating of ice records, *Earth & Plan. Sci. Lett.*, **261**, 337-349 (2007).

[21] Gundestrup et al, Bore-hole survey at Camp Century, 1989, *Cold regions science and technology*, **21**, 187-193 (1993).

---

[22] Dahl-Jensen and Johnsen, Palaeotemperatures still exist in the Greenland ice sheet, *Nature*, **320**, 250-252 (1986).

[23] Dahl-Jensen et al., Past temperatures directly from the Greenland ice sheet, *Science*, **282**, 268–271 (1998).

[24] Dahl-Jensen et al., Basal melt at NorthGRIP modeled from borehole, ice-core and radio-echo sounder observations, *Ann. Glaciology,* **37**, 207-212 (2003).

[25] Waelbroeck et al., Sea-level and deep water temperature changes derived from benthic foraminifera isotopic records. *Quat. Sci. Rev.*, **21**, 295-305 (2002).

[26] Johnsen and Dansgaard, On flow model dating of stable isotope records from Greenland ice cores, *NATO ASI Series*, **2**, 13-24 (1992).

[27] Johnsen, Stable isotope profiles compared with temperature profiles in firn with historical temperature records, in *Proc. Symp. on Iso-topes and Impurities in Snow and Ice, I.U.G.G. XVI*, General Assembly, Grenoble, 1975, 388–392 (1977).

[28] Johnsen et al., Oxygen isotope and palaeotemperature records from six Greenland ice-core stations: Camp Century, Dye-3, GRIP, GISP2, Renland and NorthGRIP, *J. Quart. Scien.*, **16**(4), 299-307 (2001).

[29] Masson-Delmotte et al., GRIP Deuterium Excess Reveals Rapid and Orbital-Scale Changes in Greenland Moisture Origin, *Science*, **309**, 118-121 (2005).

[30] Masson-Delmotte et al., Holocene climatic changes in Greenland: Different deuterium excess signals at Greenland Ice Core Project (GRIP) and NorthGRIP, *J. Geophys. Res.,* **110**, D14102 (2005).